Introduction of variability into pantograph-catenary dynamic simulations

Olivier Vo Van

To cite this version:

Olivier Vo Van. Introduction of variability into pantograph-catenary dynamic simulations. Mechanics [physics.med-ph]. Ecole nationale supérieure d'arts et métiers - ENSAM, 2016. English. NNT : 2016ENAM0021 . tel-01404271

HAL Id: tel-01404271
https://pastel.hal.science/tel-01404271

Submitted on 28 Nov 2016

2016-ENAM-0021

École doctorale nº 432 : Science des Métiers de l'ingénieur

Doctorat ParisTech

THÈSE

pour obtenir le grade de docteur délivré par

l'École Nationale Supérieure d'Arts et Métiers

Spécialité " mécanique"

présentée et soutenue publiquement par

Olivier VO VAN

le 6 juillet 2016

Introduction of variability into Pantograph-Catenary dynamic simulations

Directeur de thèse: **Etienne BALMES**
Co-encadrement de la thèse: **Jean-Pierre MASSAT**

Jury

M. Jerôme ANTONI, Professeur, LVA, INSA Lyon	Président
M. Stephano BRUNI, Professeur, MECC, Politecnico di Milano	Rapporteur
M. Izhak BUCHER, Professeur, Dynamics Laboratory, Technion	Rapporteur
M. Etienne BALMES, Professeur, PIMM, Arts & Métiers ParisTech	Examinateur
M. Jean-Pierre MASSAT, Docteur, I&P, SNCF Réseau	Examinateur

T
H
È
S
E

Arts et Métiers ParisTech - Campus de Paris
PIMM

Acknowledgements

Once upon a time "me", starting an internship proposed and directed by Etienne Balmès at SNCF and supervised by Jean-Pierre Massat. After this trial during which I relentlessly studied fatigue with my new friend OSCAR, Jean-Pierre proposed me to continue the adventure for no less than three more years. And I accepted, but only after a small break travelling the Asian part of the world. This is how my doctoral thesis started within the framework of a CIFRE in the French railway company SNCF in partnership with the PIMM laboratory at Arts & Métiers ParisTech.

Through these three years that I first feared to live as potential imprisonment, I discovered the freedom inherent in a PhD well supervised. For that and for the non-quantifiable help (that would thus have made any numerical models diverge), I would sincerely like to thank Etienne Balmès. His continuous scientific rigour regarding my results, comprehension skills when even I don't understand what I explain and his wise suggestions, often enlightened me along this tricky path. I thank Jean-Pierre Massat too for having trusted me and given me time he didn't have to discuss about all the industrial aspect of my PhD and more particularly, for teaching me his art of communication for presentations. His expectation in that field seemed unreachable and I hope the iterative scheme introduced finally converged to them.

My acknowledgements obviously go to Stephano Bruni and Izhac Bucher for having accepted to read my work and to be thesis referees for me, and to Jerôme Antoni for taking the role of president of jury. I am deeply grateful that all members agreed to nominate me for the Bezier prize.

I also thank all colleagues that participated to my punctual meeting, my supervisors, Mac-Lan, Xavier, Frank, Guido, Rabbie, Arnaud, Gérard, Andréa and more, for valuable information and observations, and heated debate on each slide I presented. I would like to particularly thank Guido without whom damping tests would have never been possible, and Jean-Philippe for his decoding of Etienne's explanations.

Then I would like to thank my two sportive trainees, Lucie Baudin and Pauline Bonnet for having standing me as supervisor and of course for their help in my work. I hope that they appreciated to discover the scientific research with me and that at least 50% of them will consider doing a PhD!

I am also grateful to all the PhD students of the group formed at SNCF for sharing their knowledge and experience, especially to Ivan with who I shared my office, climbed up summits with snowshoes or crampons, ice axes and rope or just shoes; and to Noura for accepting to debate with me about anything I had in mind.

Finally, I thank my family, my close friends and particularly Marie-Emilie, for clearing my mind when I needed (even when I did not need by the way). Thinking about completely unrelated things always helps to step back and put things into perspective.

May 2016

Contents

Résumé en français

Introduction

Contexte général

Le réseau ferré français est constitué de plus de $30000km$ de voies dont la moitié est alimentée en électricité. Le réseau électrifié est le plus intensément utilisé puisque plus de 90% du trafic de passagers se fait sur celui-ci. En Chine, ce sont plus de $60000km$ de voies électrifiées qui sont en service actuellement, avec un réseau en pleine croissance. Le train à alimentation électrique est donc en continuelle expansion dans le monde. L'énergie électrique est habituellement collectée à l'aide d'une ligne de contact située en hauteur sur la voie et d'un pantographe fixé au dessus du train. Ce système d'alimentation est le seul viable à haute vitesse en milieu extérieur actuellement.

Ce système a pourtant ses limitations. Les ondes générées par l'interaction pantographe-caténaire se propageant dans les câbles vers l'avant du pantographe sont le principal facteur limitant la vitesse des trains. L'onde se propageant vers l'arrière du pantographe peut quant à elle perturber le captage d'un second pantographe le cas échéant.

Par ailleurs, les conséquences d'un accident caténaire peuvent engendrer un retard de l'ensemble du trafic ayant des conséquences économiques importantes. Il est donc nécessaire d'avoir une bonne estimation de la durée de vie des composants de la caténaire. Pour ce faire, des contrôles visuels et des mesures de géométrie sont effectués périodiquement. Ces contrôles sont lents et peu adaptés à l'intensité du trafic actuelle et future.

Pour augmenter la périodicité du contrôle de l'état de la caténaire, le train instrumenté IRIS320 a été équipé d'un pantographe permettant de mesurer l'effort de contact jusqu'à $320km/h$. L'objectif était d'exploiter ces efforts de contact pour détecter les défauts dans la caténaire et à long terme développer les stratégies de maintenance conditionnelle. La thèse de Jean-Pierre Massat [1] ouvrait ce sujet et a mené à de bonne détections de défauts types mais les résultats n'étaient pas assez fiables pour être industrialisés. L'une des conclusions de ces travaux a été que la variabilité de l'effort mesurée était trop importante car trop sensible à la vitesse du train et au vent. De plus, les efforts étant filtrés à $20Hz$, les défauts locaux sont très difficilement détectables.

Les mesures dynamiques sont très limitées, les seules grandeurs observées sont les forces accélérations dans le pantographe et le soulèvement du fil de contact au poteau. De plus, les conditions d'essais sont limitées par le prix et il est difficile d'obtenir les bonnes vitesses, combinaisons de pantographes, vent, ... Il est donc indispensable d'enrichir les essais grâce à des modèles numériques donnant accès à toutes les variables d'intérêt et permettant de tester des conditions critiques rares. Depuis 2003, SNCF et SDTools développent le logiciel OSCAR permettant la simulation dynamique pantographe-caténaire. Cette thèse représente l'aboutissement actuelle du logiciel et a pour objectif d'orienter la conception de caténaires en développant la compréhension du système couplé ainsi que d'améliorer la robustesse de l'outil de simulation en introduisant les variabilités potentielles. Ces travaux ont été rendus possibles grâce à une forte amélioration des performances d'OSCAR qui permet maintenant d'effectuer des études paramétriques et statistiques détaillées.

Contributions de la thèse

Les modèles d'interaction pantographe-caténaire sont généralement exploités pour la conception de couples permettant une réduction de la maintenance et une augmentation de la durée de vie. Pour l'homologation virtuelle, l'outil de simulation peut être utilisé pour détecter les conditions les plus critiques et ainsi réduire le nombre d'essais nécessaires. Pour améliorer la conception du couple, la première étape est de comprendre les phénomènes intervenant dans le système. Chacun des éléments du couple a son propre comportement dynamique et le contact glissant génère des ondes dans les câbles qui complexifient fortement l'étude.

Les ondes générées à l'avant du pantographe représentent le principal verrou à la très haute vitesse. Quand la vitesse du train s'approche de celle des ondes dans les câbles, les niveaux d'efforts et de soulèvements augmentent fortement et endommagent la caténaire et le pantographe. À vitesse plus conventionnelle, l'onde se propageant vers l'arrière perturbe le contact mécanique du pantographe suiveur.

La **première contribution de cette thèse** est le développement d'une meilleure compréhension de l'interaction dynamique entre le pantographe et la caténaire. Cette interaction a été décomposée en différents phénomènes tels que la réponse dynamique du pantographe à la géométrie de la caténaire, la propagation des ondes et le comportement dynamique de la caténaire. Comprendre la contribution de chacun de ces phénomènes est indispensable à l'amélioration de la conception.

La **deuxième contribution** concerne la réduction de l'incertitude épistémique existant dans le modèle. Ainsi, la raideur de contact a été confrontée aux théories de contact locales, l'amortissement a été recalé sur des essais originaux réalisés sur une caténaire à taille réelle et l'influence de la taille des mailles du modèle éléments finis (EF) a été analysée. La deuxième orientation majeure de ces travaux est la caractérisation des incertitudes et la proposition de stratégies pour son exploitation La **troisième contribution** concerne la caractérisation statistique des paramètres physique de la caténaire à l'aide des mesures disponibles. Une première analyse de sensibilité a permis d'orienter les travaux en comparant différentes sources de variabilité. Une étude sur une portée isolée a ensuite été effectuée puis étendue à l'ensemble du canton. À partir de ce modèle statistique de géométrie de caténaire, la **quatrième contribution** a été de propager ces incertitudes à travers les modèles statiques et dynamiques, de définir les critères adéquats de chacun de ces modèles et de discuter de l'utilisation possible de critères liés à la géométrie statique de la caténaire pour caractériser la qualité de contact dynamique.

R.1 État de l'art

La majorité des lignes ferroviaires électriques longue distance sont équipées de caténaires, structures composées d'un ensemble de câbles, dans lequel circule le courant. Celui-ci est capté à l'aide d'un pantographe qui est fixé sur le toit du train. Le glissement du pantographe sous la caténaire est un problème mécanique non linéaire complexe.

Ce chapitre reprend les problématiques actuelles industrielles dans la section R.1.1 puis scientifiques dans la section R.1.2. Une analyse de sensibilité préliminaire est ensuite développée en section R.1.3 pour orienter sur le choix des travaux à développer par la suite.

R.1.1 Contexte industriel

Les deux ensembles mécaniques nécessaires au captage sont la caténaire et le pantographe. La figure R.1 détaille les composants de la caténaire. Elle est constituée d'un câble porteur (bleu) qui soutient un fil de contact (orange) pour le maintenir horizontal à l'aide de pendules placés ponctuellement entre les portées. Le câble porteur est accroché aux poteaux par l'intermédiaire de consoles. Le fil de contact est quant à lui accroché à la console par l'intermédiaire d'un bras de rappel qui permet d'appliquer un effort horizontal sur le fil et ainsi induire un désaxement pour répartir l'usure du pantographe sur une large bande. La tension mécanique dans les câbles est régulée grâce à des équipements tendeurs (système de masses et poulies) qui permettent de garder une tension quasi constante sur une large plage de température.

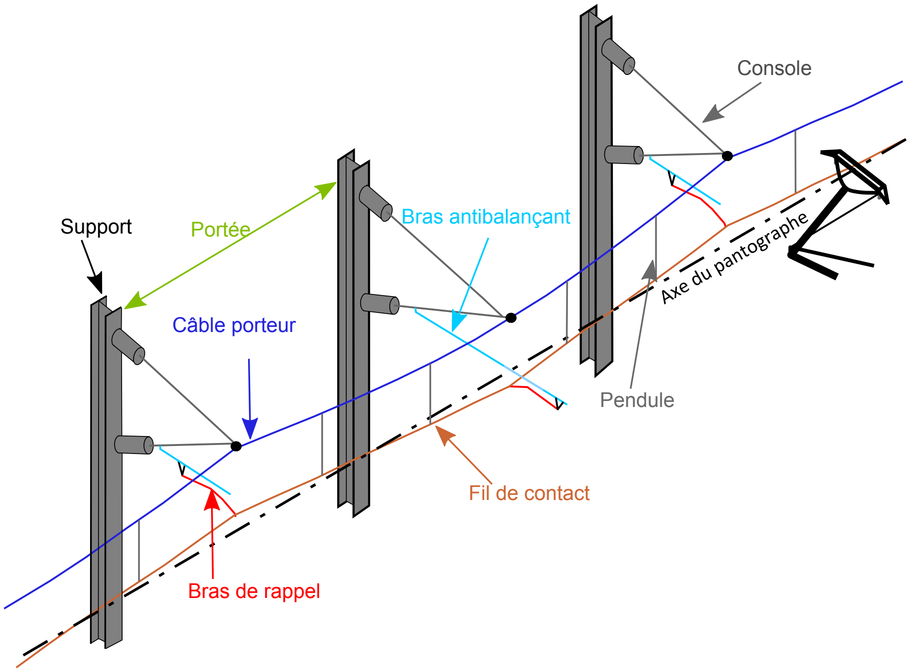

Figure R.1: Composition d'une caténaire $25kV$

Le pantographe est un assemblage de tubes articulés représenté figure R.2 qui adapte son déploiement en fonction de la caténaire pour conserver un contact permanent avec le fil de contact. L'effort statique est contrôlé à l'aide d'un coussin pneumatique et de bielles. La partie du pantographe en contact avec la caténaire s'appelle la bande de frottement, c'est la pièce d'usure du système. Elle est fixée sur un archet qui est lui-même fixé sur le grand cadre par l'intermédiaire de boites à ressort servant à absorber les vibrations hautes fréquences.

Le principal problème rencontré dans cette interaction dynamique entre le pantographe et la caténaire est la dégradation du fil de contact et des bandes de frottement due à une usure mécanique lorsque l'effort appliqué est trop important ou à une usure électrique lorsque l'effort appliqué est insuffisant. En effet, il se forme dans ce cas des arcs électriques qui endommagent rapidement le système. L'évaluation de la qualité du contact se fait actuellement à l'aide de deux critères détaillés dans la norme européenne EN50317 [2]. Le premier est un critère électrique basé sur des mesures optiques, NQ (non-qualité)

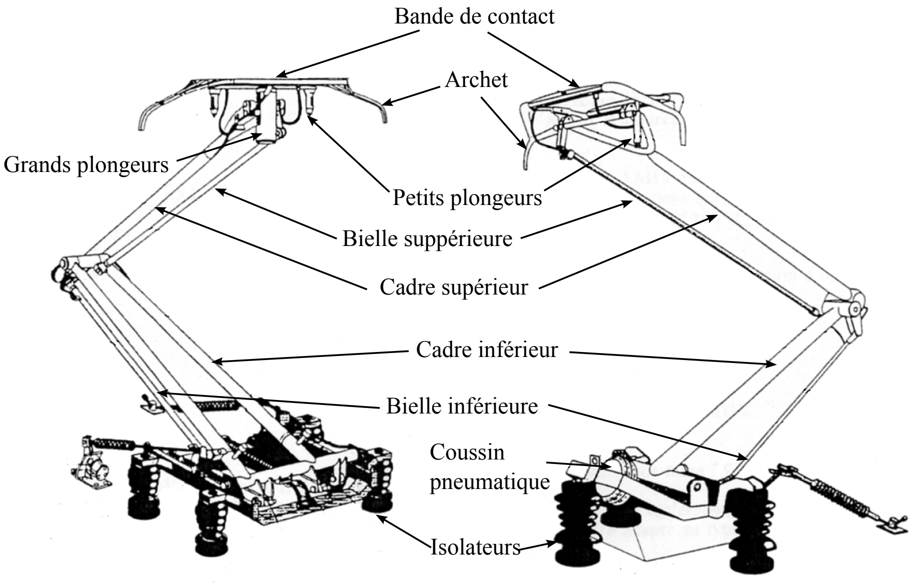

Figure R.2: Composition des pantographes GPU (gauche) et CX (droite)

dont la valeur doit être inférieure à 0.2. Uniquement les arcs d'une durée de plus de $5ms$ sont pris en comptes. Leur temps cumulé est divisé par le temps pendant lequel le courant collecté est supérieure à 30% du courant nominal.

$$NQ = \frac{100 \cdot (\text{Temps d'arc cumulé})}{\text{Temps de captage réel}} \tag{R.1}$$

Le deuxième critère est mécanique et utilise l'effort contact. Il est basé sur l'hypothèse que l'effort de contact filtré à $20Hz$ suit une loi normale et que les arcs électriques se forment lorsque l'effort est nul (ou négatif). Cela signifie que la probabilité d'arc est de moins de 0.14% si la condition

$$F_m - 3 \cdot \sigma(F_c)_{20Hz} > 0 \tag{R.2}$$

est remplie. Ce critère mécanique est donc en théorie équivalent au critère électrique mais cette équivalence n'a pour l'instant jamais été démontrée.

Ces critères sont utilisés lors de l'homologation de matériels roulants ou de caténaires. Afin d'éviter de devoir homologuer chaque train pour chaque caténaire, des spécificités techniques d'interopérabilité (STI) ont été développées en Europe. Malgré cela, le nombre d'essais pour homologuer un train reste important. L'utilisation d'outils de simulation pourrait permettre de réduire ce nombre comme l'a montré le sous-projet PantoTRAIN du projet européen TrioTRAIN lancé en 2009. L'un des principaux problèmes est actuellement la variabilité des résultats des essais qui ne peut pas être reproduite à l'aide des simulations déterministes.

Du point de vue de la maintenance de la caténaire, les normes françaises IN1797 [3] indique que la géométrie de la caténaire (hauteur du fil de contact par rapport au rail) doit être contrôlée périodiquement. Ces normes permettent de s'assurer que la géométrie de la caténaire est proche de la géométrie de conception. C'est de cette manière que la qualité de captage est supposée être assurée. Il n'existe donc actuellement pas de lien direct entre normes de maintenance et qualité de captage.

R.1.2 Contexte scientifique

Le modèle d'interaction pantographe-caténaire est utilisé pour de nombreuses applications industrielles pour la maintenance (usure, fatigue) comme pour la conception (optimisation du couple pantographe-caténaire, étude de propagation des ondes) et de nombreux outils de ce type ont été développés dans le monde [4]. De son coté, SNCF développe depuis 2004 un de ces outils de simulation sous le nom de OSCAR (Outil de Simulation du CAptage pour la Reconnaissance des défauts). C'est sous ce logiciel que l'ensemble des travaux a été effectué.

La caténaire, figure R.3 (gauche), est modélisée en éléments finis par des poutres pour les câbles, des masses pour les griffes et des barres pour les autres éléments. Le pantographe est modélisé par un système masses-ressorts (droite) qui permet de représenter les premiers modes de vibration du pantographe. Le contact est effectué à l'aide d'une raideur de contact représentant l'interpénétration entre la bande de frottement et le fil de contact.

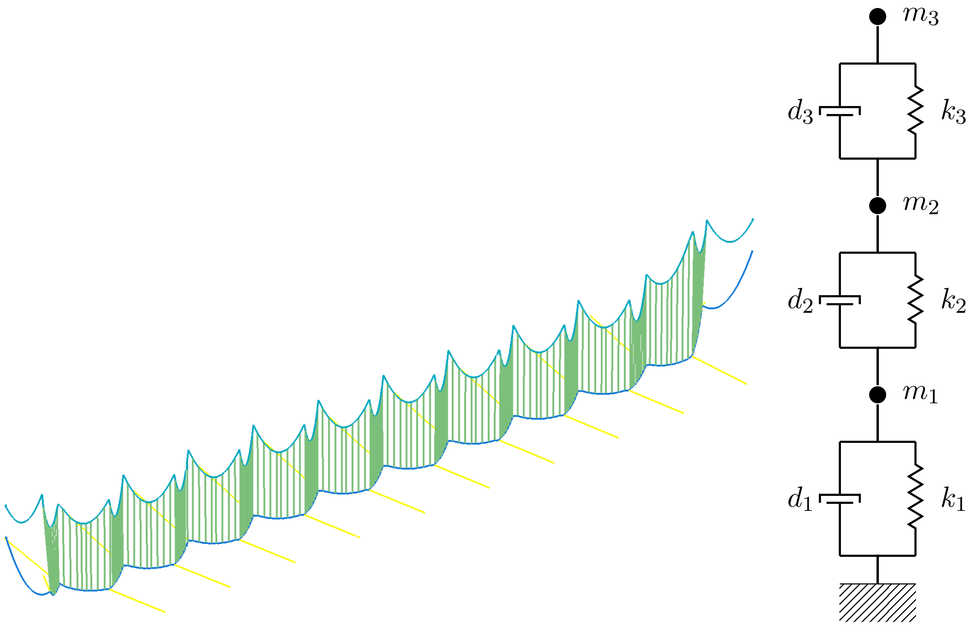

Figure R.3: Modèle éléments finis d'un canton de caténaire (gauche) et modèle masses-ressorts d'un pantographe (droite)

L'objectif de la simulation dynamique est d'obtenir l'effort de contact et les soulèvements de la caténaire afin d'évaluer la qualité de captage. Les récentes améliorations des outils de simulation et l'augmentation rapide de la puissance de calcul permet aujourd'hui de réaliser rapidement des études paramétriques. Des cartes d'efforts de contact et des amplitudes de leur spectre spatial en fonction de la vitesse du pantographe ont ainsi pu être obtenues. La figure R.4 montre deux de ces cartes. On observe clairement une périodicité spatiale de l'effort de contact avec un maximum local positionné en fin de portée avant le dernier pendule. Cette périodicité se retrouve aussi sur le spectre d'amplitude. On observe de nombreuses lignes verticales et de courbes qui se croisent. Certaines de ces courbes deviennent droites lorsqu'on observe ce spectre dans le domaine spatial. Les variations de l'effort de contact sont donc générées par des phénomènes spatiaux et temporels.

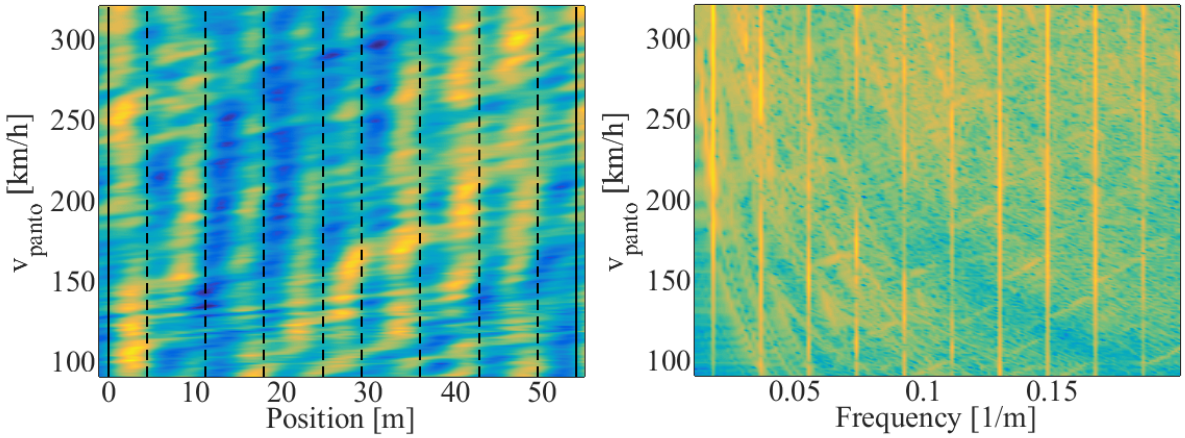

Figure R.4: Effort de contact le long d'une portée filtré à $0.22m^{-1}$ avec les pendules indiqués en lignes discontinues et les poteaux en trait plein (gauche) et l'amplitude de son spectre spatial (droite) en fonction de la vitesse du pantographe

La figure R.5 montre le soulèvement du fil de contact sous un bras de rappel et le spectre d'amplitude de son accélération. A gauche, on observe clairement une zone de transition aux environs de $170km/h$. A droite, un réseau de courbes peut être observé et la coïncidence de celles-ci entraine une localisation fréquentielle d'énergie importante pour certaines vitesses du pantographe.

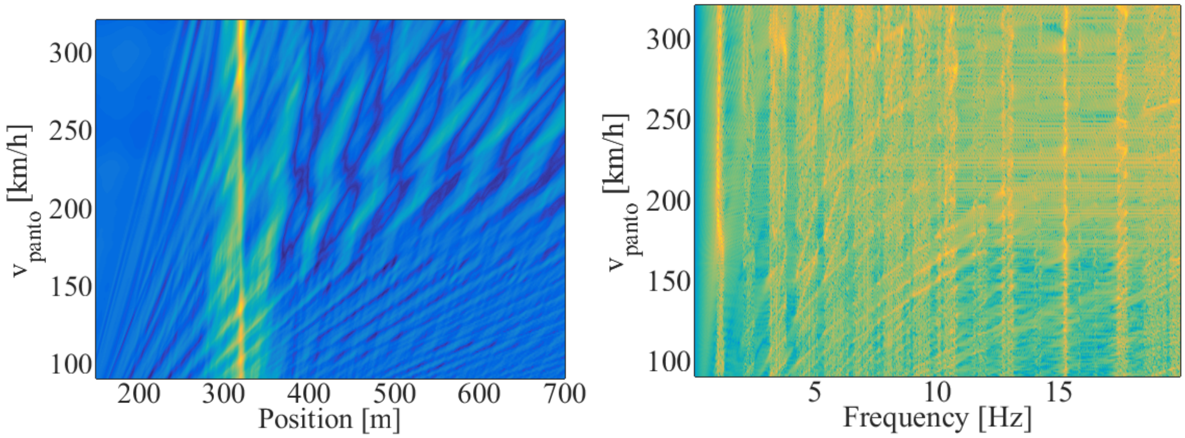

Figure R.5: Soulèvement du fil de contact sous un bras de rappel en fonction de la position du pantographe (gauche) et amplitude du spectre temporel de ce soulèvement (droite) en fonction de la vitesse du pantographe

Les phénomènes identifiés qui apparaissent sont la réponse dynamique du pantographe à la géométrie statique de la caténaire, les propagations des ondes dans les câbles et leur réflexion/transmission sur les pendules, bras de rappel ou poteaux.

L'outil de simulation est suffisamment évolué pour étudier ces phénomènes. Pourtant, de nombreuses incertitudes subsistent. Certaines sont irréductibles, elles sont générées par des sources aléatoires qu'il est possible de caractériser statistiquement. La figure 1.28 reprend l'ensemble des sources potentielles de cette variabilité.

Un autre type d'incertitude, dite épistémique, peut être réduit par l'amélioration des connaissances. C'est le cas par exemple de l'incertitude de modèle. Dans notre cas, il existe une incertitude sur la modélisation et les valeur d'amortissement choisis ainsi que sur la valeur de la raideur de contact.

R.1.3 Analyse de sensibilité préliminaire

Seulement trois des paramètres physiques identifiés en tant que source de variabilité peuvent être simulés actuellement, la géométrie de la caténaire, l'usure du fil de contact et l'effort aérodynamique appliqué sur le pantographe.

Ces trois sources de variabilité ont donc été modélisées à partir de mesures. Pour chacune d'elles, un signal a été généré aléatoirement à partir du spectre d'amplitude mesuré et d'une phase aléatoire par transformée de Fourier inverse.

Mille simulations ont été réalisées pour chaque source indépendamment. Les efforts temporels ne pouvant être directement comparés, trois critères ont été conservés et l'écart type de ces critères sur l'ensemble des simulations est comparé

- $\sigma(\mu(F_c)_i)$ l'écart type de l'ensemble des moyennes d'effort de contact
- $\sigma(\sigma(F_c)_i)$ l'écart type de l'ensemble des écarts types d'efforts de contact
- $\sigma(\frac{\sigma(F_c)_i}{\mu(F_c)_i})$ l'écart type des coefficients de variation des efforts de contact.

Le tableau R.1 montre que ce sont la géométrie et l'aérodynamique qui influent le plus sur $\sigma(\frac{\sigma(F_c)_i}{\mu(F_c)_i})$, donc sur le captage. Ces sources de variabilité influent de façon différente. La force aérodynamique joue en particulier sur l'effort moyen et introduit peu de variations autour de cet effort moyen alors que l'inverse est observé pour la géométrie.

Table R.1: Écart type de trois moments statistiques de l'effort de contact

Critères Sources d'incertitude	$\sigma(\mu(F_c)_i)$	$\sigma(\sigma(F_c)_i)$	$\sigma(\frac{\sigma(F_c)_i}{\mu(F_c)_i})$
Géométrique	0.18	1.2	0.0087
Aérodynamique	3.5	0.21	0.0068
Usure	0.02	0.24	0.0019

Le manque de mesures concernant la force aérodynamique appliquée sur le pantographe rend son étude difficile. La seule source de variabilité détaillée par la suite sera donc la géométrie de la caténaire.

R.2 Propriétés dynamiques du pantographe et de la caténaire

L'effort de contact dynamique est composé de plusieurs phénomènes qui peuvent être étudiés séparément. La section R.2.1 étudie l'impacte de la géométrie statique de la caténaire sur l'effort de contact. La section R.2.2 détaille un modèle analytique de propagation des ondes et de leur réflexion, transmission lors du passage de différents points de la caténaire. Enfin, la section R.2.3 présente l'impact de ces ondes et de leurs coïncidences sur un effort de contact.

R.2.1 Réponse dynamique du pantographe à la géométrie statique de la caténaire

La géométrie de la caténaire correspond à la hauteur du fil de contact le long de la caténaire. La figure R.6 (droite) montre cette géométrie le long d'une portée. On observe bien l'effet chainette qui se forme entre les pendules indiqués en trait discontinu. A gauche, le modèle du pantographe est représenté avec le fil de contact. Les entrées du modèle sont la vitesse du fil de contact V_{CW} et l'effort statique F_0. Les ondes V_r, $V_{t+,panto}$ et $V_{t-,panto}$ ne sont pas considérées ici puisqu'on cherche à calculer l'effort F_{geom} dû uniquement à la géométrie.

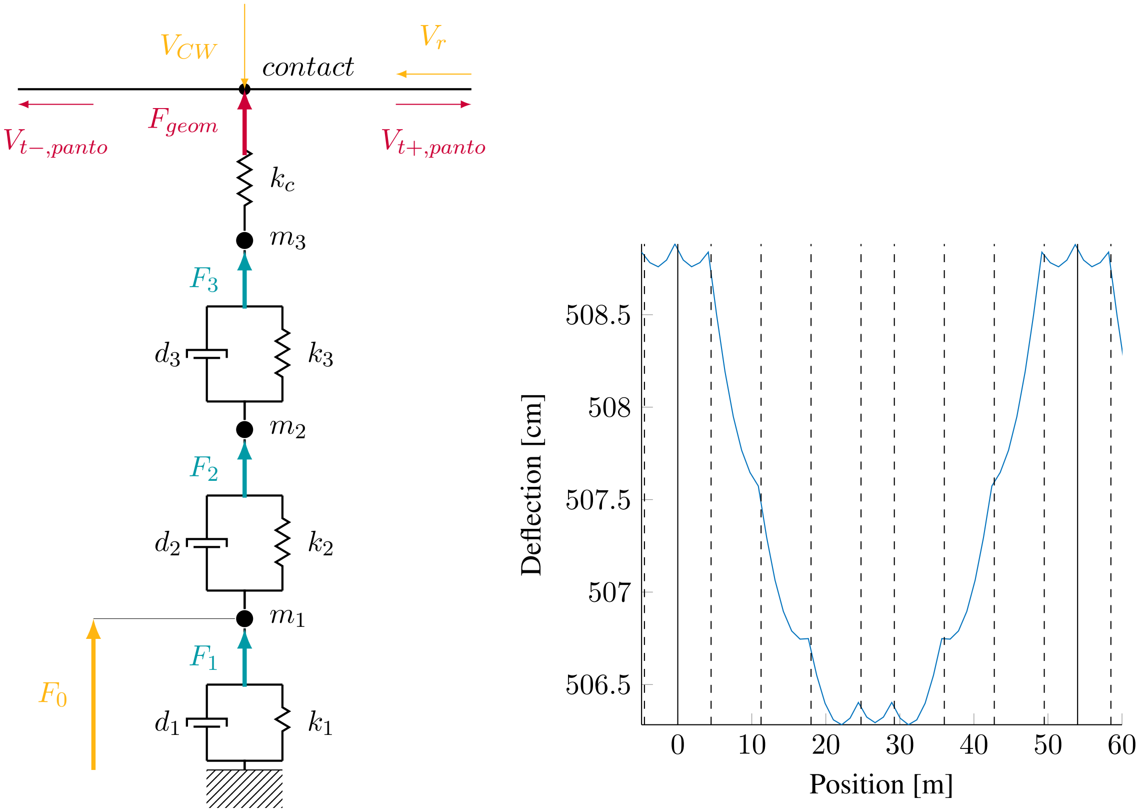

Figure R.6: Modèle du pantographe avec le fil de contact (gauche), hauteur du fil de contact le long d'une portée (droite)

Le problème est linéaire et peut être calculé dans le domaine de Fourier,

$$F_{geom}(\omega) = v_{panto} Z_{panto} V_{CW}(k) + F_m \tag{R.3}$$

où v_{panto} est la vitesse du pantographe, Z_{panto} est l'impédance dynamique du pantographe en prenant en compte la raideur de contact, et $V_{CW}(k)$ est la transformée de Fourier de la dérivée spatiale de la hauteur du fil de contact le long de la caténaire. L'effort moyen F_m n'influe que sur la fréquence $\omega = 0$.

La figure R.7 montre la carte correspondant au spectre d'amplitude de F_{geom} en fonction d'une vitesse normalisée par la vitesse de propagation des ondes dans les câbles (voir section 2.2). Cette carte est comparée à celle de l'effort de contact dynamique F_c. Le puis observé le long de la courbe discontinue correspond à un puis de Z_{panto} à la fréquence de $4Hz$ qui varie dans le domaine de fréquence spatiale. Les lignes verticales sont donc dues à la géométrie de la caténaire qui est périodique. Une fréquence spatiale fondamentale peut être identifiée, correspondant à la plus grande sous-structure répétée, la portée,

$$k_{span} = \frac{1}{d_{span}} \tag{R.4}$$

où d_{span} est la longueur d'une portée.

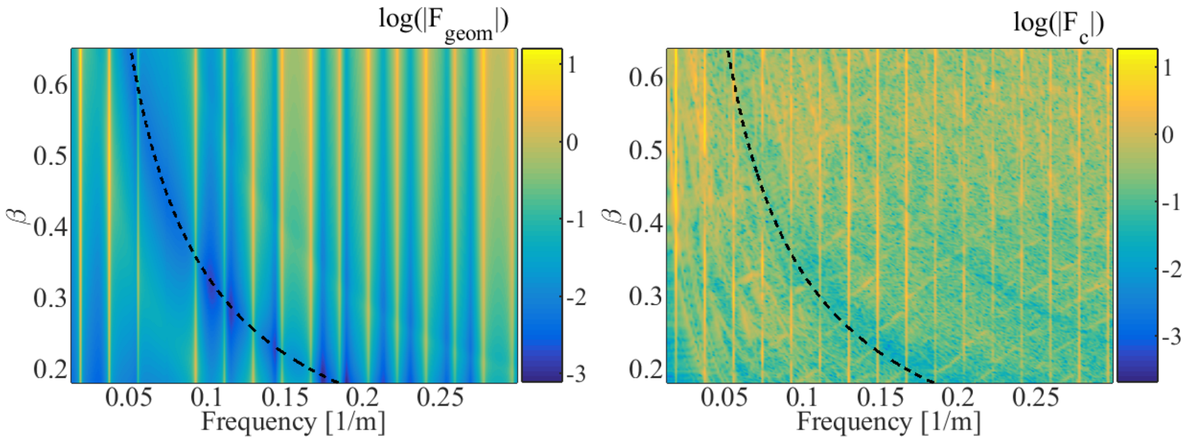

Figure R.7: F_{geom} (gauche) et F_c (droite)

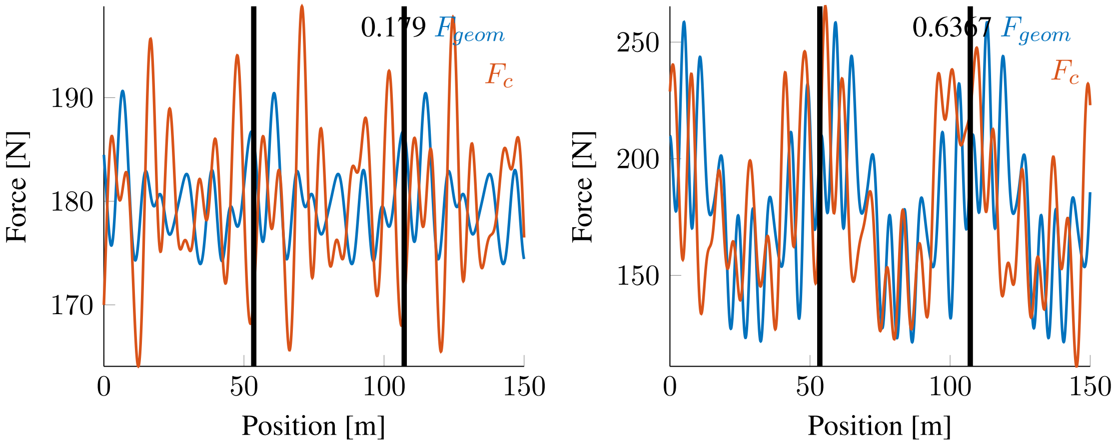

Figure R.8: Force de contact due la géométrie (bleu) et simulée (rouge) pour deux vitesses du pantographe, $90km/h$ (gauche) and $320km/h$ (droite)

La transformée de Fourier inverse de $F_{geom}(\omega)$ peut être calculée et comparée aux simulations. La figure R.8 montre ces efforts filtrés à $20Hz$ pour deux vitesses, $90km/h$ et $320km/h$. À haute vitesse, les signaux sont très proches et la plus grande partie de la réponse dynamique du pantographe est donc due à la géométrie de la caténaire. Cette conclusion n'est vraie que pour un signal filtré à $20Hz$. Si les signaux filtrés à $70Hz$, cette ressemblance est beaucoup moins claire.

R.2.2 Propagation d'ondes, réfections et transmissions

L'objectif de cette section est de modéliser analytiquement les réflexions et transmissions des ondes arrivant sur différents obstacles de la caténaire. Le premier cas étudié est la réflexion z_r et la transmission z_t sur une masse m d'une onde incidente z_i se propageant dans un fil comme détaillé sur la figure R.9. L'hypothèse de corde a été prise, la dispersion fréquentielle qui apparait à haute fréquence n'est donc pas prise en compte.

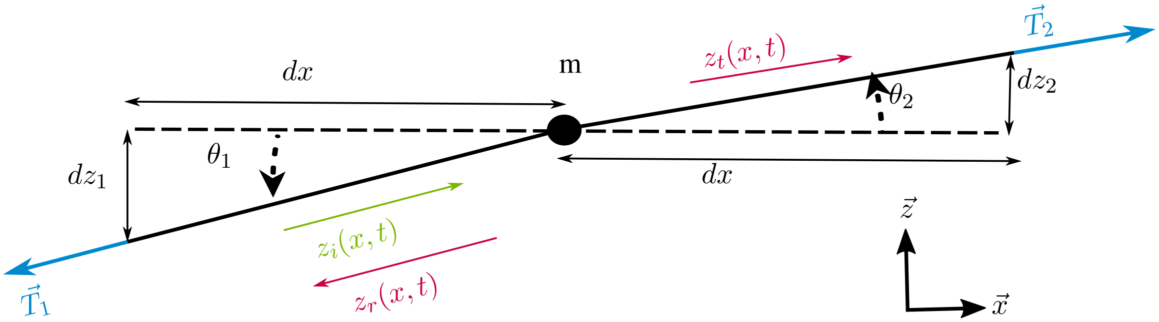

Figure R.9: Fil de longueur $2dx$ avec une masse m en $x = 0$

Puisque le problème est linéaire, chacune des ondes z peut être décrite sous la forme d'une double transformée de Fourier dans le temps et l'espace, Φ. La solution du problème est

$$\begin{Bmatrix} \Phi_r \\ \Phi_t \end{Bmatrix} = \begin{bmatrix} \dfrac{-i\omega m}{\sqrt{\mu T} + i\omega m} \\ \dfrac{\sqrt{\mu T}}{\sqrt{\mu T} + i\omega m} \end{bmatrix} \{\Phi_i\} = \begin{bmatrix} R_{mass}(\omega) \\ T_{mass}(\omega) \end{bmatrix} \{\Phi_i\} \tag{R.5}$$

où T est la tension dans le fil et μ la masse linéique du fil.

La figure R.10 (gauche) montre les variations de ces coefficients R_{mass} et T_{mass} en fonction de la fréquence. À fréquence nulle, l'onde est donc entièrement transmise.

La figure de droite compare le modèle analytique avec la simulation et une mesure effectuée avec une masse suspendue sur un câble. La différence avec la mesure est principalement due à la raideur introduite par le fil qui relie la masse au câble.

Le deuxième cas est celui de la réflexion sur un pendule comme indiqué sur la figure R.11. L'onde incidente arrive dans le fil de contact (CW) et est transmise dans le câble porteur (MW) dans les deux directions, réfléchie et transmise dans le fil de contact.

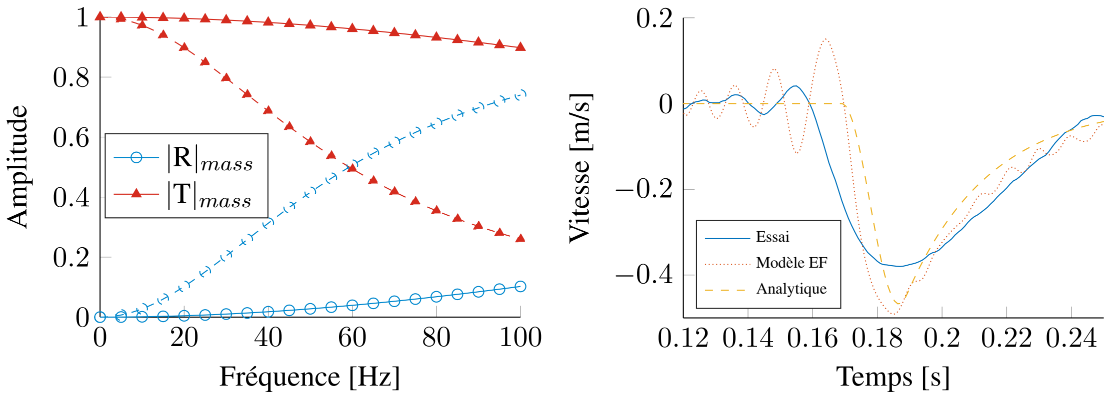

Figure R.10: Coefficients de transmission (rouge) et réflexion (bleu) pour des masses de $200g$ (train plein) et $1kg$ (trait discontinue) (gauche), comparaison de la vitesse de l'onde réfléchie calculée par le modèle analytique avec le modèle éléments finis (EF) et la mesure (droite)

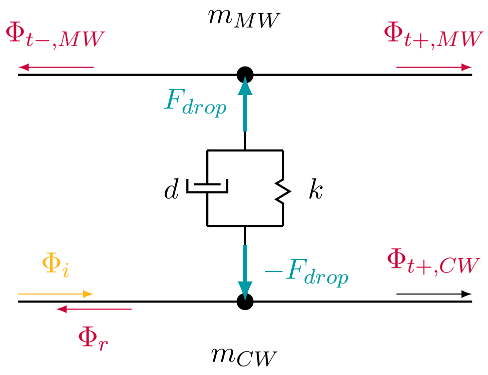

Figure R.11: Modèle de pendule avec une onde incidente Φ_i dans le fil de contact, générant trois ondes transmises, une onde réfléchie et un effort dans le pendule F_{drop}

De la même façon, des coefficients de réflexion et transmission peuvent être calculés en fonction de la fréquence,

$$\begin{Bmatrix} \Phi_r(\omega) \\ \Phi_{t+,CW}(\omega) \\ \Phi_{t-,MW}(\omega) \\ \Phi_{t+,MW}(\omega) \\ F_{drop} \end{Bmatrix} = \begin{bmatrix} R_{drop,CW} \\ T_{drop,CWtoCW} \\ T_{drop,CWtoMW} \\ T_{drop,CWtoMW} \\ Z_{drop} \end{bmatrix} \{\Phi_i(\omega)\} \tag{R.6}$$

La figure R.12 montre ces coefficients en fonction de la fréquence. L'amplitude à $0Hz$ est non nulle, ce qui signifie qu'après le passage de l'onde, la vitesse dans le fil change de niveau.

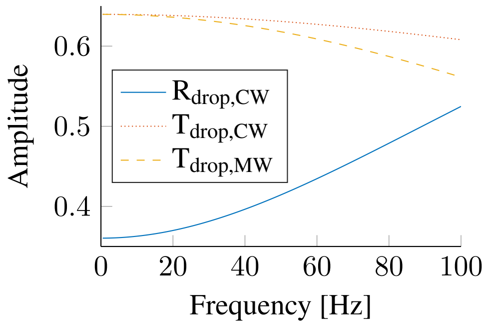

Figure R.12: Coefficients de réflexion et transmission pour une onde incidente dans le fil de contact

Lors d'un lâcher de masse sous un pendule, l'onde propagée dans le porteur puis réfléchie sur le pendule suivant est compensée par l'onde générée dans le fil de contact et transmise au porteur et inversement. Finalement, le niveau de vitesse avant et après le passage de ces ondes reste inchangé comme observé sur la figure R.13 où le modèle analytique de la somme des ondes est comparé à la somme des ondes calculés par simulation sans pendule à l'endroit du lâcher (FEM A) et à la simulation du cas entier avec pendule (FEM B).

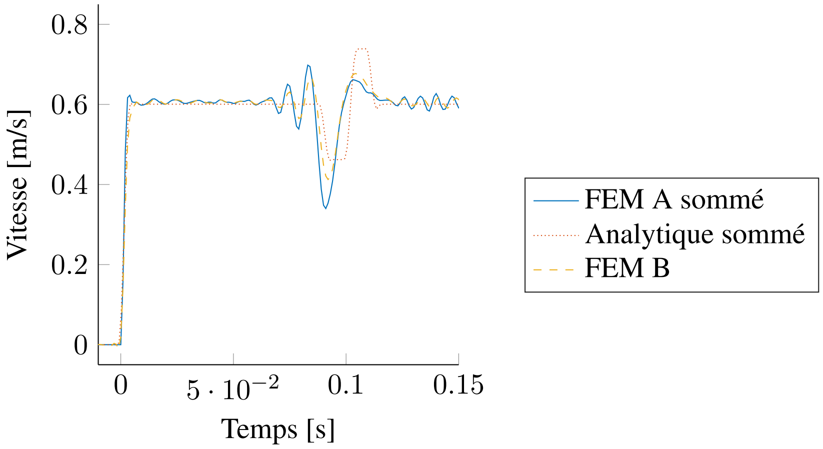

Figure R.13: Comparaison de la somme des ondes transmises et réfléchies simulées avec FEM A (bleu), simulé avec FEM B (jaune) et calculé analytiquement (rouge)

Le dernier cas est celui du comportement des ondes autour d'un support. La réflexion d'une onde sur le bras de rappel est négligeable et équivalente à celle sur une faible masse alors que la réflexion dans le câble porteur sur le support est complète. Il n'y a donc pas compensation des ondes propagées, ce qui entraine donc une variation du niveau de vitesse. La figure R.14 montre ces changements de niveau après que l'onde propagée dans le câble porteur et réfléchie sur le poteau a rejoint le point 1, puis que cette même réflexion soit réfléchie encore deux fois et revient au point 1. Le dernier échelon est due à la réflexion sur le premier pendule de la portée suivante de l'onde propagée dans le fil de contact.

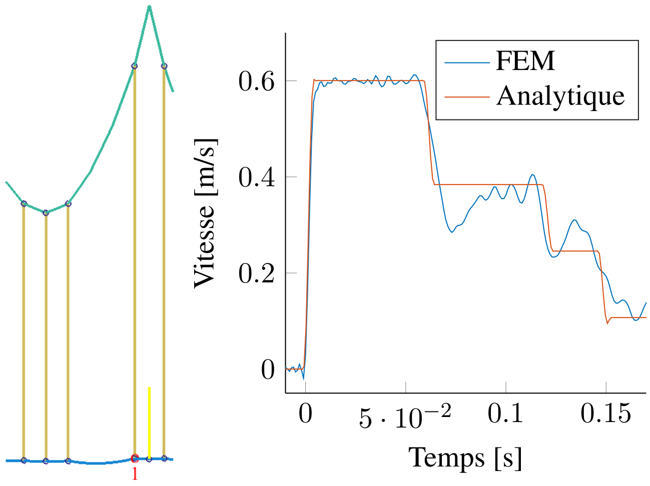

Figure R.14: Configuration de la simulation (gauche), comparaison de la simulation avec le modèle analytique (droite)

R.2.3 Temps et fréquences caractéristiques

Maintenant que les deux principaux phénomènes ont été identifiés, les cartes affichées en section R.1.2 peuvent être expliquées. Tout d'abord, sur la carte des spectres d'amplitude de la vitesse de soulèvement d'un point de la caténaire montrée figure R.15, les bandes verticales correspondent aux modes de la caténaire. Ces modes sont intimement liés aux vitesses de propagation des ondes dans les câbles et il a été montré que cette dépendance est principalement liée à la somme de ces vitesses. Dans la suite, la vitesse relative est donc définie par

$$\beta = \frac{2v_{panto}}{c_{CW} + c_{MW}} \tag{R.7}$$

où c_{CW} et c_{MW} sont respectivement les vitesses des ondes dans le fil de contact et le câble porteur.

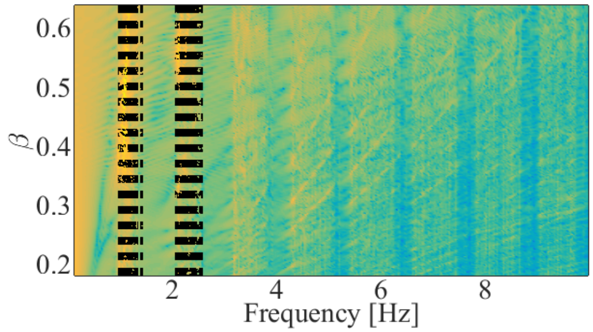

Figure R.15: Amplitude du spectre temporel de la vitesse verticale du fil de contact en fonction de β avec les modes de caténaire indiqués en lignes verticales noires

D'autres lignes apparaissent moins nettement. Ce sont les ondes générées par l'effort du pantographe due à la géométrie. Cet effort étant périodique dont la fréquence fondamentale est celle du passage des poteaux, k_{span}, les ondes générées vers l'avant $k_{wave,cat,+}$ et l'arrière $k_{wave,cat,-}$ sont aussi un signal périodique qui se décompose en fréquences spatiales,

$$k_{wave,cat,\pm} = \frac{n}{1 \pm \beta} k_{span} \qquad \forall n \in \mathbb{N}^* \tag{R.8}$$

où β est le rapport de la vitesse du pantographe avec la vitesse de propagation des ondes dans les câbles.

La figure R.16 montre le réseau de courbes déduites de ces deux fréquences. Aucune autre courbe n'apparait clairement sur ces cartes, l'ensemble des phénomènes a donc bien été pris en compte.

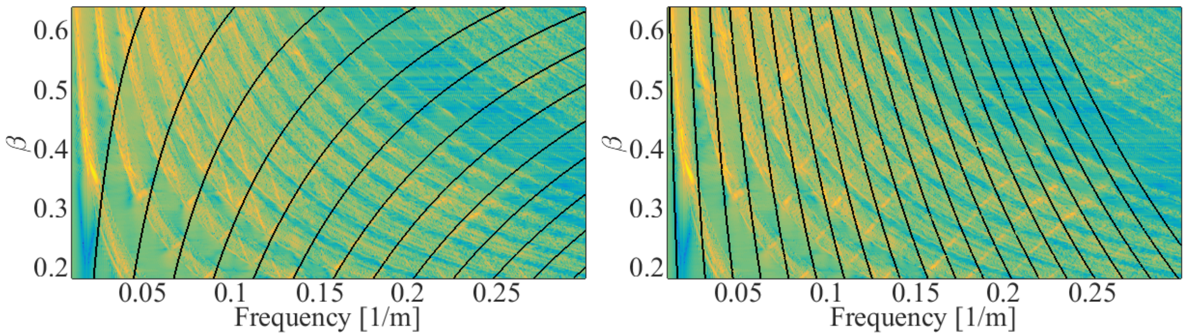

Figure R.16: Amplitude du spectre spatial de la vitesse du fil de contact en fonction de β avec les courbes noires représentant $k_{wave,cat,+}$ (gauche) et $k_{wave,cat,-}$ (droite)

Dans le repère mobile du pantographe, le même type de fréquence peut être calculé,

$$k_{wave,panto,\pm} = \frac{1 \pm \beta}{\beta} \frac{n}{2} k_{span} \qquad \forall n \in \mathbb{N}^* \tag{R.9}$$

Les courbes déduites de ces fréquences affichées figure R.17 s'ajoutent donc aux lignes verticales déjà identifiées dans la section R.2.1.

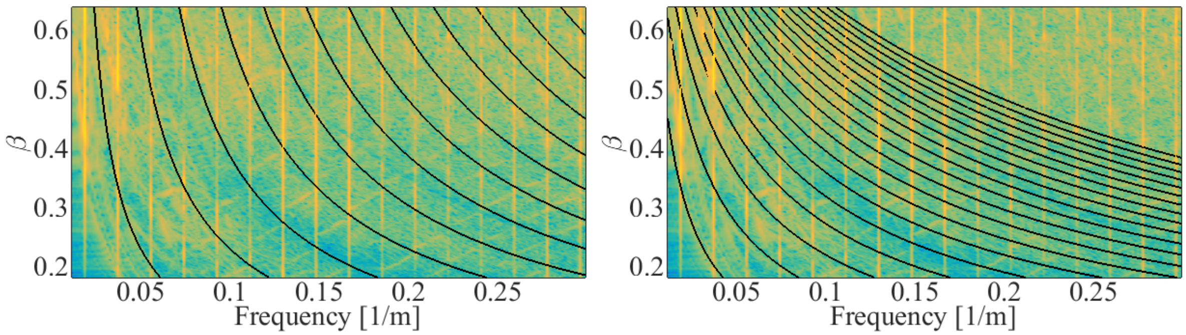

Figure R.17: Amplitude du spectre spatial de l'effort de contact F_c en fonction de β avec les courbes noires représentant $k_{wave,panto,+}$ (gauche) et $k_{wave,panto,-}$ (droite)

La coïncidence des ondes avec le passage du pantographe est particulièrement visible sur la phase de la première harmonique k_{span} du spectre spatial de l'effort de contact affichée sur la figure R.18. Pour des $\beta < 0.33$, l'ensemble des ondes propagées vers l'arrière ont le temps de rattraper le pantographe avant qu'il ne change de portée. Ensuite, la vitesse $\beta = 0.4$ correspond au cas où la fréquence de passage des portées $f_{span} = v_{panto} k_{span}$ est égale à la fréquence du premier groupe de modes de la caténaire, aux environs de $1Hz$. Les autres variations sont moins importantes mais représentent toujours une coïncidence des deux phénomènes identifiés.

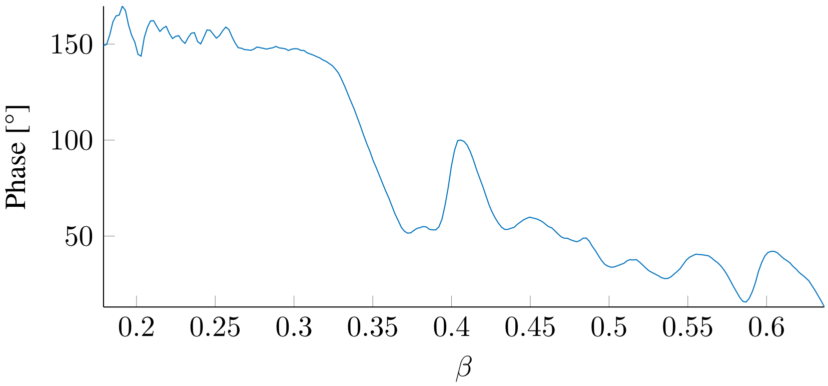

Figure R.18: Phase de la fréquence fondamentale k_{span} du spectre spatial de l'effort de contact en fonction de β

Le cas le plus critique de la coïncidence entre les modes de la caténaire et la vitesse du pantographe est lorsqu'il y a deux pantographes. Dans ce cas, la distance entre les deux pantographes d_{panto} influe très fortement sur le captage comme le montre la figure R.19 où les périodes définies par les modes de caténaire sont indiquées par les lignes discontinues.

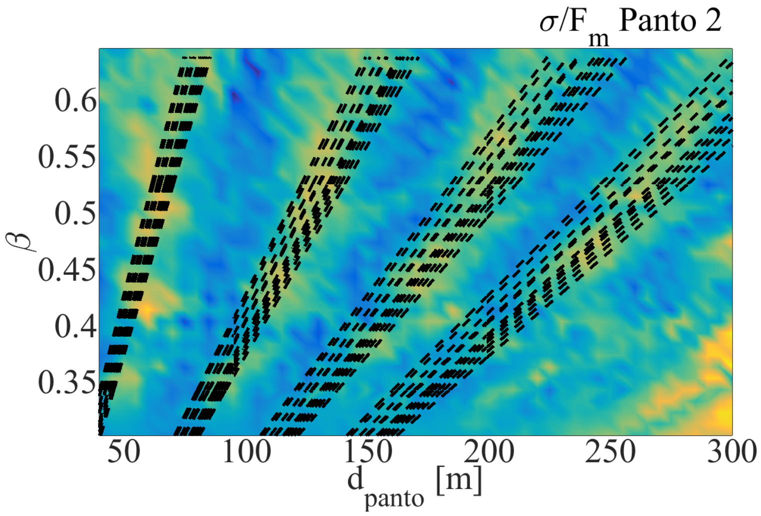

Figure R.19: σ/F_m du pantographe suiveur en fonction de β et de d_{panto}

R.3 Étude de l'incertitude épistémique

L'incertitude épistémique correspond à celle qui est réductible et n'est due qu'à une méconnaissance du système. Elle peut donc être réduite si l'on dispose de mesures ou de connaissances complémentaires. La section R.3.1 concerne la valeur à donner à la raideur de contact. Ensuite, la section R.3.2 traite de l'amortissement dans les différentes parties de la caténaire. Enfin, la section R.3.3 détaille la taille limite des éléments.

R.3.1 Raideur de contact

Le contact entre deux surfaces engendre des contraintes qui sont liées à l'interpénétration des deux matériaux. La théorie de contact de Hertz établit une valeur de cette raideur de contact pour une surface de contact donnée de $12mm^2$ à $k_{c,max} = 6MN/m$. Cette valeur n'est physiquement jamais atteinte en raison des irrégularités de surface et une borne inférieure est généralement définie au tiers de cette valeur [5], $k_c = 2MN/m$.

Or, la valeur donnée actuellement dans le modèle dynamique pantographe-caténaire est de $50kN$ ou $300kN$. La figure R.20 montre que ces valeurs ont un impact direct sur la bande de fréquence conservée.

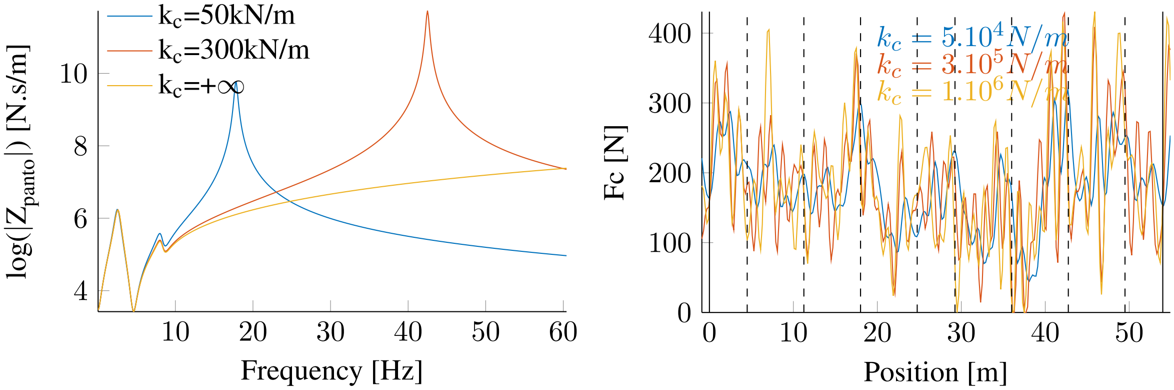

Figure R.20: Impact de la raideur de contact sur Z_{panto} (gauche) et sur F_c (droite)

Une étude paramétrique sur la raideur de contact k_c a donc été menée figure R.21 pour identifier la valeur à partir de laquelle cette raideur n'influe plus sur la dynamique. Le critère choisi pour évaluer la dynamique est σ/F_m. Ce critère est stable pour des valeurs de k_c supérieures à $1MN/m$. On observe cependant une rapide divergence du calcul si la raideur de contact choisie est supérieure à $5MN/m$. La valeur $k_c = 2MN/m$ est donc cohérente puisqu'elle est incluse dans l'intervalle défini par la théorie de contact de Hertz. Elle permet de plus de s'assurer qu'elle n'impactera pas l'effort dynamique dans l'intervalle $[0 - 70Hz]$.

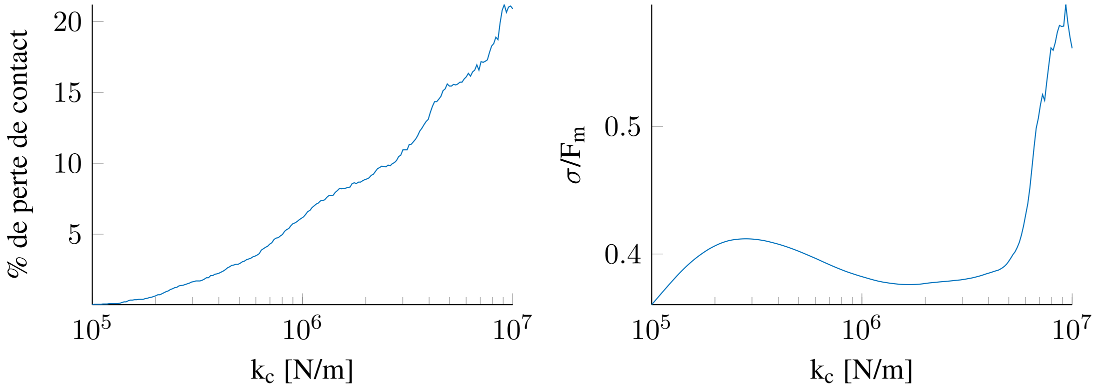

Figure R.21: Proportion de perte de contact de l'effort non filtré (gauche) et coefficient de variation σ/F_m de l'effort de contact filtré à $70Hz$ (droite) en fonction de k_c

R.3.2 Caractérisation de l'amortissement

L'amortissement dans la caténaire a jusqu'alors été défini pour que les simulations d'efforts de contact soient les plus proches possibles des mesures. Les coefficients d'amortissement étaient donc des variables de réglage. Pour résoudre le problème, des essais de lâcher ont été effectués sur une caténaire à taille réelle et quatre accéléromètres tri-axiaux ont été installés sous les pendules sur le fil de contact ou le câble porteur.

À partir de ces mesures, la fonction de réponse fréquentielle (FRF) a été calculée comme le montre la figure R.22. Des groupes de modes apparaissent clairement, ils correspondent aux modes de portée. L'identification de chaque mode peut ensuite être effectuée.

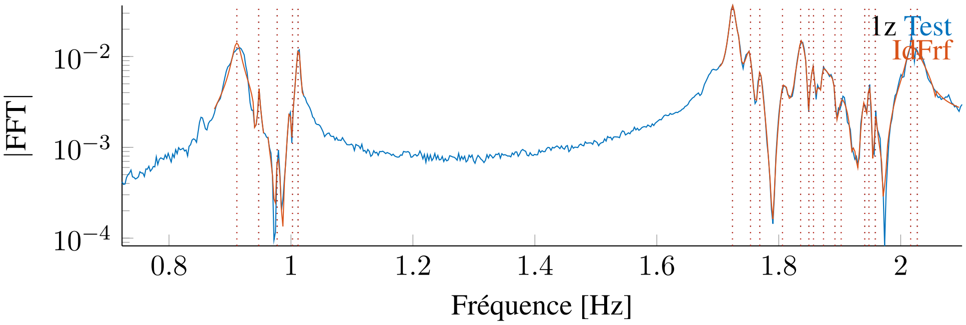

Figure R.22: Identification des modes complexes

La figure R.23 (gauche) affiche les résultats des amortissements identifiés sous forme de boites à moustaches. Ces amortissement sont très faibles et correspondent à la valeur d'amortissement des matériaux. Trois modèles d'amortissement sont comparés par la suite, le modèle de Rayleigh utilisé dans le Benchmark [4] (bleu), le modèle de Rayleigh par morceaux utilisé dans OSCAR en actualisant les valeurs d'amortissement dans les câbles pour correspondre aux mesures, et ce même modèle de Rayleigh complété par un amortissement modal pour remplacer l'amortissement des deux premiers groupes de modes [6]. L'amortissement dans les pendules et les bras de rappel est nulle dans les deux derniers modèles. La différence entre ceux-ci et le premier apparait clairement aux fréquences supérieures à $10Hz$.

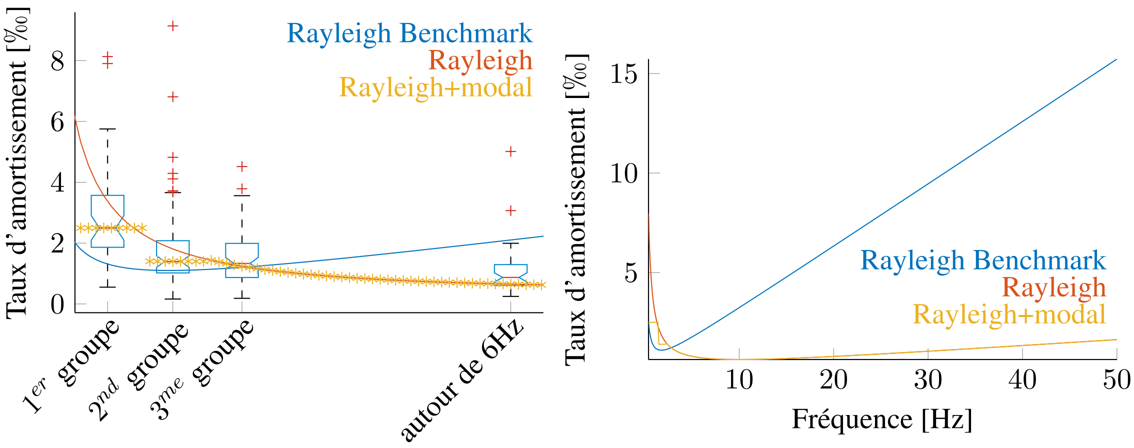

Figure R.23: Comparaison des taux d'amortissement identifiés (boites à moustache), Rayleigh Benchmark (bleu), Rayleigh par morceaux actualisé (rouge) et Rayleigh par morceaux actualisé + Modal (jaune) pour des plages basse (gauche) et moyenne (droite) fréquences

Un amortissement nul dans les pendules entraine une instabilité autour de la fréquence naturelle de vibration du système masse-ressort composé du pendule et des griffes qui permettent de l'accrocher aux câble. Un faible amortissement proportionnel à la raideur est donc introduit pour éviter cette instabilité.

L'introduction d'amortissement dans le bras de rappel entraine un sur-amortissement de certains modes et un sous amortissement des autres. Le bras de rappel ne semble donc pas dissiper d'énergie à travers ses liaisons pivots. L'amortissement lié à celui-ci est donc laissé nul.

La figure R.24 compare les différents modèles d'amortissement à la mesure lors d'un lâcher de masse. Pour des temps courts (gauche), le contenu haute fréquence est beaucoup plus visible sur les modèles actualisés qui n'ont aucune différence. Pour les temps longs (droite), on observe encore que ces modèles actualisés représentent bien mieux l'amplitude observée sur la mesure. L'amortissement modal engendrant une importante augmentation du temps de calcul et n'ayant que très peu d'impact sur la dynamique, ce sera le modèle d'amortissement de Rayleigh par morceaux qui sera conservé.

Du point de vue des simulations dynamiques, le tableau R.3.2 résume l'impact du nouveau modèle d'amortissement sur différents critères issus de l'effort de contact. On observe que cet impact est particulièrement important pour les moyennes fréquences, entre $20Hz$ et $70Hz$.

Table R.2: Critères usuels sur l'effort de contact

modèle d'amortissement	Pantographe	σ/F_m $20Hz$	σ/F_m $70Hz$	RMS* $]0-5]$ Hz	RMS $[5-20]$ Hz	RMS $[20-70]$ Hz
Initial	avant	0.27	0.35	33.1	34.4	37.8
Actualisé	avant	0.25	0.36	32.9	28.1	45.6
Initial	arrière	0.36	0.42	48.7	39.6	37.3
Actualisé	arrière	0.38	0.50	48.4	44.5	54.8

*racine carrée de la moyenne

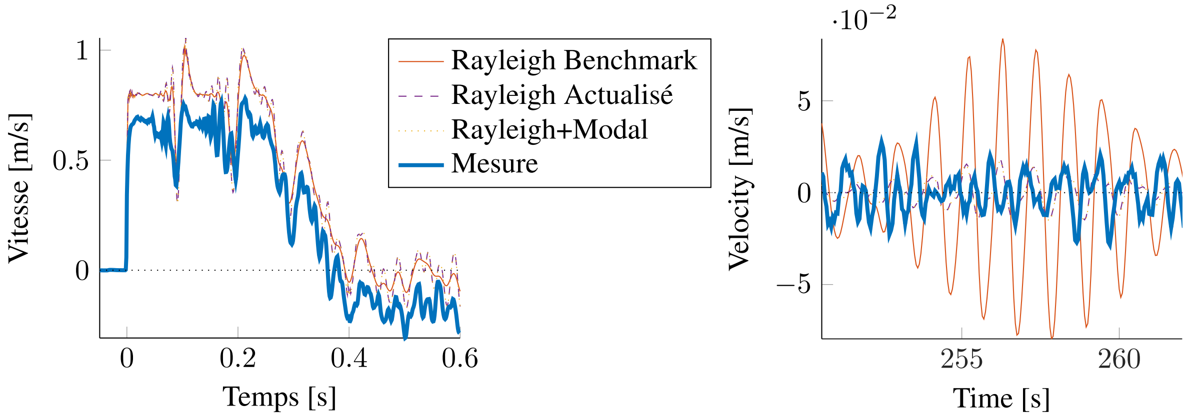

Figure R.24: Vertical velocity of the contact wire where the mass is dropped for initial waves and residual vibration.

R.3.3 Taille des éléments et flexibilité

La flexibilité est une valeur importante de la caténaire. Elle est considérée comme un paramètre de conception dans la norme Européenne EN50119 [7]. Pour une force vertical appliquée sur le fil de contact, la flexibilité correspond au ratio du soulèvement par la force appliquée. Dans les simulations, le calcul de l'effort de contact entre les nœuds nécessite l'interpolation de la flexibilité entre les nœuds. La figure R.25 montre cette interpolation avec les nœuds indiqués par les traits discontinus verticaux et les pendules par des traits pleins. Cette interpolation induit une ondulation de la taille des éléments.

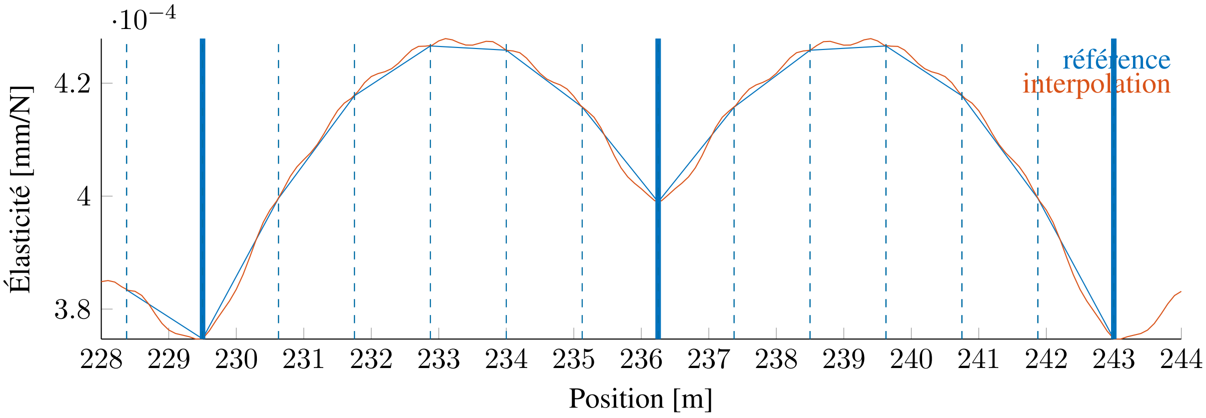

Figure R.25: Interpolation de la flexibilité entre les nœuds

La figure R.26 montre un effort de contact filtré à $70Hz$ calculé pour une vitesse $v_{panto} = 320km/h$ pour des éléments du fil de contact de taille $0.5m$ et $1.5m$. L'amplitude du spectre de l'effort de contact autour de $60Hz$ est significativement plus haut pour les éléments de taille $1.5m$. Cette fréquence correspond exactement à la fréquence de passage des éléments lorsque ceux-ci ont une longueur de $1.5m$. La taille des éléments doit donc être inférieure au mètre si la bande de fréquence considérée est de $[0 - 70]Hz$ pour des simulations à vitesse nominale. Cette taille doit être réduite si la vitesse du pantographe diminue.

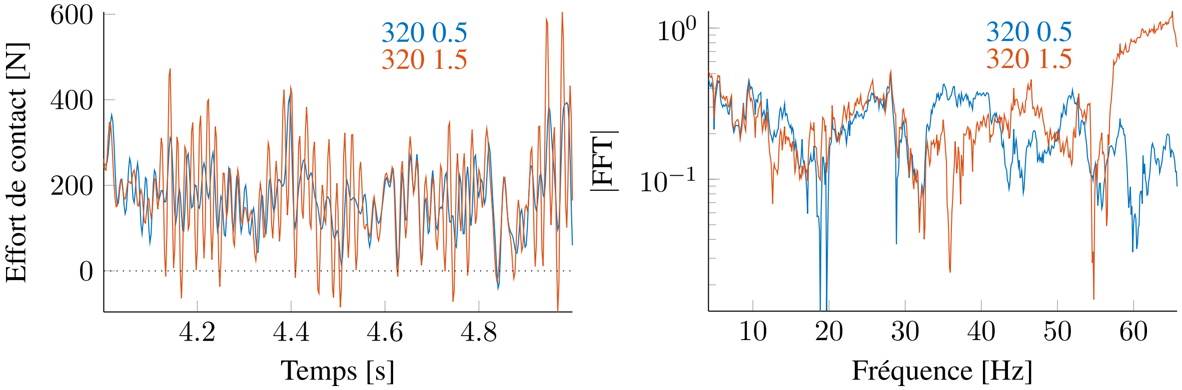

Figure R.26: Effort de contact filtré à $70Hz$ (gauche) et amplitude de son spectre (right) pour des éléments de fil de contact de taille $1.5m$ (bleu) et $0.5m$ (rouge) et une vitesse $v_{panto} = 320km/h$

R.4 Définition statistique de l'incertitude aléatoire liée aux paramètres physiques

Les paramètres aléatoires correspondent aux sources d'incertitudes qui ne peuvent être réduites puisqu'elles sont intrinsèquement variables. La section R.1.3 a montré que les paramètres liés à la géométrie étaient la plus grande source de variabilité. Cette partie détaille donc la définition statistique de ces paramètres de géométrie. Tout d'abord, une analyse de sensibilité préliminaire est effectuée en section R.4.1 pour définir les paramètres à conserver pour le problème statistique inverse développé dans la section R.4.3. Enfin, le modèle statistique de l'ensemble d'un canton est exposé dans la section R.4.4.

R.4.1 Analyse de sensibilité locale

La portée est la structure standard la plus large de la caténaire. La figure R.27 illustre les différents paramètres qui peuvent influencer la géométrie statique de la caténaire, i.e. lorsque uniquement les tensions mécaniques dans les câbles et la gravité sont appliqués. Ces paramètres sont

- $H_{CW,gauche}$ et $H_{CW,droit}$, les hauteurs du fil de contact respectivement à gauche et à droite au niveau du bras de rappel,
- ΔH_{gauche} et ΔH_{droite} les distances entre le fil de contact et le câble porteur au niveau du support,
- $L_{drop,i}$ la longueur du $i^{ème}$ pendule de la portée,
- T_{CW} et T_{MW}, respectivement la tension dans le fil de contact (CW) et dans le câble porteur (MW)

La hauteur $H_{drop,i}$ du fil de contact sous le $i^{ème}$ pendule est une variable de sortie résultant du calcul statique.

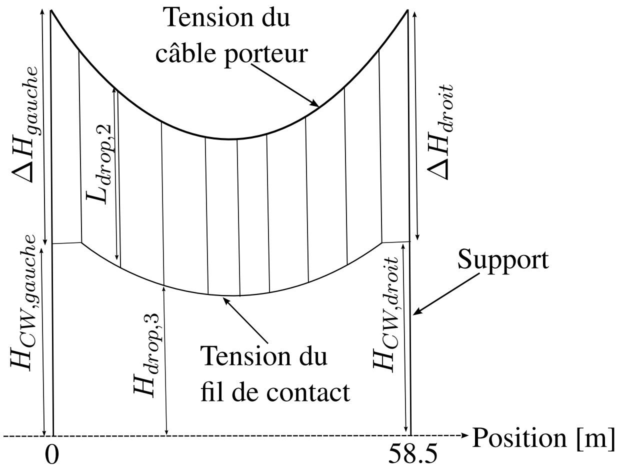

Figure R.27: Paramètres définissant la géométrie statique de la caténaire sur une portée

L'analyse de sensibilité préliminaire consiste en une variation de $\pm 20\%$ de chacun de ces paramètres indépendamment puis en l'observation de la flèche du fil de contact qui en résulte. Il est apparu que la tension dans le fils de contact, T_{CW} et les hauteurs du fils de contact au poteau $H_{CW,gauche}$ et $H_{CW,droit}$ n'avaient que peu d'impact. Les paramètres ΔH_{gauche} et ΔH_{droite} sont des paramètres fictifs qui permettent de représenter les portées suivantes et précédentes. La variation de ce paramètre ne sera pas contrôlée lors qu'un canton complet sera généré aléatoirement. Les trois groupes de paramètres conservés sont donc $\Delta H_{gauche,droite}$, les longueurs de pendules $L_{drop,i}$ et la tension dans le câble porteur T_{MW}

R.4.2 Mesures de géométrie de la caténaire

Deux types de mesures de la géométrie de la caténaire sont disponibles, les mesures quasi-statiques et les mesures optiques.

Les mesures quasi-statiques sont effectuées à l'aide d'un pantographe qui mesure la hauteur de l'archet, donc du fil de contact, en appliquant un effort faible de $36N$. Le véhicule circule à une vitesse de $40km/h$. Ces conditions de mesure génèrent une modification de la hauteur réellement mesurée qui s'apparente plus à un soulèvement mesuré qu'à une hauteur statique. Un schéma de correction itératif suivant les étapes de la figure R.28 a donc été mis en place après avoir créé le modèle de chaque canton mesuré.

Ces mesures une fois corrigées, les portées sont classées par type (i.e. par longueur) et la flèche est calculée le long de chaque portée. La table R.3 indique la quantité de mesures disponibles pour chaque longueur de portées. La figure R.29 montre l'ensemble des mesures disponibles pour la portée de type $N2$ de $58.5m$ de long.

Table R.3: Nombre de mesures quasi-statiques par portée

Longueur de portée	49.5	54	58.5
Nombre de portées	87	113	117

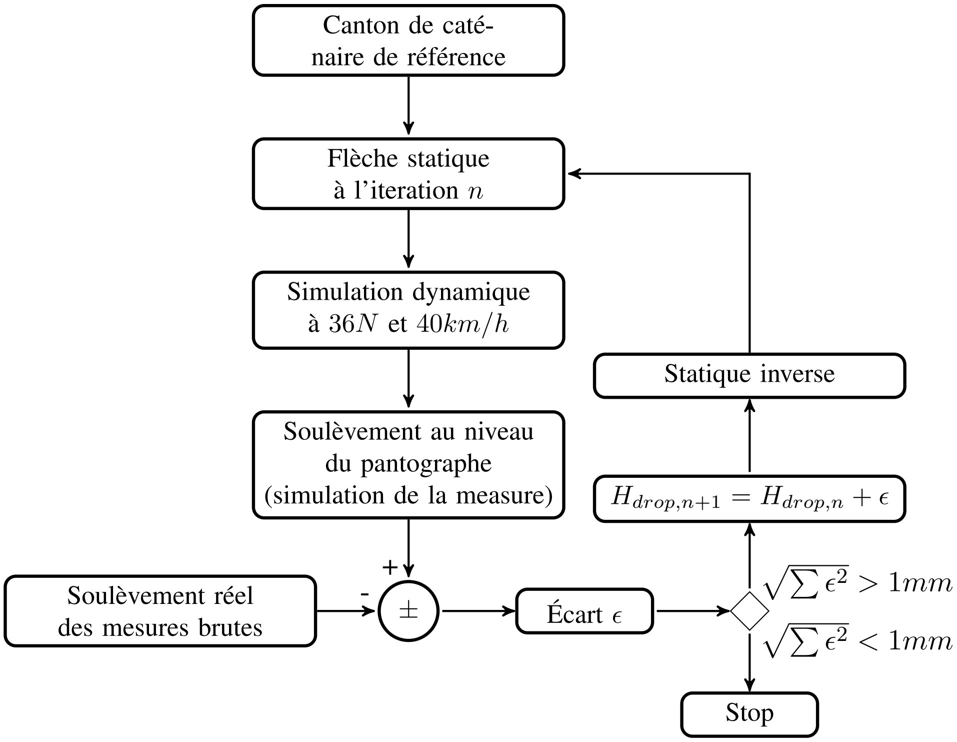

Figure R.28: Schéma itératif de correction de la mesure

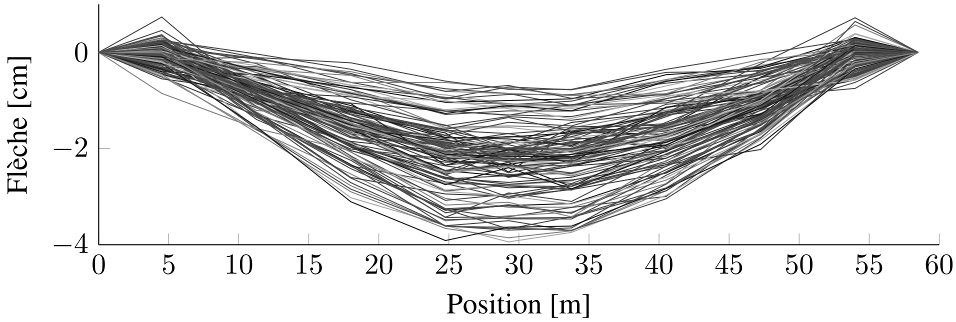

Figure R.29: Flèche mesurée sous chaque pendule d'une portée de type $N2$ de $58m$

Les mesures optiques ont une meilleure résolution et aucune correction n'est nécessaire. La flèche peut donc être directement extraite et la table R.4 résume les mesures disponibles. Malgré qu'elles soient d'une bien meilleur qualité, les mesures optiques ne sont actuellement qu'au stade de développement et ne seront donc pas déployées à court terme dans la politique de maintenance. L'identification des distributions statistiques des paramètres s'effectuera donc avec les mesure quasi-statiques et les mesures optiques serviront à vérifier les résultats d'identification.

Table R.4: Nombre de mesures optiques par portée

Longueur de portée	40.5	45	49.5	54	58.5
Nombre de portées	392	567	205	32	14

R.4.3 Définition statistique des paramètres de géométrie

L'objectif de cette partie est d'identifier les distributions statistiques (*p.d.f.*) les plus probables des paramètres d'entrée choisis dans la section R.4.1 pour représenter les mesures extraites dans la section R.4.2. Le problème est mal posé puisqu'il y a plus de variables d'entrée que de points d'observation de sortie. Le problème statistique inverse peut être représenté par le schéma R.30 avec

$\mathbf{f}^{exp}$ l'ensemble des paramètres variables qui définissent l'état mécanique réel du système

$\mathbf{w}^{exp,obs}$ les observations des sorties mesurées sur le système mécanique réel

$\mathbf{u}^{exp,nobs}$ les variables du système mécanique réel qui ne sont pas observées

$\mathbf{f}$ les autres paramètres, non variables qui sont nécessaires pour définir le modèle mécanique complet

$\mathbf{X}$ les paramètres variables pris en compte dans l'étude, ils sont supposés aléatoire et l'objectif est de définir leur *p.d.f.*

$\mathbf{W}^{obs}$ les sorties du modèle observées

$\mathbf{U}^{nobs}$ les sorties du modèle qui ne sont pas observées

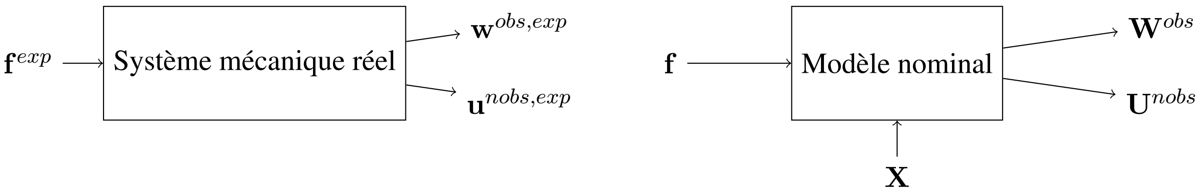

a) Réalité *b) Modèle*

Figure R.30: Représentation du système étudié

Le problème revient donc à définir statistiquement $\underline{\mathbf{X}}$ à l'aide des μ_{exp} observations $\mathbf{w}_1^{exp,obs}$, ..., $\mathbf{w}_{\mu_{exp}}^{exp,obs}$. La structure globale de résolution est développée par Soize [8] et résumée par le schéma de la figure R.31.

La portée choisie est de type $N2$, de longueur $58.5m$ et est composée de 9 pendules. La variable aléatoire ΔH représentant l'encombrement au poteau est supposée la même à gauche et à droite de la portée. Le vecteur $\underline{\mathbf{X}}$ est donc de dimension 11 pour les 9 $L_{drop,i}$, ΔH et T_{MW}. Le principe du maximum d'entropie [9] permet de choisir une distribution paramétrique de $\underline{\mathbf{X}}$, des lois Gamma indépendantes pour chacune des composantes du vecteur. Chacune des ces lois Gamma est paramétrée par sa moyenne et son écart type, ce qui définis un vecteur s de 22 hyper-paramètres. Le tirage aléatoire de taille $N = 1000$ de $\underline{\mathbf{X}}$ suit la méthode du carré latin pour accélérer la convergence par rapport à un tirage de Monte-Carlo classique. La simulation de la flèche statique des N tirages est ensuite effectuée

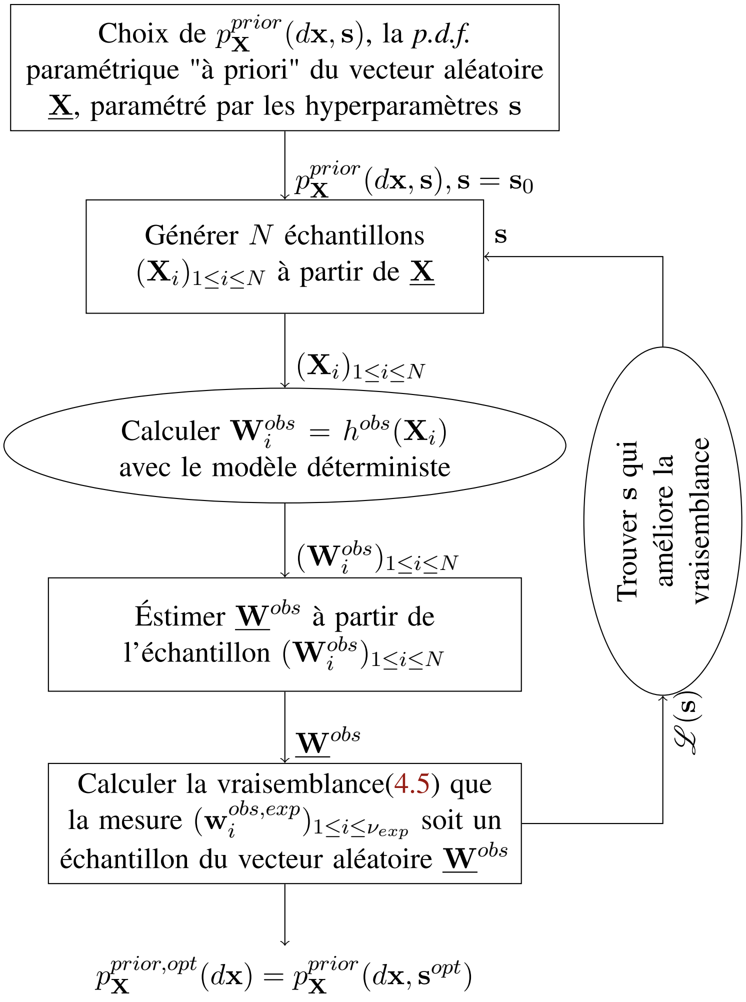

Figure R.31: Méthodologie générale pour la résolution d'un problème statistique inverse

par OSCAR, ce qui permet d'obtenir l'échantillon $(\mathbf{W}_i^{obs})_{1\leq i\leq N}$. Cet échantillon est ensuite utilisé pour estimer $\underline{\mathbf{W}}^{obs}$ qu'on suppose être de la forme d'un vecteur aléatoire gaussien multivarié. Une fois ce vecteur aléatoire défini, on calcule la vraisemblance que les mesures $(\mathbf{w}_i^{obs,exp})_{1\leq i\leq \nu_{exp}}$ soient tirées du vecteur aléatoire $\underline{\mathbf{W}}^{obs}$ à l'aide de la fonction de vraisemblance [10]

$$J(\boldsymbol{s}) = ln(p^{prior}_{\boldsymbol{W}^{obs}}(\boldsymbol{W}_1^{obs,exp};\boldsymbol{s}) + ... + ln(p^{prior}_{\boldsymbol{W^{obs}}}(\boldsymbol{W}^{obs,exp}_{\nu_{exp}};\boldsymbol{s}). \tag{R.10}$$

Le problème d'optimisation de cette fonction est résolu par la méthode des simplexes.

L'ensemble du problème a été résolu sous python à l'aide du module OpenTurns [11]. Les résultats obtenus après trois jours de calculs et 3330 évaluations de $J(\boldsymbol{s})$ sont indiqués dans le tableau R.5 et semblent cohérentes. La comparaison des mesures avec l'intervalle de confiance sur la figure R.32 à 98% montre que le modèle statistique correspond bien aux mesures. Les lois Gamma obtenues sont finalement très proches de lois Gaussienne puisqu'elles vérifient le test de normalité de Kolmogorov-Smirnov. Pour simplifier le problème, les lois Gamma seront replacées par des lois Gaussiennes de mêmes paramètres.

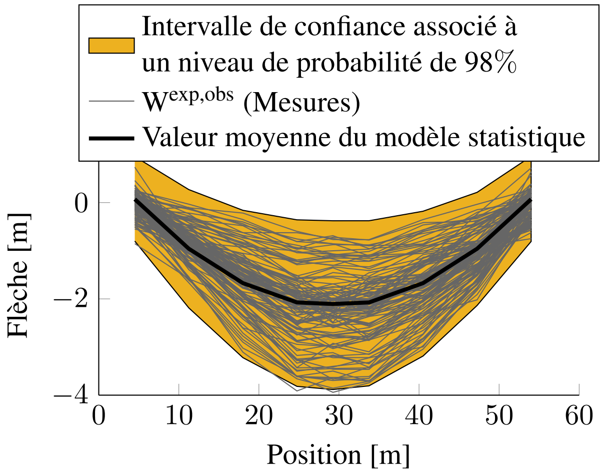

Figure R.32: Flèche mesurée $\boldsymbol{W}^{exp,obs}$ et intervalle de confiance à 98% de $\underline{\mathbf{W}}^{\mathbf{obs}}$

$\boldsymbol{X}$ \ $\boldsymbol{s}$	$\mu[SI]$	$\sigma[SI]$
T_{MW}	20575	818
ΔH	1.388	0.0065
$L_{drop,1}$	1.244	0.0067
$L_{drop,2}$	1.098	0.0050
$L_{drop,3}$	0.998	0.0045
$L_{drop,4}$	0.945	0.0045
$L_{drop,5}$	0.934	0.0038
$L_{drop,6}$	0.945	0.0044
$L_{drop,7}$	0.998	0.0035
$L_{drop,8}$	1.098	0.0034
$L_{drop,9}$	1.244	0.0070

Table R.5: Hyper-paramètres optimaux $\boldsymbol{s}^{opt}$

R.4.4 Modèle statistique de l'ensemble d'un canton de caténaire

Dans un canton complet, du point de vue de la dynamique, le paramètre ΔH est relâché et deux nouveaux paramètres apparaissent. Tout d'abord, la tension dans le fil de contact T_{CW} qui a une influence bien connue sur la dynamique, est définie par une distribution Gaussienne de moyenne égale à la valeur nominale et d'écart type égal à celui de la tension dans le câble porteur T_{MW}.

Ensuite, la hauteur du câble porteur est prise en compte à l'aide d'un vecteur aléatoire gaussien multivarié dont la matrice de covariance est définie par

$$C_{\boldsymbol{X}} = \begin{bmatrix} a & b & c & 0 & \cdots \\ b & a & b & c & \ddots \\ c & b & \ddots & \ddots & \ddots \\ 0 & c & \ddots & \ddots & \ddots \\ \vdots & \ddots & \ddots & \ddots & \ddots \end{bmatrix} \tag{R.11}$$

où les coefficients a, b et c ont été définis à l'aide des mesures.

La figure R.33 montre l'intervalle de confiance à 99% définie pour ce vecteur aléatoire comparé aux mesures. Le vecteur aléatoire représente les mesures de façon cohérente. Finalement, la caractérisation statistique de l'ensemble des paramètres aléatoires liés à la caténaire est résumée dans la table R.6

Table R.6: Distribution des paramètres d'entrée

Paramètre	T_{MW}	T_{CW}	$\boldsymbol{L_{drop}}$	$\boldsymbol{H_{MW,Mast}}$
Distribution	Gaussienne	Gaussienne	Gaussienne	Gaussienne multivariée
σ	$1000N$	$1000N$	$7mm$	matrice $C_{\boldsymbol{X}}$ (4.12)

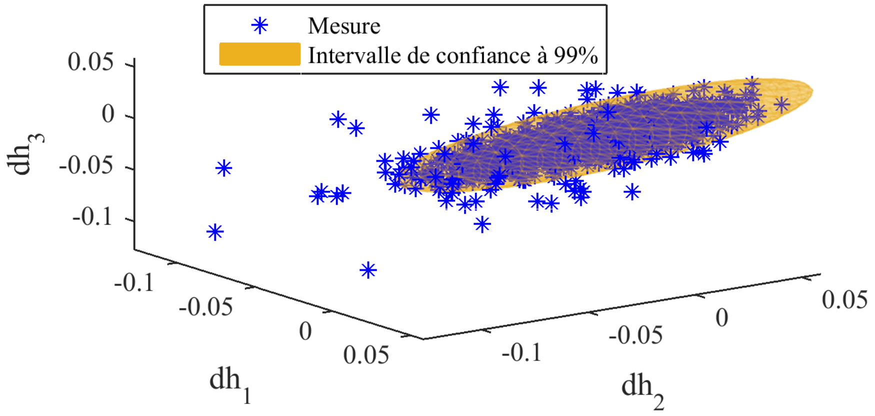

Figure R.33: Intervalle de confiance à 99% (jaune) et mesures (bleu) pour trois variations de hauteur consécutive par rapport à la hauteur nominale du câble porteur au support

R.5 Analyse de sensibilité sur les sorties

Toutes les sources de variabilité de l'effort de contact liées à la caténaire ont été caractérisées par des distributions statistiques dans la section R.4. L'étape suivante est de propager cette incertitude dans le modèle dynamique et d'observer l'impact de la variabilité de ces paramètres d'entré sur des critères liés à la géométrie de la caténaire et à l'interaction dynamique pantographe-caténaire. La section R.5.2 développe les critères utilisés. La section R.5.2 détaille ensuite la méthode d'analyse de sensibilité de Sobol pour classer les sources d'incertitude, ainsi que les résultats obtenus et étudie la corrélation qui peut exister entre les critères géométriques et dynamique. Enfin, la section R.5.3 examine la dépendance des critères dynamiques aux paramètres d'entrée.

R.5.1 Définition des critères de sortie

Deux types de critères sont définis, les géométriques et dynamiques. Les critères géométriques sont toutes les valeurs scalaires qui peuvent être déduites de la mesure de la hauteur du fil de contact le long de la caténaire. Cette hauteur est en effet ce qui est mesuré lors des tournées de maintenance. Actuellement, seulement deux critères géométriques sont contrôlés, la hauteur du fil de contact au poteau $H_{CW,mast}$ et la différence de hauteur du fil de contact à deux poteaux consécutifs $\Delta H_{CW,Span}$ [3]. Quelques autres critères ont été ajoutés arbitrairement pour tenter de représenter des phénomènes plus locaux ou reflétant potentiellement mieux la qualité de captage.

Le seul critère sur la qualité de captage lié à une grandeur mécanique et indiqué dans les normes [2] est le coefficient de variation σ/F_m calculé sur l'effort de contact filtré à $20Hz$. Ce coefficient doit rester inférieur à 0.3 pour qu'un bon captage soit assuré. Mais ce critère est fondé sur le fait que le signal filtré à $20Hz$ suit une distribution gaussienne de même écart type que l'effort réel. Or, il a été montré que l'écart type est plus important pour une fréquence de filtrage plus élevée. Par ailleurs, ce coefficient de variation calculé sur une fenêtre glissante de $50m$, $Moving(\sigma/F_m)$ nous montre qu'il est fortement variable le long du canton et que ce critère plus local peut permettre de détecter des zones à risque.

Un autre critère développé est un équivalent à celui lié à l'électricité indiqué dans les normes, NQ. Des mesures simultanées d'effort de contact et d'arcs électriques ont permis de montrer qu'en supposant que les arcs se formaient pour un effort de contact filtré à $70Hz$ inférieur à $45N$, on pouvait définir un critère mécanique équivalent au critère NQ. Dans le cas des simulations réalisées pour l'analyse de sensibilité, le captage étant très bon, ce seuil a été relevé à $80N$ pour observer des résultats exploitables.

L'ensemble des critères dynamiques est calculé pour des fréquences de filtrage de $20Hz$, correspondant aux capacités actuelles de mesure, et de $70Hz$ correspondant aux limites actuelles du modèle en raison de l'influence de la raideur de contact à plus haute fréquence.

R.5.2 Analyse de sensibilité de Sobol

Des analyses de sensibilité locales ont été réalisées en section R.1.3 et R.4.1 pour éliminer rapidement certaines variables de l'étude. Les paramètres restant étant statistiquement déterminés dans la section R.4 et les critères de sorties définis dans la section R.5.1, une analyse de sensibilité globale peut être menée. L'intérêt principal de ce type d'analyse est de prendre en compte les variations liées à des combinaisons de paramètres d'entrée en faisant varier ceux-ci simultanément sur l'ensemble de leur domaine.

L'analyse de Sobol est basée sur une décomposition de la variance sous forme de variance conditionnelle. Le modèle est considéré comme une boite noire représentée par une fonction $Y(\boldsymbol{X})$ où $\boldsymbol{X}$ est le vecteur aléatoire d'entrée, $\boldsymbol{X} = (T_{MW}, T_{CW}, \boldsymbol{L_{drop}}, \boldsymbol{H_{MW,Mast}})$ et Y une sortie de dimension 1. Les indices de Sobol du premier ordre $S_{1,i}$ et totaux $S_{T,i}$ sont définis pour chaque critère séparément par [12, 13]

$$S_{1,i} = \frac{Var_{X_i}(E_{X,\sim i}(Y|X_i))}{Var(Y)}, \tag{R.12}$$

$$S_{T,i} = \frac{E_{X_i}(Var_{X,\sim i}(Y|X_i))}{Var(Y)}, \tag{R.13}$$

où Var est la variance, E l'espérance et $X_{\sim i}$ l'ensemble des variables d'entrée excepté X_i.

Le calcul de ces indices n'est pas possible analytiquement. Il existe cependant des estimateurs pour les approximer. Pour cela, il est nécessaire de réaliser deux tirages A et B du vecteur aléatoire $\boldsymbol{X}$ de taille $N = 1000$ à partir desquels sont définis six ensembles

$$\begin{cases} A = [T_{CW}(A), T_{MW}(A), \boldsymbol{H_{MW,Mast}}(A), \boldsymbol{L_{drop}}(A)] \\ B = [T_{CW}(B), T_{MW}(B), \boldsymbol{H_{MW,Mast}}(B), \boldsymbol{L_{drop}}(B)] \\ A_B^1 = [T_{CW}(B), T_{MW}(A), \boldsymbol{H_{MW,Mast}}(A), \boldsymbol{L_{drop}}(A)] \\ A_B^2 = [T_{CW}(A), T_{MW}(B), \boldsymbol{H_{MW,Mast}}(A), \boldsymbol{L_{drop}}(A)] \\ A_B^3 = [T_{CW}(A), T_{MW}(A), \boldsymbol{H_{MW,Mast}}(B), \boldsymbol{L_{drop}}(A)] \\ A_B^4 = [T_{CW}(A), T_{MW}(A), \boldsymbol{H_{MW,Mast}}(A), \boldsymbol{L_{drop}}(B)] \end{cases} \tag{R.14}$$

À partir de ces ensembles, plusieurs estimateurs ont été comparés et ceux retenus sont

$$S_{1,i} = 1 - \frac{\frac{1}{2N}\sum_{j=1}^{N}\left(Y(B)_j - Y(A_B^i)_j\right)^2}{\frac{1}{2N}\sum_{j=1}^{N}\left(Y(A)_j^2 + Y(A_B^i)_j^2\right) - \left(\frac{\overline{Y(A)}+\overline{Y(A_B^i)}}{2}\right)^2}, \tag{R.15}$$

$$S_{T,i} = \frac{\frac{1}{2N}\sum_{j=1}^{N}\left(Y(A)_j - Y(A_B^i)_j\right)^2}{\frac{1}{2N}\sum_{j=1}^{N}\left(Y(A)_j^2 + Y(A_B^i)_j^2\right) - \left(\frac{\overline{Y(A)}+\overline{Y(A_B^i)}}{2}\right)^2}. \tag{R.16}$$

L'ensemble des résultats est détaillé sous forme de diagrammes circulaires en annexe E. La hauteur du câble porteur est le paramètre le plus influent sur les critères de géométrie actuels. La figure R.34 montre que ce paramètre est à l'inverse le moins influent sur les critères dynamiques qui sont principalement dépendants des tensions dans les câbles T_{CW} et T_{MW} et pour les critères plus locaux, des longueurs de pendules L_{drop}

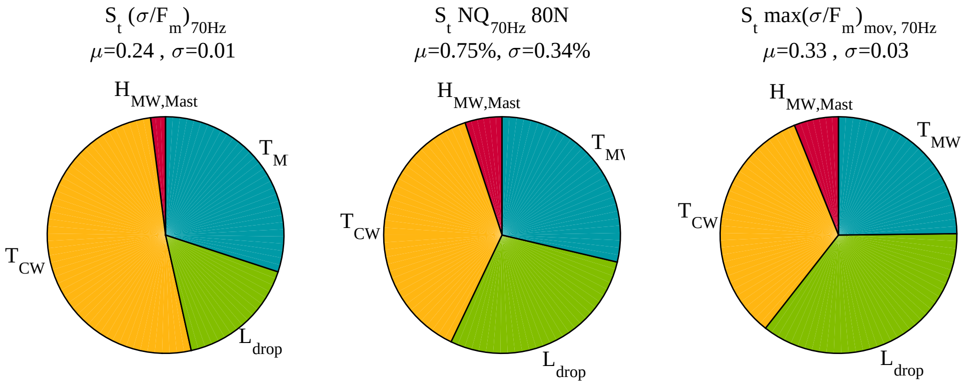

Figure R.34: Indices de Sobol d'ordre total des quatre paramètres sur les critères dynamiques $(\sigma/F_m)_{70Hz}$ (gauche), NQ_{70Hz} (centre) et $max(\sigma/F_m)_{mov,70Hz}$ (droite)

Certains critères géométriques ajoutés tels que ceux observés sur la figure R.35 sont dépendants chacun d'un paramètre en particulier. Ces critères sont donc potentiellement intéressants pour tenter de caractériser la qualité de l'interaction dynamique à partir de la mesure de la géométrie de la caténaire. Pour ce faire, il est nécessaire qu'une relation monotone existe entre une combinaison de critères géométriques et les critères dynamiques. Les coefficients de corrélation de Spearman ont donc été calculés pour les combinaisons linéaires des deux critères géométriques les plus corrélés. La figure R.36 montre la meilleure corrélation obtenue. Celle-ci est largement insuffisante pour être exploitée. Aucun des critères géométriques définis n'est donc adapté pour caractériser la qualité de captage dynamique.

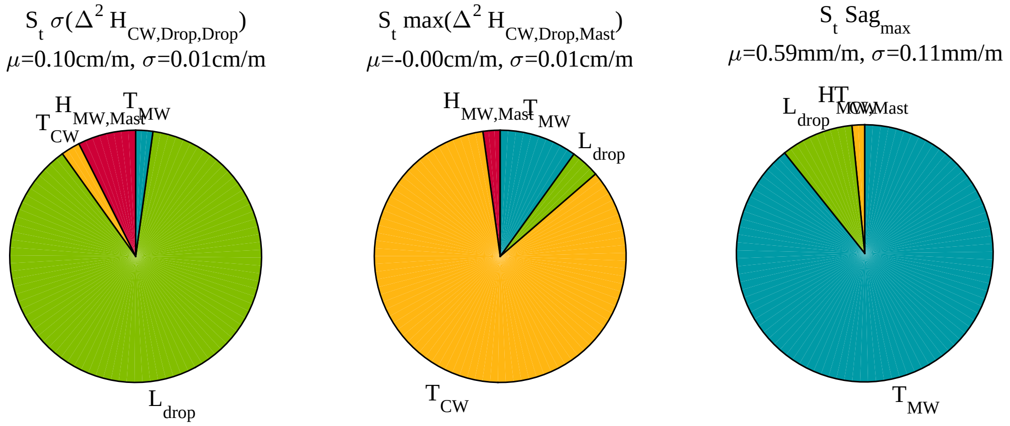

Figure R.35: Indices de Sobol d'ordre total des quatre paramètres sur les critères géométriques $\sigma(\Delta^2 H_{CW,Drop,Drop})$ (gauche), $max(\Delta^2 H_{CW,Drop,Mast})$ (centre) et Sag_{max} (droite)

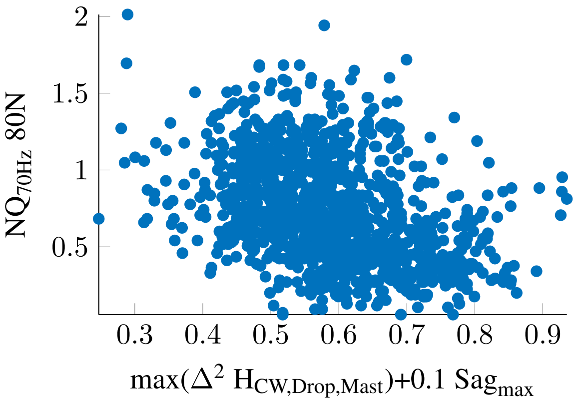

Figure R.36: Variation de NQ_{70Hz} en fonction de la combinaison linéaire des critères de géométries la plus corrélée selon Spearman

R.5.3 Dépendance des critères dynamiques aux paramètres d'entrée

Les critères dynamiques sont principalement dépendants des tensions dans les câbles et des longueurs de pendules. La figure R.37 montre les variations de $(\sigma/F_m)_{70Hz}$ en fonction de chacune des tensions. Aucune corrélation ne semble exister.

La figure R.38 montre qu'une forte corrélation apparait entre $(\sigma/F_m)_{70Hz}$ et la somme des tensions $T_{CW} + T_{MW}$. Cette corrélation n'est pas monotone et ne peut donc pas être détectée par le coefficient de Spearman. Lorsque les paramètres $H_{MW,mast}$ et L_{drop} sont fixés, cette corrélation est très régulière comme le montre la figure de droite. L'origine de cette corrélation vient de la dépendance des modes de la caténaire à la somme des vitesses dans les câbles comme indiqué dans l'équation (R.7).

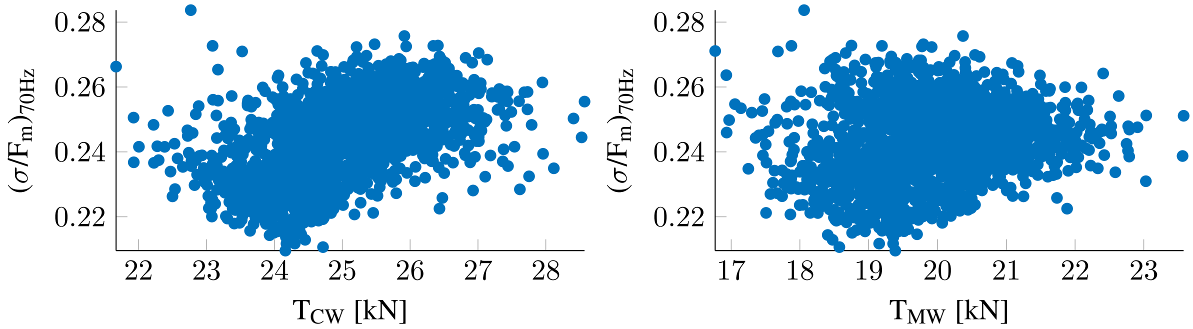

Figure R.37: Évolution de $(\sigma/F_m)_{70Hz}$ en fonction de T_{CW} (gauche) et T_{MW} (droite) quand les quatre paramètres d'entrée varient

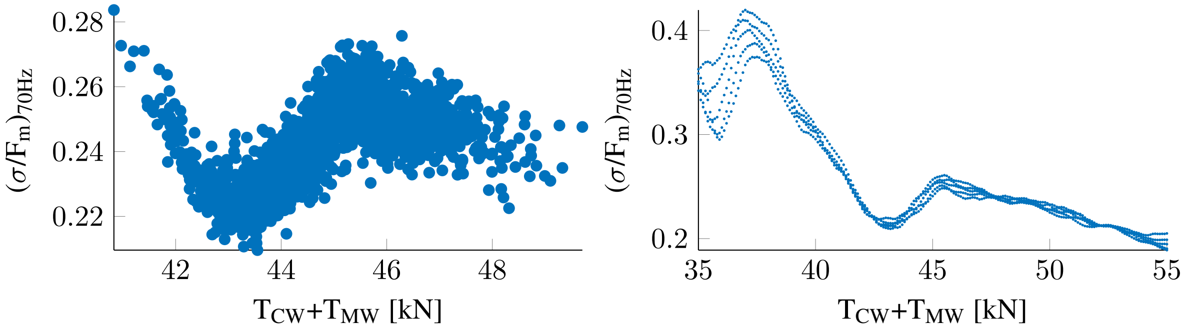

Figure R.38: Évolution de $(\sigma/F_m)_{70Hz}$ en fonction de $T_{CW} + T_{MW}$ quand les quatre paramètres d'entrée varient (gauche) et quand uniquement les tensions varient (droite)

R.6 Conclusions et Perspectives

Conclusions

Le premier ensemble de contributions de la thèse concernait la validation et la compréhension de modèles. La caténaire a tout d'abord été étudiée dans le chapitre R.2. Des essais ont été exploités pour confirmer la validité des modèles utilisés pour les câbles. La caractérisation de la dispersion a montré l'influence du vide entre les brins du câble porteur. L'hypothèse de corde dans laquelle la raideur de flexion est négligée s'est montrée bien adaptée aux basses fréquences bien qu'influençant notablement le transitoire. Différents cas de réflexion/transmission ont été étudiés analytiquement et comparés aux simulations et aux essais. Les conclusions intéressantes sont en particulier:

- une masse placée sur le fil de contact génère des réflexions seulement pour les moyennes et hautes fréquences et n'a par conséquent qu'un impact local;
- les ondes générées à un pendule dans les deux câbles se compensent aux pendules précédents et suivants;
- au niveau d'un poteau, les ondes dans le câble porteur sont entièrement réfléchies alors que la réflexion sur le bras de rappel est négligeable. Ce comportement donne beaucoup d'importance

aux pendules entourant le poteau et au rapport des impédances dynamiques des fils.

Concernant l'interaction dynamique pantographe-caténaire, les travaux ont permis de distinguer les effets et les fréquences caractéristiques liés à la géométrie statique, la propagation des ondes et les modes de la caténaire dans le repère fixe de celle-ci ainsi que dans le repère mobile associé au pantographe.

La coïncidence des fréquences ou des temps caractéristique a permis d'expliquer la majorité des variations des quantités d'intérêt tels que l'effort de contact et le soulèvement. Un résultat particulièrement intéressant est que la somme des vitesses dans les câbles est un paramètre dimensionnant dans la caténaire.

Les principales incertitudes épistémiques liées aux paramètres du modèle ont été examinées dans le chapitre R.3. La valeur physique de la raideur de contact obtenue par la théorie de Hertz est cohérente. La fréquence de résonance de contact ainsi obtenue est du même ordre de grandeur que le premier mode de flexion de l'archet. Pour interpréter des efforts de contact à des fréquences au delà de $70Hz$, il est donc nécessaire de tenir compte de ces flexibilités locales.

Des essais ont été réalisés pour caractériser l'amortissement et les coefficients obtenus sont significativement plus faibles que ceux couramment utilisés pour des fréquences de plus de $5Hz$. Ces résultats sont compatibles avec l'hypothèse que l'énergie est uniquement dissipée à travers l'amortissement des matériaux. L'effort de contact dans la bande de fréquence moyenne était donc fortement sous-estimé. Cette mauvaise estimation était en grande partie due au fait que les normes conseillent de filtrer l'effort de contact à $20Hz$. Il est à noter que des études menées par SDTools ont montré que la stratégie de mesure actuelle n'est en réalité pas compatible avec une estimation des efforts de contact à plus haute fréquence. La dernière incertitude épistémique considérée est liée à la taille des éléments du fil de contact. Il a été démontré en particulier que de bons résultats dans la bande de fréquence $[0 - 70Hz]$ nécessitaient des éléments de moins d'$1m$ pour des vitesses de pantographe de l'ordre du nominal et que cette taille devait être réduite si la vitesse diminuait.

Le deuxième ensemble de contributions de cette thèse concernait la caractérisation d'incertitude et son exploitation. L'étude de sensibilité initiale présentée en section R.1.3 comparait les variabilités issues de la géométrie de la caténaire, de l'usure du fil de contact et de la charge aérodynamique. Elle a permis d'orienter les travaux suivants sur la géométrie de la caténaire en particulier.

Dans le chapitre R.4, des mesures de géométrie ont été exploitées pour caractériser statistiquement les paramètres qui influençaient la géométrie de la caténaire. Le problème inverse bien posé consistant à ne modifier que les longueurs de pendules a mené à une solution biaisée. D'autres paramètres ont donc été introduits et le problème mal posé qui en résultait devait être traitée comme un problème statistique inverse. La solution a montré que les variations de tension dans le câble porteur étaient relativement importantes pour une caténaire dont la tension est régularisée. Les origines de cette variabilité ont été examinés et celle-ci semble finalement plausible. Après avoir défini les paramètres qui influençaient la géométrie statique, les variations de tension du fil de contact ont été supposées identiques à celles du câble porteur en raison d'un manque d'information.

Les distributions de ces paramètres ont été ensuite utilisées dans le chapitre R.5 pour réaliser une analyse de sensibilité sur des critères géométriques et dynamiques grâce aux indices de Sobol. L'objectif était de déterminer des critères géométriques plus adaptés à la qualité de captage dynamique que ceux actuellement utilisés par la maintenance. Une conclusion importante a été qu'aucun critère géométrique ne semblait suffisamment corrélé aux critères dynamiques. La seule façon de garantir une bonne qualité de captage est donc soit d'effectuer des mesures dynamiques, soit d'améliorer le contrôle des tensions mécaniques dans les câbles. La politique de maintenance devrait néanmoins être conservée pour des raisons de sécurité, en particulier pour le contrôle du gabarit et du désaxement.

Perspectives

De nombreuses observations du chapitre R.2 peuvent être prises en compte pour la conception de caténaires. En particulier, la réduction de l'impédance dynamique du câble porteur semblait fortement améliorer la qualité de contact. Il serait donc intéressant de chercher de nouvelles formes ou de nouveaux matériaux pour le câble porteur qui remplissent les conditions mécaniques et électriques nécessaires tout en ayant une plus faible masse linéique. Les ondes se réfléchissant dans le câble porteur aux poteaux semblent aussi avoir de l'importance. Le captage pourrait potentiellement être améliorée si un moyen d'atténuer les ondes associées était trouvé, par exemple en utilisant une pièce dissipative.

Bien que les caténaires soient généralement optimisées pour une vitesse de conception, la vitesse d'exploitation moyenne est généralement plus faible. Il existe donc un compromis entre les performances certifiées à une vitesse de conception et la performance moyenne à vitesse d'exploitation plus faible. Ce compromis serait plus pertinent dans l'optique d'optimisation de la maintenance. Des améliorations peuvent aussi être faites dans le cas de trains équipés de plusieurs pantographes captant simultanément du courant.

Les conclusions de l'analyse de sensibilité doivent être étendues à d'autres pantographes et à des unités multiples pour s'assurer de leur généralisation. Néanmoins, les variations de tensions dans les câbles semblent importantes pour des caténaires qui sont supposées être régularisées en tension. Ces variations influençant significativement la qualité de captage, il serait intéressant de développer des outils de mesure qui pourraient contrôler ces tensions. De plus il serait utile d'identifier les sources de ces variabilités et d'établir une procédure pour les réduire pour la conception de futures caténaires.

Les méthodes de mesure d'efforts de contact sont actuellement le point le plus bloquant pour des développements futurs de critères dynamiques plus adaptés tels que NQ_{meca} ou pour la validation de modèles. Dans un premier temps, les mesures actuellement utilisées pourraient être conservées et des estimateurs plus robustes tels qu'un filtre de Kalman pourraient être développés pour obtenir un effort de contact mesuré valide à plus haute fréquence. Dans un second temps, de nouvelles instrumentations et de nouvelles procédures d'évaluation des efforts dans le pantographe devraient être trouvées.

Avec l'amélioration des procédures de mesure de l'effort de contact, les trains de mesures tels que IRIS320 ou les trains commerciaux équipés de pantographes instrumentés permettraient d'acquérir une grande quantité de données et donc de suivre l'évolution dans le temps de la dégradation de la caténaire ainsi que de quantifier les autres sources de variabilité. La détection de défauts deviendrait ainsi fiable et les mesures dynamiques pourraient finalement être utilisées pour une maintenance conditionnelle de la caténaire.

L'homologation virtuelle reste une perspective importante. Les simulations devenant de plus en plus précises et robustes, leur utilisation dans le processus d'homologation des trains est aussi plus légitime.

Enfin, de nombreux résultats ont été rendus possibles grâce à une amélioration significative du logiciel de simulation OSCAR et de sa capacité à gérer des études paramétriques larges. Ces travaux illustrent donc le passage global de la mécanique numérique utilisant une simulation pour valider les performances vers l'utilisation d'un grand nombre de simulations pour optimiser les performances, la maintenance et la robustesse vis à vis des variabilités irréductibles.

Introduction

General background

Half of the approximately $30000km$ French rail network is electrified. These electrified lines are used for 90% of the passenger traffic and are thus the most intensively used lines. In China, there are more than $65000km$ of electrified lines and this figure is expected to increase significantly. Electric train networks are thus still in expansion around the world.

The electric current is generally collected using an overhead contact line, also called a catenary, and a pantograph that is attached to the train and slides under the catenary. This system is currently the only one that can be used in open environments and for high speed trains.

Current stability is generally not an issue since power electronics are used in the train for this purpose. The main issues that can appear are mechanical: it is essential to maintain a proper dynamical behaviour of the system to avoid any catenary break that would induce disruption of the traffic and costly delays.

In order to keep the catenary and pantograph system under control, railway track managers define specific survey and maintenance policies. In France, the main controls are visual inspection and periodic geometry measurements. Such controls are slow and not adapted to the intensive traffic, so that optimizing their use and frequency is of great interest.

To increase the periodicity of data records, dynamic contact force measurements have been performed since 2006 on an instrumented train called IRIS320 that can run at $320km/h$ and thus be inserted in the traffic of any line. The objective of this equipment is to use contact force measurements to allow diagnostics of catenary defects and in the long term develop conditional maintenance strategies. Initial work was carried out by Jean-Pierre Massat [1] and led to good detection of defects, but results were not robust enough to be industrialized. Indeed, among the conclusions of this work, a high variability of the measured contact force was observed. This scatter was due to the strong sensitivity of results to the train velocity and wind. Moreover, the $20Hz$-filtered contact force was too smoothed to detect very local phenomena.

Tests are inherently limited in their instrumentation: the only dynamic measurements are forces and accelerations on the pantograph and uplift at masts. Furthermore, testing conditions are limited by the cost and the difficulty associated with obtaining the proper train speed, pantograph combination, wind,...

It is thus essential to complement tests with numerical models and simulations giving access to all quantities of interest. Various simulation software for the study of dynamic interaction between the pantograph and the catenary have been developed by several companies or laboratories. The need for such simulations is acknowledged in chapter 1. The OSCAR software package, used in this work, has been under continuous development by SNCF and SDTools since 2003. This thesis is thus the main outcome of a pathfinder project initiated by SNCF Innovation & Recherche to guide the design of catenaries through a better understanding of the dynamical behaviour of the coupled systems, by means of a relevant numerical modelling and robust simulations that take into account variabilities. The proposed analyses were made possible by notable advances in the performance of OSCAR that now allows detailed parametric and statistical studies.

Thesis contributions

Typical uses of pantograph/catenary interaction models are related to design and virtual certification. Obviously better design can reduce maintenance, augment life-span and thus optimize the life cycle cost of the system. For the certification aspect, initial simulations can be used to detect the most critical operating conditions that need to be experimentally tested and to identify the configurations for which simulation results are enough. The use of simulations can thus limit the number of certification tests needed.

For any design process, the first necessary step consists in understanding phenomena that affect the system response. The dynamic interaction between the pantograph and the catenary is a complex coupled system. Both parts have their own dynamic behaviour, the static geometry of the catenary plays a major role and the moving contact generates waves in the catenary wires.

The wave generated frontward is the main issue for very high speeds. When the pantograph speed approaches the wave propagation velocity, levels of force and displacement drastically increase and can significantly damage the catenary and the pantograph. At more conventional speed, the backward wave can also be an issue when the train circulates with two lifted pantographs. This wave interferes with the mechanical contact of the rear pantograph with trends that need to be understood.

The **first contribution of this work** is the development in chapter 2 of a better understanding of the dynamic interaction between the pantograph and the catenary. The different phenomena such as the dynamic response of the pantograph to the catenary geometry, wave propagations and catenary dynamic behaviour have been observed separately. Understanding the contribution of each phenomenon to the dynamic behaviour of the coupled system is thought to be critical for design optimization. The analysis of the many possible coincidences gives a much better chance of properly analysing evolution of performance with different parameters.

The **second contribution** is a discussion in chapter 3 on epistemic model parameters that were previously used to tune the model for closer reproduction of dynamic measurements. In particular, damping is identified from original tests carried out on a full-size catenary [14], contact stiffness is confronted with local theories and the impact of mesh refinement is analysed.

The second major orientation of this work is a characterization of uncertainties and the proposal for strategies for their exploitation.

The **third contribution** is the statistical characterisation of physical parameters of the catenary using available measurements. The preliminary analysis published in [15], presented at IAVSD 2013 [16] and in section1.3 was led to choose the relevant source of variability to be modelled. The study of an isolated span was presented at ISMA 2014 [17] and the extension to the full section is detailed in chapter 4.

Given the statistical model of catenary geometries, the **last contribution** is the propagation of uncertainties through the static and dynamic models and the subsequent analysis criteria relevant for current collection quality. This work was presented at Railways 2016 [18] and is further detailed in chapter 5 where the choice of criteria, their dependence on unknown parameters and the ability to use either geometric or dynamic criteria as indicators of contact quality are discussed.

Chapter 1

State of the art

There are two main ways to supply electricity to a train. The first is to use an electrical strip usually installed laterally along the railway track. This third rail is a rigid bar on which a current collector slides. The strong security requirement for this technology makes it unsuited for long distances and is thus more common for urban transport like subway or tramway. Moreover, its rigidity makes the third rail inappropriate for train speeds of more than $160km/h$.

For long distance, the electricity is supplied by overhead lines. The first in history was presented at the International Electric Exposition in Paris in 1881. Since then, many improvements have been made thanks to more than a century of empirical knowledge. Today, there is still no alternative technology to the catenary for long distance high speed trains.

On the train side, current collection is ensured by a pantograph, an articulated tubular structure. The objective of the pantograph is to follow the height of the catenary without any shock in order to keep permanent contact.

The sliding of the pantograph under the catenary leads to a complex mechanical problem on which are added current transfer issues.

Section 1.1 states the main industrial problems linked with pantograph-catenary interaction and section 1.2 develops the state of the art in the field of pantograph-catenary dynamic interaction. A preliminary sensitivity analysis [15] is detailed in section 1.3 and used to orient the choice of further developments.

1.1 Industrial context

The two main mechanical subsystems required to ensure current conduction are the catenary and the pantograph. The pair forms a coupled system: a pantograph is usually designed to ensure good current collection quality under a particular catenary in a particular range of speeds. In order to develop trans-european high speed lines, Technical Specifications for Interoperability (TSI) [19] have been set by the European Railway Agency. The catenaries and pantographs studied here have all been certified against these standards.

After presenting the components of the catenary in section 1.1.1 and the pantograph in section 1.1.2, section 1.1.3 will address the general objective which is to ensure good current collection quality. Electrical and mechanical criteria of quality are thus developed before discussing existing problems associated with train certification in section 1.1.4 and maintenance in section 1.1.5.

1.1.1 The catenary

A catenary has to ensure a continuity of the mechanical contact with the pantograph. The curve described by the contact point along the catenary is called the contact line and is physically represented by the **contact wire** (CW) as shown in figure 1.1.

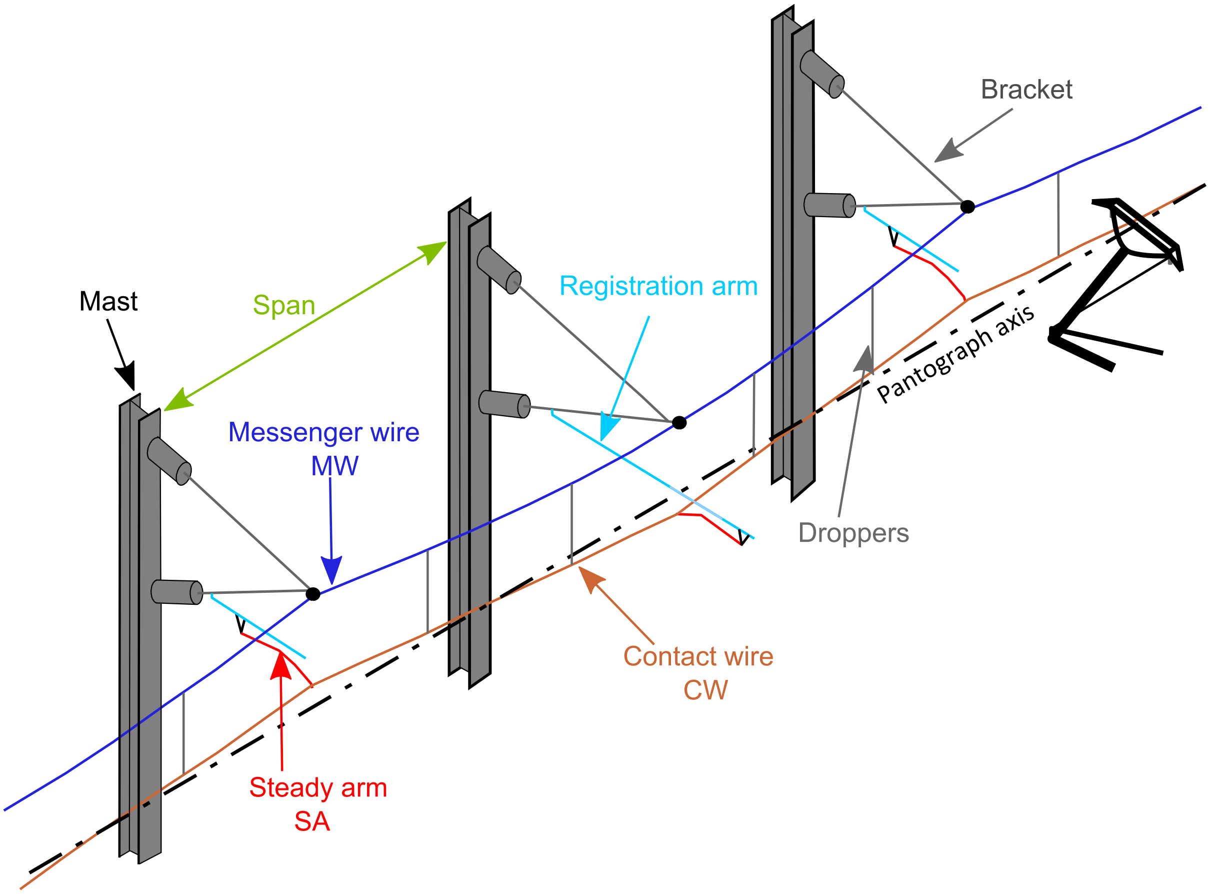

Figure 1.1: Composition of a typical $25kV$ catenary

The CW needs good mechanical resistance and high electric conductivity, and as a result is usually composed of hard copper or of an alloy of copper and tin. Its section is usually of $150mm^2$ on high speed lines. Figure 1.2 (left) shows the grooves on each side of the CW used to attach the claws for steady arm and droppers. On the right, a dropper is attached to cables.

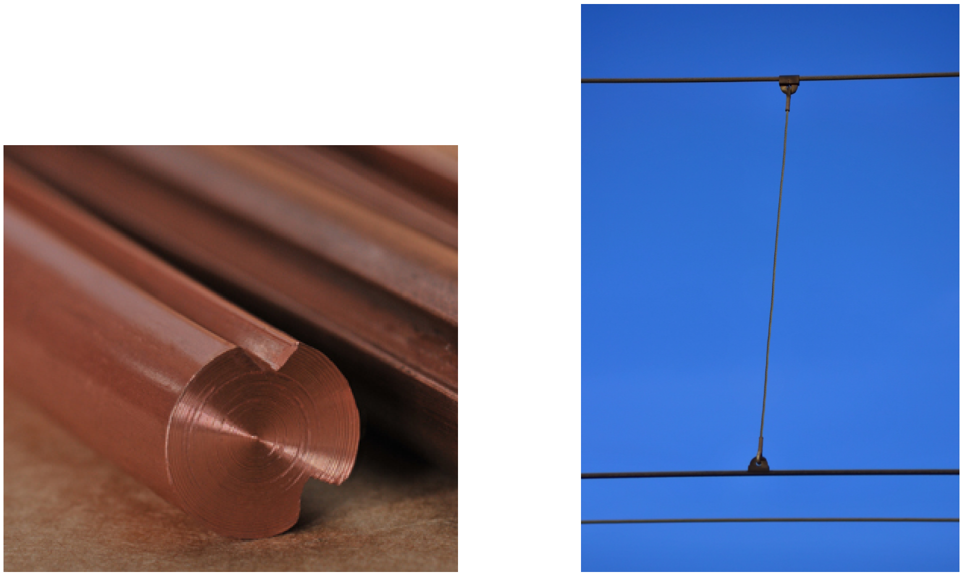

Figure 1.2: Contact wire (CW) (left) and dropper (right)

The CW is subject to stagger of $\pm 20cm$ to spread the wear on the full width of the pantograph contact strip. This stagger is obtained using steady arms which are attached to the CW by claws and are supposed to apply only a horizontal force. A small rotation of the CW is observed and expected here.

The **steady arm** (SA) only works in traction. It is attached by a pivot to a registration arm which allows application of this traction on both sides of the CW keeping all the masts on the same side. This registration arm is then attached to the bracket by another pivot link. Figure 1.5 shows pictures of some of them.

In the vertical plane, the CW sags under its own weight. To keep it flat, a **messenger wire** (MW) is positioned vertically above the CW and holds it thanks to droppers placed every $4.5m$ or $6.75m$ on the catenary studied here. The MW is a braided wire made of 37 yarns of bronze and is directly attached to the bracket. This bracket is linked to the mast by two pivots that allow the wires to move along the track direction.

Masts are positioned almost periodically, usually every $45m$ to 63.5 (closer in curbs) thus defining spans. Exact periodicity never occurs because of track plans and environment. This break of periodicity is also thought to avoid particular oscillation frequencies linked to the span length.

Two kind of catenaries will be studied in this work. The $V300$ and $V350$ are both used on high speed lines in France and designed for nominal train speed of $300km/h$ and $350km/h$ respectively. They are under an electric tension of $25kV$ and can be subjected to a current of $400A$.

Catenary sections have a length of $1km$ to $1.5km$. The MW is tensioned at $14kN$ for $V300$ and $20kN$ for $V350$. The CW is mechanicaly tensioned at $20kN$ for $V300$ and $25kN$ for $V350$. These mechanical tensions need to be regulated because of length variations induced by temperature changes. That is why, at each extremity, cables are tensioned by masses using a tension system composed of five pulleys shown in figure 1.3 that applies a tension T of five times the weight P of the suspended mass.

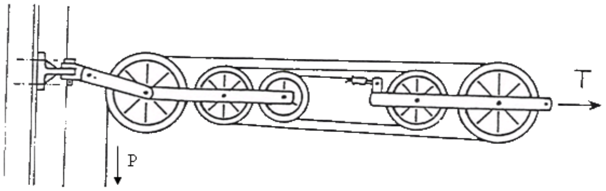

Figure 1.3: Tension device composed of 5 pulleys

Anchors are placed on the bracket in the middle of the section to prevent progressive sliding of wires in the track direction.

To ensure continuity of contact, an overlap area, shown in figure 1.4, is created between each catenary section. In this area, the pantograph is supposed to be in contact with two contact wires. This passage is delicate since the catenary must be well tuned to avoid shocks and allow a smooth passage.

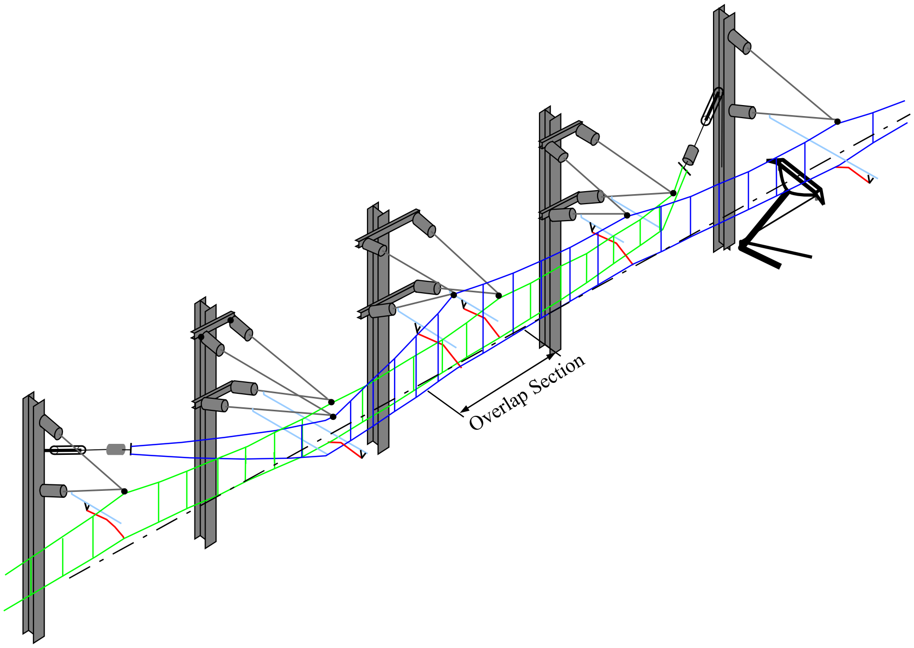

Figure 1.4: Overlap section between two catenary sections

1.1.2 The pantograph

The pantograph is an assembly of articulated tubes fixed on the roof of the train, usually placed on the locomotive. It applies a force on the CW to keep mechanical contact and ensure the transfer of electric current to the locomotive. It is composed of two main parts: the large frame and the bow. Many large frame designs exist around the world and the two main types used with French high speed trains are GPU and CX. Figure 1.6 shows the composition of these two pantographs. The main difference is that the lower frame is composed of two bars for GPU and only one bar for CX.

Figure 1.5: Mechanical bounds between bracket and mast (left), MW and mast (center) and registration arm and SA (right)

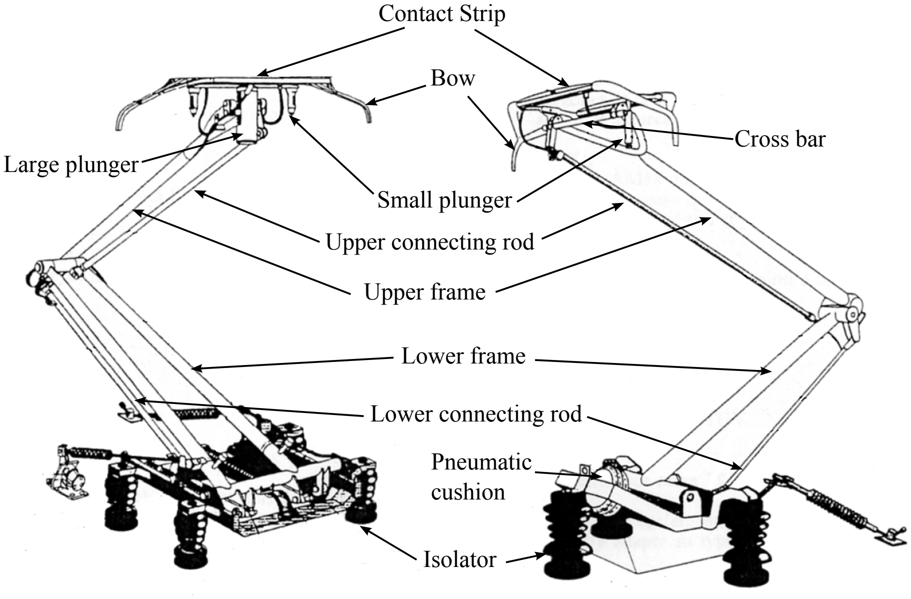

Figure 1.6: Composition of pantographs GPU (left) and CX (right)

On the main frame is attached a bow where the contact strip is fixed. This contact strip is long enough to cover all the stagger of the CW. It is a wear component usually made of carbon that is changed almost every other week. Horns are placed on both extremities of the bow to prevent the CW from sliding under the bow, which would seriously damage the catenary and probably destroy the pantograph.

The force applied by the pantograph to the CW is composed of two parts. The first is the command applied by the pneumatic cushion which ensures a minimum static contact force of $70N$ and then increases this force proportionally to the square of the train velocity. These curves are given by the TSI [20].

The second component is the aerodynamic force which greatly depends on the type of pantograph and also increases proportionally to the square of the train velocity. Usually, on the GPU frame, spoilers are added to calibrate this force. This force may vary with the wind speed or due to gusts generated by passing trains. The CX frame was designed to cancel this aerodynamic lift, but its aerodynamic behavior strongly depends on the one of the bow fixed at its top.

Three kinds of bows usually equip the previous frames. The first is composed of two independent contact bands. An example of this bow is shown in figure 1.7 (bottom). The aim of this technology is to have always one band in contact with the CW. Moreover, this also provides redundancy if one band were to break and is thus considered a security feature. Such bows can hardly weigh less than $8kg$. This suspended mass deteriorates the pantograph dynamics. Furthermore aerodynamic lift is strong, which makes its tuning complicated.

Mono-bloc bows exist with one and two contact strip. The two strip kind is the most popular in France and can be seen in figure 1.6. The last, with one strip, shown in figure 1.7 (top), is the lightest and usually weighs less than $5kg$ and has a light aerodynamic lift.

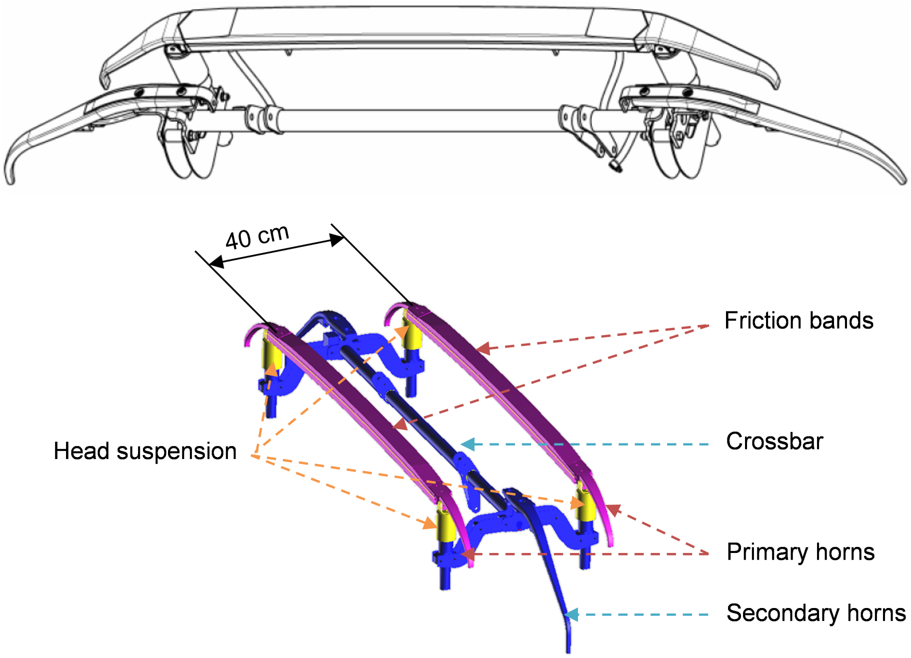

Figure 1.7: Mono-band bow (top) and bow with two independent bands (bottom)

Efforts in new pantograph design have long been to design active control systems [21, 22, 23, 24, 25, 26] but have not yet been used in commercial trains. Efforts are also aimed at reducing the suspended weight, mainly represented by the bow, to improve dynamic behavior, limit or control aerodynamic lift of the whole system, and develop the interoperability between the different European networks [27].

1.1.3 Current collection quality

Evaluating the quality of contact between the pantograph and the catenary is a tricky task. On one side, electrically, the current flow has to be stable. A minimum of contact surface is thus needed otherwise an electric arcs appears which can perturb the locomotive feeding and damage both pantograph and CW. On the other side, mechanically, if the pantograph applies a too high force on the catenary, wear of the strip band and contact wire will increase.

The imperfection criterion, called "Non-Quality" criterion (NQ) is a French electric criterion based on the observation of the light emitted by electric arcs by a camera. Are taken into account arcs longer than $5ms$, when current flowing inside the pantograph is more than 30% of the nominal collected current and the train velocity is higher than $220km/h$. NQ is defined by the percentage of arcs during the real current collection time,

$$NQ = \frac{100 \cdot (\text{Cumulative time of arc})}{\text{Real current collection time}} \tag{1.1}$$

The standard is to enforce $NQ < 0.2$.

The optical measurement system has to be sensitive to the wavelengths of the light produced by copper ($220nm$ to $225nm$) or copper alloy ($323nm$ to $329nm$) as indicated in European standards EN50317 [2]. This criterion is the electric one. It is the simplest way to evaluate the current collection quality since it is very simple to install and to adjust. Nevertheless, it does not consider the wear induced by mechanical friction and only considers light inside a specific wave length range. Moreover, it is highly sensitive to local default of the catenary and weather conditions, and is thus poorly reproducible.

Another current collection criterion, that does not encounter these issues, is commonly used. It is is based on the force applied by the pantograph on the contact wire and is thus more a criterion on mechanical interaction quality.

The contact force F_c measured thanks to an equipped pantograph is filtered at $20Hz$. At this frequency, the time signal is supposed to follow a Gaussian distribution and thus the mean contact force F_m and the standard deviation of the filtered signal $\sigma(F_c)_{20Hz}$ can be defined. Supposing now that an arc appears when the mechanical contact is lost, which means that the contact force is equal to $0N$, the probability of arcing is less than 0.14% if the condition

$$F_m - 3 \cdot \sigma(F_c)_{20Hz} > 0 \tag{1.2}$$

is fulfilled. This criterion also plays the role of high limit for the contact force and thus controls wear by friction. This criterion is the one used in European standards EN50317 [2]. Thresholds are detailed in EN50367 [28].

This contact force does not always follow a Gaussian distribution, particularly after filtering. That is why the threshold to consider a good current collection quality has been raised to $30N$ in Germany or $40N$ in Italy [29].

Current methods to evaluate collection quality are known to be limited. That is why several studies on contact force or contact loss measurement have been led in the past decade [30, 31, 32]. Nevertheless, the correlation between mechanical and electrical criteria has yet never been discussed in detail. Section 5.1.2 discusses a mechanical criterion that can represent the electrical one.

1.1.4 Train Certification

Train certification is required for a train running on a specific track and catenary. The TSI have been created to reduce the amount of in-line tests and ease cross-certification. A TSI certified train does not require any in-line test to run under a TSI certified catenary. But if one of the two system is not certified, in-line tests have to be performed to demonstrate their compatibility. This certification process is still extremely long. In the case of a non TSI certified train, the test campaign has to cover every configuration the train can have : all permutations of train set and raised pantograph, all catenaries of the new line.

The increase of traffic on high speed lines makes the process even harder and more expensive. The European Railway Agency (ERA) has published a report [33] to list all the requirement and costs of a full train certification.

Using simulation tools is a good way to reduce this expense. The first step has been to introduce the European standard EN50318 [34] to certify these pantograph-catenary interaction simulation tools. Then, a European project called TrioTRAIN was launched in 2009 to promote interoperability by the use of virtual certification. The sub-project PantoTRAIN has shown that a 70% reduction of the number of measurement may be possible.

An issue which has to be addressed to develop virtual certification is the variability of measurements. Figure 1.8 shows an example of a real certification. The tests displayed with dots have to respect the standards indicated in plain lines, i.e. the red dots have to be under the red line, blue dots between the blue lines and yellow dots over the yellow line. It is clear that a precise value of the mean contact force F_m is hard to obtain. Moreover, for identical speed and F_m, variations of $\sigma(F_c)$ are found. Accounting for this variability in numerical models is thus an objective of the present work.

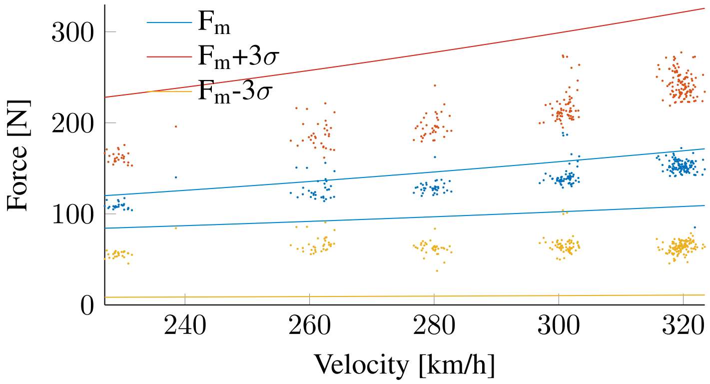

Figure 1.8: Example of certification map built to validate tests in one configuration for five different speeds

1.1.5 Catenary maintenance

In France, annual maintenance costs of catenaries total more than 200M€. Around 13% are used for catenary renewal, 16% for CW renewal and 14% for monitoring. More than 51% of the budget is allocated to preventive maintenance and only 2% for curative maintenance.

The monitoring is divided in two parts, the simple watch to control if anything obviously needs maintenance, and measurement done by engines. These engines measure the wear of the contact wire and the height of the contact wire along the track, which is called the catenary geometry.

This geometry is controlled periodically, every one or two years by a machine that cannot be used for velocities over $40km/h$. That is why it runs during the night. If an anomaly is observed on measurements, maintenance is done during the next scheduled preventive maintenance round, except if this anomaly is too high and has to be urgently corrected.

The good dynamic behavior of the pantograph-catenary system is supposed to be assessed by the catenary design. The French standards on catenary geometry indicated in IN1797 [3] aim at ensuring that the catenary geometry is not far from the one designed. The relation between geometry and dynamic is not clear and some countries directly use dynamic criteria to monitor the catenary. Evaluating this relation will be a second objective of the present work.

1.2 Scientific context

1.2.1 Introduction

Obtaining predictive pantograph-catenary interaction models opens the path for several industrial uses in maintenance or design.

Wear is a first maintenance issue. Wear of the strip band on the pantograph has been studied in [35, 36]. These wear components have a short lifetime and it is difficult to improve them without spoiling the lifetime of the contact wire. Wear of the contact wire has been studied in [37, 38, 39, 29]. These studies have shown that the driving parameter is the contact force, hence the need of a good prediction of this quantity.

With the evolution of materials used for CW and the use of carbon for contact bands, wear of CW has been drastically reduced and a new problem recently appeared the fatigue of the CW. Several studies on the subject [40, 41, 42, 43, 44, 45] have shown that contact force is again the main indicator of fatigue risk.

Wave propagation in the cables is also a well-known problem as it is the main limit to the train velocity. Its impact on dynamic has been studied analytically [46] and experimentally [47], with differing results. The issue of relevant propagation speeds will thus be addressed in section 2.2.

Numerical models can also be used for designing or optimizing pantograph [26] or catenaries [48] or both together [49]. Other applications such as the virtual certification discussed in section 1.1.4 are also expected.

Simulation of the dynamic interactions is thus the key for many industrial improvement. Pantograph and catenary model and their interaction are detailed in section 1.2.2. A parametric analysis of the dynamic interaction is then developed in section 1.2.3. Finally, section 1.2.4 prepares choices made for the rest of the thesis by addressing the possible sources of uncertainty that influence dynamic interaction.

1.2.2 The Pantograph-Catenary interaction model

The catenary described in section 1.1.1 is an assembly of wires, generally modelled as tensioned beams [1] described by the local equilibrium equation

$$EI\frac{\partial^4 z}{\partial x^4} - T\frac{\partial^2 z}{\partial x^2} + \mu\frac{\partial^2 z}{\partial t^2} = F, \tag{1.3}$$

with E the Young Modulus, I the moment of inertia, μ the linear mass, T the axial load and F an external force applied on the beam.

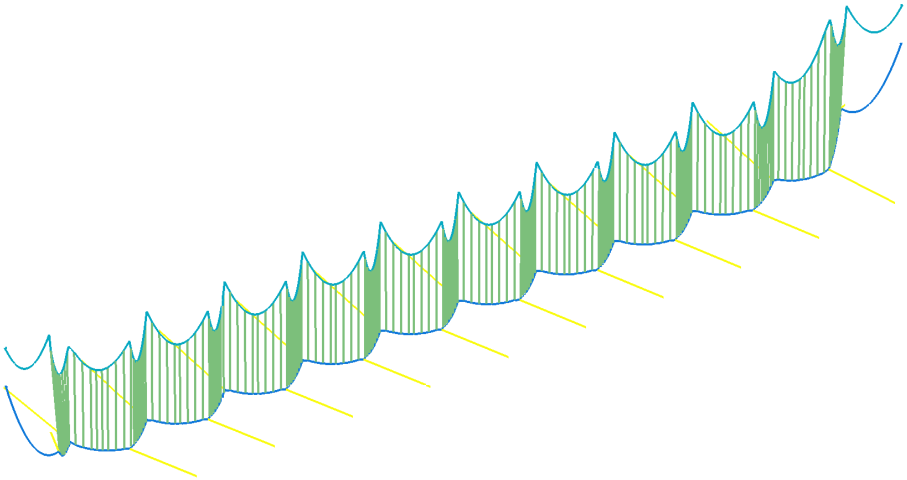

Figure 1.9: Model of a catenary section

Although the pantograph-catenary system is non-linear due to the one-sided contact laws and dropper slackening,

Semi-analytical models based on assumed sine motion of the wires have been developed to understand fundamental phenomena [50, 51, 46] or to validate Finite Elements Models (FEM) [1]. The initial idea was that these models could have a lower cost, but they are clearly less flexible than 3D finite element models, which is the method of choice for the most general software packages [4]. OSCAR, the French pantograph-catenary dynamic simulation tool developed by SNCF and SDTools [52] uses this approach with few restrictions to allow contact computations. This software is a fulfilment of thirty years of work, took the OSCAR name in 2004 and is certified against the European standard EN50318 [34].

In the default behaviour of OSCAR, droppers are modelled as bars with non-linear stiffness to represent the loss of stiffness in compression. Steady and registration arms are represented using bars or beams with pin flags thus allowing pivot motion at their ends. Brackets, when represented, use either springs or beams. The various claws (for droppers, arms or junctions) are modelled using concentrated masses, except for detailed local studies such as fatigue analyses [42, 45] where beams with offsets are used to properly represent the local stiffness.

The first step of a catenary computation is an evaluation of the static position taking into account the effects of gravity and tensioning of the wires. Figure 1.10 shows two spans of the catenary subject to the tensions T_{CW} and T_{MW} in the cables with gravity applied to the masses, beams and bars.

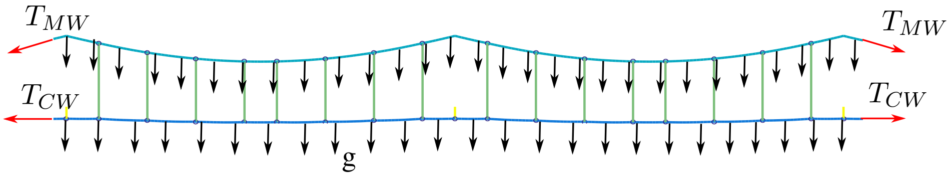

Figure 1.10: Forces applied for the static computation

The static position of the catenary and in particular of the CW, illustrated in figure 1.11, is known to have a large impact on contact forces. This position, called geometry of the catenary or sag, can be optimized as done in [53] and [54]. Similarly [55] has worked on optimal knuckle junctions. Installation guidelines [56] have been released for Shinkansen based on a link between geometry criteria and dynamic current collection quality. The contact force induced by catenary geometry will be further detailed in section 2.1.

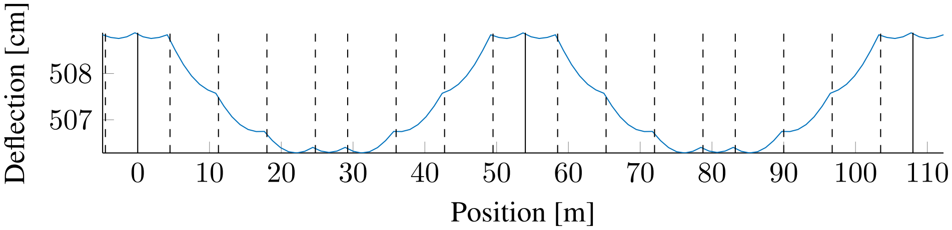

Figure 1.11: Height of the contact wire along two spans

The design objective being a static geometry in loaded condition, the choice of an initial geometry before loading is a somewhat open issue. Building guidelines typically specify dropper lengths and positions and adjustment are performed at the masts. Design strategies for the choice of dropper lengths are typically based resolution of an inverse problem based on string assumptions.

OSCAR implements a dropper adjustment procedure that seeks an initial geometry by adjusting dropper lengths that will reach equilibrium for a target CW position. This procedure will in particular be used for statistical studies on geometries in chapter 4.

Another issue of interest is that slope discontinuities between elements tend to generate contact force fluctuations. OSCAR thus typically uses initial meshes before loading where the CW geometry in unloaded condition is flat.

Catenary damping is generally modelled as a Rayleigh damping (proportional to mass and stiffness), velocity proportional damping or modal damping. In OSCAR, damping is a piecewise Rayleigh model, each element type of the system has different Rayleigh coefficients. The elements are separated in four groups: CW, MW, Droppers and SA. No damping has been set on point masses. Damping is currently the most critical parameter as dynamic results are highly sensitive to it and values are fixed by calibrating simulations on dynamic measurements. [4]. As part of this work, tests have been led on a full size catenary to determine the most appropriate damping models and coefficients. Results will be detailed in section 3.2.

In most studies, pantographs are simply modelled as two, three or four lumped-masses connected by possibly non-linear springs representing the first few modes [57]. Figure 1.12 shows a three mass model.

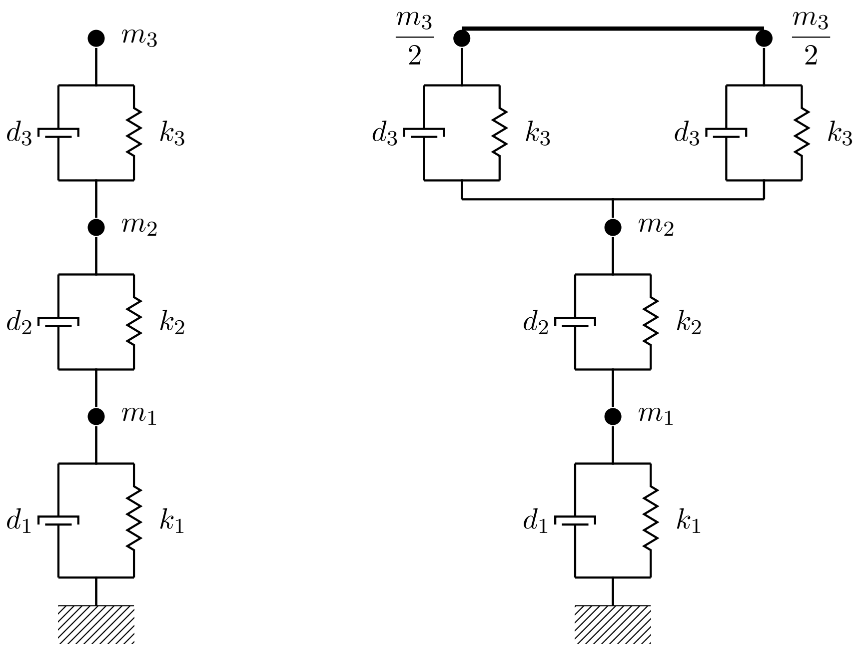

Figure 1.12: 3 masses (left) and 3 masses with friction band (right) models of pantograph

The bow is linked to the main frame by small spring systems called small plungers. The mass m_3 corresponds to the mass of the bow with the upper part of these small plungers. The stiffness k_3 and damping d_3 are approximately those of the spring system.

The mass m_2 corresponds to the mass of the upper frame with upper connecting rod and the lower part of small plungers. The mass m_1 is for the lower frame and values of d_1 and k_1 correspond to the pneumatic cushion.

Stiffness k_2 and viscous damping d_2 are fixed thanks to measurement to get the two first bending modes of the frame, which correspond to the upper frame bending with a mobility of the lower frame, around 12 Hz, and the bending of the upper frame alone [58], shown in figure 1.13.

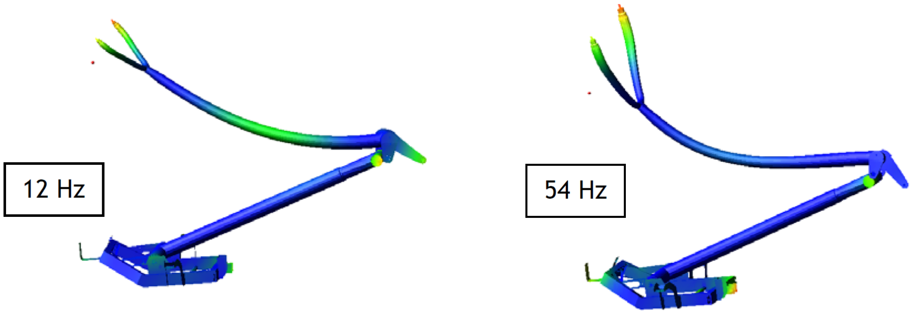

Figure 1.13: First bending modes of the pantograph frame

The first bending mode of the bow can be taken into account by separating the upper mass in two as shown on the right 1.12. When the bow is made of two independent bands, the upper mass is then divided in four.

A first level of refinement consists in adding non-linearities between the different masses. When detailed modeling of the pantograph is needed for detailed accounting of non-linearities and flexibilities, multi-body models such as the one in figure 1.14 have been used [59, 60, 61, 62, 63] in computations involving cosimulation with the FE code. With such models, the full dynamics of the pantograph can be taken into account. Sample applications are prediction of the risks of incidents such as passage of wires under the lateral horns or integration of active control laws.

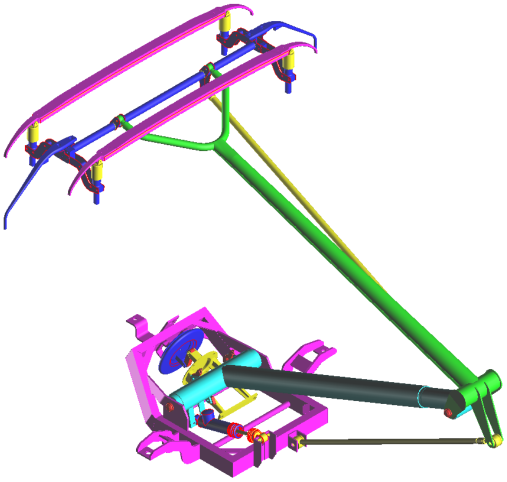

Figure 1.14: Multi-Body model of a pantograph

The dynamic behavior of the pantograph can be critical for current collection. That is why it is studied through dynamic simulations and several optimizations of its design parameters have been led either on a lumped mass model [64, 65] or a multi-body model [63].

The Hardware in the Loop (HIL) simulations [66, 67] consists in coupling a real pantograph controlled by an actuator which is commanded by a catenary model. This closed loop mixing a test bench and real time software allows to study precisely the pantograph behaviour with realistic loadings. HIL thus allows removing some model uncertainties such as pantograph non-linearities or contact stiffness.

The sliding contact between the pantograph and the catenary is usually modelled using a contact stiffness. Using a Lagrange based method would avoid introducing a parameter but leads to the introduction of high frequency dynamic behavior associated with the passage of elements [68]. The contact stiffness however has significant impact on the contact dynamics and proper understanding of its validity is still an open topic that will be partially addressed in 3.1.

Explicit solving is usually too slow for industrial application. Implicit numerical integration schemes are thus commonly used. The most spread are the Newmark scheme, used in OSCAR, and the alpha scheme.

1.2.3 Analysis of the dynamic interaction

The quality of mechanical interaction between the pantograph and the catenary is linked to the contact force applied by the pantograph to the CW. A sample of a 20Hz-filtered contact force simulated with a train passing at 90km/h and 320km/h in a nominal configuration along five spans is shown in figure 1.15. Passages at masts (or under steady arms) are indicated with vertical dotted lines). The first obvious observation is that, signals being plotted against the pantograph position, the filtering frequency of 20Hz in the temporal domain gives a totally different spatial filtering if the pantograph velocity is changed. A spatial filtering is thus more appropriate to compare contact force at different speed. For a same mean contact force applied, variations are higher when speed increases. Moreover, a periodic scheme can easily be seen at 320km/h at the scale of the span. The aim of this section is to give a first understanding of phenomena which contribute to this periodic signal.

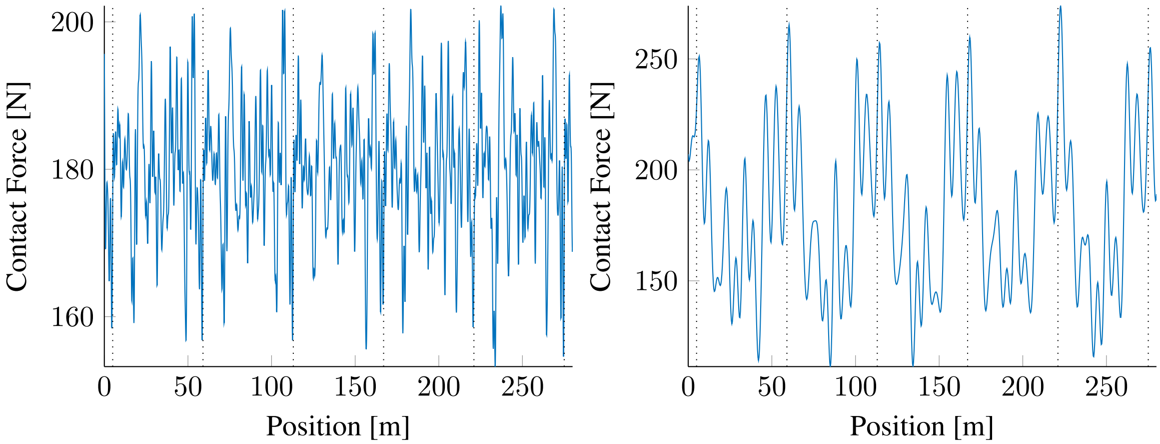

Figure 1.15: $20Hz$-filtered contact force simulated at $90km/h$ (left) and $320km/h$ (right)

Recent improvements in computation capacity enable simulation of contact forces and catenary displacements for a large range of velocities. Contact force can thus be drawn as a color map depending on the position of the pantograph and its velocity as shown in figure 1.16 for two different spatial filtering. These contact forces have been normalized to avoid hiding information at low speed for which contact force variations are lower. The $0.22m^{-1}$ and $0.8m^{-1}$ low pass spatial filtering correspond respectively to $20Hz$ and $70Hz$ temporal filtering frequency for a pantograph velocity of 320km/h. Filtering at a too low frequency limits localisation of peaks in the signals. Many lines which depend on the pantograph velocity become much clearer with the higher frequency filtering.

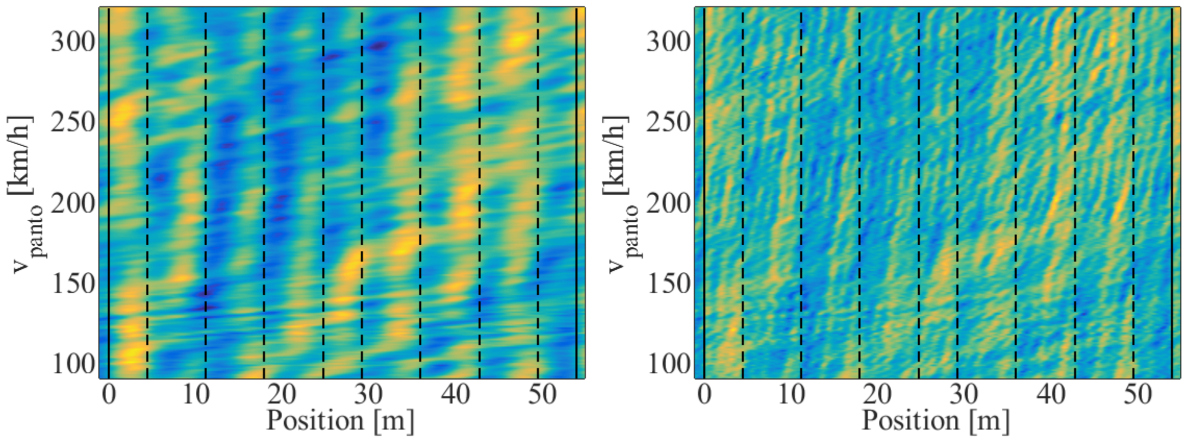

Figure 1.16: Contact force along one span filtered at $0.22m^{-1}$ (left) and $0.8m^{-1}$ (right) with SA passages in vertical solid lines and droppers passages in vertical dashed lines

A regular catenary composed of 54m-length spans only is used for simulations to enhance the observation of periodic phenomena. The contact force is then strongly periodic and the Fourier transform of this signal is easier to interpret. Figure 1.17 shows this Fourier transform against spatial (left) and temporal (right) frequencies. Several features are lines in one for a type of frequency and curves in the other. Contact force periodicity is thus caused by phenomena with temporal and spatial periodicity.

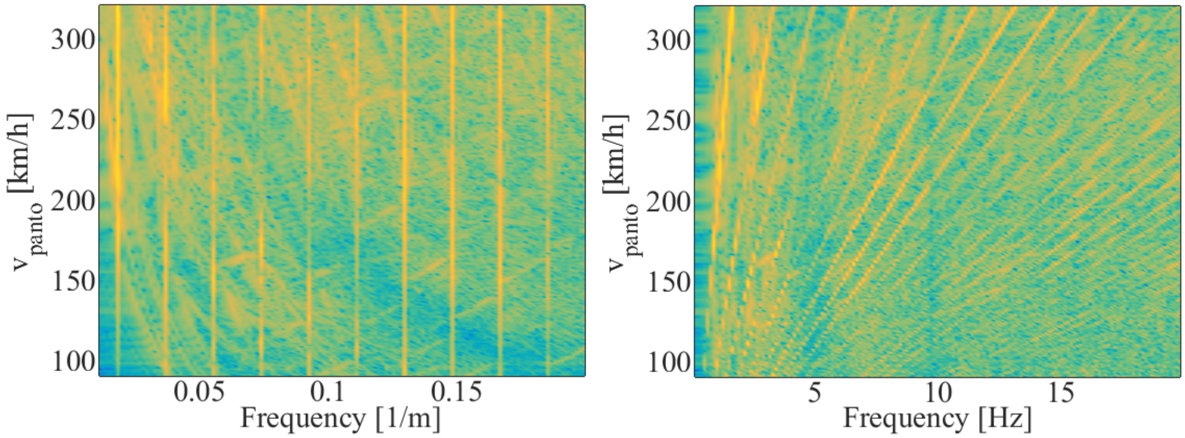

Figure 1.17: Amplitude spectrum of the Fourier transform of the contact force as a function of pantograph velocity in spatial (left) and temporal (right) frequency domain

All these observations on contact force are made in the pantograph moving frame. In the fixed frame of the catenary, many other data are available using the same map representation. Figure 1.18 shows the normalized uplift of the contact wire under a SA placed at the position $x = 320m$. On the spatial representation (left), the vertical line clearly indicates the pantograph passage under the observed point. The maximum peak observed on this line is more critical for specific pantograph velocities, for example at around $140km/h$ when another line crosses the vertical one. These non-vertical lines appear vertical in the temporal representation (right). Coincidences between temporal and spatial phenomena can thus strongly impact uplift and thus dynamic behaviour of the pantograph-catenary couple.

A clear transition appears around $170km/h$ over which on vertical line appear in the time representation. This phenomenon will be discussed in section 2.3.

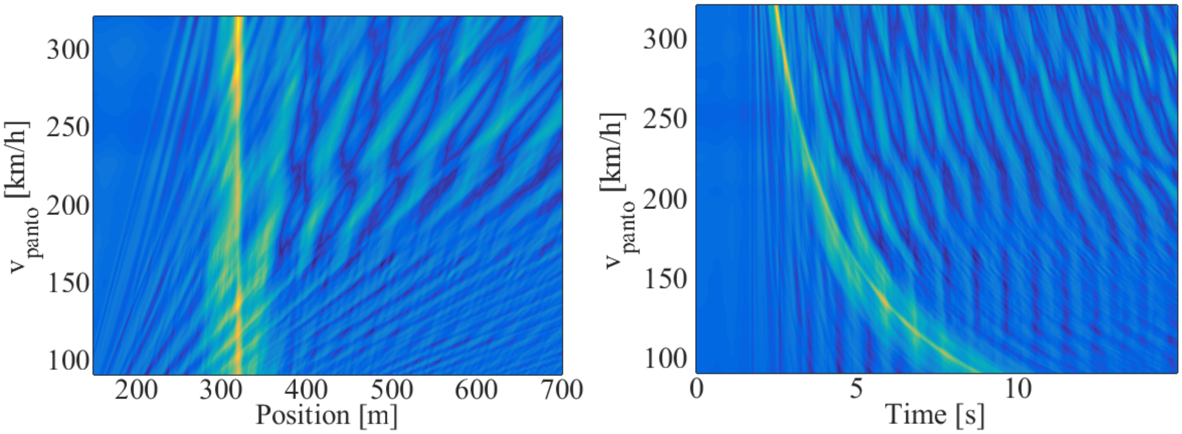

Figure 1.18: Uplift of the contact wire at the sixth SA placed in position $x = 320m$ against pantograph position (left) and time (right)

The Fourier transform of the uplift shows mainly low frequencies. Vertical acceleration of the contact wire is thus preferred to show higher frequency phenomena. Figure 1.19 shows these Fourier transform of accelerations against spatial (left) and temporal (right) frequencies. A large net of curves can be observed and again, coincidences lead to higher energies localized at specific pantograph velocities for specific frequencies.

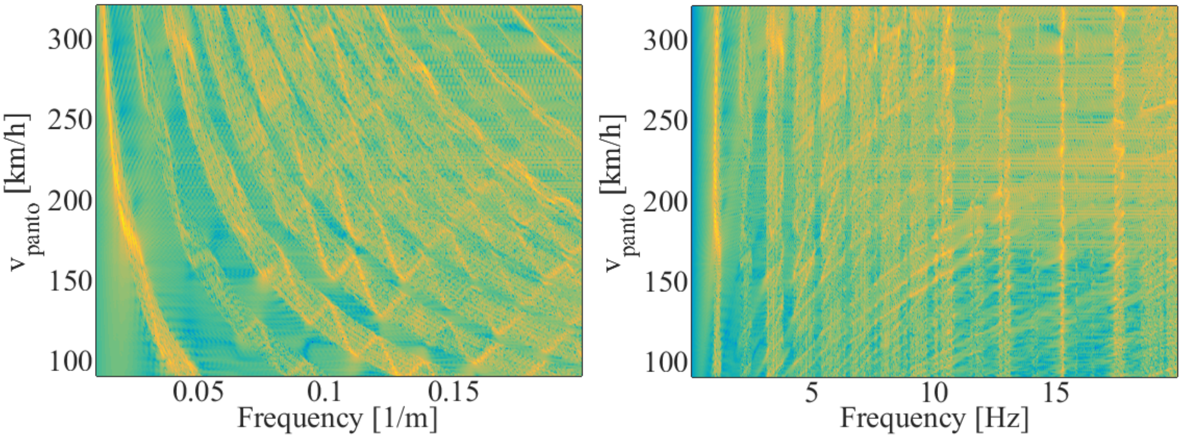

Figure 1.19: Fourier transform of the vertical acceleration of the contact wire under a SA placed in the middle of the catenary section against pantograph velocity in the spatial (left) and temporal (right) frequency domains

Finally, the uplift of the contact wire at the pantograph passage over a span as shown in figure 1.20

mix the observations made in fixed and moving frames. The transition seen in fixed frame at $170km/h$ is also observed in the spatial domain (left), while the vertical spatial frequency lines of the moving frame can be observed in the Fourier domain (right)

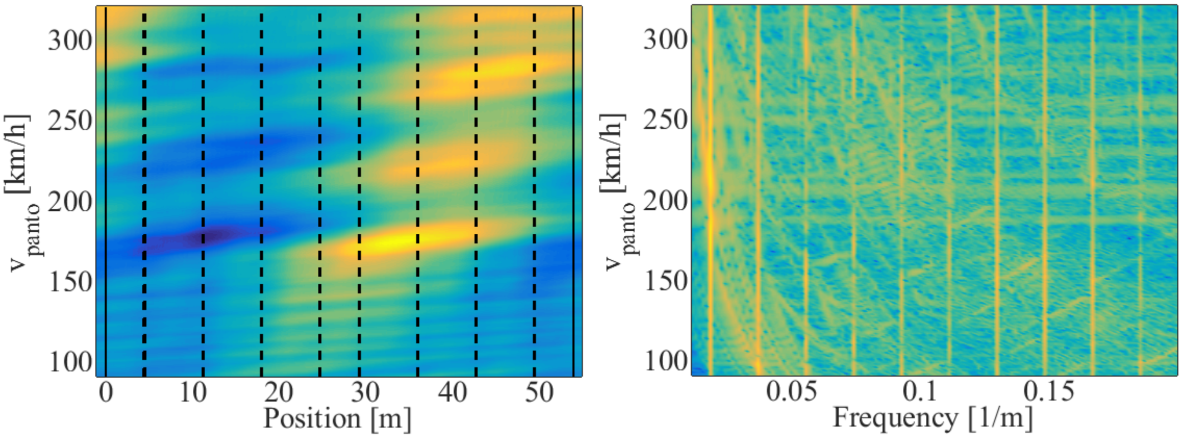

Figure 1.20: Uplift of the contact wire at the passage of the pantograph along one span (left) and its Fourier transform in spatial frequency domain (right)

The identified phenomena that occur in all these observations are the dynamic response of the pantograph to the catenary static geometry, the wave propagations in wires and reflections/transmissions at droppers, masts or SA.

Some of these phenomena clearly appeared during tests led on a full-size catenary for damping characterization. The tests consisted in mass drops at different points of the catenary with different masses while measuring accelerations with four tri-axial accelerometers. Figure 1.21 shows the full catenary model (top) with the sensors positions (red) for one configuration and the positions of the masses dropped (blue). Tests were led with sensors spread on two spans to observe the signals before and after a SA (top), only inside a span (bottom left) to observe reflections and transmissions on droppers, or in the span without any dropper (bottom right) to observe wave propagation and reflection/transmission on a mass (black) when one is added.

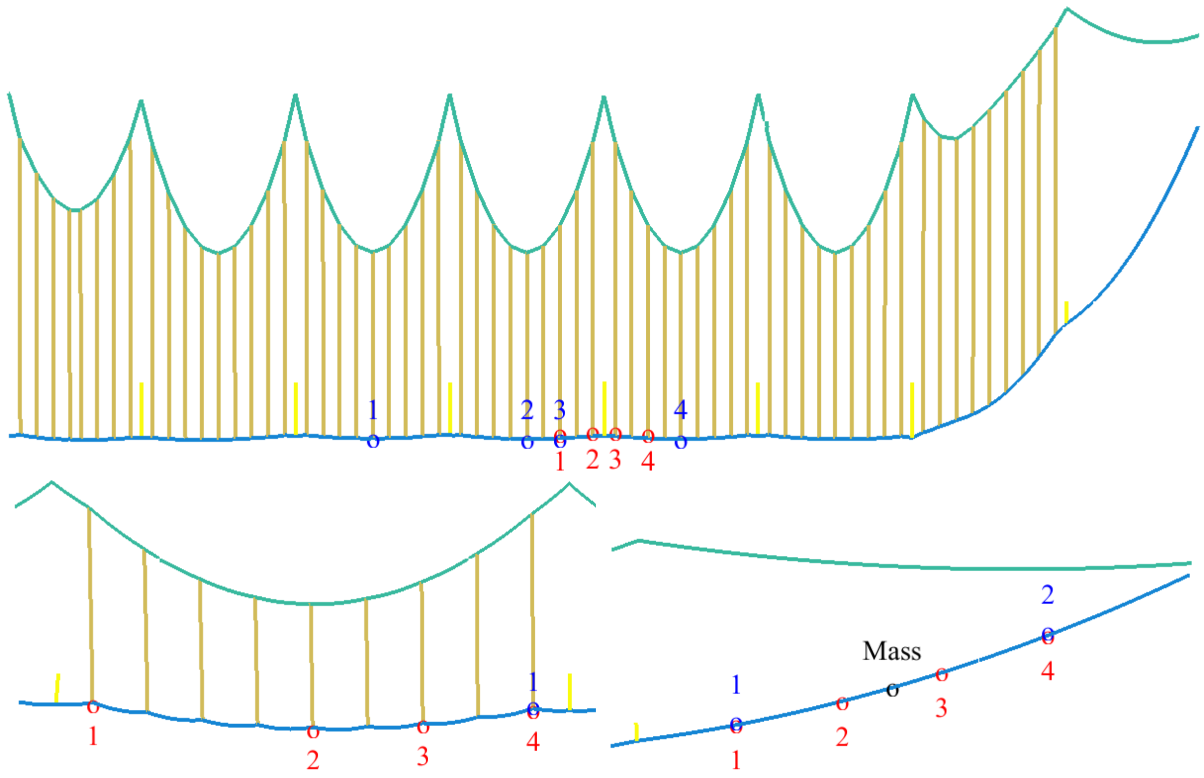

Figure 1.21: Mass drops for three sensors configurations indicated in red, different position of the mass dropped (blue) and added hung mass (black)

Figure 1.22: A mass drop test on the full size catenary

A sample of measurement in the configuration of figure 1.21 top is shown in figure 1.23 which corresponds to the vertical velocity measured in sensor 1 (red) for a mass of $40.6kg$ dropped at position 3 (blue), which is collocated with the sensor. Two droppers separate the sensor from the SA. The wave generated by the mass dropped at $t = 0$ is partially reflected at the first and second droppers which generate waves that reach the sensor at the times indicated with vertical dotted lines. The reflection on SA appears between $0.3s$ and $0.4s$ and is combined with several other reflections/transmissions.

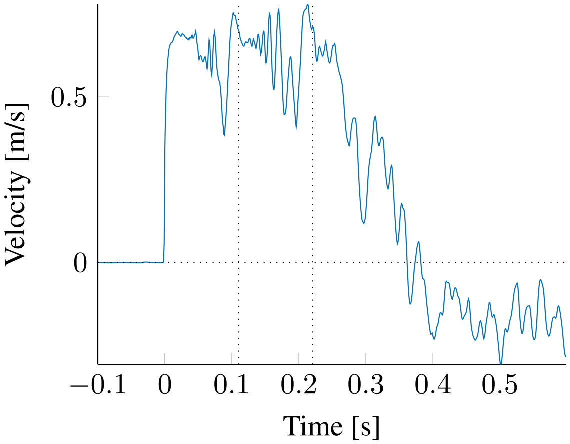

Figure 1.23: Vertical velocity measured at the position of a mass dropped

Figure 1.24 shows a simulation of a mass dropped at $t = 0$ in position $x = 0$. Wave propagation, reflection, transmission on droppers and SA are also clear.

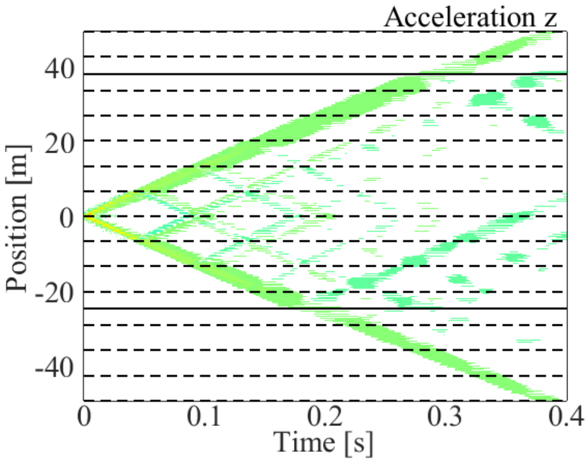

Figure 1.24: Vertical acceleration after a mass drop at $t = 0$ in $x = 0$ with positions of SA indicated in horizontal solid lines and droppers in horizontal dashed lines

The initial observations of this section have highlighted the importance of considering fixed and moving frames, spatial and temporal Fourier transforms, wave propagation in cables, reflections and transmissions at droppers and various discontinuities. Chapter 2 will thus focus on enhancing this analysis to help analysing the many coincidence phenomena that lead to the variations of dynamic response of the coupled pantograph/catenary system.

1.2.4 Uncertainties

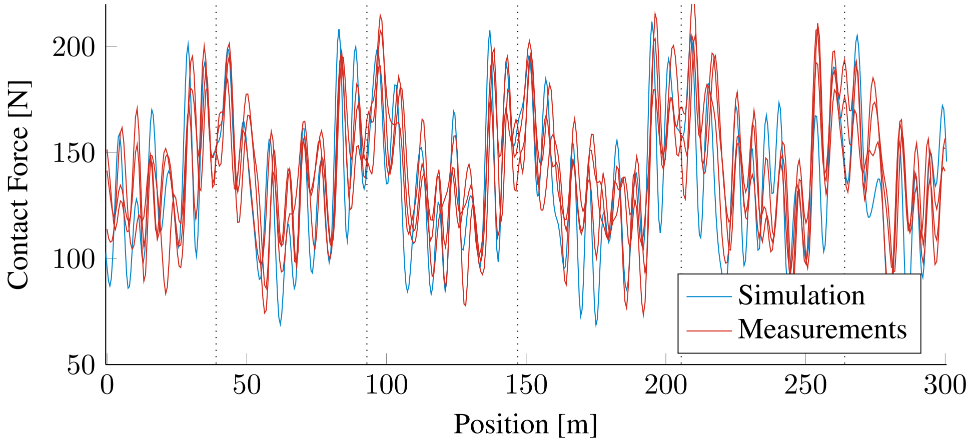

Figure 1.25: Simulation and three different measurements of the $20Hz$-filtered contact force under the same section

The contact force computed by simulation, once 20Hz filtered, is visually close to the measurements. Figure 1.25 shows a sample simulation corresponding to three different measurements of the same section. The variability in measurements is clear and opens the question of uncertainties.

Uncertainties are generally classified into two kinds. The first is variability, also called aleatory or inherent uncertainty. It is irreducible and is caused by random phenomena. The second is epistemic uncertainty that is composed of all data that could be reduced in other words known with sufficient knowledge.

In the case of pantograph/interaction models, epistemic uncertainty, often simply called uncertainty, can be classified as shown in figure 1.26. Damping and contact model are critical because of their strong impact on contact force. Damping is measurable and full size tests were led and are exploited in section 3.2 to reduce this uncertainty. The impact of the contact stiffness is detailed in section 3.1. Finally, the impact of mesh refinement is discussed in section 3.3.

The second step of uncertainty analysis is to identify all the potential sources of variability. Figure 1.28 shows these sources classified in three different groups: rolling stock, infrastructure and environment. Figure 1.27 shows pantograph collecting current during the measurement campaign for EUROPAC [69]. For the same operation conditions (speed, train, position along the line, etc.), there is no arcing when the weather is good and many arcs when humidity is high. This illustrates variability of the current collection quality, but not necessarily that of contact force since the impact of rain on arcing is not understood in detail.

Most of uncertainty sources in Figure 1.28 cannot currently be modelled due to a lack of knowledge. Section 1.3 thus presents a study focusing on known uncertainties the wind, the contact wire wear and the catenary geometry with the objective classifying their influence.

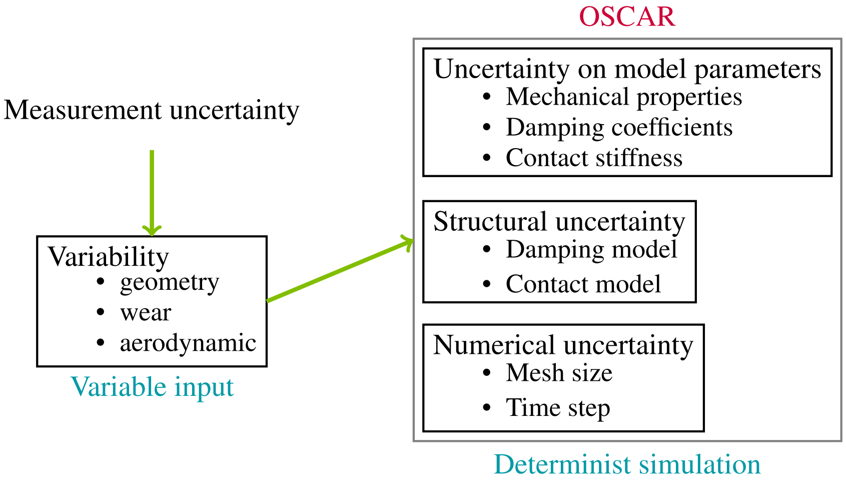

Figure 1.26: Identified epistemic uncertainty

Figure 1.27: Good (left) and bad (right) current collection quality under the same catenary type for different weathers

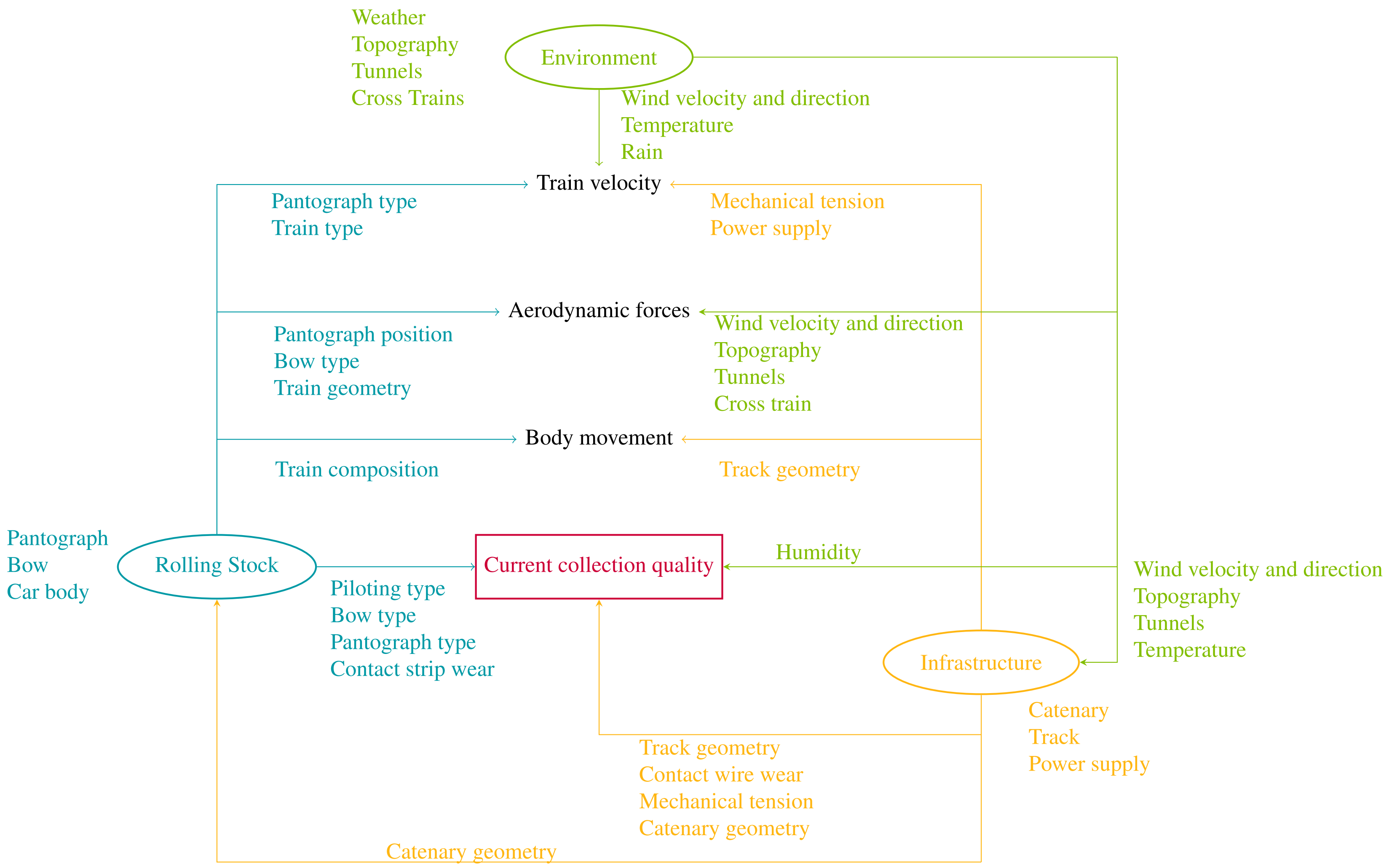

Figure 1.28: Identified variability

1.3 Preliminary characterization of variability by local sensitivity analysis

This section seeks to evaluate the impact of variabilities on the pantograph/catenary interaction. The corresponding results were published in [15]. From the list of physical variabilities identified in figure 1.28, only three are associated with available measurements:

- geometric irregularities, which correspond to the actual height of the contact wire,
- contact wire wear which is defined by the contact wire section,
- aerodynamic variability, defined as a perturbation around the mean applied aerodynamic force

Section 1.3.1 proposes a characterization of each source. Section 1.3.2 then details their influence on the contact force.

1.3.1 Characterisation of sources

The method to account for each variability depends on how each parameter influences the dynamic behaviour. All considered cases however share a random signal generation process. The classical method used here is to affect a random phase ϕ_n, in the $[-\pi, \pi]$ interval, to a spectrum of known amplitude A_n and to compute the response by inverse Fourier transform,

$$z(k\Delta x) = \sum_{n=1}^{N} |A_n| e^{\frac{j2\pi kn}{N} + \phi_n} \tag{1.4}$$

where zero mean is achieved by setting $A_0 = 0$ and the spectrum is constrained to be symmetric (that is $A_{N-n} = A_n$ and $\phi_{N-n} = -\phi_n$) to obtain a real realization by inverse Fourier transform.

Geometric irregularity characterizes differences between nominal and real geometry of the catenary particularly at mast and dropper positions. The nominal geometry is defined by perfectly regular sag of $1/2000$ and a fixed height identical for every mast. This study focuses on parameters like dropper length and mast height, which affect the contact wire static height. Figure 1.29 shows a measurement that is clearly much less regular than the theoretical design. The spatial and spectral representations are given for measurements in solid line and for the nominal height of the catenary in dashed line. Measurements are low-pass filtered using a 20-points moving average method. This corresponds to a filter at $0.25m^{-1}$ or equivalently, $4m$, which is smaller than the smallest inter-dropper distance. Higher frequency irregularities are not taken into account since they cannot be caused by geometric irregularities.

Between droppers and spans the geometry is only linked to tension, beam section and gravity which are supposed to be known. The proposed strategy is thus to use random values for contact wire height at dropper and span locations. Wear induces height modifications whose dynamic impact is very low for long wavelengths. Geometry modifications induced by wear can thus be neglected.

A random spatial signal is first generated using (1.4) and the amplitude spectrum of measurement shown in blue in figure 1.29 (right). Given this signal, an inverse static computation is performed by modifying dropper length of the nominal catenary in order to converge to the target position of contact wire at dropper and span locations. The resulting catenary mesh is then used in dynamic simulations, thus taking into account geometric irregularities. Figure 1.30 (right) shows an example of sag obtained

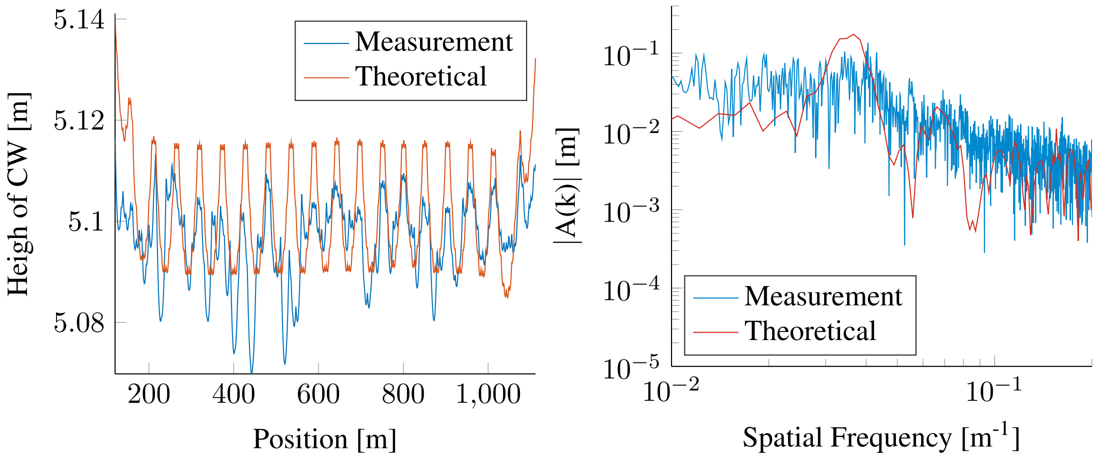

Figure 1.29: Filtered measurements (blue) and theoretical (red) CW height (left) and amplitude of spatial-spectrum of CW height (right)

from the nominal catenary model and the target height after an inverse static computation. On the left, the difference between computed sag and measurement is shown and demonstrates that the target geometry is reached with a gap of less than $1mm$ along the contact wire. The highest variations come from the approximation of the masts height, which is negligible.

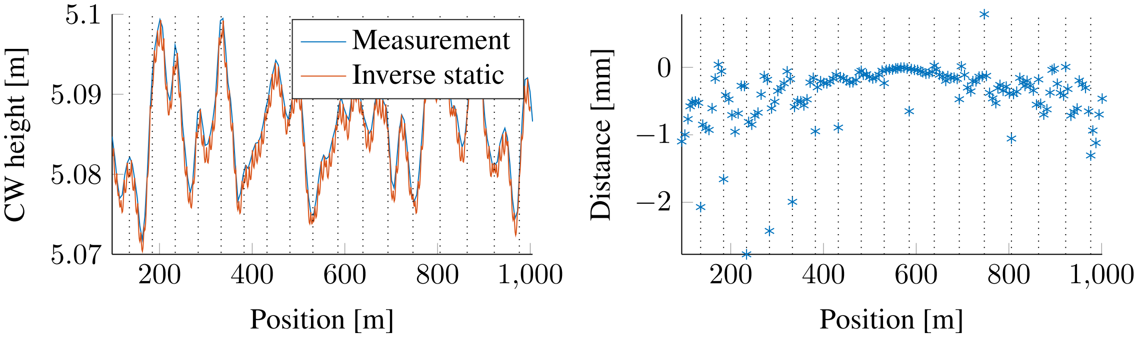

Figure 1.30: Comparison between contact wire height measured and computed by inverse static method

Wear can slightly modify dynamic behaviour of the catenary since it acts on local stiffness and on contact wire height. It is characterized by a decrease of section area A and an increase of contact wire height. In-line measurements are used to determine a mean wear over the contact wire. These global values allow to define coefficients of a wear law defined experimentally [29] as

$$A = k_1 \left(1 + \frac{i}{i_0}\right)^{-\alpha} \left(\frac{F_c}{F_0}\right)^{\beta} \frac{V}{V_0} \frac{F_c}{H} + k_2 \frac{R(F_c) i^2}{H \cdot V} \tag{1.5}$$

with

$$R(F_c) = \frac{k_r}{\sqrt{F_c}} \tag{1.6}$$

where A is the surface removed by one pantograph passage in [mm], F_c the load in [N], i the electric current and V the train speed. V_0, i_0 and F_0 are used for normalization and taken equal to nominal values, i.e. $V_0 = 3m/s$, $i_0 = 426A$, $F_0 = 190N$. k_1, k_2, α and β are the non dimensional parameters defined to fit with measurements. H is the hardness of the softer of the two materials, $H = 110HR$. Finally, k_r is a coefficient used to interpolate the relationship between R and F_c, $kr = 4.9710^{-2}\Omega.N^{1/2}$.

Contact force is thus strongly linked with CW wear. As the contact force is usually higher in the same area of the CW, the spatial distribution of wear is not totally random. To take into account this information, the contact force F_c is simulated using the nominal geometry. The wear profile obtained for one cycle $A(x)$ where x is the axial position along the catenary, is then multiplied by a target number of cycles before renewing the contact force computation. The full lifespan of the contact wire is thus separated into n linearly spaced simulations, n representing the number of cycles varying between 0 and 10^8.

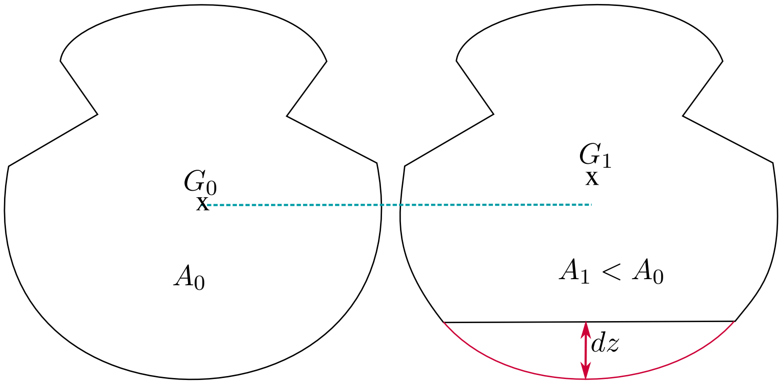

Figure 1.31: Contact wire section of new (left) and worn (right) wire, A being the section area and G the centre of gravity

Wear induces two main effects, the first is a perturbation dz to the vertical position of the contact point as it is illustrated in figure 1.31. In the time integration, solved with Newmark implicit method, dz is thus considered,

$$Kq + C\dot{q} + M\ddot{q} = k_c(z_{cat} + dz - z_{panto}) \tag{1.7}$$

where K is the stiffness matrix, C the damping matrix, M is the mass matrix, z_{cat}, height of the contact wire corrected by the section change dz and z_{panto}, height of the pantograph. q is the displacement vector and k_c the contact stiffness.

The second effect is a section reduction of the contact wire which leads to a decrease of the local stiffness. As OSCAR uses FEM, stiffness variations cannot have higher frequency than the one induced by the element size. A constant stiffness is applied for each beam element of the contact wire, by averaging the random section wear signal over the element length. Both phenomena are taken into account at the same time in this study, which does not aim at analysing their impact separately.

The aerodynamic irregularity is defined as a time varying vertical force fluctuating around the mean

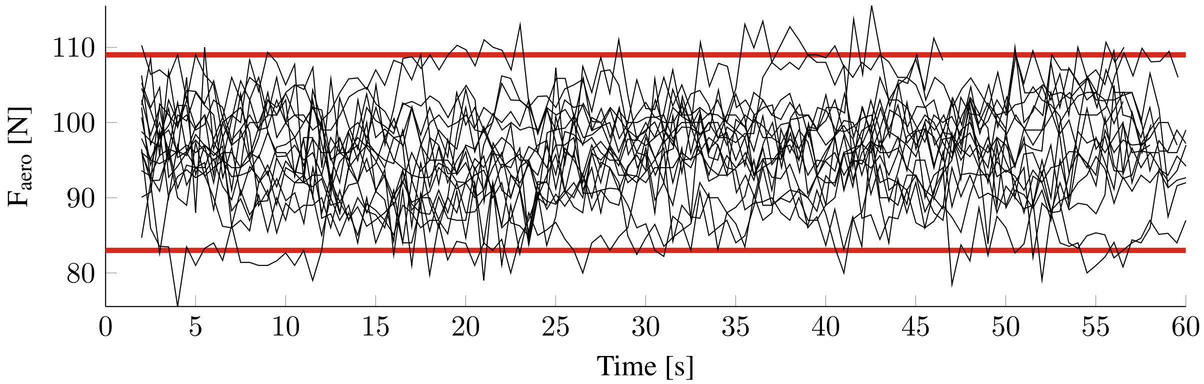

Figure 1.32: Measured aerodynamic forces (black) and 95% probability interval (red)

aerodynamic force applied on the pantograph. This variation is due to changes in different parameters such as train speed or wind speed and direction. Available measurements are used to compute the mean aerodynamic force. They are filtered at $1Hz$ and give a reasonable indication of the variation range for the aerodynamic force. For the considered case at $320km/h$ shown in figure 1.32, a mean of $96N$ and a range of variation between $83N$ and $109N$ with a 95% confidence interval are observed.

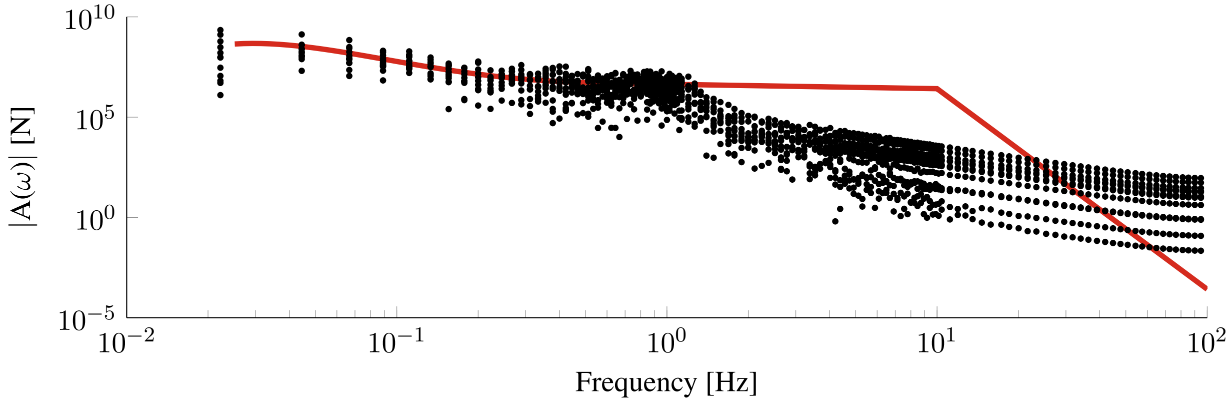

Figure 1.33: Aerodynamic force spectrum measured (black) and spectrum shape defined (red)

While defining a probability distribution for the aerodynamic force would be a classical approach, it does not contain any spectral information so that a different approach was preferred here. A design force spectrum is defined by extending measurements to higher frequencies which is used to generate a vertical load on the upper mass of the pantograph model using 1.4. Figure 1.33 shows the extension of the spectrum. This extension was done by roughly taking the mean value of the spectrum amplitude computed at $1Hz$ as fixed amplitude between $1Hz$ and $10Hz$. The frequency under $1Hz$ corresponds to a spatial frequency under $0.012m^{-1}$ for a nominal speed of $83m/s$, which is under the span frequency, equal to $0.0185m^{-1}$. The value $10Hz$ has been taken arbitrary.

1.3.2 Impact on contact force

After having generated a thousand of random geometries, wear profiles and aerodynamic forces, dynamic simulations have been computed separately, i.e. three thousand simulations. A direct comparison of contact forces in time domain is not possible, in particular due to the presence of phase differences. To address this issue, different statistical quantities are studied. The usual approach to quantify the current collection quality is compute the coefficient of variation of contact force, in other words its standard deviation $\sigma(F_c)$ divided by its mean $\mu(F_c)$. This value is computed for each simulation and for each type of irregularity, a sample of one thousand coefficients of variation is computed. Standard deviation of this variable and of other scalar values such as the standard deviation of the contact force $\sigma(F_c)$ or the mean contact force $\mu(Fc)$,

- $\sigma(\mu(F_c)_i)$ the standard deviation of the mean contact forces
- $\sigma(\sigma(F_c)_i)$ the standard deviation of standard deviations of contact forces
- $\sigma(\frac{\sigma(F_c)_i}{\mu(F_c)_i})$ the standard deviation of coefficients of variation of contact forces

are computed.

Table 1.1 summarizes results. $\sigma(\frac{\sigma(F_c)_i}{\mu(F_c)_i})$ shows that the main irregularities impacting the current collection quality are the geometric and aerodynamic ones, wear can already be taken aside. Nevertheless, the way they impact the dynamic is different. Geometry irregularity does not significantly influence the mean contact force but acts on its variations, whereas the aerodynamic irregularity mainly changes the mean contact force.

Table 1.1: Standard deviation of three statistical moments of contact force

Criteria / Irregularities	$\sigma(\mu(F_c)_i)$	$\sigma(\sigma(F_c)_i)$	$\sigma(\frac{\sigma(F_c)_i}{\mu(F_c)_i})$
Geometric	0.18	1.2	0.0087
Aerodynamic	3.5	0.21	0.0068
Wear	0.02	0.24	0.0019

Aerodynamic irregularities were roughly modelled due to lack of measurements. For instance, direction or gusts of wind were not taken into consideration. Impact of aerodynamic variability should thus be studied in detail when measurements are available. It was thus chosen in this work to focus on geometric irregularities, which have the highest impact on current collection and are associated with plenty of measurements. Chapter 4 will thus detail building of a statistical model of parameters impacting geometry and chapter 5 will use this model to illustrate possible uses an uncertain model in relation with maintenance and performance criteria.

Chapter 2

Dynamic properties of catenaries and pantographs

The simple parametric studies of section 1.2.3 highlighted the importance of considering fixed and moving frames, spatial and temporal Fourier transforms, wave propagation in cables, reflections and transmissions at droppers and various discontinuities. This chapter thus focuses on enhancing this analysis to explain the different coincidence phenomena that lead to variations of dynamic response of the coupled pantograph/catenary system.

Section 2.1 will thus deal with the dynamic response of the pantograph to a fixed rigid geometry using a simple analytical model. In section 2.2, an analysis of wave propagations in the catenary using a string model will be discussed and illustrated using mass drop tests and simulations. Section 2.3 will present the consequences of these wave propagations on the contact force and will finally resume all identified coincidences.

2.1 Influence of geometry on pantograph-catenary interaction

The geometry of the catenary corresponds to the height of the CW along the catenary, which is defined in the direction $\vec{x}$. Figure 2.1 shows an example of geometry along two spans. SA are indicated by vertical solid lines and droppers by vertical dotted lines. The catenary section, used as illustration for this section, is composed of fourteen 54m-length spans with a total length of $1135m$. The section is chosen periodic so that this geometry can be characterized by its Fourier transform in the spatial domain, $H_{CW}(k)$.

A pantograph is passing under the catenary at a speed of v_{panto}. The pantograph sees the height of the contact wire vary with a velocity $V_{CW} = ikH_{CW}(k)$ in the Fourier domain with ω the angular frequency and k the wave number. Those frequencies are linked by the velocity of the pantograph v_{panto},

$$\omega = v_{panto} \cdot k. \tag{2.1}$$

As illustrated by figure 2.2, the base lumped mass pantograph model is a 3 mass/spring/damper (m_i, d_i, k_i) system linked to the contact wire by a contact stiffness k_c. To analyze the effect of geometry, the wire is assumed to be fully rigid (fixed in its initial static position). The output wave velocities generated in front and behind the pantograph, respectively $V_{t+,panto}$ and $V_{t-,panto}$ are thus supposed

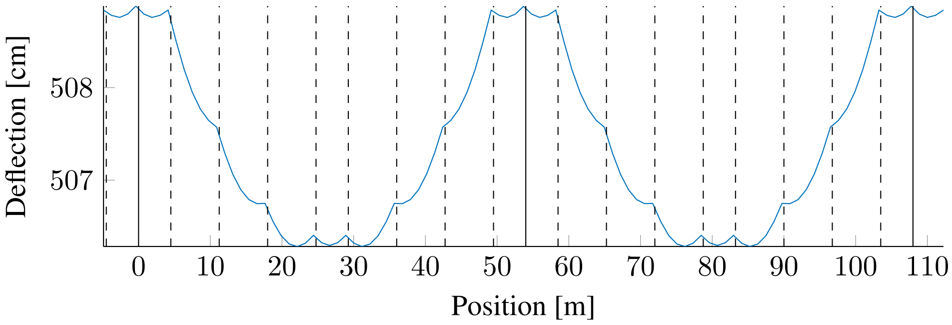

Figure 2.1: Height of the contact wire along two spans

null. For the same reason, no wave V_r in considered for now. The only output of the system is thus a force due to geometry F_{geom} and the inputs are the mean force F_0 and the velocity V_{CW}.

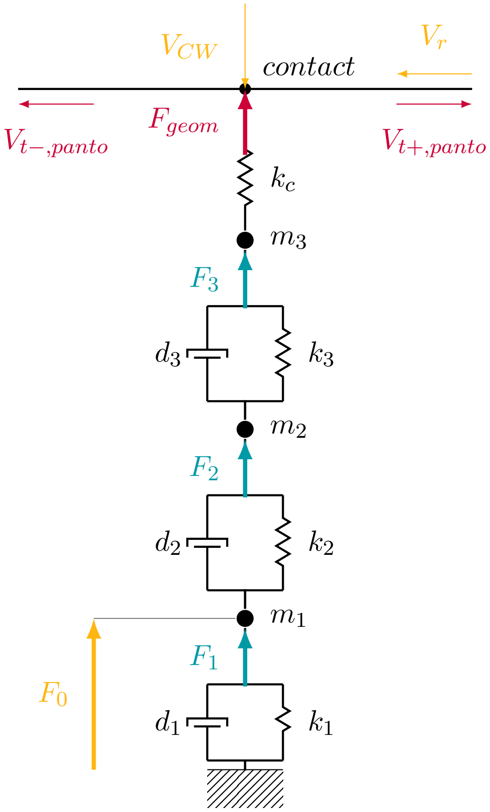

Figure 2.2: Pantograph model with the contact wire

For each damper-string cell, the relation between force and velocity is given by

$$\Delta F_j(\omega) = \Delta V_j(\omega) \cdot \left(d_j + \frac{k_j}{i\omega} \right) \tag{2.2}$$

Equilibrium at the masses, m_1, m_2 and m_3 give the system equations

$$\left[\begin{bmatrix} m_1 & 0 & 0 \\ 0 & m_2 & 0 \\ 0 & 0 & m_3 \end{bmatrix} i\omega_p + \begin{bmatrix} d_1+d_2 & -d_2 & 0 \\ -d_2 & d_2+d_3 & -d_3 \\ 0 & -d_3 & d_3 \end{bmatrix} + \begin{bmatrix} k_1+k_2 & -k_2 & 0 \\ -k_2 & k_2+k_3 & -k_3 \\ 0 & -k_3 & k_3+k_c \end{bmatrix} \frac{1}{i\omega}\right] \begin{Bmatrix} V_1 \\ V_2 \\ V_3 \end{Bmatrix} = \begin{bmatrix} F_0 \\ 0 \\ \frac{k_c}{i\omega}\cdot V_{CW,0} \end{bmatrix} \tag{2.3}$$

F_{geom}, the contact force resulting from contact point motion on the geometry, is defined by

$$F_{geom}(\omega) = \frac{k_c}{i\omega}(V_{CW}(\omega) - V_3). \tag{2.4}$$

Denoting $\mathbf{A}$ the left matrix in (2.3), $\mathbf{A}^{-1}$ can be computed and expressions of outputs evaluated

$$V_3(\omega) = (\mathbf{A}^{-1})_{3,1}\cdot F_0 + (\mathbf{A}^{-1})_{3,3}\cdot \frac{k_c}{i\omega}V_{CW}(\omega) \tag{2.5}$$

$$\begin{aligned} F_{geom}(\omega) &= \frac{k_c}{i\omega}\left(1 - (\mathbf{A}^{-1})_{3,3}\cdot\frac{k_c}{i\omega}\right)V_{CW}(\omega) && + \frac{k_c}{i\omega}(\mathbf{A}^{-1})_{3,1}\cdot F_0 \\ &= Z_{panto}V_{CW}(\omega) && + F_m \\ &= v_{panto}Z_{panto}V_{CW}(k) && + F_m \end{aligned} \tag{2.6}$$

As F_m is null for any $\omega \neq 0$, F_{geom} is mainly the product of Z_{panto} and V_{CW}. Figure 2.3 shows Z_{panto} against the temporal frequency ω in the pantograph frame and V_{CW} against the wave number k. The resulting force F_{geom} is thus a convolution of these two spectra. The amplitude spectrum of V_{CW} is clearly composed of a periodic part with a fundamental spatial frequency k_{span} defined by

$$k_{span} = \frac{1}{d_{span}} \tag{2.7}$$

where d_{span} is the length of one span, and a non periodic part at a significantly lower level.

The F_{geom} force can thus be displayed against time or spatial frequency and depends on velocity v_{panto}. Figure 2.4 compares F_{geom} to the Fourier transform of the dynamic contact force computed for different values of pantograph velocity, which is normalized by the velocity of waves in the contact wire, (see section 2.2)

$$v_{\phi,CW} = \sqrt{\frac{T_{CW}}{\mu_{CW}}} \tag{2.8}$$

$$\beta = \frac{v_{panto}}{v_{\phi,CW}} \tag{2.9}$$

where μ_{CW} is the linear mass of the contact wire. It is clear that the peaks defined by V_{CW} can be observed in F_c and the amplitudes are quite close. The influence of Z_{panto} is less clear, but can still be observed as curves from top-left to bottom-right. To highlight this trend, the frequency of the anti-resonance shown as a vertical dotted line in figure 2.3 is used. Since the anti-resonance is fixed in

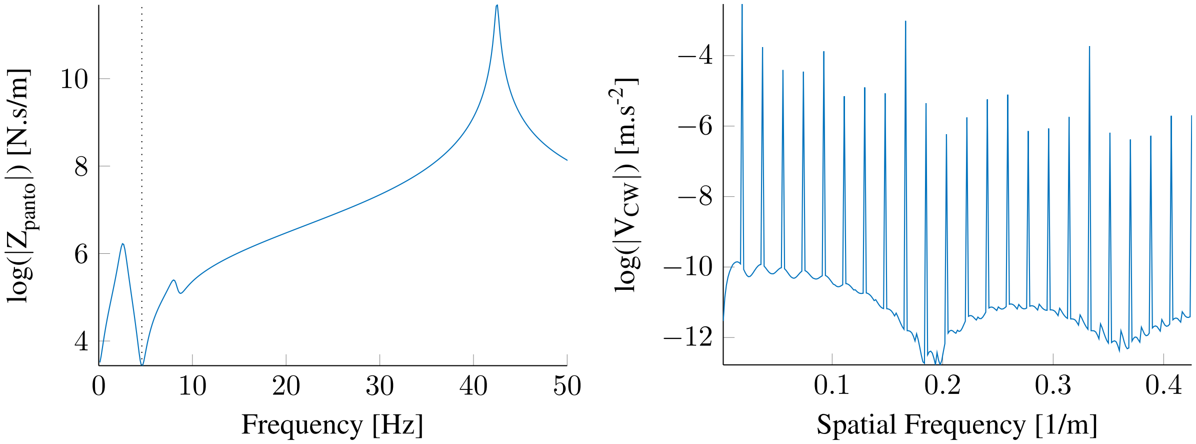

Figure 2.3: Z_{panto} (left) and V_{CW} (right)

frequency in the moving frame and a spatial frequency is used for the display, equation (2.1) leads to a shifting spatial frequency which is overlaid as a dotted curve in 2.4.

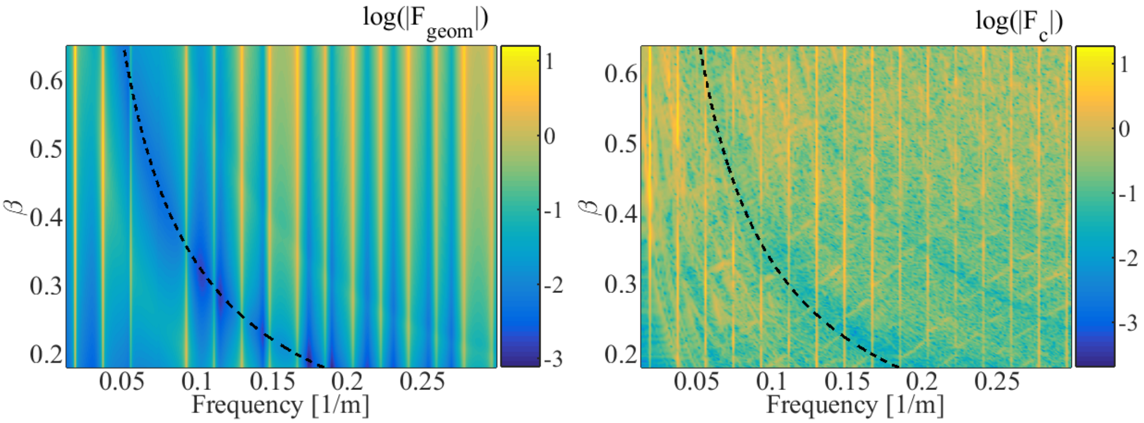

Figure 2.4: F_{geom} (left) and F_c (right)

To go back to the time domain, the inverse Fourier transform of $F_{geom}(k)$ can be computed and compared with simulations. Figure 2.5 shows this comparison for two different speeds, namely $90km/h$ and $320km/h$ corresponding to $\beta = 0.1791$ and $\beta = 0.6367$. The force variation induced directly by the geometry of the catenary increases with speed and represents the main part of the $20Hz$-filtered contact force at high speed. For low speed, other phenomena such as waves reflections may cause the contact force to significantly differ from F_{geom}.

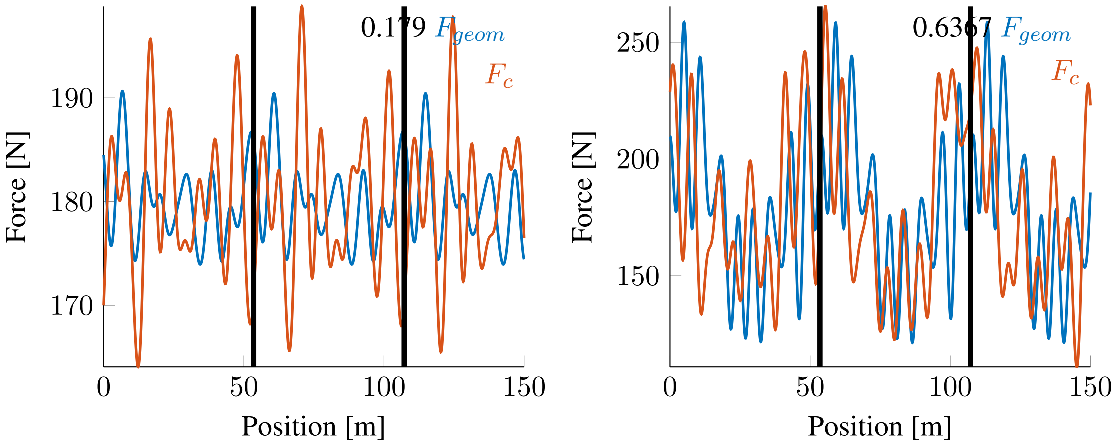

Figure 2.5: Force induced by geometry (blue) and simulated dynamic contact force (red) for two different velocities of the pantograph, $90km/h$ (left) and $320km/h$ (right)

When the contact force is observed at higher frequencies, for example using a $70Hz$ low pass filter as often in this work, the similarity between the force due to geometry $F_{geom}(x)$ and the dynamic contact force $F_c(x)$ is less clear.

In conclusion, the force due to geometry is a major contributor to low temporal frequency contact force fluctuations particularly at high speeds. This provides an extremely fast meta-model of contact force evolutions that could be used for pantograph or catenary design. This model is limited by the fact that it does not represent wave propagation effects which will thus be analyzed in the next section.

2.2 Wave propagation, reflection and transmission

The low frequency limitation of the effect of geometry can, in part, be attributed to wave propagation in cables of the catenary. Such propagation is known to have a strong impact on pantograph-catenary dynamic interaction [47, 46] and this section will analyse the issue.

Wave dispersion is the first characteristic of a wave guide. Figure 2.6 shows the vertical velocity of the contact wire after a mass drop $20m$ away from the sensor. Oscillations can be observed progressively increasing before the step corresponding to the wave arrival at the sensor. These oscillations are an experimental observation of wave dispersion and this will be detailed in section 2.2.1 by comparing behaviour of the non-dispersive string and Euler-Bernoulli beam models.

As was illustrated in figure 1.24, waves reaching a change (claw mass, dropper, SA, ...) are subject to modifications. Reflection and transmission coefficients are thus computed and results are compared with measurements and simulations for passages on mass in section 2.2.2, dropper in section 2.2.3 and SA in section 2.2.4.

2.2.1 Wave propagation in wires and beams

Considering a beam of Young Modulus E, moment of inertia I and linear mass μ under an axial load T, equations of motion for an unconstrained Euler-Bernoulli beam with tension are well known

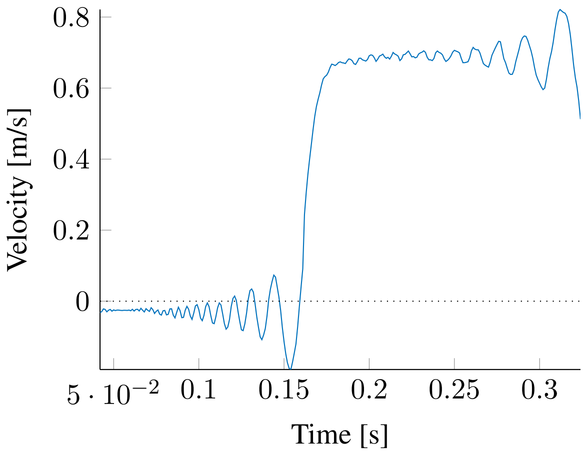

Figure 2.6: Dispersion of wave propagated observed after a mass drop $20m$ away from the sensor

(for example [70],p.196) and take the form

$$EI\frac{\partial^4 z}{\partial x^4} - T\frac{\partial^2 z}{\partial x^2} + \mu\frac{\partial^2 z}{\partial t^2} = F, \tag{2.10}$$

where F is the external force applied on the beam.

With the string hypothesis, the bending moment is neglected and defining the velocity

$$c_0 = \sqrt{\frac{T}{\mu}}, \tag{2.11}$$

the equation becomes

$$\frac{\partial^2 z}{\partial t^2} = c_0^2\frac{\partial^2 z}{\partial x^2}. \tag{2.12}$$

This is known as a one-dimensional wave equation and the solution found by d'Alembert [71] takes the form of two left and right going waves

$$z(x,t) = z_+\left(t - \frac{x}{c_0}\right) + z_-\left(t + \frac{x}{c_0}\right). \tag{2.13}$$

Defining $\Phi(k,\omega)$ to be the space and time Fourier transform of $z(x,t)$, with k the wave number and ω the angular frequency, the Fourier transform of equation (2.12) becomes

$$\omega^2\Phi(k,\omega) = c_0^2 k^2\Phi(k,\omega), \tag{2.14}$$

called a dispersion equation relating frequency and wave number. Thus, here

$$k = \pm\frac{\omega}{c_0}, \tag{2.15}$$

implying that, for a string, the wave number is linearly linked to the angular frequency.

For the beam model, the dispersion equation (2.10) becomes

$$\left(EIk^4 - \mu\omega^2 + Tk^2\right)\Phi(k,\omega) = 0 \tag{2.16}$$

In analyzing waves, quantities of interest are the phase velocity c_ϕ and the group velocity c_g [71] defined as

$$\begin{cases} c_\phi = \dfrac{\omega}{k} = \sqrt{\dfrac{T + EIk^2}{\mu}} \\ c_g = \dfrac{\partial\omega}{\partial k} = \dfrac{EIk^2}{\sqrt{\mu}\sqrt{T + EIk^2}} + c_\phi \end{cases} \tag{2.17}$$

Applied to the catenary messenger wire, the group velocity was used to determine the bending moment of the equivalent beam. Indeed, there is some doubt on the appropriate value as the messenger is composed of multiple yarns shown in figure 2.7left and wires where inter-yarn slipping is possible will appear to have a lower bending moment [72] [73].

To characterize the group velocity, a mass drop is carried out on the full size catenary used to characterize the damping. The vertical acceleration is observed $20m$ away from the mass dropped, on the messenger wire. The spectrogram of this signal gives the amplitude of its Fourier transform by frequency and time bands. The wave form can thus be observed reaching the sensor at times that depend on frequency. In figure 2.7, this time scale has been replaced by a velocity scale dividing the distance to the mass by the time. The group velocity at a given frequency is then be estimated by the maximum of the spectrogram response.

Four possible models of the beam section were considered.

- the bending moment of the 37 yarns assumed non-slipping in the configuration shown in figure 2.7 represented by the red line in figure 2.7,
- 37 times the bending moment of the center of one yarn (hypothesis of no friction), represented by the cyan line, $I_y = 37\left(\pi\frac{d^4}{64}\right)$,
- bending moment of an equivalent circular section which has the surface of the sum of 37 yarns, represented by the magenta line, $I_y = \pi\frac{\left(\sqrt{37}d\right)^4}{64}$,
- the bending moment of a full section taking into account the void, represented by the black line, $I_y = \pi\frac{(7d)^4}{64}$

The red line on the right of figure 2.7, which represents the model on the left with total friction, is theoretically the maximum observable dispersion. As a higher dispersion is observed, the real bending moment is higher, which can be explained by a configuration with no sliding but a real repartition of yarns that this less compact than the theoretical value shown in 2.7 left.

For low frequencies, the wires behave like strings. Figure 2.8 shows, as a function of frequency, the relative error on phase velocity that is made under the string assumption for the contact wire and messenger wire of the case studied. The error on wave velocity at $100Hz$ is less than 0.3%.

The pantograph-catenary dynamic interaction is currently studied until $20Hz$ for European experimental standards (EN50317), and thus, for modelling (EN50318) and thus possibly the string model could be sufficient.

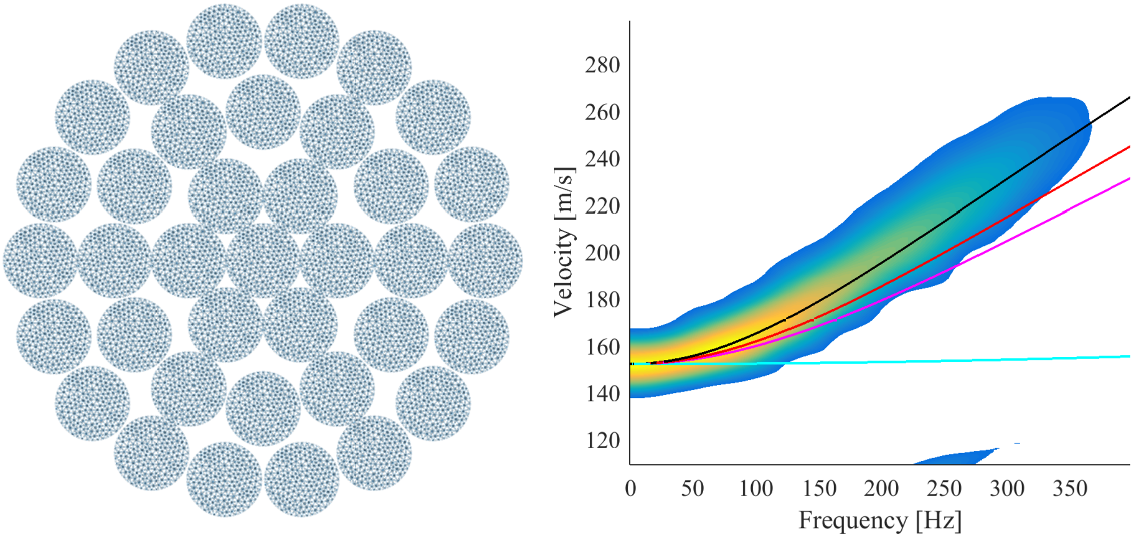

Figure 2.7: Messenger wire section composed of 37 years of diameter $d = 1.5mm$ (left) and experimental group wave velocity obtained from a spectrogram and theoretical values for four different models of inertia (right)

Nevertheless, wave dispersion is non-negligible and can be easily observed for arriving trains or for a mass drop as was shown in figure 2.6.

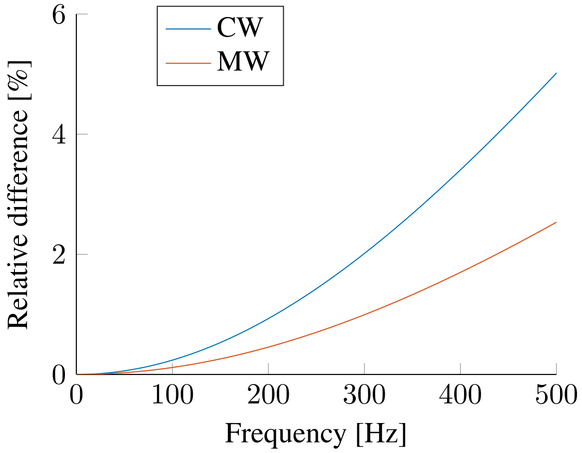

Figure 2.8: Error on phase velocity when making the string hypothesis compared to the Euler-Bernoulli beam

2.2.2 Wave reflection and transmission on a mass

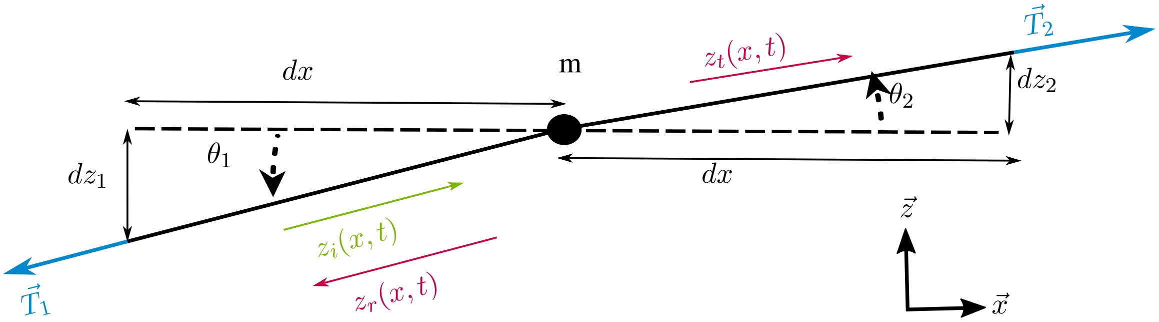

Figure 2.9: Wire of length $2dx$ with a mass m in $x = 0$

Starting with the string model, reflection and transmission coefficients can be computed when a wave meets a mass. An incident wave $z_i(x,t)$ propagates in a horizontal cable with a velocity $c = \sqrt{\frac{T}{\mu}}$ in the positive direction. When it reaches the point mass m, a reflected wave $z_r(x,t)$ and a transmitted wave $z_t(x,t)$ are generated. These waves can be expressed as

$$\begin{cases} z_i(x,t) = \int_{-\infty}^{\infty}\int_{-\infty}^{\infty} \Phi_i(k,\omega)e^{i\omega(t-x/c)}\,dk\,d\omega \\ z_r(x,t) = \int_{-\infty}^{\infty}\int_{-\infty}^{\infty} \Phi_r(k,\omega)e^{i\omega(t+x/c)}\,dk\,d\omega \\ z_t(x,t) = \int_{-\infty}^{\infty}\int_{-\infty}^{\infty} \Phi_t(k,\omega)e^{i\omega(t-x/c)}\,dk\,d\omega \end{cases} \tag{2.18}$$

with $\Phi_i(k,\omega)$, $\Phi_t(k,\omega)$, $\Phi_i(r,\omega)$ the double Fourier transform (in space and time) of the vertical displacement of the incident, transmitted and reflected waves respectively.

Newton's second law applied on the mass gives

$$-T\frac{\partial z_i}{\partial x}\bigg|_{x=0^-} - T\frac{\partial z_r}{\partial x}\bigg|_{x=0^-} + T\frac{\partial z_t}{\partial x}\bigg|_{x=0^+} = m\frac{d^2 z_m}{dt^2}. \tag{2.19}$$

where $T\frac{\partial z}{\partial x}$ represents the shear force. This leads, using equations (2.18), to

$$\frac{T}{c}\left(\Phi_i(k,\omega) - \Phi_r(k,\omega) - \Phi_t(k,\omega)\right) = i\omega m\Phi_t(k,\omega). \tag{2.20}$$

Continuity of displacement at $x = 0$ gives

$$\Phi_i(k,\omega) + \Phi_r(k,\omega) = \Phi_t(k,\omega). \tag{2.21}$$

Replacing $\frac{T}{c}$ by $\sqrt{\mu T}$ using (2.11), the system of equation determined by equations (2.20) and

(2.21) is thus

$$\begin{bmatrix} 1 & 1+\dfrac{i\omega m}{\sqrt{\mu T}} \\ -1 & 1 \end{bmatrix} \begin{Bmatrix} \Phi_r \\ \Phi_t \end{Bmatrix} = \begin{bmatrix} 1 \\ 1 \end{bmatrix} \{\Phi_i\} \tag{2.22}$$

which leads to the analytical expression of reflection and transmission coefficients

$$\begin{Bmatrix} \Phi_r \\ \Phi_t \end{Bmatrix} = \begin{bmatrix} \dfrac{-i\omega m}{\sqrt{\mu T}+i\omega m} \\ \dfrac{\sqrt{\mu T}}{\sqrt{\mu T}+i\omega m} \end{bmatrix} \{\Phi_i\} = \begin{bmatrix} R_{mass}(\omega) \\ T_{mass}(\omega) \end{bmatrix} \{\Phi_i\} \tag{2.23}$$

Figure 2.10 shows examples of reflection and transmission coefficients for masses of $200g$, corresponding to the mass of the claw linking the dropper with the contact wire, and $1kg$ which is approximately the mass of a junction claw used to locally reinforce damaged contact wires. In the frequency range commonly studied, these mass have almost no effect. The impact of a junction mass on wave reflection should only be taken into account if the frequency range analysed is over $20Hz$.

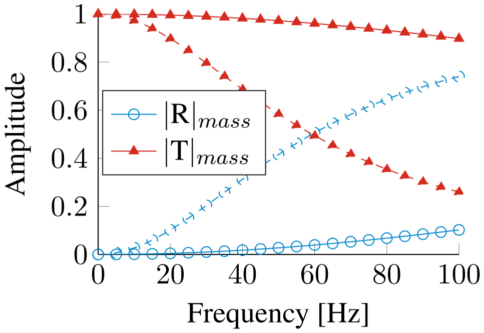

Figure 2.10: Coefficients of reflection (blue) and transmission (red) for masses of $200g$ (solid) and $1kg$ (dashed)

This analytical result can be compared with simulation and measurement. A mass drop on the contact wire has been performed for the configuration shown in figure 1.21 (bottom left). A mass of $20kg$ is dropped at position 1 and is reflected on a mass of $9.6kg$. Figure 2.11 left shows the vertical velocity $5m$ away from the mass measured without (blue) and with (red) the added mass and simulated without (yellow) and with (purple) added mass. The delay observed on the measurement where the wave reflection is supposed to appear, at $t = 15s$ is partially due to the uncertainty on the exact distance between the sensor and the mass.

On the right, the difference between tests is shown in blue and between simulations in red. The figure further shows, in yellow, the analytical value of the reflection to a step of amplitude $0.65m/s$ obtained by inverse Fourier transform of (2.23).

The oscillations before $0.15s$, correspond to high-frequency reflected waves which are quicker due to dispersion. Their amplitude is high for simulation, which is consistent with the fact that almost all the high frequency waves are reflected. The result is less clear on the test, which needs a clear explanation. Figure 2.12 shows the simulations for a mass directly attached to the wire (blue) and for a mass attached by a spring of stiffness $k = 15kN.m$ which leads to a frequency mode of $40Hz$. It is clear that the stiffness of the rope used to attach the mass explains the difference between simulation

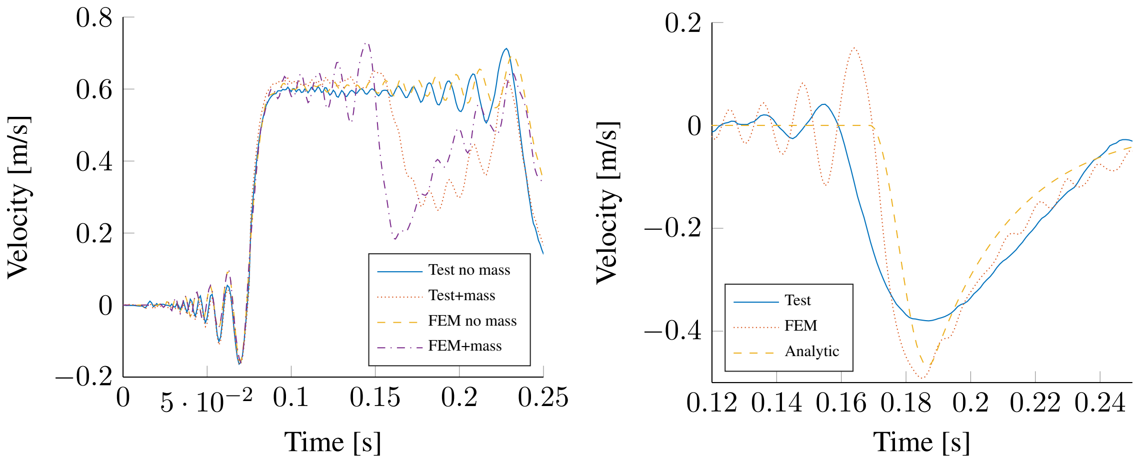

Figure 2.11: Vertical velocity of the CW $5m$ away from a mass of $9.6kg$ with and without mass, simulated and measured (left) after a drop of a $20.2kg$-mass. Comparison of the measured, simulated and analytical wave reflected (right).

and measurement. This also explains the delay observed on the red curve of figure 2.11 left.

The amplitude of vertical velocity before ($< 15ms$) and after ($> 0.25ms$) the passage of the wave are the same. This is easily related to the fact that no reflection exists at the frequency of $0Hz$.

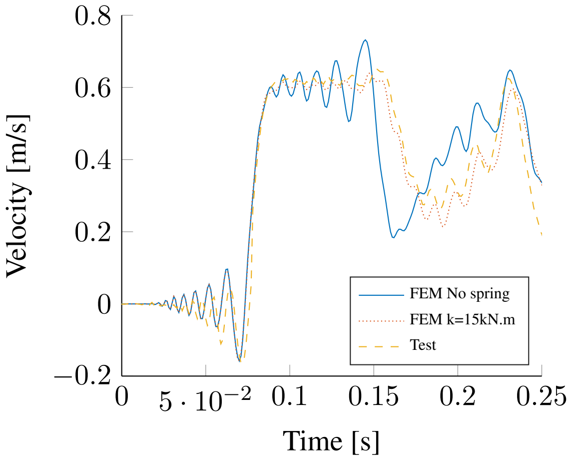

Figure 2.12: Simulation of wave reflection on a mass of $9.6kg$ directly linked to the wire (blue) and linked with a rope of stiffness $k = 15kN.m$ (red)

Simulations, tests and analytical model have thus been demonstrated to be consistent. If the Euler-Bernoulli beam model had been used in equation (2.19), the analytical result would have been identical to the simulations. The string model does not represent the dispersive behavior and this has a significant amplitude compared to the main wave amplitude.

2.2.3 Wave reflection and transmission on a dropper

The dropper is the only link between contact and messenger wires. A wave denoted $\Phi_i(k, \omega)$ propagating in the contact wire thus generates a reflected wave Φ_r and three transmitted waves shown in figure 2.13.

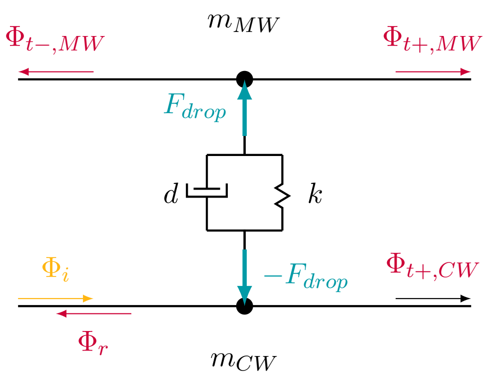

Figure 2.13: Dropper with an incident wave in the contact wire, represented by Φ_i, generating 3 transmitted waves, one reflected wave and a force in the dropper

Equilibrium at m_{CW} and m_{MW} gives equations,

$$\begin{cases} \dfrac{T_{CW}}{c_{CW}}\left[\Phi_i - \Phi_r - \Phi_{t+,CW}\right] - F_{drop} = i\omega m_{CW}\Phi_{t+,CW} \\ \dfrac{T_{MW}}{c_{MW}}\left[-\Phi_{t-,MW} - \Phi_{t+,MW}\right] + F_{drop} = i\omega m_{MW}\Phi_{t+,MW}. \end{cases} \tag{2.24}$$

Continuity of displacement at m_{CW} and m_{MW} gives two more equations,

$$\begin{cases} \Phi_i + \Phi_r = \Phi_{t+,CW} \\ \\ \Phi_{t-,MW} = \Phi_{t+,MW}. \end{cases} \tag{2.25}$$

and the impedance definition of the dropper gives the last equation

$$F_{drop} = \left[\Phi_{m_{MW}} - \Phi_{m_{CW}}\right](d + \frac{k}{i\omega}) \tag{2.26}$$

The system can be rewritten in matrix form as

$$\begin{bmatrix} \frac{T_{CW}}{c_{CW}} & \frac{T_{CW}}{c_{CW}} + i\omega m_{CW} & 0 & 0 & 1 \\ 0 & 0 & \frac{T_{MW}}{c_{MW}} & \frac{T_{MW}}{c_{MW}} + i\omega m_{MW} & -1 \\ -1 & 1 & 0 & 0 & 0 \\ 0 & 0 & -1 & 1 & 0 \\ 0 & d + \frac{k}{i\omega} & 0 & -d - \frac{k}{i\omega} & 1 \end{bmatrix} \begin{Bmatrix} \Phi_r \\ \Phi_{t+,CW} \\ \Phi_{t-,MW} \\ \Phi_{t+,MW} \\ F_{drop} \end{Bmatrix} = \begin{bmatrix} \frac{T_{CW}}{c_{CW}} \\ 0 \\ 1 \\ 0 \\ 0 \end{bmatrix} \{\Phi_i\} \tag{2.27}$$

which, once inverted gives

$$\begin{Bmatrix} \Phi_r(\omega) \\ \Phi_{t+,CW}(\omega) \\ \Phi_{t-,MW}(\omega) \\ \Phi_{t+,MW}(\omega) \\ F_{drop} \end{Bmatrix} = \begin{bmatrix} R_{drop,CW} \\ T_{drop,CWtoCW} \\ T_{drop,CWtoMW} \\ T_{drop,CWtoMW} \\ Z_{drop} \end{bmatrix} \{\Phi_i(\omega)\} \tag{2.28}$$

where $T_{CW,MW}$ is the coefficient of transmission from the contact wire to the messenger wire and R_{CW} is the coefficient of reflection of the wave in the contact wire reflected on the dropper. The same work can be done for an incident wave coming from the messenger wire leading to three other coefficients R_{MW}, T_{MWtoCW} and T_{MWtoMW}.

Figure 2.14 shows the absolute value of these coefficients for the nominal configuration. Their variation with frequency is light and for this particular case, the waves are more transmitted than reflected.

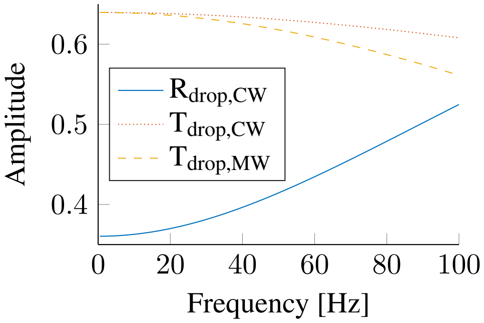

Figure 2.14: Coefficients of reflection and transmission for an incident wave in the contact wire

Figures 2.15 and 2.16 show these reflection/transmission coefficients with variations on each parameters. The mechanical tensions are the only parameters that modify low frequencies. Changing tension implies changing waves velocities and in the case shown, $T_{CW} = 20kN$ and $T_{MW} = 14kN$, which lead to $c_{CW} = 122m/s$ and $c_{MW} = 152m/s$. The coefficients at frequency of $0Hz$ can be written as

$$T_{drop,CWtoCW}(\omega = 0) = T_{drop,CWtoMW}(0) = -R_{drop,MW}(0) = \frac{\frac{T_{CW}}{c_{CW}}}{\frac{T_{CW}}{c_{CW}} + \frac{T_{MW}}{c_{MW}}} \tag{2.29}$$

$$T_{drop,MWtoMW}(\omega = 0) = T_{drop,MWtoCW}(0) = -R_{drop,CW}(0) = \frac{\frac{T_{MW}}{c_{MW}}}{\frac{T_{MW}}{c_{MW}} + \frac{T_{CW}}{c_{CW}}} \tag{2.30}$$

For the catenary on which tests were made, a wave generated in the contact wire is lightly reflected and mainly keeps propagating while generating two waves in the messenger wire of amplitude equal to the transmitted wave. Once in the messenger wire, the wave is mainly reflected at dropper and less transmitted to the three other parts. A wave in the MW is thus more likely to be trapped between droppers than transferred to the CW.

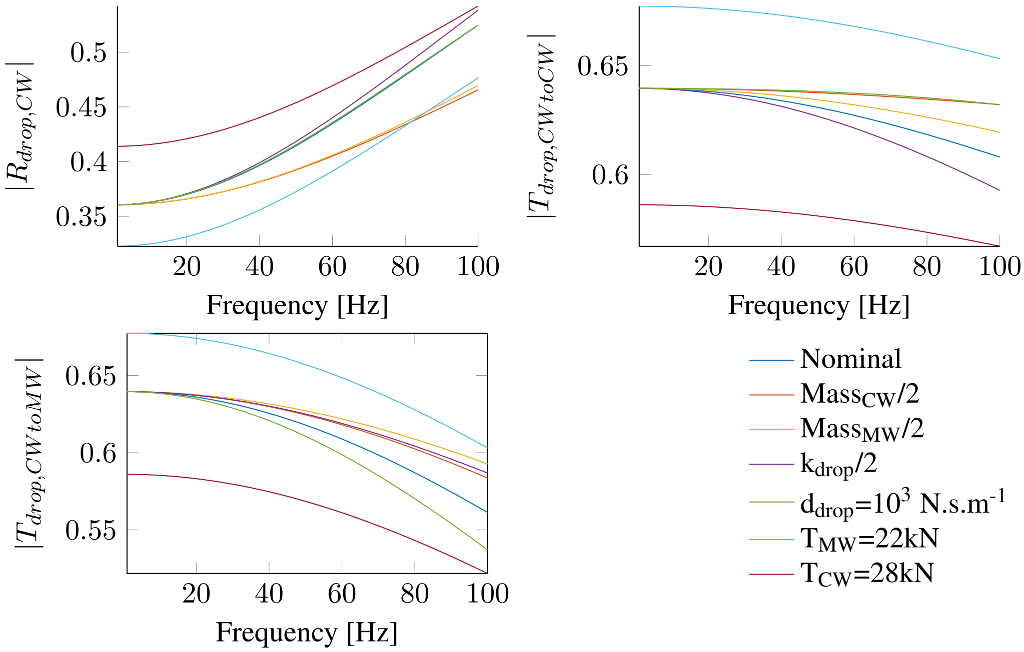

Figure 2.15: Coefficients of reflection and transmission for an incident wave in the CW with variation of different parameters

But in usual catenary designs, $\frac{T_{CW}}{c_{CW}}$ is close to $\frac{T_{MW}}{c_{MW}}$, which leads all the coefficients to have values around 0.5 and an equipartition of waves in MW and CW. The impact of this repartition is not clear. For the rest of the study, the transmission coefficient at zero frequency

$$a = \frac{\dfrac{T_{CW}}{c_{CW}}}{\dfrac{T_{CW}}{c_{CW}} + \dfrac{T_{MW}}{c_{MW}}} \tag{2.31}$$

is introduced to quantify wave repartition.

The proposed analytical model can be used to analyze tests and simulations. For example, in the test configuration of figure 1.21 top, for a mass of $40.6kg$ dropped at position 3 the velocity observed at sensor 1 is shown in figure 2.17. Vertical lines indicate the times at which wave propagated and reflected reach the sensor. The dashed line is for the wave propagated and reflected in the CW, the dotted line is for the wave propagated and reflected in the MW and the dash-dotted line is for the wave propagated in the MW and transmitted to the CW.

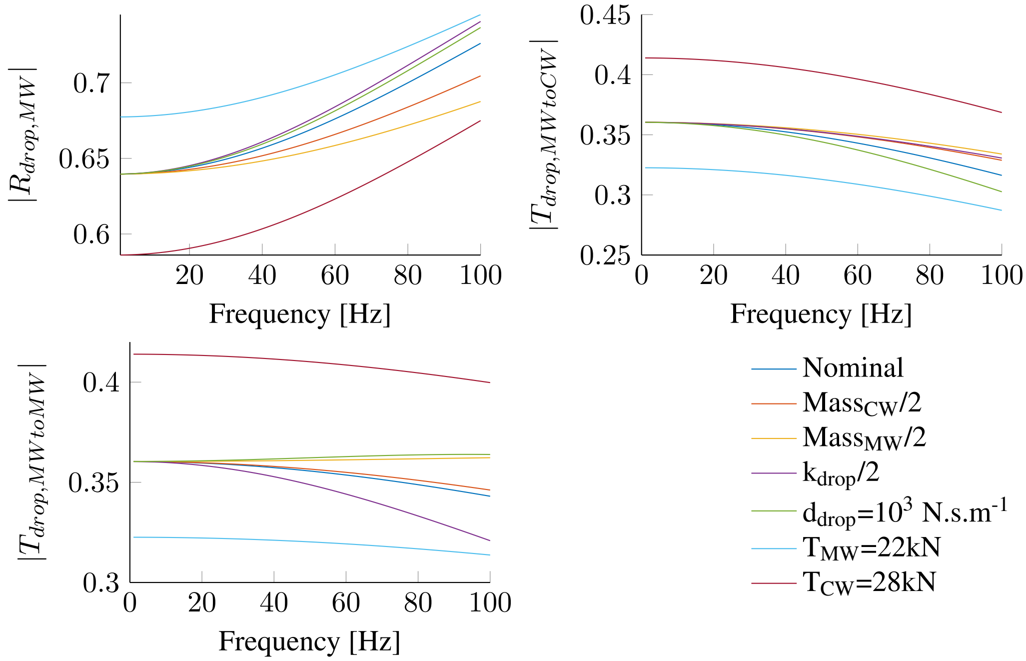

Figure 2.16: Coefficients of reflection and transmission for an incident wave in the MW with variation of different parameters

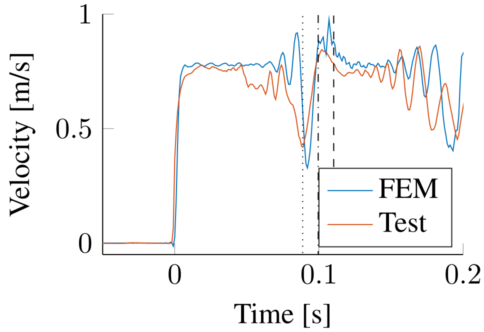

Figure 2.17: Simulation and measurement of vertical velocity

The combination of all waves makes the signal difficult to interpret. Simulations are thus used to decompose this signal and compare results with the analytical model.

First, a simulation of a mass drop of $20.2kg$ at position 1 on the CW of the FEM A shown in figure 2.18 without dropper is done. The vertical velocity step and the following wave reflected $r_{drop,CW}(t)$ on the dropper of the left is shown in figure 2.19 top with solid lines. The wave transmitted to the MW $t_{drop,CWtoMW}(t)$ and observed at position 2 is shown in dashed line. $t_{drop,CWtoMW}$ is observed before $r_{drop,CW}$ because $c_{MW} > c_{CW}$.

The second simulation is a mass drop on the MW at position 2 on the same FEM A. The mass needed to have the same step level has to be changed considering the dynamic impedance of the wire and thus multiplied by $\frac{T_{MW}/c_{MW}}{T_{CW}/c_{CW}}$, which gives a mass of $11.4kg$. The vertical velocity step and the following wave reflected $r_{drop,MW}$ on the left dropper is shown in figure 2.19 bottom using solid lines. The wave transmitted to the CW $t_{drop,MWtoCW}$ and observed at 1 is shown using dashed line.

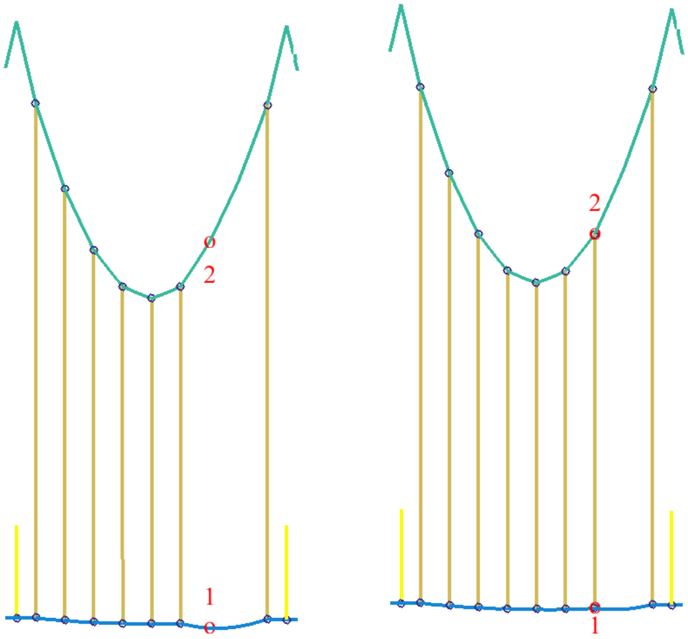

Figure 2.18: FEM A without (left) and FEM B (right) with dropper linking 1 to 2

The last simulation is a mass equal to the sum of masses dropped previously, namely $31.6kg$ dropped at position 1 on FEM B in which there is a dropper linking 1 and 2. The signal observed at 1 is compared in figure 2.20 to the sum of waves observed in CW and MW , weighted by coefficients determined in (2.29) for the sake of simplicity

$$(r_{CW} + t_{drop,MWtoCW})a + (r_{MW} + t_{drop,CWtoMW})(1 - a). \tag{2.32}$$

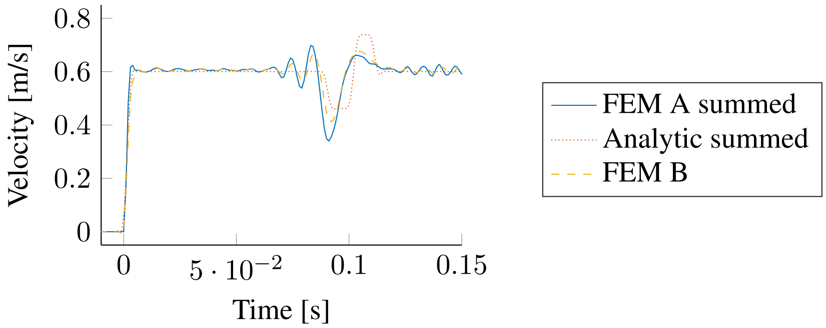

Figure 2.20: Comparison between the sum of the transmitted/reflected waves computed using FEM A (blue), using FEM B (yellow) and analytically computed (red)

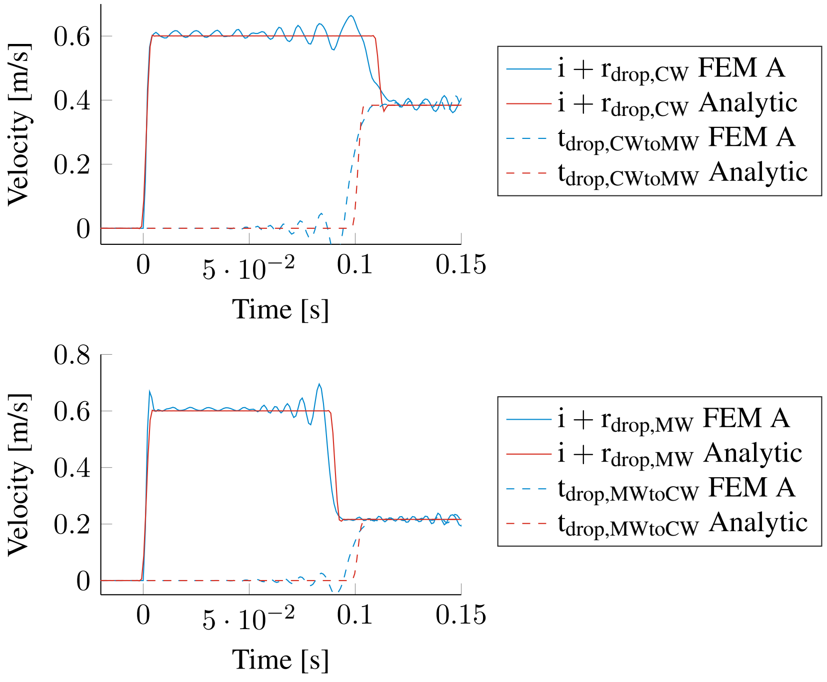

Figure 2.19: Analytical and simulated wave reflections and transmissions

The mean level of vertical velocity does not change around the vertical lines of figure 2.17 because of the compensation of waves transmitted and reflected in CW and MW. The small oscillations observed are due to the difference of wave velocities in cables. These oscillations are thus minimized if the velocities in cables are equal, $c_{CW} = c_{MW}$, which is the case for French V350 type catenaries. The proposed model is thus helpful in analyzing the influence of droppers in wave propagation within the catenary.

2.2.4 Wave behavior around the mast

The passage of the pantograph at the position of the mast is known to be the source of current collection issues with frequent arcing. At this position, the MW is linked to the mast as shown in figure 1.5 center and the CW is connected to the SA.

In OSCAR, the MW is linked to the mast by a ball joint link, authorizing rotation in the transversal and vertical axis of the MW. Vertical displacement is thus not possible and the incident waves reaching this link are fully reflected using a string model and nearly fully in the beam case.

The SA shown in figure 2.21 is an elbow arm used in traction to apply a stagger to the CW. The SA is not exactly horizontal and the part attached to the registration arm, as shown in figure 1.1, is around $20cm$ higher than the contact wire. The arm is however articulated which gives a very low stiffness in the radial direction and induces a light coupling between vertical and horizontal directions.

Figure 2.22 illustrates these waves for a mass drop and confirms that the MW wave is fully reflected, while the reflection due to the SA is negligible.

The wave in the CW that has not been reflected by the SA is reflected later on the first dropper of the following span. This time, as there is no wave transmitted in the MW after the mast, there is neither

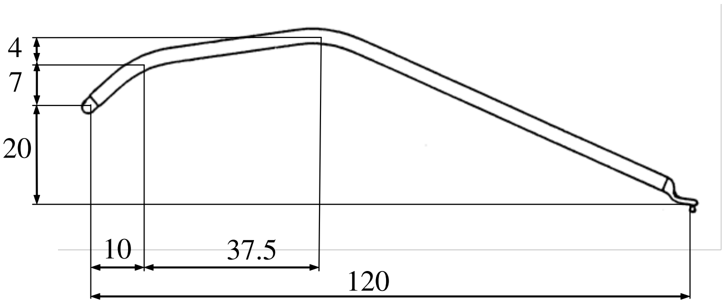

Figure 2.21: Steady arm

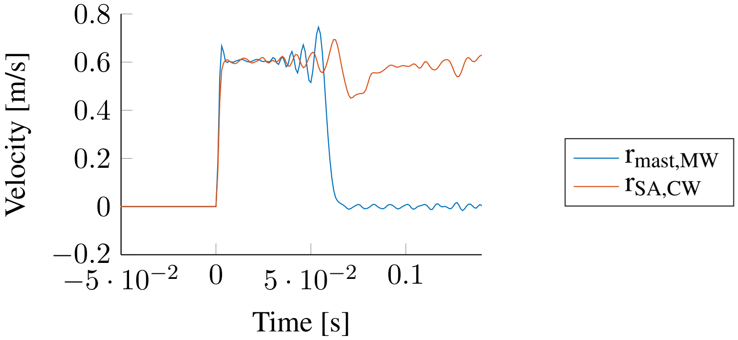

Figure 2.22: Reflections against a mast in the MW (blue) and against a SA in the CW (red) after a mass drop

$t_{drop,MWtoCW}$ nor $t_{drop,CWtoMW}$ $r_{drop,MW}$ on the right side.

For a mass dropped at the last dropper, corresponding to position 1 of figure 2.23 left, the wave $r_{mast,MW}$ generates a new wave on the opposite side which is also reflected on the mast. This wave reaches the dropper before $r_{drop,CW}$.

The velocity level after these three reflections, once normalized by the level of the step is equal to 1 minus the level of the three waves, which gives

$$2a^2 - a. \tag{2.33}$$

In our case, $a = 0.64$ which leads to a level of $0.1m/s$ for a step of $0.6m/s$.

An intuitive assumption is that the function (2.33) should be maximized. If that is the case, a should be maximized, which means for example minimizing $\frac{T_{MW}}{c_{MW}}$, while keeping c_{MW} constant (for dropper wave equilibrium). As

$$c_{MW} = \sqrt{\frac{T_{MW}}{\mu_{MW}}}, \tag{2.34}$$

one has

$$\frac{T_{MW}}{c_{MW}} = \sqrt{\mu_{MW} T_{MW}} \tag{2.35}$$

thus mu_{MW} and T_{MW} should be reduced simultaneously, or equivalently, mu_{CW} and T_{CW} increased simultaneously.

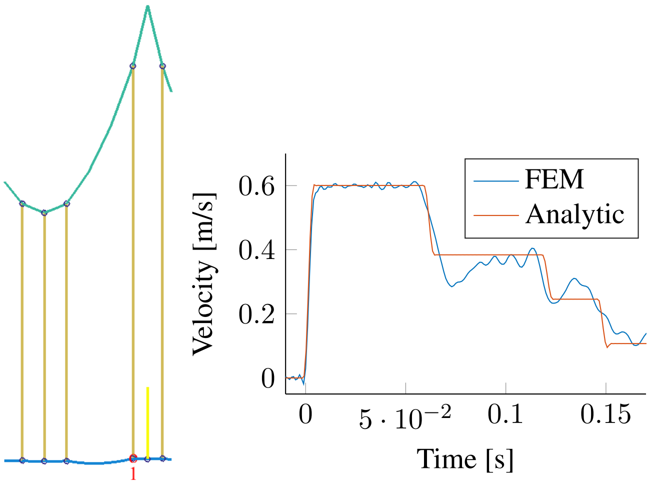

Figure 2.23: Simulation configuration (left), comparison between FEM and analytic model of a mass dropped under the last dropper of a span (right)

Figure 2.24 shows the comparison of the nominal simulation in blue with simulation for linear mass and tension of the MW both reduced by 33%. Variations of contact force are significantly reduced and the usual criterion σ/F_m drops from 0.41 to 0.35 at $70Hz$. This simple illustration demonstrates the usefulness of the proposed interpretations in finding design strategies.

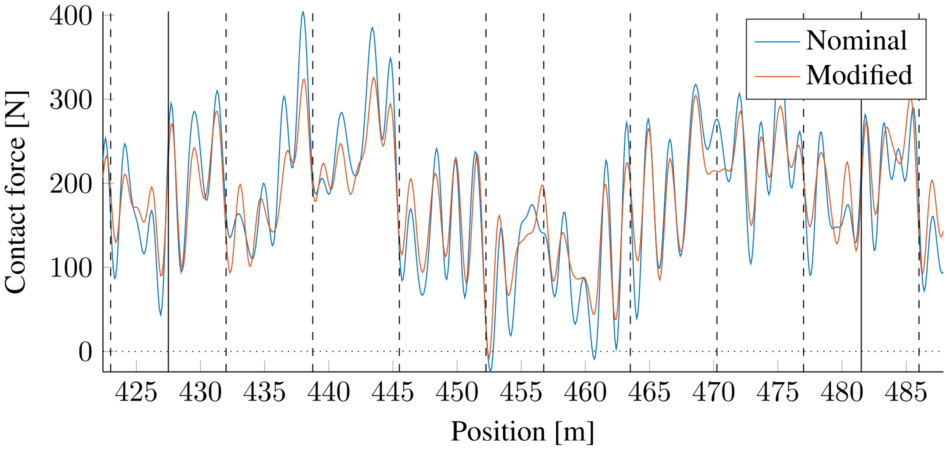

Figure 2.24: Impact of a reduction of the messenger wire impedance by 33% keeping the same wave velocity c_{MW} on a $70Hz$-filtered contact force

2.3 Characteristic times and frequencies

In section 1.2.3, it has been seen that the contact force is a periodic signal that is composed of multiple phenomena. Sections 2.1 and 2.2 have developed the influence of the geometry on the contact force and of wave propagation, transmission and reflection on the catenary dynamics. In this section, both of these phenomena will be analysed through dynamic simulations in addition to the effects of catenary modes and other specific coincidences. Section 2.3.1 details the modal response of the catenary. Then, the phenomena observed in different frames are detailed. Section 2.3.2 addresses the fixed frame of the catenary and section 2.3.3 the moving frame of the pantograph. Finally, section 2.3.4 discusses other possible coincidences and section 2.3.5 details the case of two pantographs.

2.3.1 Catenary modes

To analyse catenary modes, an SNCF catenary type V350 composed of 54m-length spans is considered here. The waves inside the wires have approximately the same velocity. The pantograph velocity is thus normalized by that of the wires,

$$\beta = \frac{v_{panto}}{c_{CW}} \approx \frac{v_{panto}}{c_{MW}}. \tag{2.36}$$

Simulations were led for a pantograph running over $3000m$ even if the catenary is only $1100m$ long so that the frequency resolution is increased in the Fourier domain. The impact of pantograph is thus reduced and the free response of the catenary is more pronounced.

To visualize modes, a range of speeds between $90km/h$ and $320km/h$ is considered. On the map displayed in figure 1.19, the first obvious lines observed are those which do not change with pantograph velocity v_{panto} and are thus vertical in the temporal Fourier domain. These lines correspond to the modal frequencies of the catenary. Figure 2.25 shows the frequency lines for the first two groups of modes, under $3Hz$. As the inter-span coupling is limited each group tends correspond to a well identified mode of a given span. There are thus as many modes in the first group under $1.5Hz$ as spans in the catenary section. The same thing holds for the second group and so on. At higher frequencies, coupling increases so that the group spread is larger and one tends to have overlap of different groups.

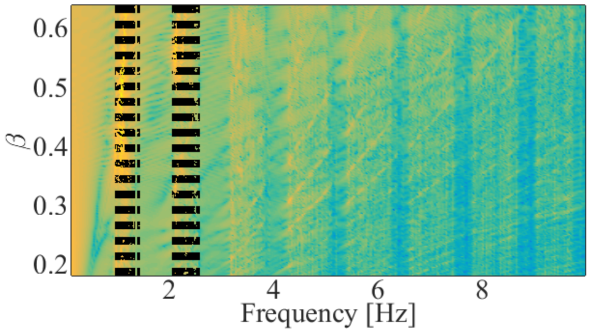

Figure 2.25: Amplitude of vertical velocity of the contact wire in the temporal Fourier domain as a function of β with catenary modes indicated as vertical lines

Section 2.2 illustrated that the influence of the messenger wire properties can be dissociated into two relevant parameters: the dynamic impedance $\sqrt{\mu_{MW}T_{MW}}$ and the wave velocity c_{MW}. Variations of c_{MW} were considered while keeping constant the dynamic impedance by changing the MW section. Figure 2.26 shows the catenary modes computed on a full catenary (left) and on a $54m$ span (right).

Modes that quickly change with c_{MW} correspond to horizontal modes of the messenger wire. The horizontal stiffness of droppers being close to zero, these modes have very little coupling with the CW leading to the high sensitivity to c_{MW}. The frequency spread of the band is very thin showing that these modes are nearly independent between spans. Modes that stay stable are the horizontal modes of the contact wire. Once again, the bandwidth is thin showing that the horizontal stiffness induced by steady arms makes spans independent for these modes.

The last type of mode groups corresponds to vertical modes coupling CW and MW. The frequency spread indicates that spans are coupled and the intermediate sensitivity to c_{MW} indicates that the energy is balanced between the CW and MW. These vertical modes are those excited by pantograph motion and visible in figure 2.25. Important modes are thus dependent velocities in both the CW and MW. The value currently thought to be relevant is the mean $(c_{CW} + c_{MW})/2$. This conclusion is comforted by results obtained in section 5.3. In the following, the normalised velocity will thus be defined as

$$\beta = \frac{2v_{panto}}{c_{CW} + c_{MW}} \tag{2.37}$$

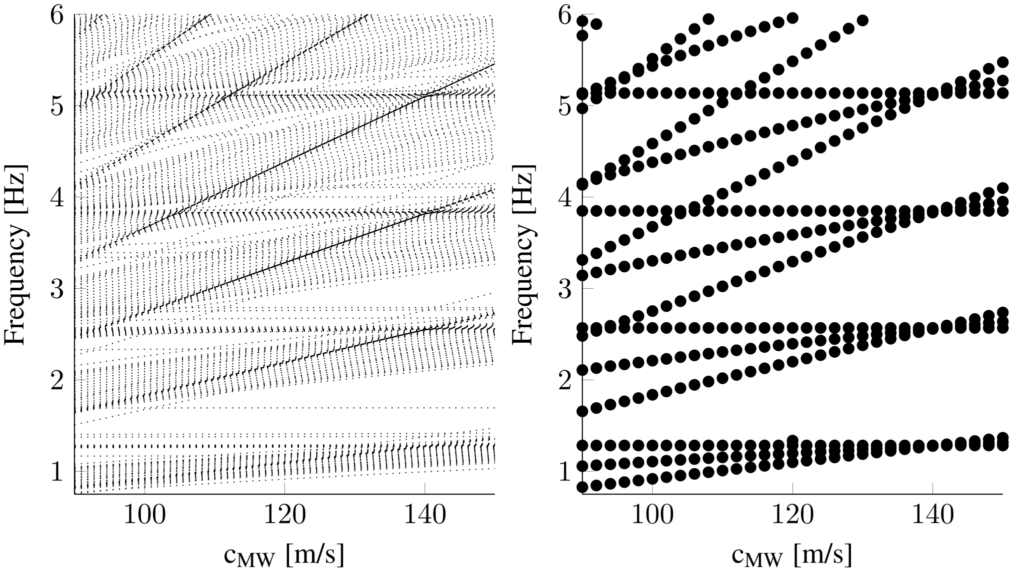

Figure 2.26: Frequency modes computed for a full catenary (left) and one $54m$-length span (right) as a function of c_{MW}

2.3.2 Coincidences in the fixed frame

Section 2.1 illustrated that the contact force due to the catenary geometry is mostly spatially periodic with a fundamental spatial frequency corresponding to the span length d_{span}. At each peak of force, a wave is generated. Supposing this wave is, for the sake of simplicity, generated at the SA at $t_{1,0}$, if the vertical velocity of the catenary is observed later at x_{obs} as shown on figure 2.27, the wave reaches the observation point with the delay

$$t_1 - t_{1,0} = \frac{d_1}{c_{CW}}. \tag{2.38}$$

When the pantograph reaches the next SA at

$$t_{2,0} = t_{1,0} + \frac{d_{span}}{v_{panto}}, \tag{2.39}$$

it generates another wave which reaches x_{obs} placed at a distance $d_1 - d_{span}$ to the dropper after a delay

$$t_2 - t_{2,0} = \frac{d_1 - d_{span}}{c_{CW}}. \tag{2.40}$$

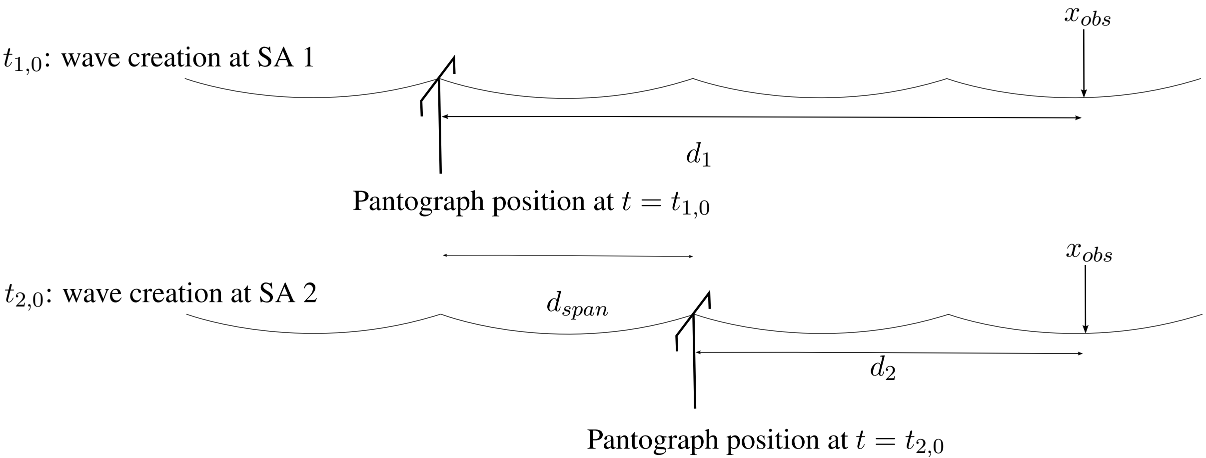

Figure 2.27: Wave propagation illustration, view from catenary

The same analysis can be done for x_{obs} placed before the pantograph. The characteristic periodicity of wave propagated by successive dropper passage regularly distant of d_{span} is thus

$$t_2 - t_1 = d_{span}\left(\frac{1}{v_{panto}} \pm \frac{1}{c_{CW}}\right) = \frac{d_{span}}{v_{panto}}(1 \pm \beta) \tag{2.41}$$

with "$-$" when x_{obs} is after the pantograph and "$+$" when x_{obs} is behind.

To illustrate these characteristic times, figure 2.28 right shows the uplift induced by the waves generated by the pantograph passing successive steady arms. These times are marked with red dashed lines. The left figure shows a map of the velocity of uplift for each position of the catenary against time. The black solid line indicates the pantograph position, the red dashed lines highlight the waves generated by the pantograph when it passes under a steady arm and the black dotted line indicates the position of the point observed on the right figure.

As the generated signal is periodic, its Fourier transform will be composed of all harmonics of the base frequency

$$\frac{1}{t_2 - t_1}. \tag{2.42}$$

Thus,

$$f_{wave,cat,\pm} = \frac{n \cdot v_{panto}}{d_{span}(1 \pm \beta)} \qquad \forall n \in \mathbb{N}^* \tag{2.43}$$

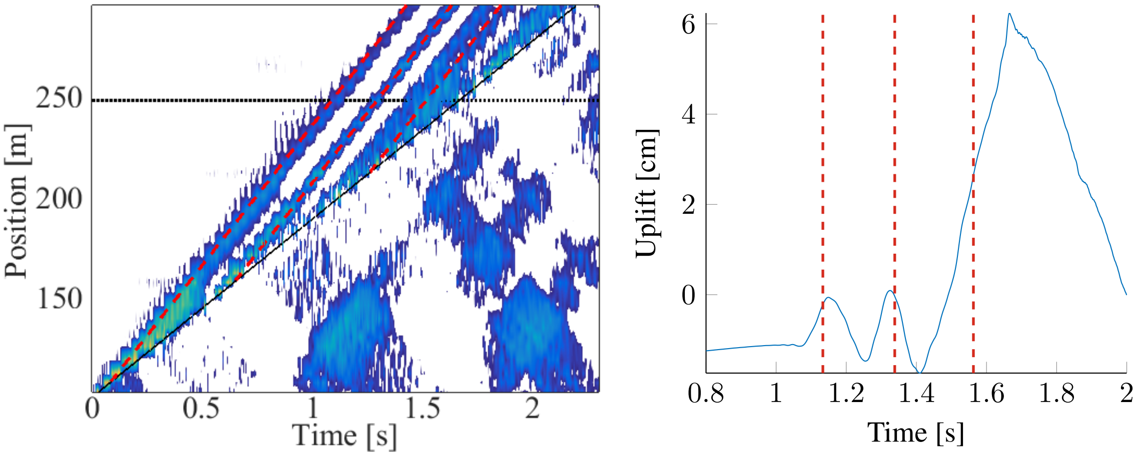

Figure 2.28: Map of velocity of uplift along the catenary against time (left) and Uplift of the catenary at a position $x = 247.5m$ (right)

Introducing $k_{span} = 1/d_{span}$ first defined in (2.7) leads, in the spatial frequency domain, to

$$k_{wave,cat,\pm} = \frac{n}{1+\beta} k_{span} \qquad \forall n \in \mathbb{N}^* \tag{2.44}$$

Figure 2.29 shows these frequencies on map of amplitudes of vertical wire velocities a function of frequency and train velocity. Analytical definitions of the harmonics, shown as black curves, clearly coincide with areas of higher amplitude in the spectra. The network of harmonics is particularly clear when it coincides with modal groups of the catenary.

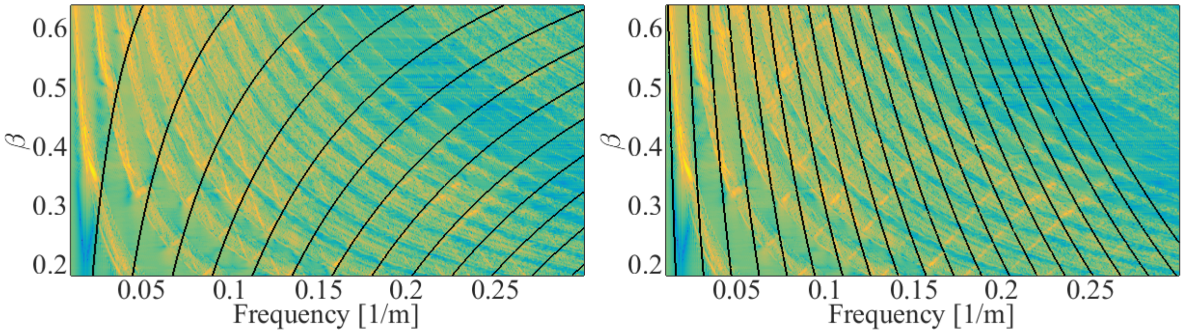

Figure 2.29: Amplitude of vertical velocity of the contact wire in the spatial Fourier domain as a function of β with black curves representing $k_{wave,cat,+}$ (left) and $k_{wave,cat,-}$ (right)

2.3.3 Coincidences in the moving Frame

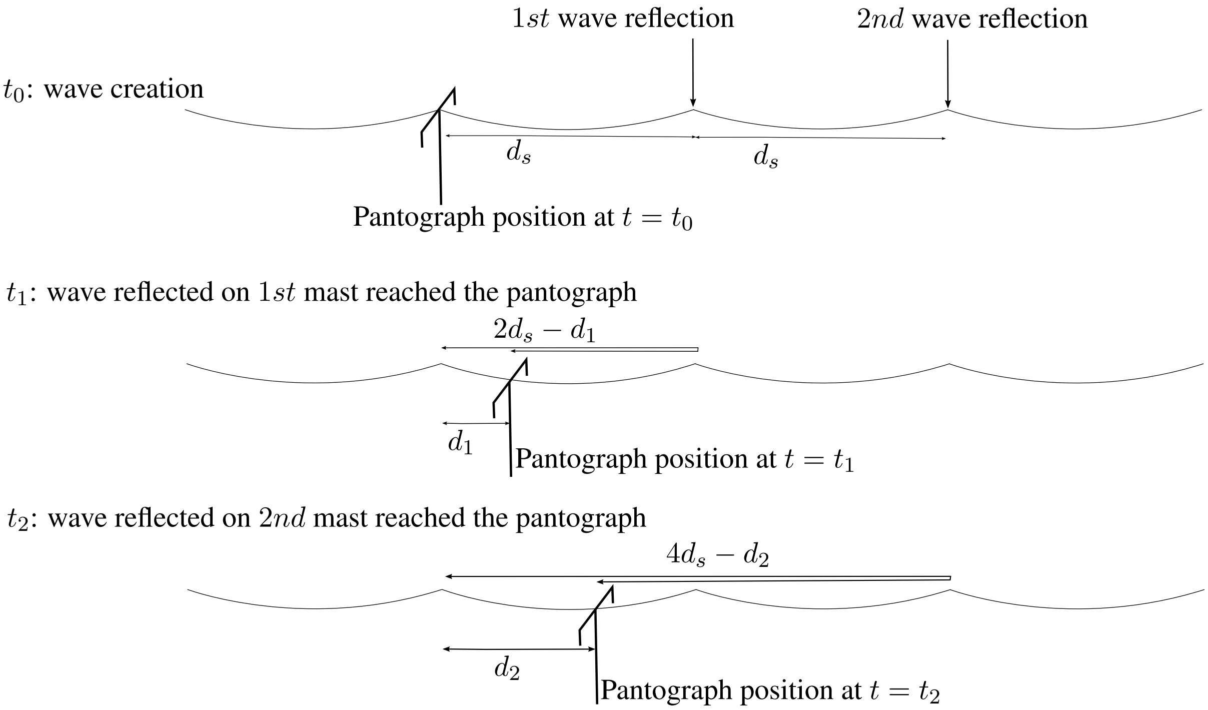

Figure 2.30: Wave propagation illustration, view from pantograph

From the pantograph point of view, the characteristic times are described in figure 2.30 when the pantograph moves under a periodic profile of spatial period d_s. At t_0, the pantograph passes under a change (SA or dropper) and generates a wave which reflects on the next change and reaches the pantograph at t_1 after the pantograph has moved of a distance d_1.

$$t_1 - t_0 = \frac{2d_s - d_1}{c_{CW}} = \frac{d_1}{v_{panto}} \tag{2.45}$$

From this equation, the distance d_1 can be computed as

$$d_1 = 2d_s \frac{beta}{1 \pm \beta} \tag{2.46}$$

and a characteristic spatial frequency can be defined as

$$k_{wave,panto,\pm} = \frac{1 \pm \beta}{2\beta} k_s \tag{2.47}$$

with $k_s = 1/d_s$.

The part of the wave which is not reflected and keeps propagating is also partially reflected on the next dropper and reaches the pantograph at the time t_2 after the pantograph has moved of a distance d_1.

$$t_2 - t_0 = \frac{4d_s - d_2}{c_{CW}} = \frac{d_2}{v_{panto}} \tag{2.48}$$

The same analysis can be performed for a wave propagating behind the pantograph. The characteristic periodicity of successive wave reflections on droppers from the pantograph point of view is thus

$$t_2 - t_1 = \frac{2d_s}{c_{CW} \pm v_{panto}} = \frac{2d_s}{c_{CW}(1 \pm \beta)} \tag{2.49}$$

with "$+$" when propagating on the front side and "$-$" when propagating behind, which leads to the same characteristic frequency defined in (2.47).

Two kinds of reflections have been observed at two different scales. The first one is the span scale, which is the largest in spatial domain and the smallest in the spatial frequency domain. This is thus the fundamental frequency observed. The second one is the dropper scale, which is the smallest in the spatial domain and thus the one observed here after. All these distances are multiples of $2.25m$, so that harmonics will coincide.

Figure 2.31 shows the contact force simulated along one span for a range of pantograph velocities. This velocity is normalised by c_{CW} using β. The black lines indicate mast positions, grey lines indicate dropper positions and red curves indicate the position where the pantograph is supposed to meet the wave generated at passage under the previous dropper and reflected on the next dropper. For higher β, the point where the pantograph meets the reflection gets closer to the next dropper.

On this figure, a change of behaviour can be observed around $\beta = 0.33$. This corresponds to the pantograph speed v_{panto} after which the backward wave shown in figure 2.30 meets the pantograph in a different span. At that particular velocity, the backward wave reflection meets the pantograph exactly after this span.

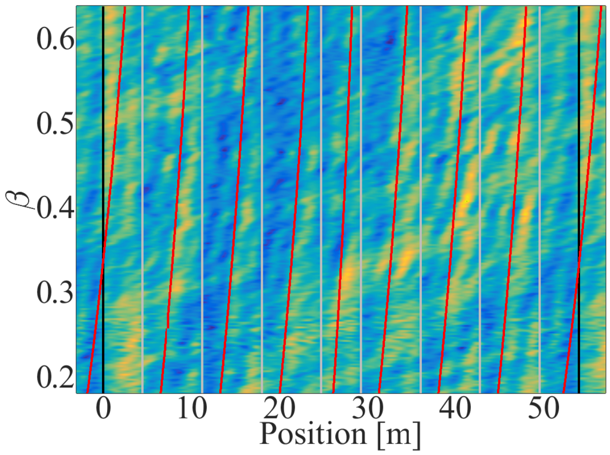

Figure 2.31: Contact force along one span as a function of β

Visualizing the relevance of characteristic times does not imply knowledge of where maxima occur. The contact force is highly dependent on the catenary geometry as explained in section 2.1 and figure 2.31 shows that the maxima of contact force are not placed under droppers. The approximation of F_c

by F_{geom} displayed in figures 2.5 and 2.4 showed that the amplitudes of Fourier transforms are easier to compare than spatial signals. Characteristic times are thus converted to characteristic spatial frequencies and the distance d_{span} is replaced by all the spatial frequencies of peaks of V_{CW} shown in figure 2.3. These frequencies are multiples of the span spatial frequency, $k_{span} = 1/d_{span}$ and wave frequencies can be defined as

$$k_{wave,panto,\pm} = \frac{1 \pm \beta}{\beta} \frac{n}{2} k_{span} \qquad \forall n \in \mathbb{N}^* \tag{2.50}$$

Figure 2.32 shows an amplitude map of vertical velocity of the contact wire in the spatial Fourier domain as a function of β and the curves corresponding to $f_{wave,panto,+}$ on the left and $f_{wave,panto,-}$ on the right. These frequencies appear clearly only for low frequency and low β.

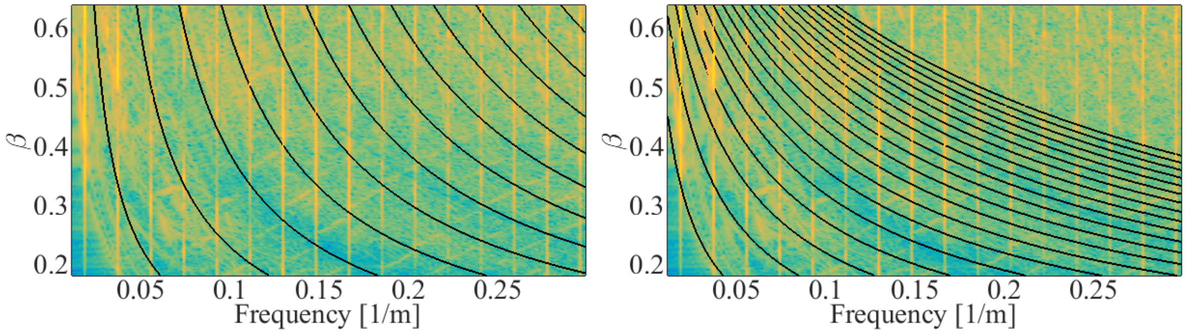

Figure 2.32: Amplitude of the contact force F_c in the spatial Fourier domain as a function of β with black curves representing $k_{wave,panto,+}$ (left) and $k_{wave,panto,-}$ (right)

2.3.4 Other coincidences

The amplitude of the first vertical line of the contact force amplitude spectrum shown in figure 2.32 increases with β in the same way as F_{geom} determined in section 2.1 but with small variations around. These variations are clearer if the phase of this fundamental frequency is compared to that of F_{geom} as shown in figure 2.33.

The notable phase gap for $\beta < 0.33$ corresponds to low velocity domain where waves reflected successively on two spans meet the pantograph in the same span as shown with figure 2.31. It is also the velocity under which reflections of waves generated backward the pantograph reach the pantograph in the same span.

The peak at $\beta = 0.4$ correspond to the particular pantograph velocity v_{panto} at which the span passage temporal frequency $f_{span} = k_{span} \cdot v_{panto}$ coincides with the first group of vertical catenary modes around $1Hz$ (1 span simply supported bending). In our case, $k_{span} = 1/54m^{-1}$ and the span passage frequency is equal to $1Hz$ for $v_{panto} = 54m/s$, which gives, for $c_{CW} = c_{MW} = 138m/s$, $\beta = 0.4$.

At velocities where the phase is higher, it is observed that the contact force amplitude is lower. The maxima observed in the phase can thus be better operating points than minima. In other words, current collection quality can be expected to be better if the pantograph meets the reflected waves under droppers.

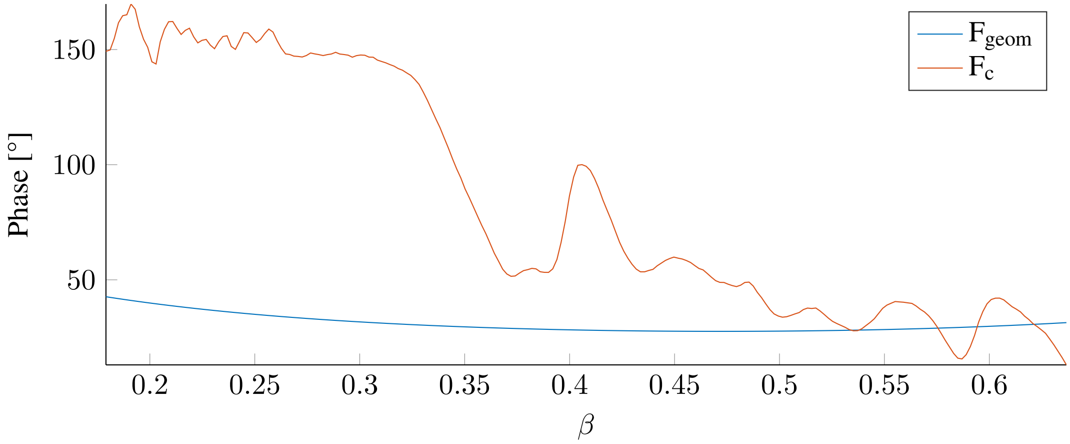

Figure 2.33: Phase of contact force of the fundamental spatial frequency k_{span} as a function of β

2.3.5 Multi-pantograph configurations

High speed trains are often composed of two train sets and are thus equipped with two pantographs collecting current simultaneously. The current collection quality of the second pantograph strongly depends on the dynamic state of the catenary after the passage of the first pantograph. It is thus highly sensitive to the distance between pantographs, d_{panto}. The usual distance d_{panto} is of $200m$, the length of a train set.

Figure 2.34 shows the current collection quality criterion σ/F_m as a function of distance d_{panto} and normalized velocity $\beta = \frac{v_{panto}}{c_{CW}}$. This criterion shows oscillations with d_{panto} and the period of these oscillations increases non-regularly with β.

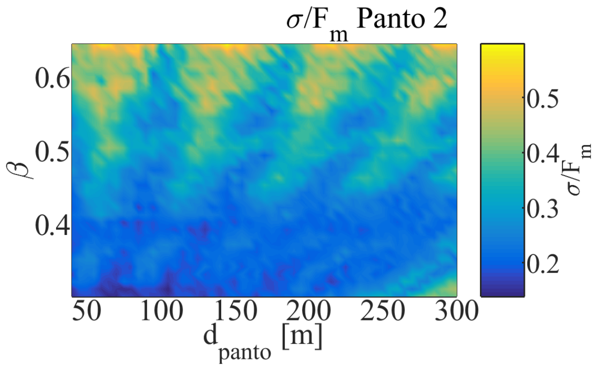

Figure 2.34: σ/F_m of the trailing pantograph as a function of β and d_{panto}

The variation with β of the periodic oscillations along d_{panto} shows that the phenomenon is not due to geometry, otherwise it would not depend on β. Catenary vibration modes are thus assumed to be the cause. It has been seen in figure 2.25 that modes are grouped. Figure 2.35 shows a mode of the first group where the first span bending mode (highest amplitude at mid-span an low level on edges) is observed at every span with a different amplitude due to the span coupling.

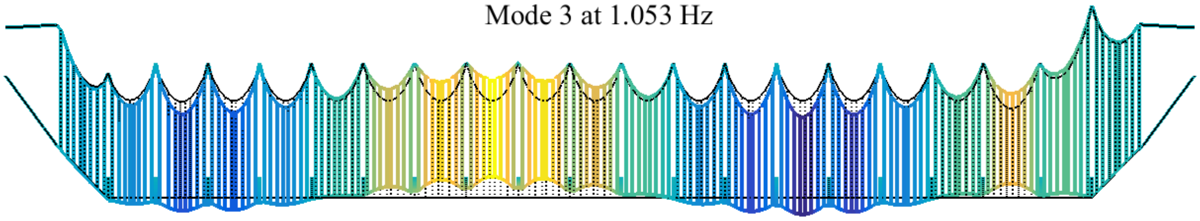

Figure 2.35: Third vibration mode of the catenary section

Denoting the modal frequencies f_{modes}, the spatial period d_{modes} can be defined as

$$d_{modes} = \frac{v_{panto}}{f_{modes}}. \tag{2.51}$$

Figure 2.36 shows the evolution of multiples of d_{modes} for the first group of modes as a function of β compared to the map of the dynamic criterion normalized for each β in order to highlight low velocity behavior. Vertical displacement of the contact wire is higher for the first group of modes. Furthermore, all maxima of σ/F_m are approximately placed inside the bands defined by d_{modes} even if noticeable variations are observed inside these bands.

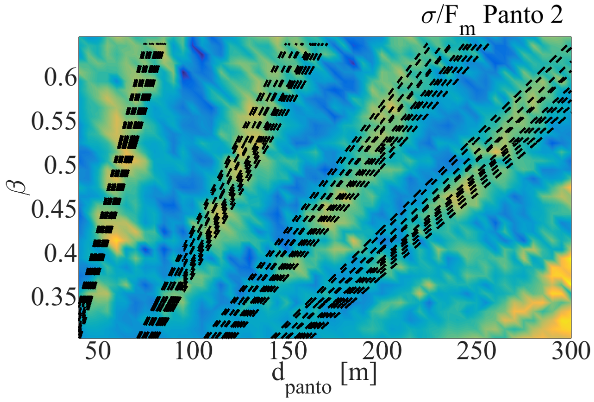

Figure 2.36: σ/F_m of the trailing pantograph as a function of β and d_{panto}

Figure 2.37 shows the amplitude of the catenary vertical displacement spectrum on the left and a zoom on frequencies around $1Hz$. The first peak slightly changes with β. For β increasing between 0.4 and 0.6, the frequency increases and thus distance d_{modes} decreases, which is consistent with observations in figure 2.36. Evolution of the frequency as a function of β is due to the coupling with the pantograph, changing dynamic properties of the full system.

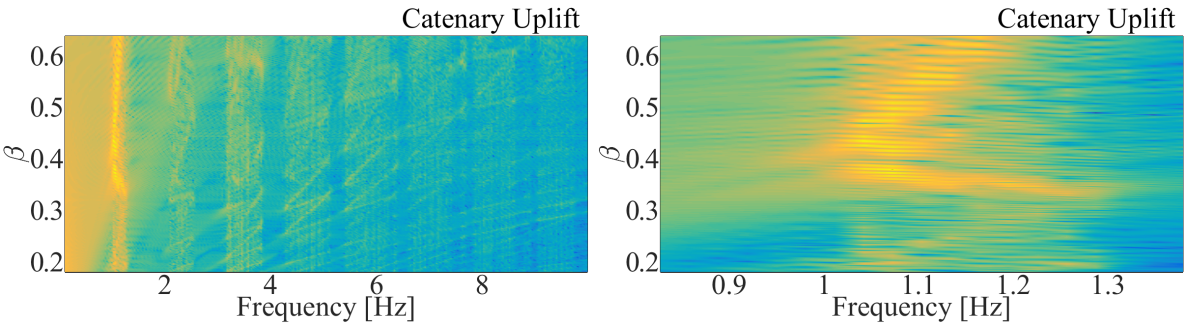

Figure 2.37: Amplitude of the spectrum of vertical displacement of one CW point as a function of β

Figure 2.38 (left) shows the vertical velocity of one fix point of the catenary as a function of β and of the distance between the pantograph and the observation point, for simulations led with one pantograph only. On the left, the map observed previously is shown again as a comparison. It is clear that the current collection quality of the trailing pantograph is closely linked with the catenary vertical velocity seen by the trailing pantograph. When this velocity is at its maximum, the current collection is better.

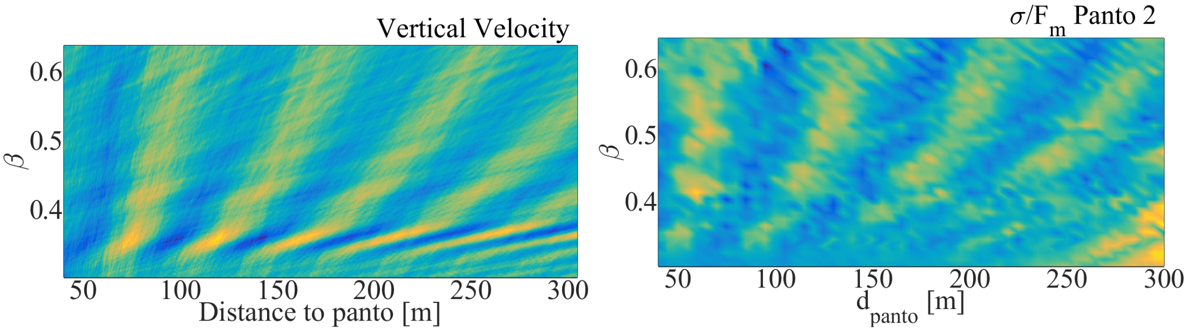

Figure 2.38: Vertical velocity of the CW as a function of β and of the distance between the pantograph and the observation point (left), σ/F_m of the trailing pantograph as a function of β and d_{panto}

The distance d_{panto} can be optimised for a given catenary and a given speed. A periodic catenary induces a tighter band of first frequency modes and thus amplifies the phenomenon. On the contrary, if the objective of the catenary is to be adapted for any train speed and any distance d_{panto}, the periodicity of the catenary at the scale of spans has to be broken. The current collection quality of the trailing pantograph would thus be less variable with speed and d_{panto}.

2.3.6 Summary of coincidences

The dynamic interaction between the pantograph and the catenary has been shown to depend on multiple components. This section thus provides a summary of the main factors.

The static geometry of the catenary generates force fluctuations at harmonics of the span length

$$k_n = \frac{n}{d_{span}}$$

In this fixed frame, spatial and temporal frequencies are related by $\omega = v_{panto} k$ so that the geometry excites temporal frequencies

$$f_n = \frac{n v_{panto}}{d_{span}}$$

The pantograph resonances defined in 2.1 are defined in the temporal frequency domain linked with the moving frame and thus change in spatial frequency.

For an observation in the fixed catenary frame, waves generated by the moving pantograph with a geometric period of d_{span} generate harmonics at frequencies corresponding to characteristic times detailed in 2.3.2. The frequencies of those harmonics are

$$k_n = \frac{n}{(1 \pm beta) d_{span}}$$

In the moving frame, reflections on the fixed features of the catenary generate variations of pantograph states or uplift at contact location containing strong components at spatial harmonics

$$k_n = \frac{n(1 \pm \beta)}{2\beta d_{span}}$$

A notable transition occurs when waves generated backward are no longer fast enough for their reflection to reach the pantograph within the same span. This transition to high speeds was illustrated in section 2.3.4.

Catenary modes generate excitations at frequencies f_{mode} and wave numbers $k_{mode} = f_{mode}/v_{panto}$ in the fixed frame. Seen from the pantograph the frequency of these modes should appears shifted even though this was not illustrated.

In the case of multi-pantographs, figure 2.38 showed that the emphasis of the rear pantograph with the vertical velocity of a fixed point of the catenary, which is directly linked to f_{mode}, had a significant influence on the current collection quality of the rear pantograph.

Chapter 3

Epistemic uncertainties

This chapter deals with epistemic uncertainties that can be reduced using measurements or parametric studies. Section 3.1 addresses the contact model and it is shown that a contact stiffness derived from Hertz theory gives a coherent value. In section 3.2, tests are carried out and used to calibrate the catenary damping in a frequency range as large as possible using different damping models. Finally, section 3.3 tackles the convergence problem linked with element size.

3.1 Contact Stiffness

Contact between surfaces generate stresses that control the penetration. At the macro-scale, contact can be idealized and the mathematically simple Signorini model is typically used. This model states that the gap can only be positive and that for zero gap surface forces can develop. This model typically ignores local details associated with asperities or local deformation. Hertz contact theory considers that the area affected by local deformation is small compared to the dimensions of interest and thus introduces a contact stiffness to represent small scale deformations compatible with the Signorini model.

In pantograph catenary interaction, the area of friction band graphite in contact with the contact wire is small and a higher scale model is desired. Assuming that contact of two cross cylinders, Hertz contact theory [74, 75] gives a contact stiffness

$$k_c = 2aE^* \tag{3.1}$$

with a, the radius of the contact surface assumed to be circular, and $E^* = \frac{E}{1-\nu^2}$ the reduced modulus of the less rigid material (here graphite). The radius a can be computed from the measured surface of contact which evaluated in [76] to $12mm^2$ in static conditions for a mean force applied equal to $90N$ and leads to $a = 2mm$. The contact surface is indeed dependent on the contact force and the hypothesis that this surface is constant allows to linearise the contact stiffness.

For $E = 30GPa$ Young's modulus of graphite and $\nu = 0.23$ the Poisson ratio, the maximum value of k_c obtained is $k_{c,max} = 6MN/m$. This theoretical value is however never reached due to roughness of interfaces [5] and a lower boundary of k_c is a third of that found with Hertz theory, $k_{c,min} = 2MN/m$.

In numerical simulations, the upper bound given by Hertz theory might be too high and be pushed to infinity, thus leading to the use of Lagrange multipliers to verify Signorini's assumption. It is also possible to simplify Hertz contact by introducing a linearised contact stiffness, which can then be seen as the numerical trick of penalization [77], but in that case, this contact stiffness has a physical interpretation that could be studied if measurements were available.

The total impedance of the pantograph Z_{panto}, including the contact stiffness, has been computed in section 2.1. Figure 3.1 shows Z_{panto} for different values of k_c. It appears that the highest peaks in Z_{panto} and thus in contact force due to geometry F_{geom} are due to this contact stiffness. The frequency value of this resonance can be approximated by $\sqrt{\frac{k_c}{m_3}}$ where m_3 is the upper mass of the pantograph model described in figure 1.12. For the mass m_3 chosen here, the pantograph/catenary simulations standard [34] gives a value $k_c = 50kN$, which, for frequencies around $20Hz$, increases the amplitude of Z_{panto} and thus F_{geom}, which may not be realistic.

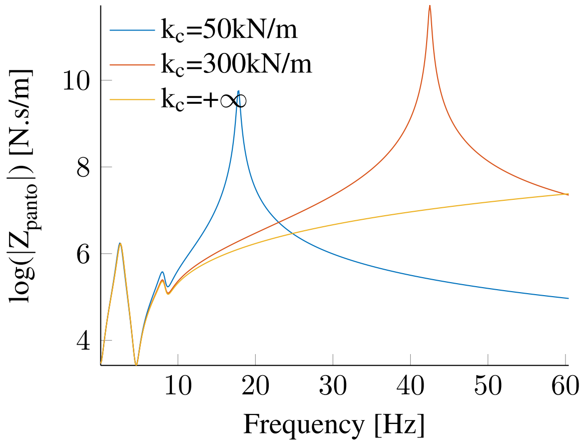

Figure 3.1: Impact of the contact stiffness k_c on Z_{panto}

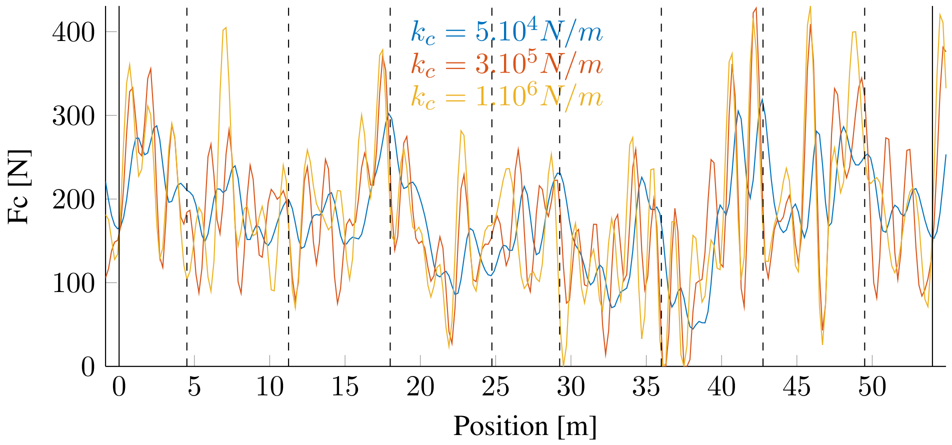

Figure 3.2: Impact of the contact stiffness k_c on $70Hz$-filtered contact force F_c

Figure 3.2 shows the $70Hz$-filtered contact force for three different values of k_c. Since they are all significantly different, determining the value of k_c is thus critical.

A parametric study on stiffness k_c has thus been led. Figure 3.3 left shows the evolution of contact loss as a function of k_c. The value is always increasing thus showing a need to properly evaluate the contact stiffness. The result is however based on non-filtered simulated contact force, which in this case corresponds to a frequency of $880Hz$. Figure 3.3 right shows the coefficient of variation σ/F_m of the $70Hz$-filtered contact force. This quantity shows a local maximum for k_c around $300kN/m$. This is consistent with figure 3.1, on the frequency range of $[0-70]Hz$, if the value of k_c is too low, it acts as a low-pass filter for a large part of the frequency band, and if $k_c = 300kN/m$, the area under the curve of Z_{panto} is maximum (red curve is always over the yellow curve on the frequency range observed), which leads to a higher variance of F_c. Finally, the fast increase above $6MN/m$ can probably be associated with numerical problems.

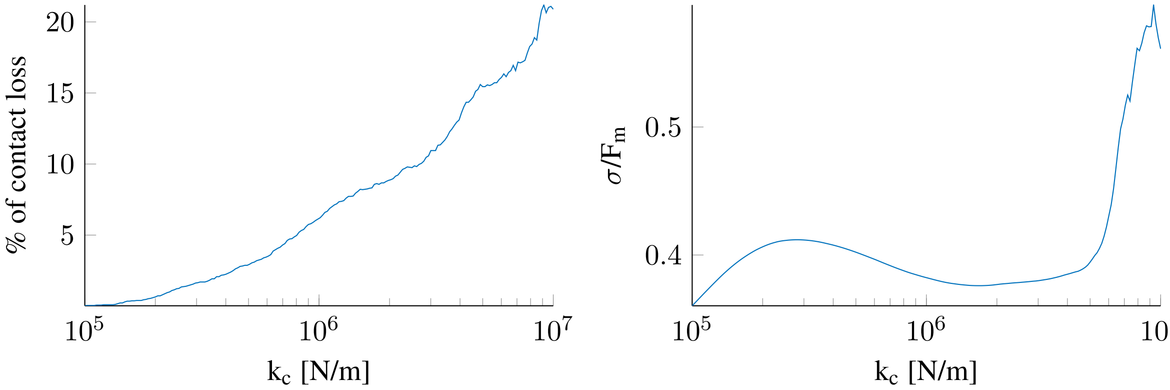

Figure 3.3: Proportion of contact loss of the raw contact force (left) and coefficient of variation of the $70Hz$-filtered contact force (right) as a function of k_c

The most realistic approach to characterize the contact stiffness is to measure the contact resonance as considered in [5] but its value strongly depends on the contact load. Without any information about this contact resonance frequency, the value of k_c should be chosen high enough to reduce its effect on contact force in the targeted frequency band and low enough to avoid convergence issues such as those observed for values of k_c higher than $5MN/m$. Any value of k_c between $1MN/m$ and $4MN/m$ are thus good and in the realistic range of Hertz theory. Nevertheless, a heavier the mass m_3 will lower the contact resonance frequency. If $k_c = 2MN/m$, for an upper mass $m_3 = 4.25kg$, the resonance is observed at $110Hz$ and for a heavy upper frame of $m_3 = 7.5kg$, this frequency drops to $85Hz$. The contact resonance is thus close to the first bending mode of the pantograph that has been measured in the same frequency range [58]. Figure 3.4 shows the amplitude spectrum of an unfiltered raw measurement of contact force. A significant amount of energy is located around the $93Hz$ frequency thus due to either first bending mode of the bow, or contact resonance. Consequently, interpretation of contact force at frequencies over $70Hz$ should take into account these local flexibilities.

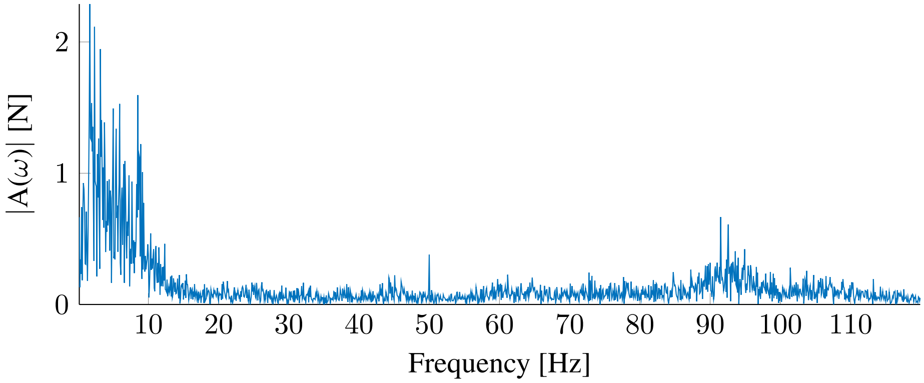

Figure 3.4: Amplitude spectrum of measured contact force

In practice, a value of $k_c = 2MN/m$ avoids convergence issues and, for the range of existing m_3, simulations are not perturbed by the contact resonance if the contact force is low-pass filtered at $70Hz$.

3.2 Damping characterization

The damping calibration used in most studies is based on dynamic measurements of pantograph-catenary interaction. It is thus difficult to separate the effects of the pantograph from those of the catenary. Damping is thus commonly used to tune the simulation in order to be as close as possible to the dynamic measurement, which is supposed to be used for validation. A recent benchmark [4] has concluded on the importance of the damping model in the contact forces computed by the numerical models. Moreover, tuning models by tweaking the damping ratio can potentially hide other modelling errors.

The effort described in this section was thus to build the damping model with experimental measurements of the catenary alone. Section 3.2.1 describes mass drop experiments on a full scale catenary that were performed in Vaires sur Marnes in 2014. From these measurements, identification is used to estimate modal damping in various frequency bands as detailed in section 3.2.2. Three different damping models are then compared in section 3.2.3. Droppers and steady arm contributions are addressed in sections 3.2.4 and 3.2.5 respectively. Finally, section 3.2.6 evaluates the impact of the damping change on a typical pantograph-catenary dynamic simulation.

3.2.1 Experiment

The objective of this section is to detail experiment conditions and check the quality of measurements.

The tests have been performed on a SNCF catenary design of type V300. The height of the contact wire under steady arms has been fixed to $1.8m$, which allows easier access to the structure. The catenary has never been electrified and except masts and messenger wire, all the catenary has been renewed for these tests. Four tri-axial accelerometers were installed under droppers on the contact wire or over droppers on the messenger wire.

Excitation was obtained by dropping masses attached to the contact or messenger wires. Multiple mass and sensor configurations, as well as tensions were considered in the test campaign. An overview of the configurations tested during the campaign is given in appendix A.

Before analysing measurements, repeatability of the experiment was checked. Figure 3.5 shows test 2 (configuration B) repeated 3 times. Accelerations obtained are very similar even one minute after the drop. There is no need to check the coherence of these measurements. The noise is almost null, and a single experiment is thus sufficient to identify modal damping.

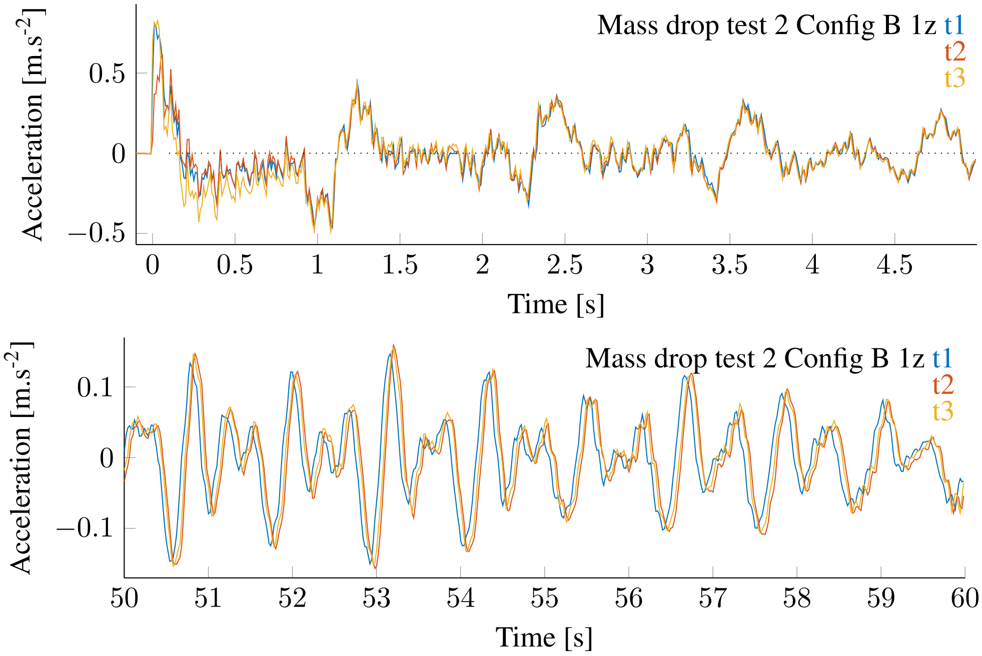

Figure 3.5: Repetition of test 2 in configuration B three times

Since the signal does not decay to zero in the considered buffer, a specific window might be needed to reduce the leakage on measurements. A commonly used window for signals that do not decay quickly enough is the exponential window. But this window introduces additional damping in measurements and low frequencies are more damped than high frequencies. Figure 3.6 shows an example of an exponential windowed signal compared with a rectangular windowed measurement. For low frequencies (i.e. $< 10Hz$), the signal is strongly damped and notably distorted. For higher frequencies, the exponential window becomes useful as it limits the noise which becomes more important.

As only low frequencies will be studied here, transfer functions with no windowing were used for the identification. A mass drop being close to a white noise, the frequency response function (FRF) gives a good estimate of the transfer function and no force sensor is needed.

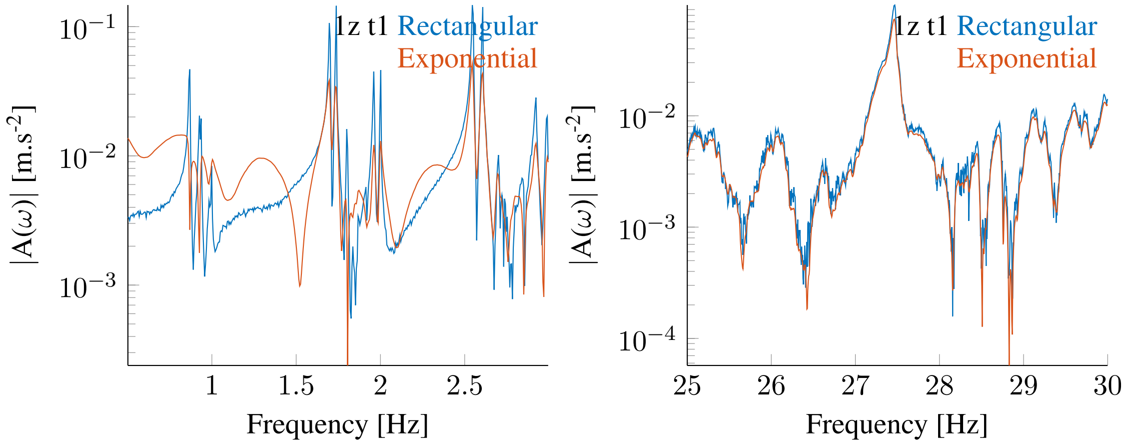

Figure 3.6: Fourier transform of test 2 (configuration B) with rectangular and exponential windows for different ranges of frequencies

3.2.2 Damping identification

From the transient drop response, FRF can be computed and are shown in figure 3.7. Groups of modes clearly appear at low frequencies 0.9 to 1.1 Hz, 1.9 to 2.2 Hz, ... as shown by the vertical red lines in the figure which correspond to modal frequencies.

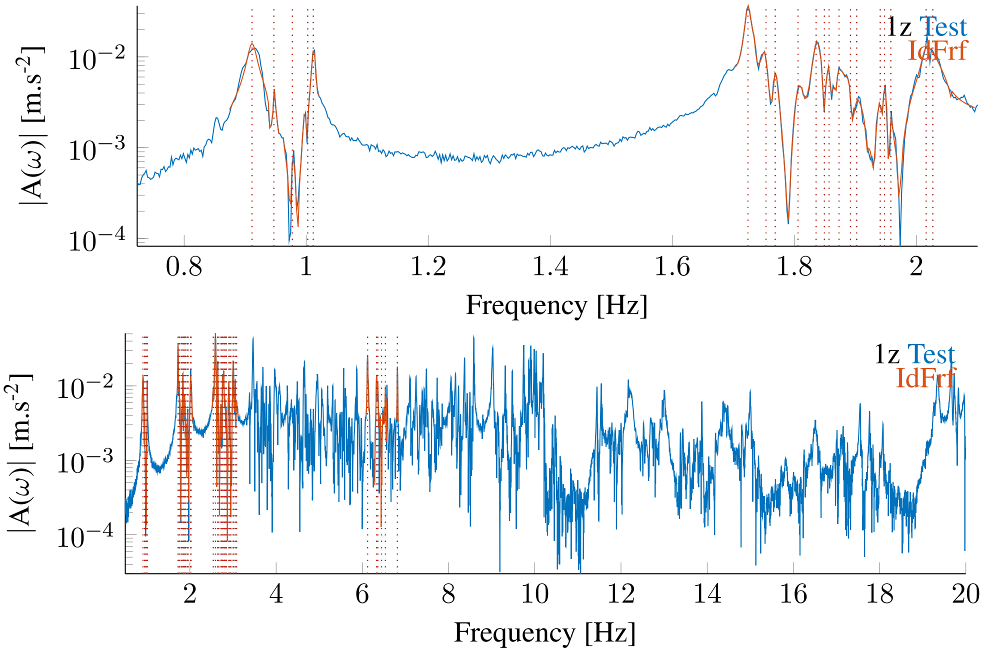

Figure 3.7: Complex mode identification

These groups are simply related to span modes (first vertical bending, horizontal bending, ...), with some frequency split due to span coupling as observed in figure 2.26. Figure 3.8 shows an example of a span mode. For the first group of modes (vertical bending), there are thus 6 modes associated with the 6 spans of the test catenary. Above 5 Hz, the frequency separation between mode groups becomes too small to allow a clear separation.

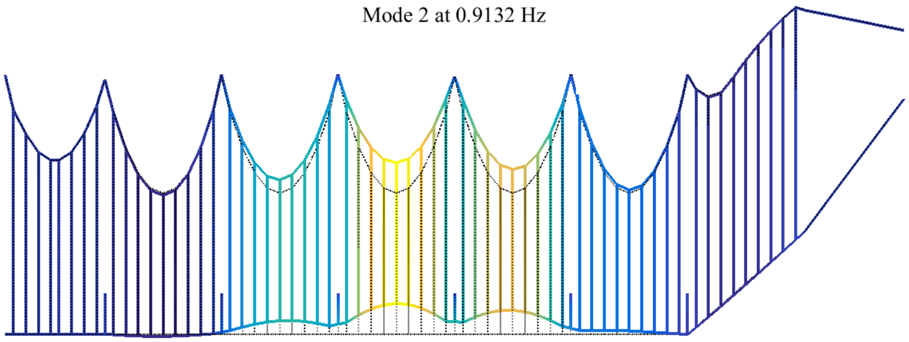

Figure 3.8: Vertical bending mode of the fourth span

The extraction of damping values from FRF is an identification step and the non-linear frequency domain output error method, introduced in [78], is used. In the identification, complex modes are used but, as damping is low, these are close to normal modes and the values can be used in modelling [79].

Figure 3.9 illustrates the difficulty of identifying 6 modes in the first group. More specifically the second mode at $0.74Hz$ does not fit the data very well and this is consistent with an over estimated damping ratio.

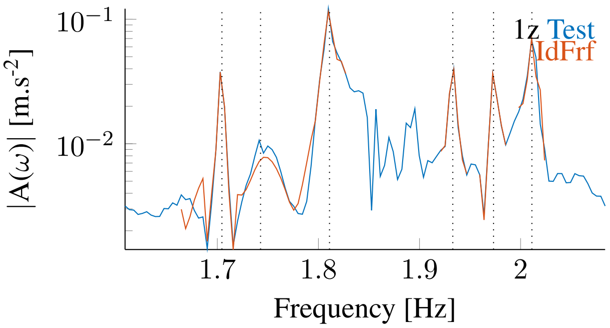

Figure 3.9: Damping over evaluated for test 6 at $1.74Hz$

For a robust identification, five points inside the $-3dB$ band are considered good practice. For a damping of $\zeta = 0.5\%$ at the frequency $f = 0.9Hz$ of the first modes, a measurement time of $555s$ would be needed. Since the damping is even lower and longer signals would require maintained excitation with a shaker, there is a significant uncertainty on the damping for low frequencies.

At higher frequencies, figure 3.7 shows that damping remains low even though the strong modal density makes identification more difficult. Selected modes around 6 Hz were thus retained for later comparison. Appendix B lists all the identified damping.

Figure 3.10 groups all the relevant tests and shows the dispersion for the first three groups of modes thanks to a box plot. The variability of identified damping decreases with frequency as expected. Moreover, outliers (dots of of figure 3.10 right) could always be traced to obvious over-evaluation of the damping as done in 3.9. Damping ratios are notably below 1% for the whole observed frequency range. There is a slight decrease for the first 3 groups of modes. Then, although only the band around $6Hz$ was analysed in detail, the measured responses do not show a damping variation at higher frequencies.

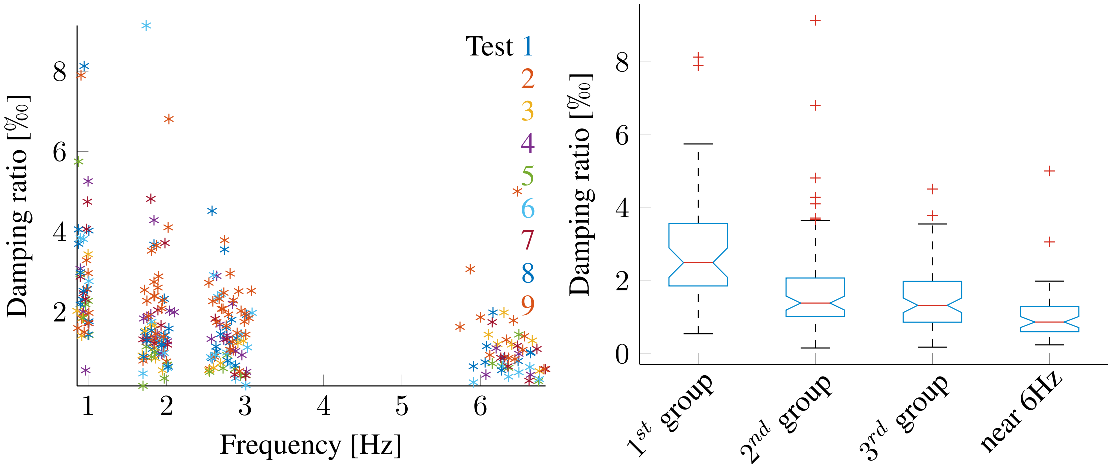

Figure 3.10: Identified damping ratio for the tests 1 to 9

3.2.3 Damping model

Selecting a proper damping model has always been a critical subject in vibration problems. A number of models have been developed and a summary can be found in [80].

Without any experimental data, Rayleigh damping (also called proportional or classical damping [81]) is typically used. It is a viscous damping proportional to the mass and stiffness matrices. Viscous damping is the only analytical dissipation model that is linear, it is thus needed for the sake of computation time.

A piecewise Rayleigh model has been used in OSCAR [6, 1], giving more flexibility to control the model but also more parameters to determine. The four elements of the catenary structure, namely the contact (CW) and messenger wires (MW), the dropper (drop) and the steady arm (SA) have thus their own contribution thanks to two coefficients each in

$$[C] = \sum_e \alpha_e \left[K^e\right] + \beta_e \left[M^e\right]. \tag{3.2}$$

Using the modal strain energy methods (MSE [82]) which is generally valid for low damping, one can estimate modal damping [6] by

$$\zeta_j = \frac{1}{2\omega_j}\left(\sum_e \beta_e(\phi^T M^e \phi)\right) + 2\omega_j\left(\sum_e \alpha_e \frac{\phi^T K^e \phi}{\omega_j^2}\right) \tag{3.3}$$

with ω_j the temporal frequency in rad/s.

A test on consistency of the method is led by arbitrarily setting $\alpha_{CW} = 10^{-4}$, $\alpha_{MW} = 5 \cdot 10^{-5}$,

$\beta_{CW} = 0.1$, $\beta_{MW} = 0.05$ and all the four other coefficients fixed to 0. Figure 3.11 shows the damping identification on the simulation of a mass drop. A small level of error exists since an identified damping appears over the red line, which is not possible in this model. All identified damping ratio are however found between the two theoretical curves, which means that damping in cables act on all modes and that damping in SA and droppers cannot be treated by this method. They will thus be treated separately in sections 3.2.4 and 3.2.5.

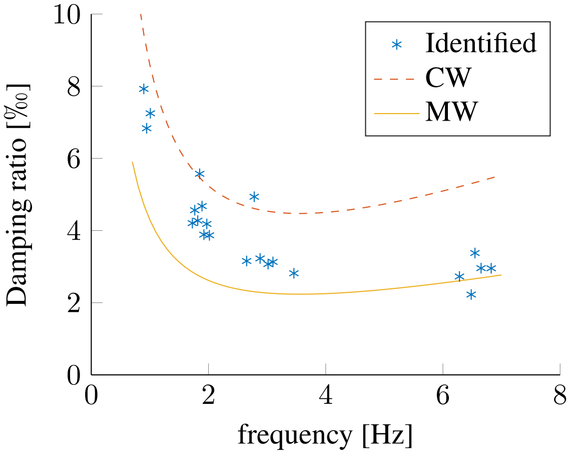

Figure 3.11: Example of identified damping ratio on a mass drop simulation using arbitrary CW and MW Rayleigh coefficients.

Ref. [6] showed that using a combined modal and Rayleigh damping respectively for low and high frequencies allows a more flexible representation of the catenary damping. The method consists in fixing the modal damping ratio found by identification and compensating the linear Rayleigh damping for some of the first modes.

Fixing the exact identified damping using modal damping is not relevant for a few reasons. First, the uncertainty on identification of low frequency is very high compared to the damping value. Secondly, pairing measured and computed modes is difficult with the low number of available sensors. Finally, the aim of this study is to have a damping configuration as generic as possible for a use with a large range of catenary types.

It was thus chosen to fix the same modal damping for all modes in a group for the first two groups and use the median identified damping.

Figure 3.10 shows that identified damping decreases with frequency to reach values of around $1‰$. Cremer et al., in [83] (p.191) give flexural loss factors of copper $\eta = 2‰$ and brass $\eta = 1‰$. Damping ratio can thus be deduced as $\zeta = \eta/2$. Supposing damping ratio of bronze is similar to that of brass, thuse leads to $\zeta_{CW} = 1‰$ and $\zeta_{MW} < 0.5‰$. These values are compatible with test results so that at high frequencies material damping can be assumed to be the only significant effect, while at low frequencies some additional mechanisms explain the higher damping found.

The choice of Rayleigh damping coefficients must thus be compatible with these values for frequencies as high as possible.

Table 3.2.3 summarizes the coefficients chosen for both damping models and figure 3.12 shows the resulting damping in a frequency range of $[0 - 70Hz]$. It appears that the previous Rayleigh damping coefficients lead to a similar damping ratio for low frequencies but is far higher for medium frequencies.

Table 3.1: Damping coefficients

	Benchmark Rayleigh	Rayleigh	Rayleigh+Modal
α_{CW}	$1 \cdot 10^{-4}$	$7 \cdot 10^{-6}$	$7 \cdot 10^{-6}$
β_{CW}	$1.21 \cdot 10^{-2}$	$4 \cdot 10^{-2}$	$4 \cdot 10^{-2}$
α_{MW}	$1 \cdot 10^{-4}$	$7 \cdot 10^{-6}$	$7 \cdot 10^{-6}$
β_{MW}	$1.21 \cdot 10^{-2}$	$4 \cdot 10^{-2}$	$4 \cdot 10^{-2}$
α_{drop}	$1 \cdot 10^{-4}$	0	0
β_{drop}	$1.21 \cdot 10^{-2}$	0	0
α_{SA}	$1 \cdot 10^{-4}$	0	0
β_{SA}	$1.21 \cdot 10^{-2}$	0	0
$\zeta_{1^{st} group}$			$2.5 \cdot 10^{-3}$
$\zeta_{2^{nd} group}$			$1.4 \cdot 10^{-3}$

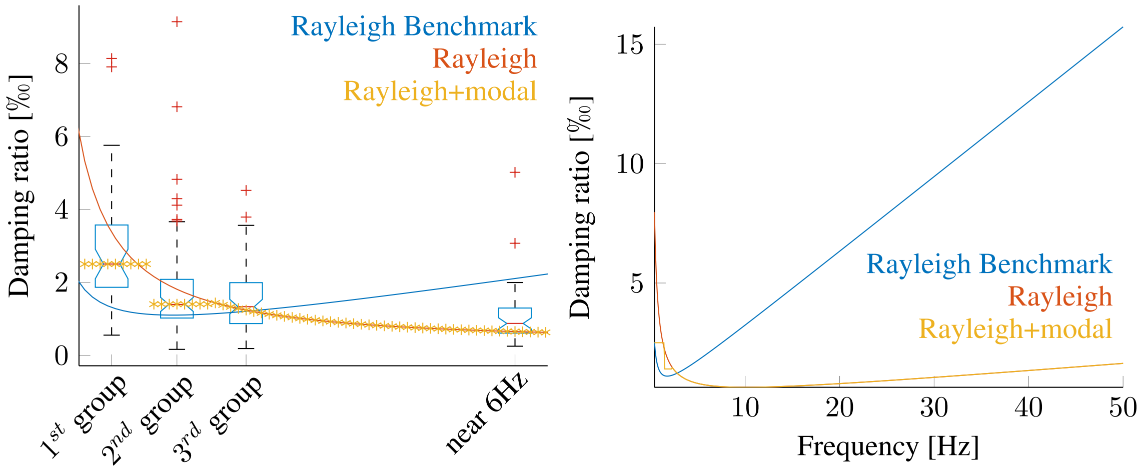

Figure 3.12: Comparison of identified (box-plot), Benchmark Rayleigh (blue), updated piecewise Rayleigh (red) and updated piecwise Rayleigh+Modal (yellow) damping ratio for low (left) and medium (right) frequency range

3.2.4 Dropper damping

The dropper, displayed in figure 1.2 is a braided metallic wire. Setting the dropper damping to zero introduces high frequency oscillations at the dropper where the mass is dropped as shown in figure 3.13. This numerical problem can be solved by setting the stiffness proportional damping α_{drop} to a non-zero value.

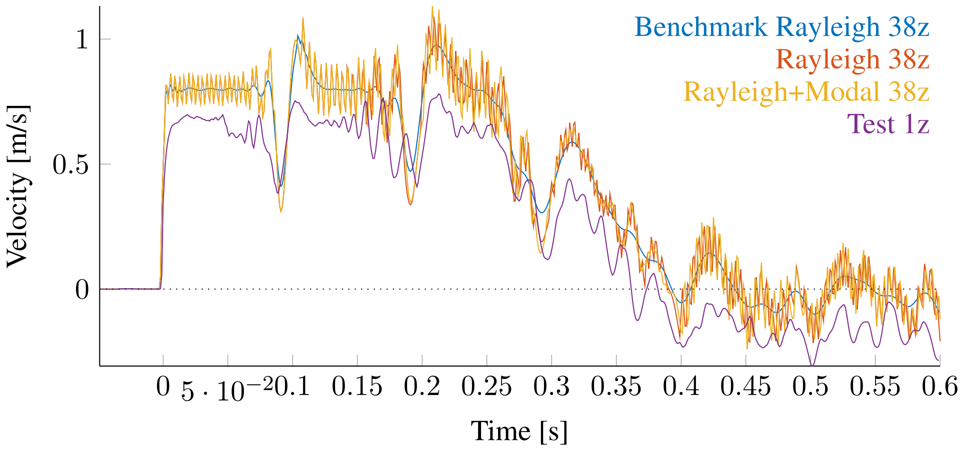

Figure 3.13: Velocity of sensor 1 in test 8 compared with simulations using three different damping models

Figure 3.14 shows the evolution of the maximum compensation force in a mid-span dropper (left) as a function of α_{drop}. A transition zone is observed between 10^{-4} and 10^{-2}, after which the dropper is locked. On the left, the total cumulated time droppers of a span are in compression for simulations at $v_{panto} = 320km/h$ is null for $\alpha_{drop} > 10^{-2}$. To analyse these results, it is useful to detail the dynamic stiffness of the dropper which is given by

$$K_{drop,dyn} = K_{drop} \cdot (1 + i\alpha_{drop}\omega). \tag{3.4}$$

The dropper is a braided metallic wire and a loss factor η_{drop} of less than 1% is thus expected. For $v_{panto} = 320km/h$, the dropper passage frequencies go from $12Hz$ to $18Hz$ which leads to a value of α_{drop} between $8.8 \cdot 10^{-5}$ and $1.3 \cdot 10^{-4}$ in order to have $\eta_{drop} = \alpha_{drop}\omega = 1\%$.

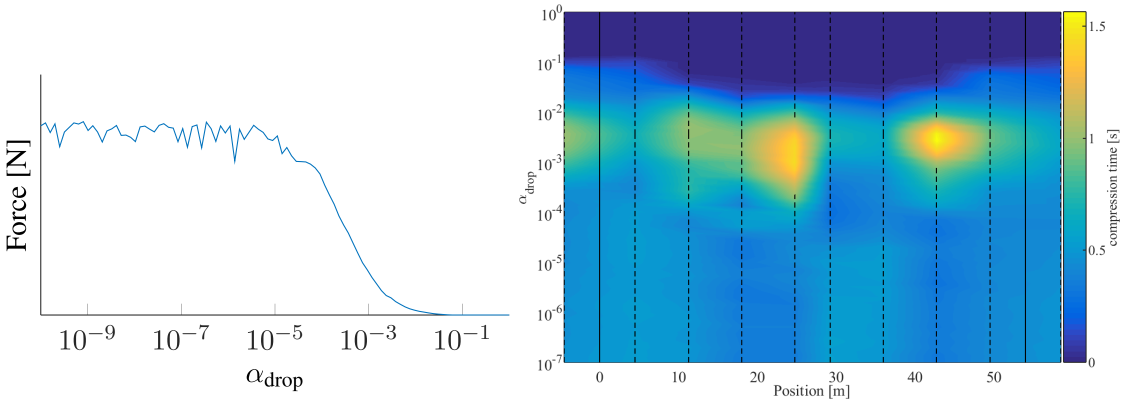

Figure 3.14: Maximum dropper compensation force (left) and total time droppers are in compression (right) as a function of α_{drop} at $v_{panto} = 320km/h$

For any $\alpha < 10^{-5}$, the total time of compression is constant. Figure 3.15 shows that for $\alpha < 10^{-5}$, dropper damping has no influence on dynamic simulations. For any $\alpha > 10^{-2}$, $\eta_{drop} > 1$ in the frequencies of interest and the dropper is highly dissipative and thus is never in compression. The range $[10^{-5} - 10^{-2}]$ is where dropper damping can influence the response. This is thus a range of interest for catenary designs involving damped droppers.

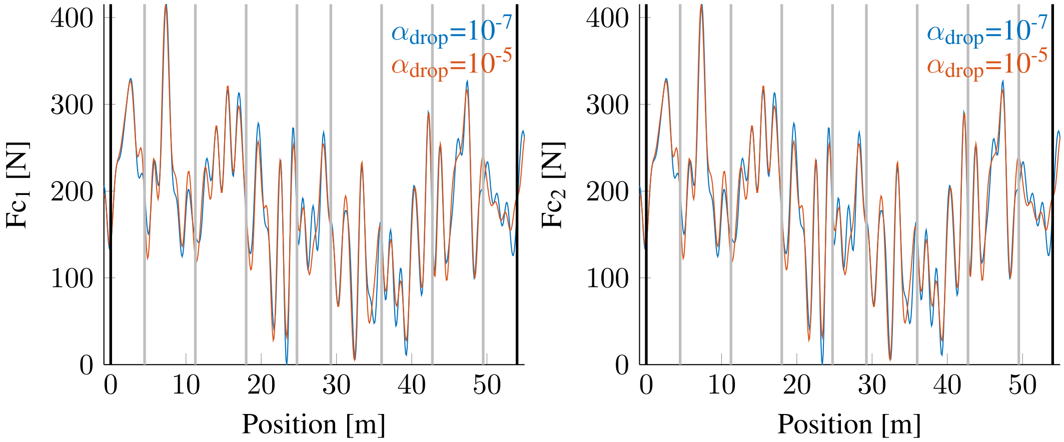

Figure 3.15: Comparison between $\alpha_{drop} = 10^{-5}$ and $\alpha_{drop} = 10^{-7}$ in $70Hz$-filtered contact forces of two pantographs

Trying to explain oscillations that were seen in figure 3.13 , figure 3.16 shows the vertical velocity simulated at the dropper where the mass is dropped. With a value of α_{drop} set to 10^{-5}, numerical oscillations that appear at the frequency of $330Hz$ dissipate quicker. This frequency corresponds to the natural frequency of the spring-mass system composed by the dropper with claws, which was evaluated to $355Hz$. Unfortunately, the only tests where accelerations of the top and bottom of the dropper were measured simultaneously at the mass drop are those in configuration B which are sampled at $500Hz$. Nevertheless, it would be of interest to characterize dropper damping using adapted tests.

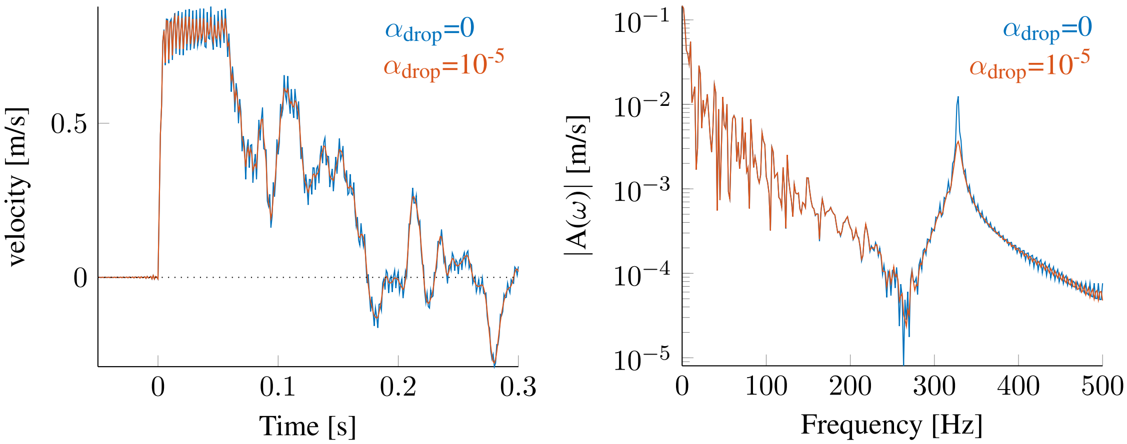

Figure 3.16: Comparison of vertical velocity (left) and its amplitude spectrum (right) between $\alpha_{drop} = 0$ and $\alpha_{drop} = 10^{-5}$ for a mass drop

3.2.5 Steady Arm damping

Seeing joints such as those shown in figure 1.5, assuming some level of damping due to friction seems realistic. To evaluate the influence of these joints, figure 3.17 shows $70Hz$-filtered contact force for a simulation at $v_{panto} = 320km/h$ with SA modelled either as beam or as bar. When modelled as beam, the claw linking the SA to the CW is blocked in rotation around the CW axis. The slight difference confirms that sensitivity exists.

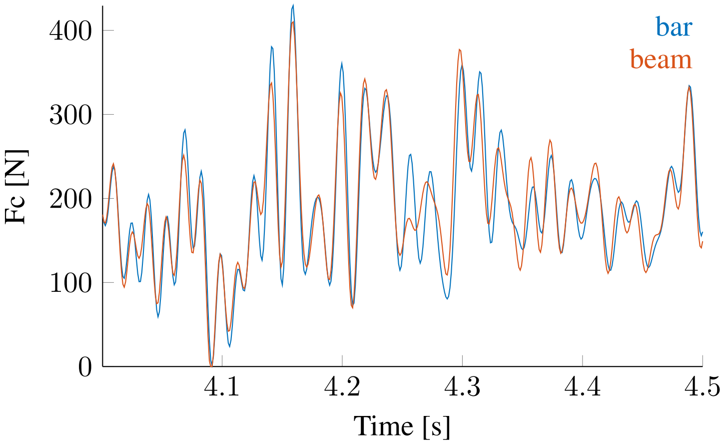

Figure 3.17: $70Hz$-filtered contact force simulated with SA modelled as bar (blue) and beam (red)

To represent damping associated with rotation of the steady arm, a vertical damper at the claw SA/CW claw is introduced leading to an effect similar to that of a rotational damper at the SA root. Figure 3.18 shows the resulting identified damping on the simulation with the previous Rayleigh coefficients and the SA dampers. This contribution increases damping starting with the second group of modes (around $2Hz$) and its impact decreases with frequency (almost no difference visible after $12Hz$). This trend is not consistent with the experiment which only sees higher damping for the first two mode groups.

Another question of interest is to establish whether the β_e coefficients of CW and MW are relevant or actually compensate for damping really occurring in the SA. To test this idea, coefficients β_{CW} and β_{MW} are set to lower values corresponding to material damping and vertical damping at the SA is fixed to have a coherent amplitude of oscillations after $100s$ as shown in figure 3.19 left. The right graph, indicates that the first mode at frequency $0.9Hz$ is over-damped while other modes of the group are under-damped.

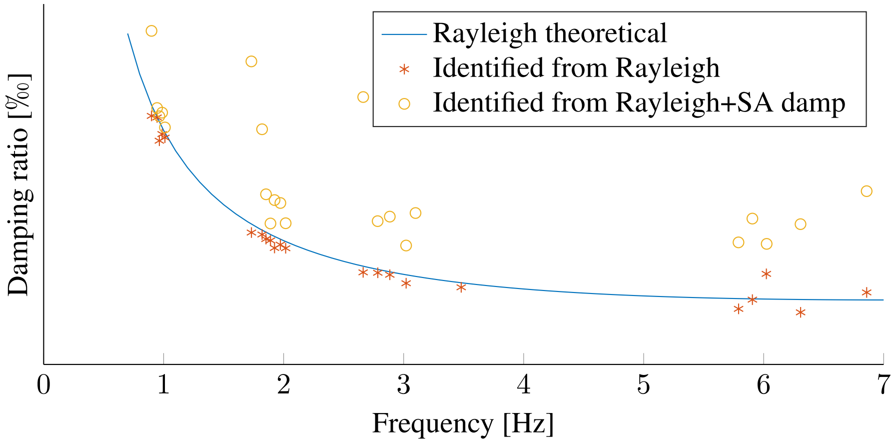

Figure 3.18: Comparison between identified damping ratio for simulations with Rayleigh only (asterisk) and Rayleigh with vertical dampers at steady arms (circle).

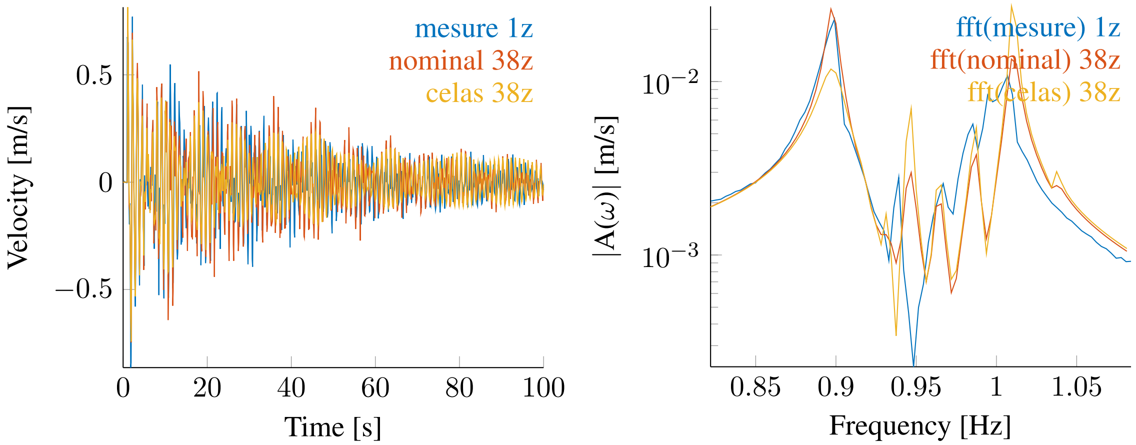

Figure 3.19: Vertical velocity (left) and the spectrum of its amplitude (right) of measurement (blue), simulation with Rayleigh damping only (red) and simulation with low Rayleigh damping and SA vertical damper

The proposed steady arm damping model is thus inconsistent with measurements and for further work steady arm damping will thus remain set to zero.

3.2.6 Evaluation of final damping model

Two damping models were finally considered, the first with Rayleigh on contact and messenger wires only, the second with modal damping on the two first groups of modes with a compensation of Rayleigh damping at these modes. Simulation of a mass drop is first compared with measurements and with the reference Rayleigh model. The impact on a typical pantograph-catenary interaction is then observed thanks to commonly used criteria to compare models with measurements.

Figure 3.20 shows the velocity of the contact wire, when a mass of $40kg$ is dropped. The first observation is that Rayleigh and Rayleigh+Modal models give exactly the same results. The damping variation between the two models thus has no influence. The velocity of the reference Rayleigh model is smoothed as expected by the high damping applied in the medium frequency range. Tests show that the signal effectively contains energy in the medium frequency domain and validates the new Rayleigh model in this frequency range. The second part of the figure focuses on residual vibrations after a long time and shows that low-frequency damping of the reference is somewhat too small and validates the one chosen in the new Rayleigh model.

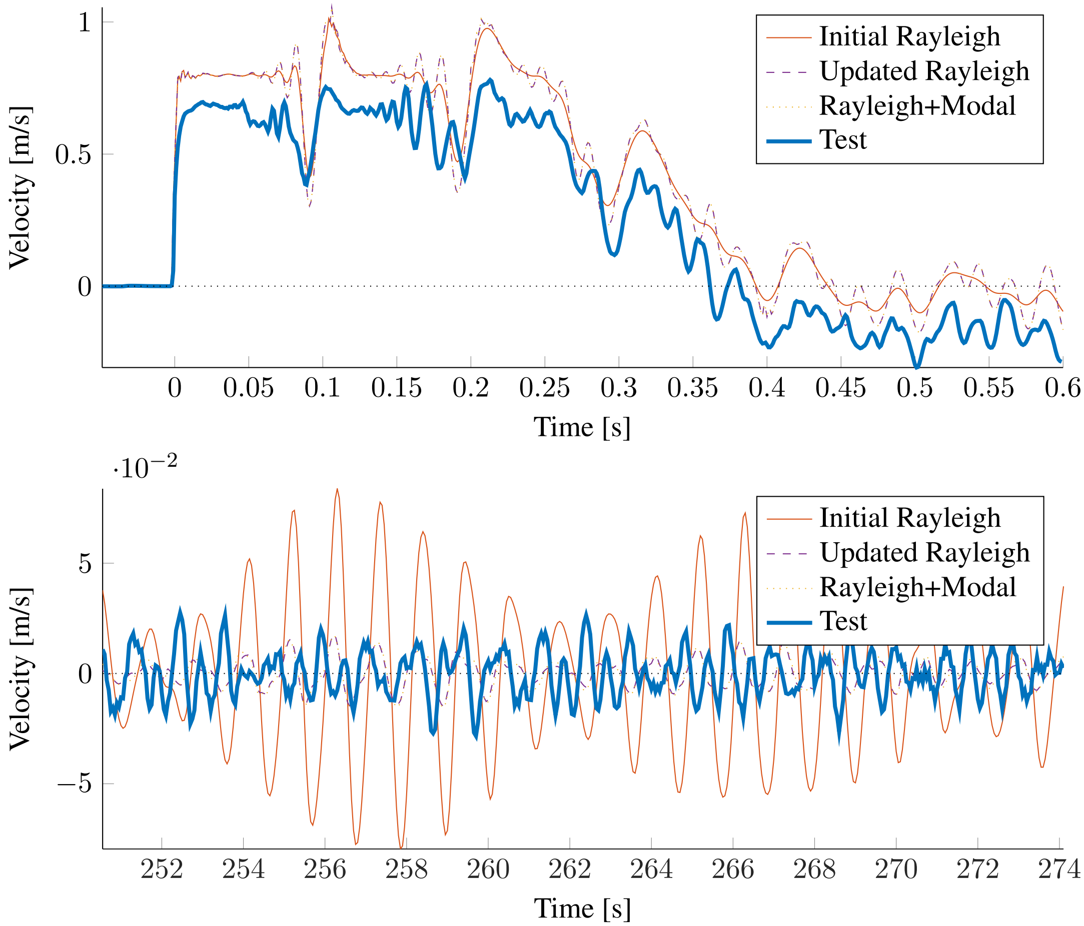

Figure 3.20: Vertical velocity of the contact wire where the mass is dropped for initial waves (top) and residual vibration (bottom).

Figure 3.21 shows the $70Hz$-filtered contact forces of two pantographs for a simulation at the nominal speed $v_{panto} = 320km/h$. The impact of the damping update is stronger on the trailing pantograph and the new damping coefficients allow some contact loss to appear at the middle of the span.

Time-signal comparison is difficult due to phase shifting. That is why scalar criteria are commonly used for comparison. Table 3.2.6 groups such criteria. The coefficients of variation σ/F_m of the contact force filtered at $20Hz$ or $70Hz$ combine information at low and medium frequencies and do enhanced understanding of the observed variations. Root Mean Square values (RMS) inside frequency bands give more information. In particular, there is no impact for the front pantograph under $5Hz$. Moreover, the RMS between 20 and $70Hz$ increases significantly for the both pantographs, as expected. The interesting decrease of RMS value of the first pantograph in the $5-20Hz$ range illustrates the importance of properly choosing damping.

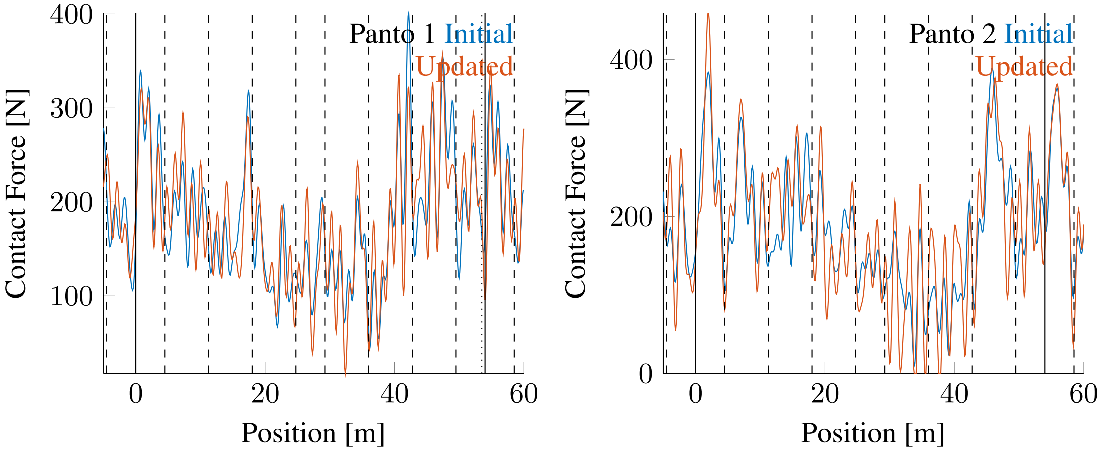

Figure 3.21: $70Hz$ filtered contact force of the heading (left) and trailing (right) pantograph over one span

Table 3.2: Usual contact force criteria

Damping model	Pantograph	σ/F_m $20Hz$	σ/F_m $70Hz$	RMS*]0 – 5] Hz	RMS [5 – 20] Hz	RMS [20 – 70] Hz
Initial	front	0.27	0.35	33.1	34.4	37.8
Updated	front	0.25	0.36	32.9	28.1	45.6
Initial	rear	0.36	0.42	48.7	39.6	37.3
Updated	rear	0.38	0.50	48.4	44.5	54.8

*Root Mean Square

3.3 Element size (flexibility)

Given a vertical force applied on the CW, the flexibility is the ratio between the uplift and the force. The flexibility is an important characteristic of the catenary and is considered as a design parameter in the European standard EN50119 [7]. In simulations, contact force between nodes needs interpolation of the flexibility between nodes. Figure 3.22 shows this interpolation with nodes indicated in dashed vertical lines and droppers in solid vertical lines. This interpolation introduces waving associated with the element size. Thus, if the maximum CW element size is fixed to $1.5m$, the contact force defined for spatial frequencies higher than $1/1.5m = 0.66m^{-1}$ are likely to be perturbed. At $v_{panto} = 320km/h$, this represents a frequency limit of $f_{lim} = 59Hz$.

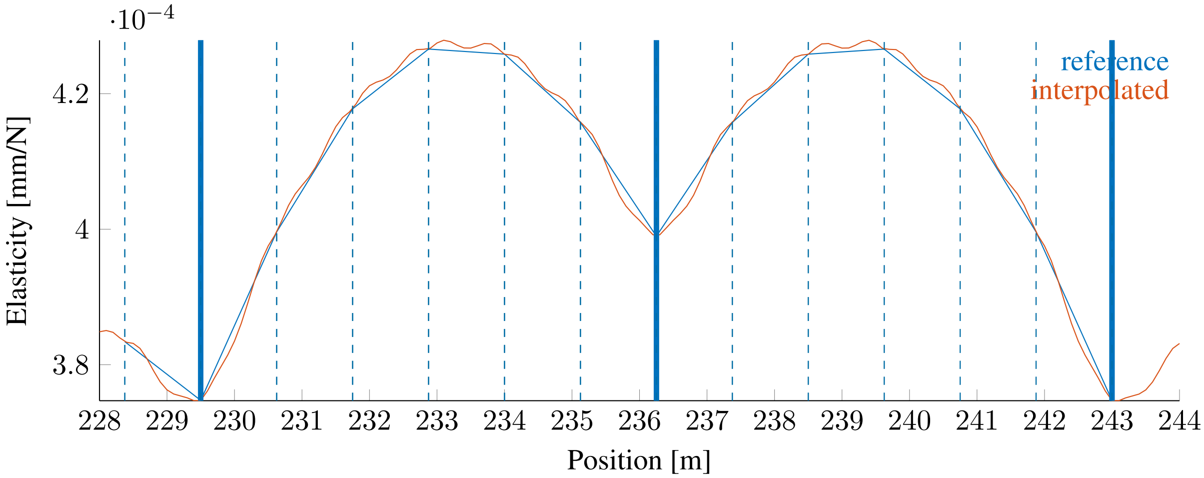

Figure 3.22: Interpolation of flexibility between nodes

Figure 3.23 shows the $70Hz$-filtered contact force for CW elements sizes of $0.5m$ and $1.5m$. The contact force amplitude around $60Hz$ is clearly higher for CW elements sizes of $1.5m$. For nominal pantograph velocities on high speed lines, elements sizes have thus to be lower than $1m$ for validity in the $[0-70]Hz$ range. If simulations at lower speeds are computed, this length has to be reduced.

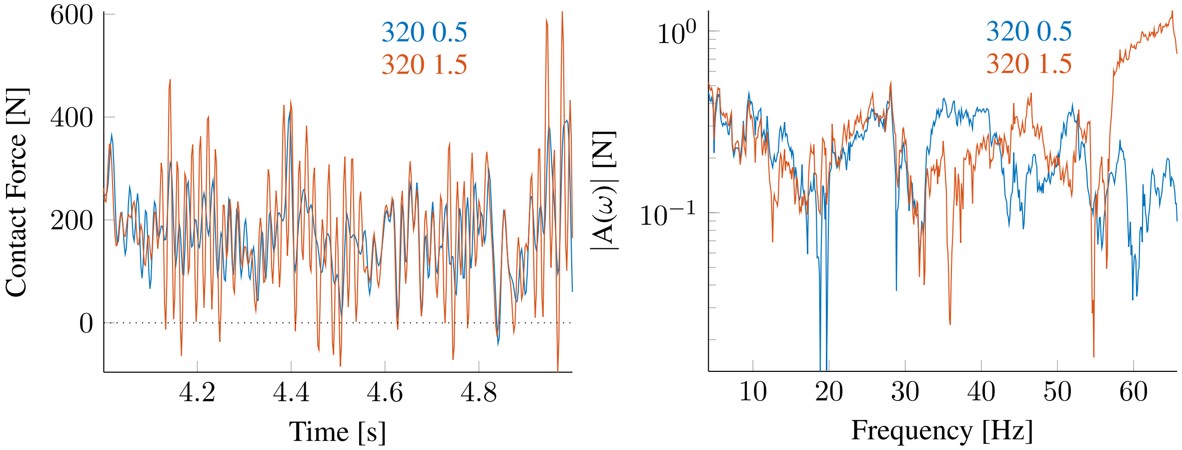

Figure 3.23: Contact force filtered at $70Hz$ (left) and amplitude of its spectrum (right) for CW elements sizes of $1.5m$ (blue) and $0.5m$ (red) for simulations at $v_{panto} = 320km/h$

Chapter 4

Statistical definition of random uncertainty on physical parameters

The catenary geometry was shown in section 1.3 to be the most critical source of variability of the contact force. A deeper study of this geometry is thus needed. This first step of the random problem considered here is the characterization of random parameters describing the geometry and the estimation of associated probability density functions ($p.d.f.$). The work is decomposed in *a priori* definition of random geometry parameters, initial selection through sensitivity analysis, and adjustment of *p.d.f.* based on measured data which corresponds to an inverse stochastic problem.

A catenary is divided into sections of about 1 km long. But every section is different. The largest standard structure of a catenary is thus a span. The associated geometry parameters are discussed in section 4.1 and a sensitivity analysis allows a first selection.

With the objective of solving the inverse stochastic problem, statistics on measured geometries are needed. Section 4.2 thus discusses available measurements and their limitations. The end result is a database of test derived span geometries. Given this data, one then seeks to adjust the *p.d.f.* of parameters retained in section 4.1 to maximize the likelihood that the test database be observed. The principles are detailed and results analysed in section 4.3.

Finally section 4.4 deals with parameters that could not be defined at the scale of the span but that could have significant impact on dynamic interactions.

The end result of the chapter is a statistical model of catenary geometry. The impact on dynamic interactions with the pantograph will then be analysed in chapter 5

4.1 Local sensitivity analysis

The span is the largest standard structure of a catenary. Figure 4.1 illustrates the different parameters that can control the static geometry of the catenary (only tension and gravity are applied). These parameters are described below:

- $H_{CW,left}$ and $H_{CW,right}$ are the height of the contact wire at the left and right steady arm of the span respectively which are considered random to represent changes induced by maintenance of either the catenary or the track.

- ΔH_{left} and ΔH_{right} are the distance between the contact wire and the messenger wire at the left and right mast of the span. This parameter is used to represent the variation of the steady arm height relatively to the messenger wire height at mast.

- $L_{drop,i}$ is the length of the i^{th} dropper of the span which is considered random to represent manufacturing tolerances and possible horizontal motion.

- T_{CW} and T_{MW} are respectively the tensions in the contact wire (CW) and in the messenger wire (MW) that can vary due to angles of brackets or frictions in joints.

- The bending stiffness in cables could vary due to wear. But quick parametric studies have shown that a very large variation is needed to see a visible impact on static deflection. It is thus negligible compared to the tensions applied in both cables.

The height of the contact wire under the i^{th} dropper of the span is defined as parameter $H_{drop,i}$ and is an output of the static computation.

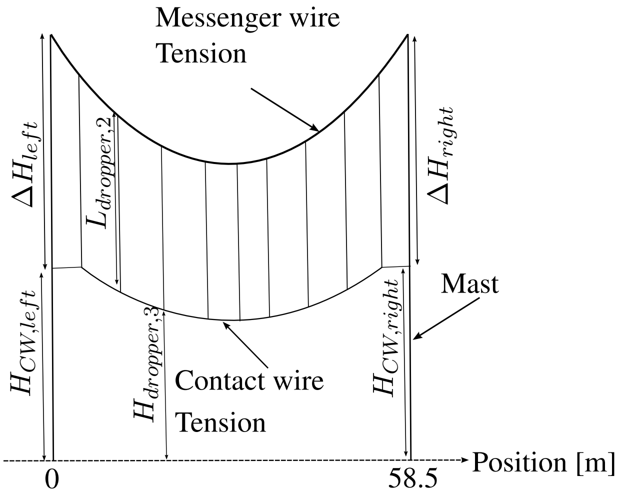

Figure 4.1: Parameters defining static geometry of a span

Figure 4.2 shows the impact of a $\pm 20\%$ variation of T_{MW} and T_{CW} on the contact wire height. The variation of T_{CW} has a negligible impact compared to that created by the variation of T_{MW}. This is expected since the conducting wire is mostly flat, while the messenger curvature is needed to support the weight. In the view of this result, T_{CW} is removed from the list of parameters that can be statistically identified.

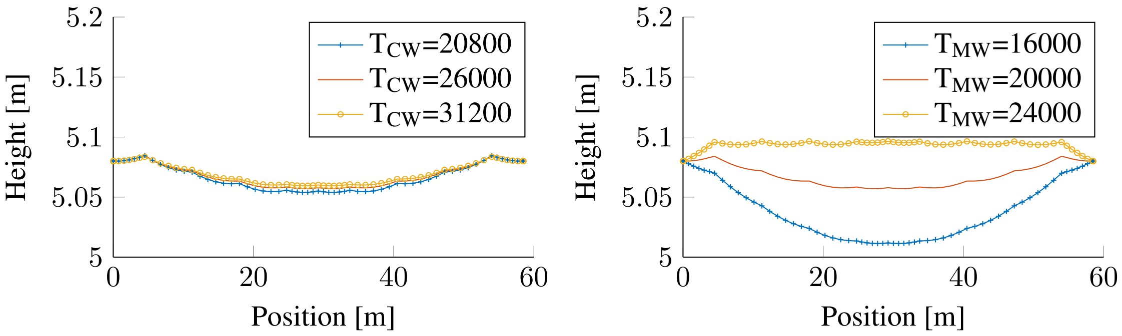

Figure 4.2: Variation of $\pm 20\%$ in T_{CW} (left) and in T_{MW} (right)

Figure 4.3 (left) shows the contact wire height in two conditions: the nominal case with $H_{CW,right} = H_{CW,left} = 508cm$ and a second configuration where the left mast has been raised of $5cm$, while retaining the contact to messenger wire distance of $140cm$, and similarly the right mast has been lowered by $5cm$ in order to amplify the potential variation of the deflection. The deflection after projection on the line linking the two steady arms, shown in 4.3 (right), is nearly identical in both cases. It is thus clear that $H_{CW,right}$ and $H_{CW,left}$ have no influence on CW deflection if ΔH_{right} and ΔH_{left} do not change. Consequently, these parameters will not be taken into account in further studies.

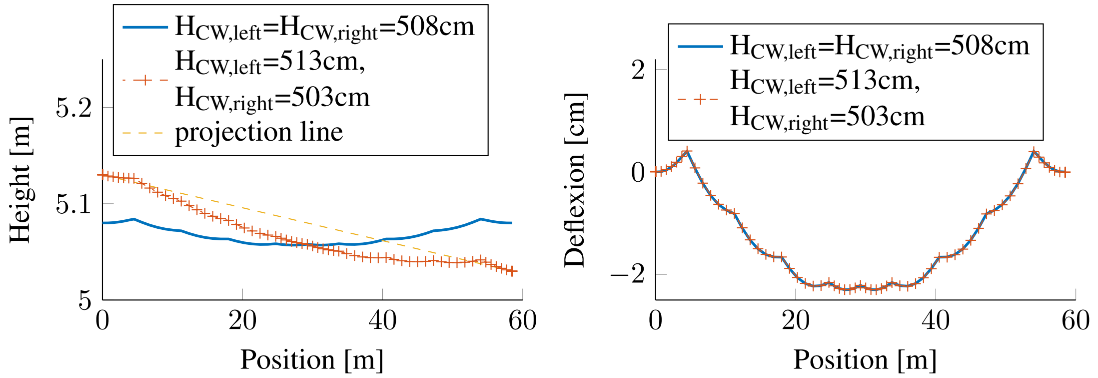

Figure 4.3: Variation of $+5cm$ for $H_{CW,left}$ and $-5cm$ for $H_{CW,right}$

Figure 4.4 left shows the impact of a $+5cm$ horizontal shift of the CW. All droppers are thus lightly inclined and the variation of height is less than $1mm$. On the right, the shift is supposed to be the same in the CW as in the MW. The difference of height induced by this shift of $5cm$ is negligible.

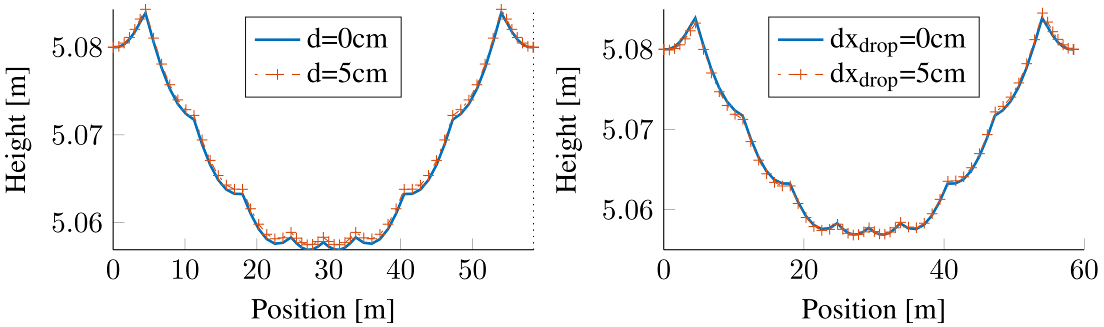

Figure 4.4: Shift of the dropper position on the CW (left) and on both cables simultaneously (right)

Finally figure 4.5 shows that ΔH impacts the sag in a non-symmetric way. This parameter is thus retained.

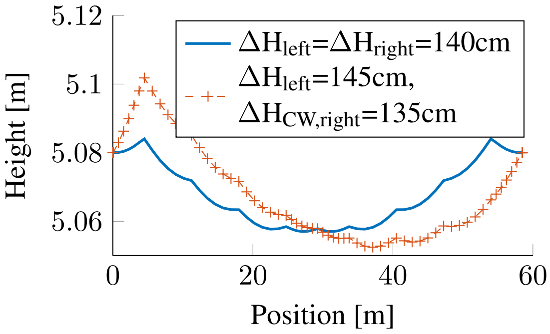

Figure 4.5: Variation of $+5cm$ for ΔH_{left} and $-5cm$ for ΔH_{right}

After this local sensitivity analysis, 11 parameters are retained and assumed independent: the 9 dropper lengths $L_{drop,i}$, the messenger wire tension T_{MW} and the distance between the contact wire and the messenger wire at the mast ΔH. It is finally assumed that dropper variations in the horizontal axial direction can be represented by dropper length variations.

4.2 Geometry measurements

In order to create a relevant statistical model, experimental characterization of the geometry is needed. In the present study, two measurement types were considered

- Quasi-static data obtained by a pantograph equipped with accelerometer, moving at a speed of $40km/h$ and applying a force assessed at approximately 36N.
- Optical data

The objective is to extract a database of span geometries from these two measurement types. Section 4.2.1 deals with quasi-static measurements and section 4.2.2 with optical ones.

4.2.1 Quasi-static measurements

Quasi-static measurements are performed through a pantograph moving at $40km/h$ kept in contact with the contact wire by applying a vertical force of approximately $36N$. This measurement thus corresponds to an uplift. A contribution of this work was to demonstrate that these experimental conditions have a significant impact on the measured sag. An iterative geometry refinement process following the steps of figure 4.6 was thus introduced.

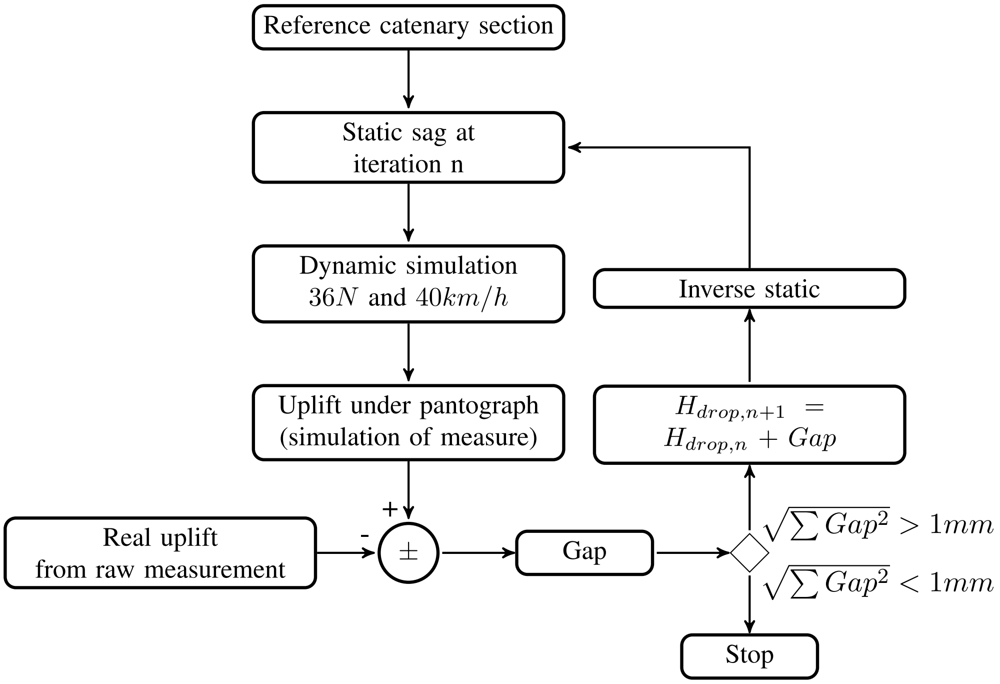

Figure 4.6: Iterative scheme for measurement correction

Figure 4.7 shows a sample measurement. The horizontal sampling is every $2cm$ and the vertical accuracy is of $1mm$. This low accuracy is insufficient to detect dropper positions and only provides a poor approximation of mast positions. The measurement of sway is thus used for mast positioning.

Once these mast positions are known, a reference catenary section is built using dropper tables [84] and fixing contact wire height at steady arm to $5.08m$ and using $\Delta H = 1.4m$. A reference catenary section is thus built.

The static sag of the nominal catenary model is then computed and a dynamic simulation is performed for conditions corresponding to the measurement, that is to say a pantograph applying a $36N$ mean-force on a train going at $40km/h$. From this dynamic simulation, the uplift under the pantograph can be computed. This value is what the equipment assumes to be the static sag, but should more appropriately be called dynamic sag or uplift. The difference between the measured and simulated dynamic sags at the steady arm and dropper positions then gives an estimate of the geometry error. This gap is assumed to be representative of the error on the static sag, so that one seeks to correct the static geometry accordingly.

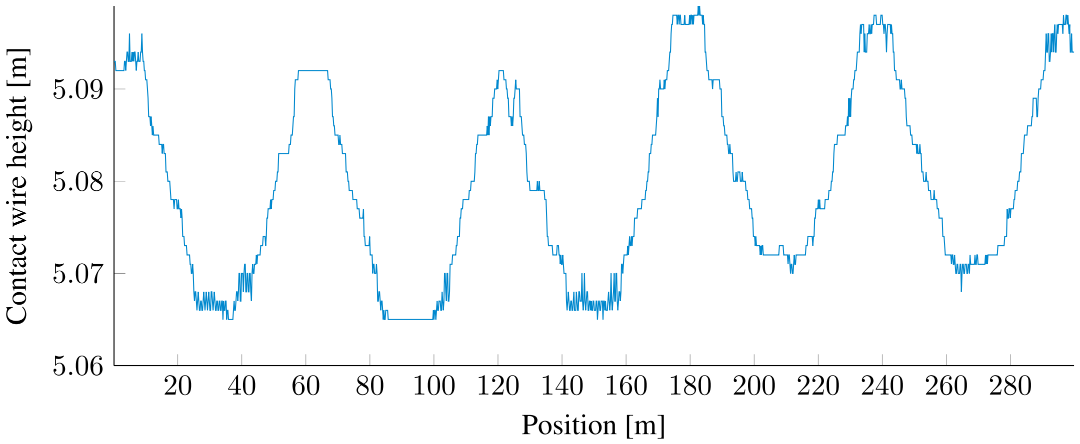

Figure 4.7: Real uplift from raw measurement

Obtaining a geometry that matches the target sag is an inverse static problem. The method applied here is to use dropper lengths as the only variable parameters. This leads to a well posed problem that has a unique solution. The updated geometry can then be used at step $n + 1$.

The convergence of the computation is controlled by computing the norm of the vector of gaps. In most cases, convergence is observed after 2 iterations with a norm $\sqrt{\sum Gap^2} < 1mm$.

When using this method, two assumptions are made

- The corrected bias is significantly higher than the remaining measurement uncertainty and the model uncertainty,
- Correction on dropper lengths only is assumed to lead to an equivalent solution to the one that could be found by letting all parameters vary.

To verify this second assumption, two similar static sags were generated. A first model was generated by setting T_{MW} to $16kN$. By modifying dropper lengths only, a second model with $T_{MW} = 20kN$ was built to have the same sag. Figure 4.8 shows that the difference is lower than $2mm$ which is the order of magnitude of the test resolution. The second assumption is thus validated.

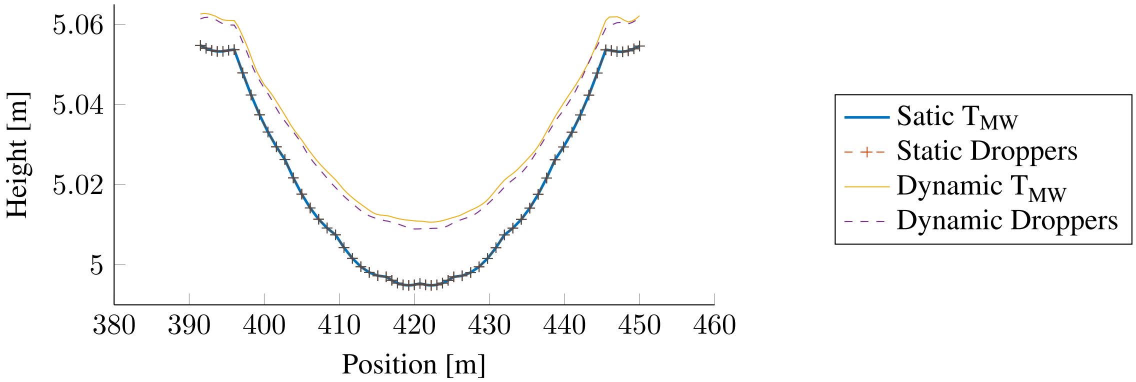

Figure 4.8: Comparison of impact of T_{MW} and $L_{drop,i}$ on the dynamic correction applied

Figure 4.9 shows the updated geometry compared to the raw measurement. The applied correction varies from $6mm$ to $15mm$, which is important compared to measurement noise and thus strengthens the first hypothesis.

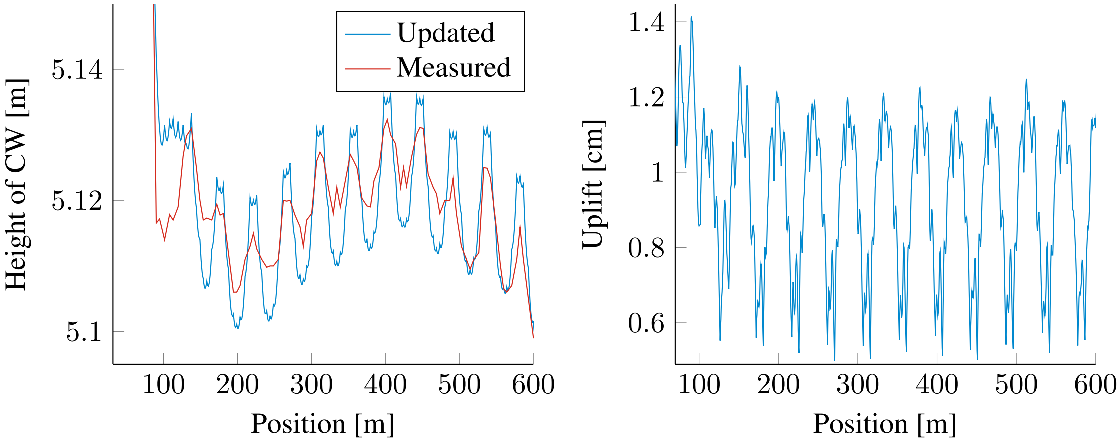

Figure 4.9: Measured and updated static sag in a catenary section (left) and simulation of the dynamic uplift under the pantograph (right)

For the database of available measurements which were obtained on the catenary between Paris and Strasbourg (LN6), a set of 117 N2-span deflections were obtained. Each had different heights at masts but as seen in section 4.1, the height of the contact wire at mast has no impact on the deflection. In order to remove these parameters from measurements, projections were done as in figure 4.3.

Table 4.1 summarizes the number of spans found for each span type. The reference data is thus a set of $\nu_{exp} = 117$ experimental observations $(\boldsymbol{W}_i^{obs,exp})_{1<=i<=\nu_{exp}}$ considered as independent realizations of a random vector $(\boldsymbol{W}_i^{obs,exp})$ of size 9. Figure 4.10 shows these realizations.

Table 4.1: Number of quasi-static measurements per span of the catenary type V350

Span length	49.5	54	58.5
Number of spans	87	113	117

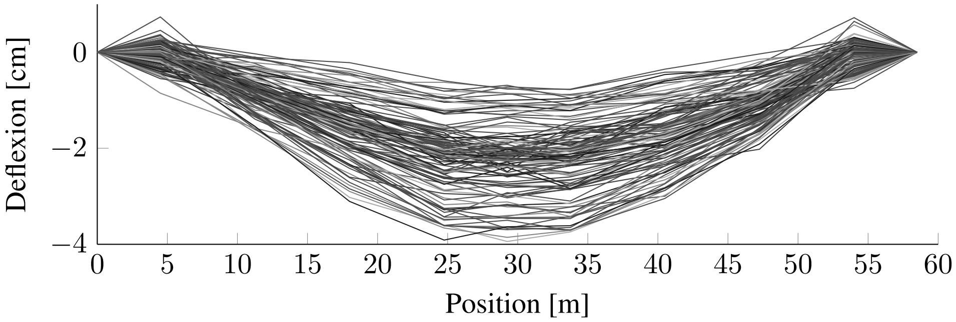

Figure 4.10: Measured deflection under each dropper of the N2-type span

4.2.2 Optical measurements

The optical measurements are sampled every 25cm on the x axis and have a resolution of 0.1mm on the y and z axes, which is ten times smaller than the quasi-static measurement. They do not interfere with the catenary. The available data are mainly for the high speed line linking Paris to Marseilles which is composed of two different types of catenary, V300 ($T_{MW} = 14kN$ and $T_{CW} = 20kN$) and V350 ($T_{MW} = 20kN$ and $T_{CW} = 25kN$). Figure 4.11 shows a sample optical measurement.

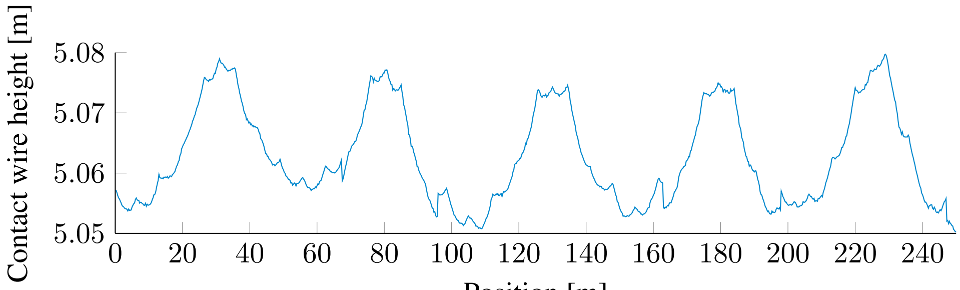

Figure 4.11: Raw optical measurement

This high quality measurement almost allows to make out dropper positions in spans. Measurements are collected by span and the table 4.2 summarizes the number of spans available for each type. Figure 4.12 shows the deflection measured for $45m$-length spans.

Table 4.2: Number of optical measurements per span of the catenary type V350

Span length	40.5	45	49.5	54	58.5
Number of spans	392	567	205	32	14

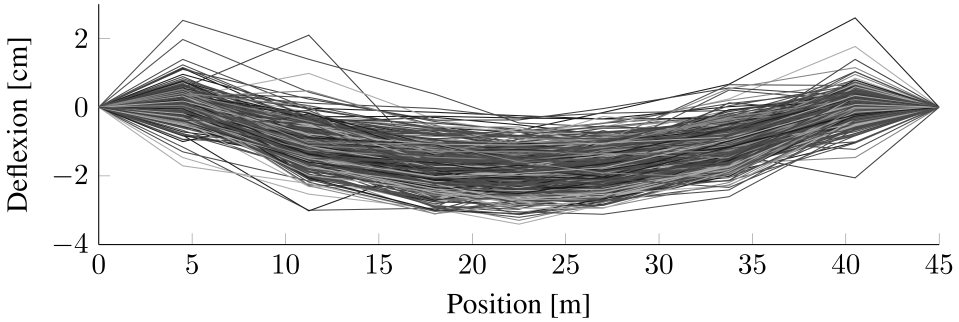

Figure 4.12: Optically measured deflection under each dropper of the N5-type span

Despite their better quality, optical measurements are still in a development stage and not deployed in maintenance policy. The identification will thus be led as if no optical measurement were available and the deflection samples of $45m$-length span $N2$ measured optically will be used to verify the identification.

4.3 Statistical definition of geometry parameters

Now that a set of measurement is available, the most appropriate *p.d.f.* can be chosen following the method for statistic inverse problem solving detailed in section 4.3.1. An example of a well posed problem is detailed in section 4.3.2, which is easy to solve but leads to a biased solution. Finally, section 4.3.3 shows the final results retained.

4.3.1 Methods for statistic inverse problem solving

The problem to be solved is to find the distributions of eleven parameters, namely the nine dropper lengths of the N2-type span, the tension T_{MW} and the fictive parameter ΔH knowing deflection at seven points, under each droppers. The problem is ill-posed and accepts an infinity of solutions. A method has thus to be followed to choose the most probable solution.

The statistic inverse problem involves the systems in figure 4.13 with

$\mathbf{f}^{exp}$ the whole experimental parameters defining the real mechanical system

$\mathbf{w}^{exp,obs}$ measured observations on the real mechanical system

$\mathbf{u}^{exp,nobs}$ variables of the real mechanical system which are not observed

$\mathbf{f}$: the other parameters which are needed to define the complete mechanical model

$\mathbf{X}$ the parameters taken into account in the study, they are supposed to be random and the goal is to find their *p.d.f.*

$\mathbf{W}^{obs}$ the observed model output

$\mathbf{U}^{nobs}$ not observed model output

The problem is to statistically define $\underline{\mathbf{X}}$ while μ_{exp} observations $\mathbf{w}_1^{exp,obs}$, ..., $\mathbf{w}_{\mu_{exp}}^{exp,obs}$ are available. The global framework used is explained by Soize [8] and summarized in figure 4.14.

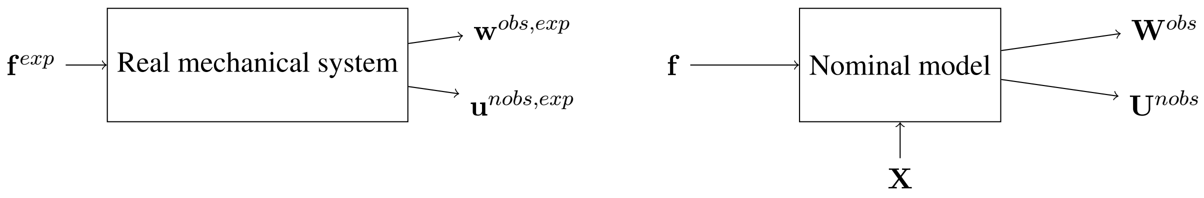

a) Reality *b) Model*

Figure 4.13: Representation of the studied system

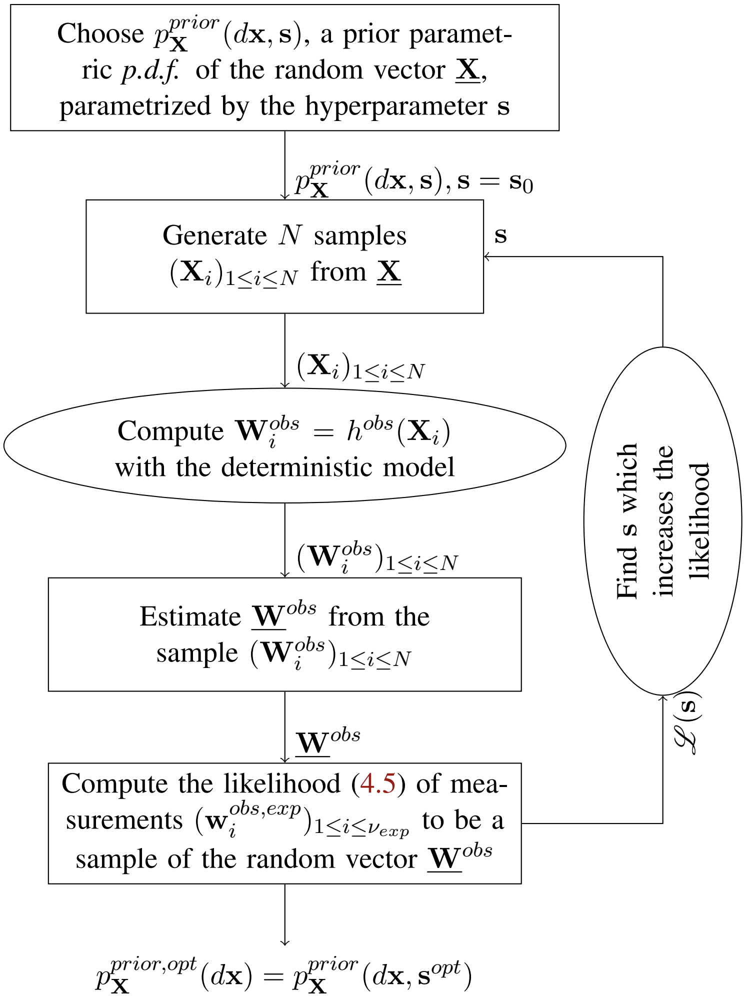

Figure 4.14: Global methodology for solving a statistical inverse problem

The input parameters chosen in section 4.1 are assembled in a random vector $\underline{\boldsymbol{X}}$ defined in (4.1).

$$\underline{\boldsymbol{X}} = [(L_{drop,i})_{1<=i<=9}, T_{MW}, \Delta H] \tag{4.1}$$

The first step needed to define the probability density function, *p.d.f.* , of $\underline{\boldsymbol{X}}$ is to choose if it follows a parametric or non-parametric model of distribution. The non-parametric models need a large amount of data which are not available. Parametric distributions are thus chosen trying to verify the maximum entropy principle (see [9]) whose aim is to maximize the uncertainty on the available information.

Without information about any correlation between scalar variables of $\underline{\boldsymbol{X}}$, this principle leads to independent distribution.

For each scalar random variable of $\underline{\boldsymbol{X}}$, the maximum entropy principle is applied again. When the only known information is that values of $\underline{\boldsymbol{X}}$ are positive, the classical choice is a Gamma distribution. The verification of the principle in that case is developed in appendix C. For each scalar distribution $\underline{X}_i$

of $\underline{\boldsymbol{X}}$, the *p.d.f.* is given by

$$p_X(x) = \frac{x^{k-1}\exp\left(-x/\theta\right)}{\theta^k\Gamma(k)} \tag{4.2}$$

with

$$\Gamma(k) = \int_0^{\infty} e^{-x}x^{k-1}\,dx \tag{4.3}$$

In order to get more readable results and a good conditioning, these p.d.f. are characterized by their expectations and standard deviations:

$$\mu = k\theta \quad \text{and} \quad \sigma = \sqrt{k\theta^2} \tag{4.4}$$

Then, $\boldsymbol{s}$ is defined as the vector of hyper-parameters, gathering the expectation μ_i and standard deviation σ_i of each random scalar X_i in random vector $\underline{\boldsymbol{X}}$. The vector $\boldsymbol{s}$ is thus a 22-length vector whose initial values $\boldsymbol{s}_0$ are set consistently with measurement magnitudes.

Given parameter $\boldsymbol{s}$ and associated *p.d.f.* definitions, random samples of $\underline{\boldsymbol{X}}$ of size N_i that can be generated by different methods and used to compute the deflection of the contact wire and more specifically $\underline{\boldsymbol{W}}^{obs}$ the output random vector defined by the $d_{W^{obs}} = 9$ non independent heights of the contact wire under droppers.

The two classical sampling methods are the Monte Carlo (MC) sampling technique or the Latin HyperSquare (LHS) technique, which are well explained in [11]. The LHS sampling method is at least as quick as the MC, but requires the independence of the input random vector, which is the case here. Figure 4.15 shows the convergence of the expectation (left) and variance (right) of the deflection under the first dropper. The expectation convergence is significantly quicker using the LHS sampling method although it is not the case for the variance.

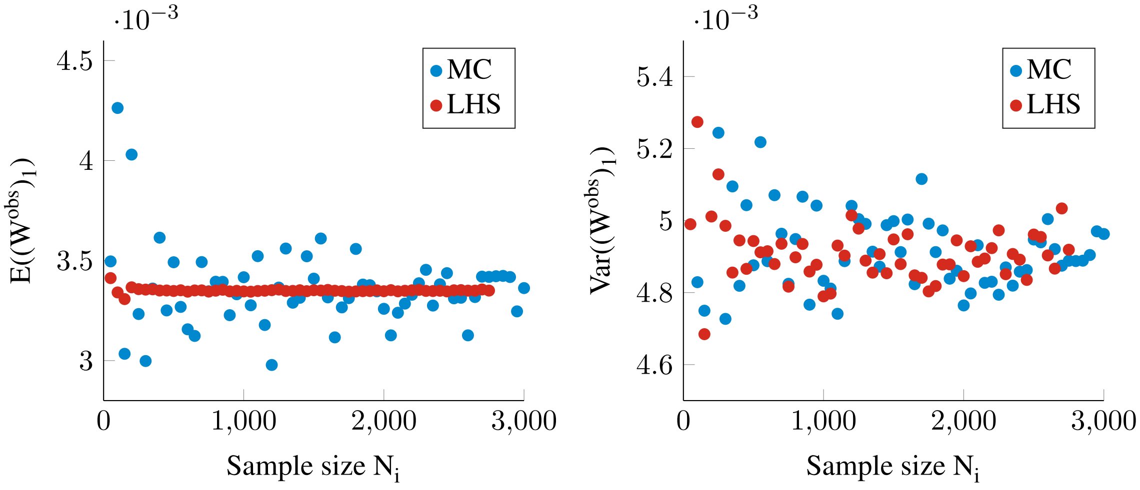

Figure 4.15: Convergence of the two first statistical moments, expectation (left) and variance (right) of the deflection under the 1^{st} dropper for two sampling methods

Two sample draws $\boldsymbol{X}_1$ and $\boldsymbol{X}_2$ of $\underline{\boldsymbol{X}}$ of size $N_1 = 10^3$ and $N_4 = 10^6$ were generated. As all marginal input distributions are supposed independent, the sampling method chosen is the Latin Hypercube Sampling method (LHS). Once the two corresponding samples $\boldsymbol{W}_i^{obs}$ computed, the distribution of $\underline{\boldsymbol{W}}^{obs}$ is estimated using two different methods:

- Parametric estimation: one uses a Gaussian distribution in order to represent the random vector $\underline{\boldsymbol{W}}^{obs}$. This method displays a quick $1/\sqrt{N}$ convergence but can introduce a bias if the parametric distribution chosen is not fitted
- Non-parametric estimation: one uses the multivariate Gaussian kernel density estimation method (called KS for Kernel Smoothing). This method is slower with a $N^{-1/(d_{W^{obs}}+4)}$ convergence but does not introduce any bias.

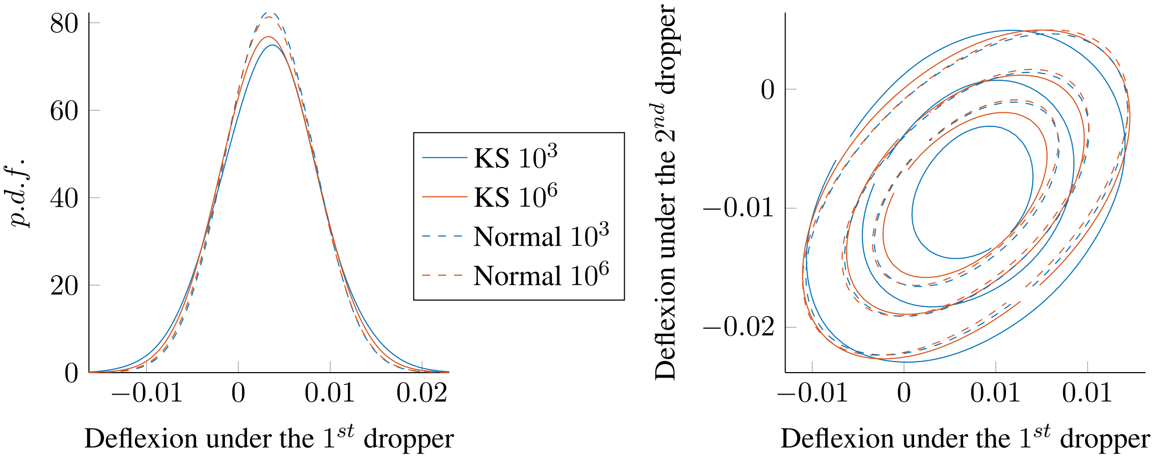

Figure 4.16: Comparison between parametric (dashed) and non-parametric (solid) estimation methods for samples of sizes 10^3 (blue) and 10^6 (red)

The theoretical convergence speed of the two methods is significantly different. For example, if one supposes a mean deflection under the 5th dropper of $-2.5cm$ with a standard deviation of $1cm$ (approximately the magnitude observed), the estimation of the mean with a sample of size 1000 will have 95% of probability to be in the interval $[-2.438cm, -2.562cm]$ with the parametric estimation method and $[-1.348cm, -3.652cm]$ with the non-parametric estimation method. One thus wants to check if the bias introduced is important. To this end, figure 4.16 compares the two methods for the i samples computed. On both figures, one sees that solid lines (i.e. non-parametric estimation) get closer to the dashed lines (i.e. parametric estimation), which seems to have already converged with a 1000-sized sample. Moreover, using $\boldsymbol{s}_0$ as initial hyper-parameters, the output samples all succeed in the Henze-Zirkler's multivariate normality test. One thus chooses to use the parametric estimation method and verify if the result does still passes the normality test.

Calling $p^{prior}_{\boldsymbol{W^{obs}}}$, the estimation of the output distribution $\underline{\boldsymbol{W}}^{\boldsymbol{obs}}$ with selected hyper-parameters $\boldsymbol{s}$, the log-likelihood [10] is defined by

$$J(\boldsymbol{s}) = ln(p^{prior}_{\boldsymbol{W}^{obs}}(\boldsymbol{W}_1^{obs,exp}; \boldsymbol{s}) + ... + ln(p^{prior}_{\boldsymbol{W^{obs}}}(\boldsymbol{W}^{obs,exp}_{\nu_{exp}}; \boldsymbol{s}). \tag{4.5}$$

The likelihood function is thus the product of the conditional probabilities to observe each experimental observation $\boldsymbol{W}^{obs,exp}_{\nu_{exp}}$ knowing $\boldsymbol{s}$. It is thus natural that $\boldsymbol{s}$ is better if $J(\boldsymbol{s})$ is higher. The maximum likelihood principle is then an optimization problem given by

$$\boldsymbol{s}^{opt} = \arg\max J(\boldsymbol{s}) \tag{4.6}$$

In the implementation, the optimization is solved with the Nelder-Mead simplex algorithm available in the `num.py` module of python.

In summary, 11 independent gamma distributions are chosen for input parameters, which create $\boldsymbol{s}$ a vector of 22 hyper-parameters to be identified. One uses the LHS method to compute a sample of $\underline{\boldsymbol{W}}^{obs}$ which is estimated by a Gaussian multivariate parametric method in order find $\boldsymbol{s}^{opt}$ which maximizes the likelihood $p^{prior}_{\boldsymbol{W^{obs}}}$ of the ν_{exp} experimental observations $(\boldsymbol{W}_i^{obs,exp})$.

4.3.2 Dropper only inverse problem

As there are only 9 observations in vector $\underline{\boldsymbol{W}}^{obs}$, an basic approach would seek to use only 9 parameters and in the present case consider variations of dropper lengths only. This section will illustrate that this results in a biased solution.

When maintaining fixed every parameters but the dropper lengths, the inverse problem is well posed as explained in section 4.2.1. The problem is thus quick to solve and results are obtained in a few minutes. The 117 $(\boldsymbol{W}_i^{obs,exp})$ thus lead to 117 sets of $L_{drop,i}$ on which statistical observation can be performed.

Table 4.3: Dropper length moments

$\boldsymbol{s}$ $\boldsymbol{X}$	$\mu - L_{nom}[cm]$	$\sigma[cm]$
$L_{drop,1}$	0.64	0.33
$L_{drop,2}$	-0.45	0.81
$L_{drop,3}$	-0.68	1.43
$L_{drop,4}$	-0.6	1.83
$L_{drop,5}$	-0.34	1.83
$L_{drop,6}$	-0.36	1.81
$L_{drop,7}$	-0.08	1.50
$L_{drop,8}$	0.19	0.98
$L_{drop,9}$	0.95	0.41

Table 4.3 shows that the expectation of dropper lengths is higher than the nominal value at the extremities and lower around the mid-span with a gap of almost $1cm$ for some cases. Moreover, the standard deviation is very high near the mid-span and low at extremities.

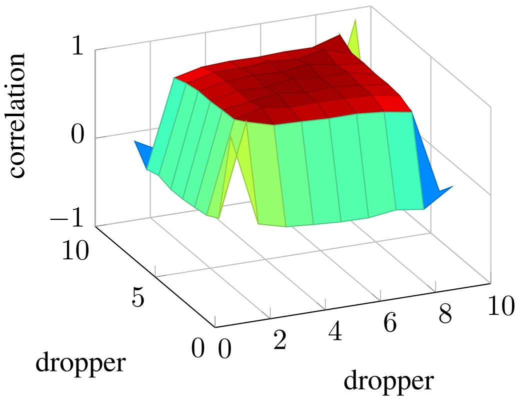

Figure 4.17: Pearson correlation matrix of dropper lengths

Figure 4.17 displays the Pearson correlation matrix which shows a very strong correlation of almost 1 between every dropper but those at the extremities.

The high disparity of dropper lengths, the high gap between nominal length and identified expectations, and the strong correlation between dropper lengths leads to the conclusion that the present result is notably biased and other parameters, not yet taken into account, have a non-negligible variability, which impacts the contact wire deflection.

4.3.3 Statistical identification

Variation of droppers only thus cannot explain the entire variability of the contact wire height. Adding one more parameter, namely the MW tension, leads to an ill-posed problem that needs the method detailed in section 4.3.1 for parameter identification.

Taking parameters discussed in section 4.1, the whole inverse statistic problem is solved under python using the OpenTURNS [11] module, while the static problem is solved by OSCAR parallelized on 40 nodes. Each single static computation lasts around 2s, which leads to an evaluation of $J(\boldsymbol{s})$ (4.5) in around 80s. The convergence is observed after 2300 iterations with 3300 evaluations of $J(\boldsymbol{s})$ in 3 days.

A first optimization led to high mean values of dropper lengths $L_{drop,i}$ compensated by a high mean value of T_{MW}. These incoherent results were corrected by fixing the mean values of $L_{drop,i}$ which are the only measured quantities during maintenance and consequently the most relevant quantity to maintain fixed. The $\boldsymbol{s}^{opt}$ resulting from the new optimization is displayed in table 4.4.

Table 4.4: Optimal statistical hyper-parameters $\boldsymbol{s}^{opt}$

$\boldsymbol{s}$ $\boldsymbol{X}$	$\mu[SI]$	$\sigma[SI]$
T_{MW}	20575	818
ΔH	1.388	0.0065
$L_{drop,1}$	1.244	0.0067
$L_{drop,2}$	1.098	0.0050
$L_{drop,3}$	0.998	0.0045
$L_{drop,4}$	0.945	0.0045
$L_{drop,5}$	0.934	0.0038
$L_{drop,6}$	0.945	0.0044
$L_{drop,7}$	0.998	0.0035
$L_{drop,8}$	1.098	0.0034
$L_{drop,9}$	1.244	0.0070

Table 4.4 shows that T_{MW} has a standard deviation of around 818N, which is a very large value since this tension is regulated by masses installed at the forward and after ends of the catenary. One thus has to investigate the reason of this large variation, which can be observed in a single catenary. A possible explanation is the cumulated axial forces applied by brackets on the MW due to temperature variations. A variation of $500N$ can be explained that way. Another potential source of tension variation is the friction in joints linking brackets to masts, but these variations have not been quantified. In any case, these source directly impact T_{MW} and not another parameter that would have the same consequences on the output height $\underline{\boldsymbol{W}}^{obs}$.

During the manufacturing of droppers, the measurement accuracy on their length is $1cm$. The $L_{drop,i}$ found thus have a coherent value of standard deviation of between $3.4mm$ and $7mm$. However, a twice higher variation around the extremities of the span is observed. This issue can be due to an interaction with ΔH that is not taken into account or to a bias induced by either measurement or model, which have been combined while correcting measurements.

For generalization of dropper length distribution to any kind of span the same standard deviation of dropper lengths is chosen and, to maximize uncertainty, its value is taken to be highest observed one, namely $\sigma_{dropper} = 7mm$.

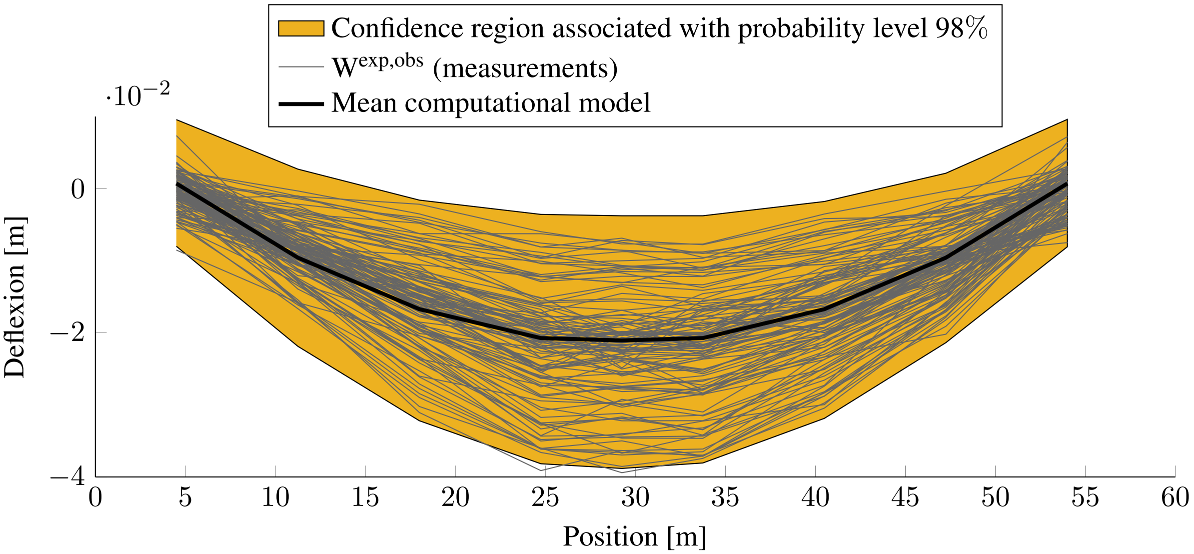

Figure 4.18: Deflection of the contact wire at dropper positions along the $58.5m$-length span from quasi-static measurements and the associated 98% confidence region

Figure 4.18 shows the confidence region in which, considering the input gamma distributions chosen with hyper-parameters $\boldsymbol{s}^{opt}$, the deflection has a 98% of probability to occur. The area has been defined by sampling an input of size $N = 1e4$ and eliminating the 0.01% extremal values for each component of $\underline{\boldsymbol{W}}^{opt}$ separately. Results fit measurements quite well.

The final *p.d.f.* of T_{MW} is shown in figure 4.19. This gamma distribution is close to a normal one. This is attested by the fact that every final input distributions have succeed to the Kolmogorov-Smirnov normality test at the 5% significance level. For the sake of simplicity, input distributions will thus be defined as Gaussian distributions with the same mean and standard deviations as those defined for the Gamma distributions.

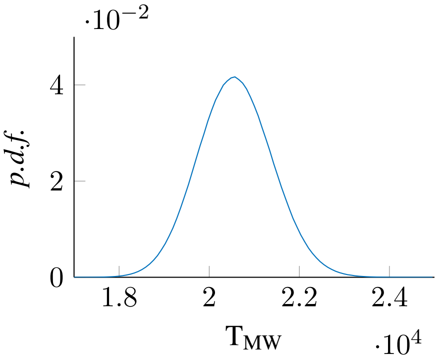

Figure 4.19: Final Gamma distribution of T_{MW}

With the objective of verifying the results obtained using quasi-static measurements of $58.5m$-length spans, a comparison with optical measurements of $45m$-length spans is considered. Figure 4.20 shows the 98% confidence region computed for dropper lengths and ΔH mean equal to nominal lengths and standard deviations equal to $\sigma_{dropper} = 7mm$, T_{MW} mean value fixed to nominal value, i.e. $\mu_{T_{MW}} = 19600N$ and standard deviation $\sigma_{T_{MW}} = 800N$. The statistical inverse problem was also solved with optical measurements and gave $\sigma_{dropper} = 7.2mm$, $\mu_{T_{MW}} = 19850$ and $\sigma_{T_{MW}} = 767N$, which are close to selected values.

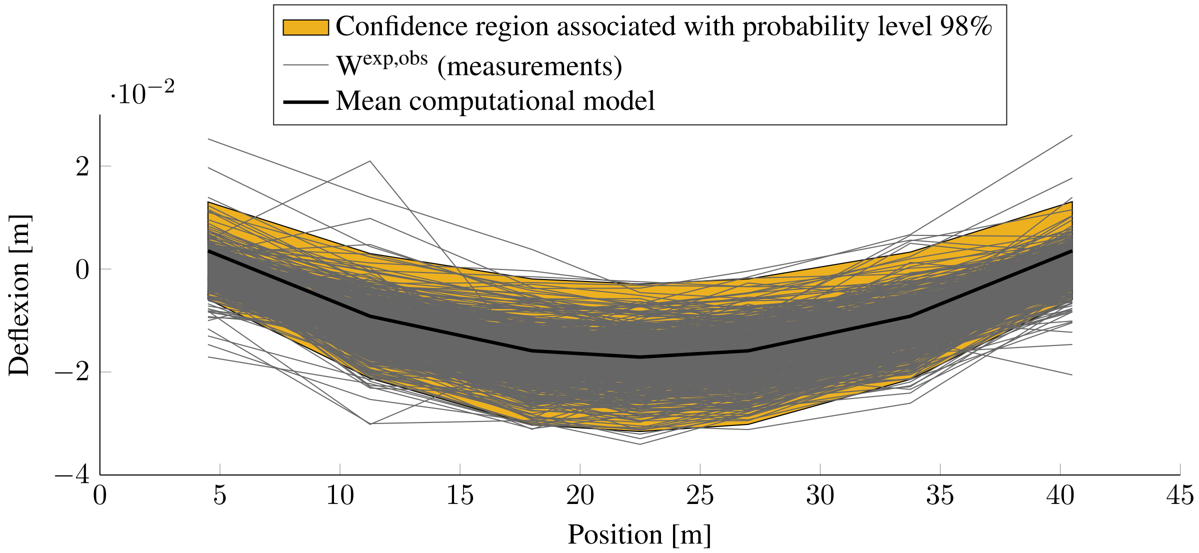

Figure 4.20: Deflection of the contact wire at dropper positions along the $45m$-length span and the 98% confidence region defined using quasi-static measurements

4.4 Statistical model for geometry of a whole section

The parameters statistically characterized until now were those influencing the sag of the CW at the scale of the span. At the scale of the whole catenary, parameters influencing the dynamic interaction can be different.

Parameters like the length or angle of the steady arm have been studied separately and do not seem to impact either geometry or dynamic response for consistent variations.

No information is available about variability of the contact wire tension T_{CW}. Nevertheless, its impact on dynamic interaction is well known. That is why it will be assumed that its variability is the same as that of T_{MW}, namely, a Gaussian variation with a standard deviation of $1000N$ and a mean value equal to the nominal value $25kN$.

The last random parameter which had a negligible influence on the sag at the span-scale is the height of the messenger wire at mast, $\underline{\boldsymbol{H}}_{\boldsymbol{MW,Mast}}$. The distribution of $\underline{\boldsymbol{H}}_{\boldsymbol{MW,Mast}}$ is defined from measurements of the contact wire height at mast, $\underline{\boldsymbol{H}}_{\boldsymbol{CW,Mast}}$. The mean value $mean(\underline{\boldsymbol{H}}_{\boldsymbol{MW,Mast}})$ will be chosen equal to $mean(\underline{\boldsymbol{H}}_{\boldsymbol{CW,Mast}}) + \Delta H_{Mast}$, with ΔH_{Mast}, the nominal distance between the contact and messenger wires at masts, which might be different between spans. In the general case, $\Delta H_{Mast} = 1.40m$. The first assumption is thus that the variations of $\underline{\boldsymbol{H}}_{\boldsymbol{MW,Mast}}$ are approximately the same as those of $\boldsymbol{H}_{\boldsymbol{CW,Mast}}$.

The second assumption is that $\underline{\boldsymbol{H}}_{\boldsymbol{MW,Mast}}$ is a Gaussian random vector of size n_{mast}, the number of masts in the model. Using the maximum entropy principle [9] (see [85] for examples) applied to a random vector $\underline{\boldsymbol{H}}_{\boldsymbol{MW,Mast}}$, it is assumed that the only available data are the mean value $\boldsymbol{m_X}$ and the covariance matrix $C_{\boldsymbol{X}}$

$$\boldsymbol{m_X} = E(\underline{\boldsymbol{H}}_{\boldsymbol{MW,Mast}}) \tag{4.7}$$

$$C_{\boldsymbol{X}} = E\left\{(\underline{\boldsymbol{H}}_{\boldsymbol{MW,Mast}} - \boldsymbol{m_X})(\underline{\boldsymbol{H}}_{\boldsymbol{MW,Mast}} - \boldsymbol{m_X})^T\right\} \tag{4.8}$$

If a singular value decomposition is applied to $C_{\boldsymbol{X}}$,

$$C_{\boldsymbol{X}} = U \cdot \lambda \cdot U', \tag{4.9}$$

the vector $\boldsymbol{H_{MW,Mast}}$ can be written [86] as a product of the root matrix R and a normalized independent, identically distributed Gaussian vector $\underline{\boldsymbol{W}}$ of size n_{mast},

$$\boldsymbol{H_{MW,Mast}} = R \cdot \underline{\boldsymbol{W}}. \tag{4.10}$$

where R is defined by

$$R = U \cdot \lambda^{1/2} \cdot U', \tag{4.11}$$

The covariance matrix $C_{\boldsymbol{X}}$, of size $n_{mast} * n_{mast}$ has to be defined from measurements. In that case, $n_{mast} = 24$ and the number of measurements of $\boldsymbol{H_{CW,Mast}}$ at n_{mast} consecutive masts is of 695. It seems large enough but $C_{\boldsymbol{X}}$ is variable when changing the size n_{mast} and covariance between spans separated of a fixed number of masts can change drastically. Two observations are made to solve this issue.

First, the geometry criteria that are linked with cable heights at mast can be the height itself, the slope or the difference of slope, thus involving a maximum of three consecutive heights. The covariance matrix is thus simplified by setting to zero covariances between $\boldsymbol{H_{MW,Mast}}$ at masts separated of three spans or more. This means that even if $\boldsymbol{H_{MW,Mast}}$ at one mast is strongly dependent to $\boldsymbol{H_{MW,Mast}}$ three masts after or before, this covariance is not taken into account. Setting these covariances to zero maximizes the variability of $\boldsymbol{H_{MW,Mast}}$ and thus its influence on dynamic interactions.

Another motivation to limit the correlation to a distance of two spans (three consecutive masts) came from the observation of figure 4.21 left. Two contact forces were computed using the same configuration and changing only the mast height at $x = 850m$ by $2cm$. The signal is filtered at $20Hz$ and an impact is observed between the previous mast around $x = 800m$ and two masts after the modified one, around $x = 950m$. Thus, if a correlation exists between two masts separated by two or more other masts, it is not necessary to take into account this correlation since this has no impact on dynamics.

However, other simulations were performed using values of model parameters that have been calibrated in chapter 3. Using the defined contact stiffness, damping and filtering the contact force at $70Hz$ changes the observation. The right figure shows that the term to term signal comparison is no longer sufficient to assess the negligible impact of a mast height on the contact force computed three spans before or after.

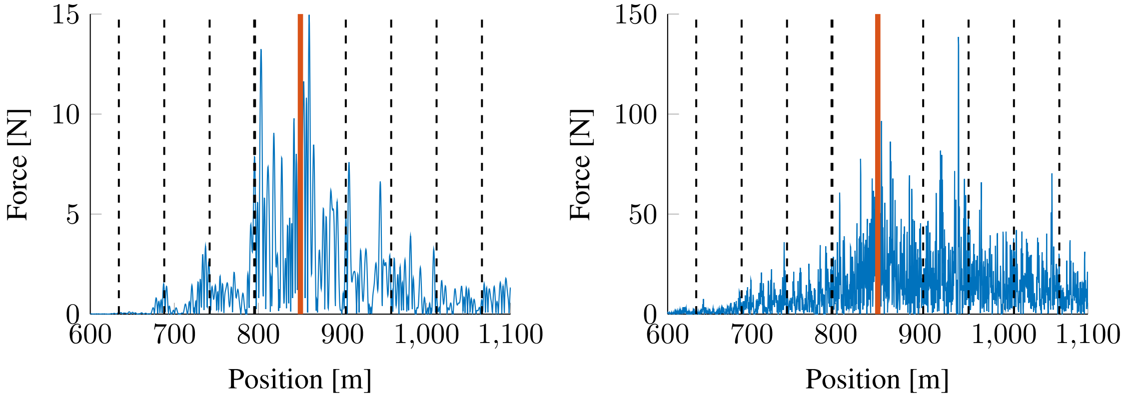

Figure 4.21: Difference of forces when the mast at $x = 850m$ is raised of $+2cm$ filtered at $20Hz$ using former damping and contact stiffness (left) and filtered at $70Hz$ using damping and contact stiffness defined in chapter 3 (right)

It finally appeared hypothesis did not need to be revised, as mast height has a significantly lower impact on dynamics than other parameters and maximizing its variability is not critical.

The second observation is that the function $C_{\boldsymbol{X}}$ can be approximated by a stationary estimator as explained by Perrin [87]. In practice, this means that inside a section, the covariance between two consecutive $\boldsymbol{H_{MW,Mast}}$ are assumed independent of their position in the section. The diagonal and super-diagonals of $C_{\boldsymbol{X}}$ are thus constant values and the matrix has the form

$$C_{\boldsymbol{X}} = \begin{bmatrix} a & b & c & 0 & \cdots \\ b & a & b & c & \ddots \\ c & b & \ddots & \ddots & \ddots \\ 0 & c & \ddots & \ddots & \ddots \\ \vdots & \ddots & \ddots & \ddots & \ddots \end{bmatrix} \tag{4.12}$$

Finally, an experimental set of 2052 measurements collected by an optical system on the $LN1$ line between the cities of Paris and Lyon lead the following coefficients:

$$a = 3.88e^{-4} \qquad b = 3.23e^{-4} \qquad c = 3.06e^{-4} \tag{4.13}$$

From the covariance matrix $C_{\boldsymbol{X}}$, the singular values σ_1^2, σ_2^2 and σ_3^2 can be computed. These values can be used to define the *p.d.f.* of the distribution in the frame (s_1, s_2, s_3) where s_i are independently distributed [86],

$$p.d.f.\ (s_1, s_2, s_3) = \frac{1}{2\pi^{3/2}\sqrt{det(C_{\boldsymbol{X}})}} exp\left(-\frac{s_1^2}{2\sigma_1^2} - \frac{s_2^2}{2\sigma_2^2} - \frac{s_3^2}{2\sigma_3^2}\right) \tag{4.14}$$

and thus the equations of iso-probability contours of the multivariate Gaussian distribution are equations of an ellipsoid,

$$\left(\frac{s_1}{\sigma_1}\right)^2 + \left(\frac{s_2}{\sigma_2}\right)^2 + \left(\frac{s_3}{\sigma_3}\right)^2 = c. \tag{4.15}$$

This sum of squared independent Gaussian distributions is known to be a Chi-Square distribution and the threshold c needed to have 99% of the distribution inside the ellipsoid can thus be determined from Chi-Square tables leading to $c = 11.345$. Figure 4.22 shows the confidence region associated with probability level 99% back in the frame of height variations dh_i.

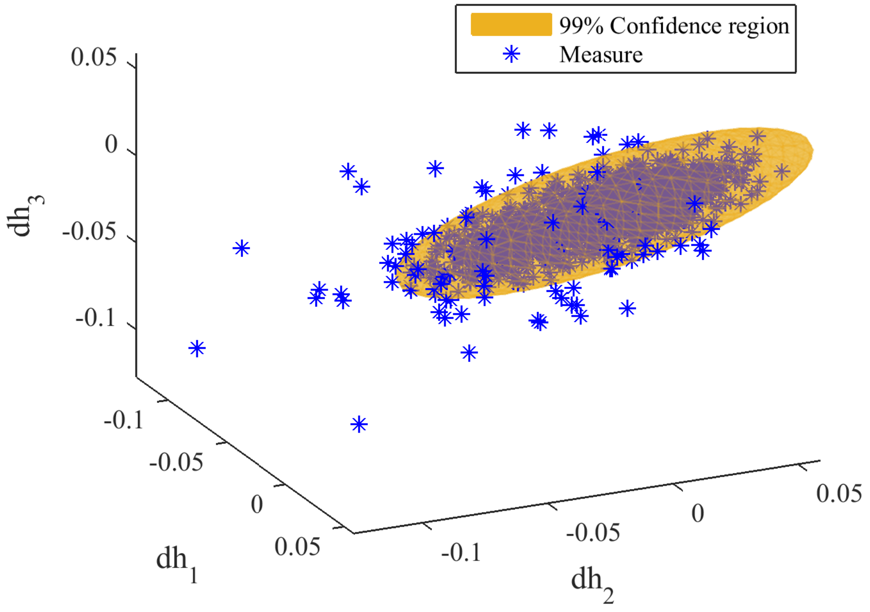

Figure 4.22: Confidence region associated with probability level 0.99% (yellow) compared with measurements (blue) of three consecutive variations of MW height at mast

Previously, the distance between contact wire and messenger wire at masts ΔH_{mast} was fixed, which is not the case. In the full catenary model, this value is not defined and depends on other parameters. It appears that leaving ΔH_{mast} to its nominal value and letting every other parameters vary leads to a standard deviation of ΔH_{mast} of $8mm$ which is approximately the same variability found previously. This parameter can thus be removed from the list of input parameters. Finally, retained input parameters variabilities can be summarized in the table 4.5.

Table 4.5: Input parameters variability

Parameter	T_{MW}	T_{CW}	$\boldsymbol{L_{drop}}$	$\boldsymbol{H_{MW,Mast}}$
Distribution	Gaussian	Gaussian	Gaussian	Multivariate Gaussian
σ	$1000N$	$1000N$	$7mm$	matrix $C_{\boldsymbol{X}}$ (4.12)

Chapter 5

Sensitivity analysis on outputs

All the relevant sources of variability linked with the catenary have been statistically characterized in chapter 4. The next step is to propagate this uncertainty in the model and observe the impact of input parameter variabilities output quantities of interest. Section 5.1 thus develops numerical criteria associated with outputs. In particular geometric criteria currently monitored in maintenance, and dynamic criteria relevant to qualify current collection quality. Section 5.2 then exposes the Sobol analysis method used for ranking sources and its results. Section 5.3 then considers the correlation between geometric and dynamic output criteria. Finally, section 5.4 addresses direct dependencies of dynamic output criteria to input parameters.

5.1 Output criteria on geometry and dynamics

Two types of criteria are defined: geometric and dynamic ones. Geometry criteria are deduced from the contact wire height and supposed to be measurable using existing vehicles. The basic objectives that are used in maintenance policy are limits on contact wire height H_{CW} and limits on slope between two consecutive masts (i.e. along a span), $\Delta H_{CW,Span}$ [3]. Dynamic criteria are used to qualify the current collection quality. The only mechanical criterion commonly used for certification [2] is the coefficient of variation of the $20Hz$-filtered contact force, which is defined as its standard deviation divided by its mean, $(\sigma/F_m)_{20Hz}$. In addition, the uplift at steady arms $Uplift$ is also controlled for security purposes. If uplifts are too high, there are indeed risks that the pantograph bow could hit the cantilever of the steady arm.

To these classical dynamic criteria, two new criteria were added, namely the $max(\sigma/F_m)_{mov}$ developed in section 5.1.1, and a mechanical equivalent to the French electric criterion NQ, developed in section 5.1.2. Other geometric criteria that could be relevant to check are added and the full list of selected output criteria is detailed in section 5.1.3.

5.1.1 Moving σ/F_m

The σ/Fm criterion given by standards is computed on a $20Hz$-filtered signal. Modifications of catenary damping and contact stiffness in chapter 3 have shown that the medium frequency range also contains significant energy and that the lack of knowledge on contact stiffness currently limits the filtering frequency to $70Hz$. Figure 5.1 shows the contact force along a span filtered at $20Hz$ and $70Hz$. Signals are significantly different and the corresponding σ/Fm criterion is equal to 0.24 at $20Hz$ and

0.34 at $70Hz$. The standard deviation is indeed reduced when filtering to lower frequencies as observed on the right figure where the distribution is narrower around the mean value, while the most important part is the distribution tail. Even if the contact force followed a normal distribution, using the σ/Fm criterion on a $20Hz$-filtered signal and supposing that there is less than 0.1% of probability to have a force of less than $Fm - 3\sigma$ would be very coarse. As the dynamic behaviour at higher frequencies was not yet known, this filtering was the only option. But it now seems more legitimate to study the signal filtered at the new frequency limit of $70Hz$.

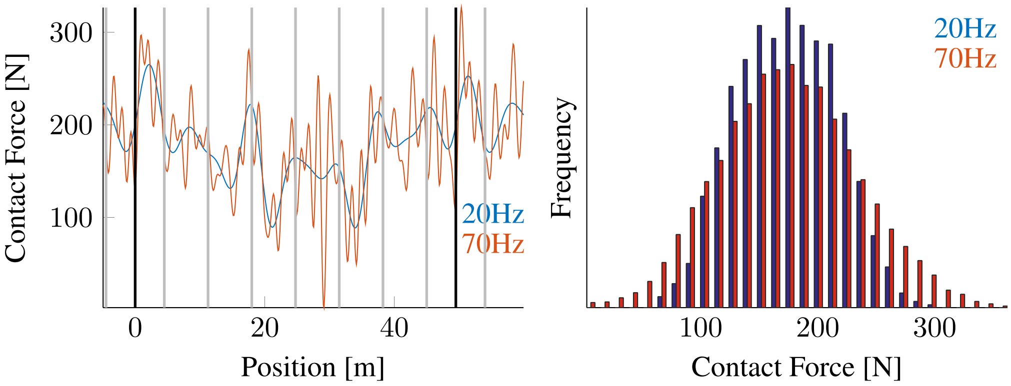

Figure 5.1: $20Hz$ (blue) and $70Hz$ (red) filtered contact force (left) and corresponding histograms (right)

The usual σ/Fm criterion is a global quantity that can potentially hide local phenomena. It is thus a good criterion to compare two pantographs running under a catenary, but not to detect defaults in the catenary. For instance, if a claw is added in a section, the local contact loss that often appears will have a small impact on the σ/Fm value computed over the whole section. To solve this issue, this quantity can be computed locally. Moving the window in which σ/Fm is computed leads to a new time signal, smoothed compared to the contact force F_c. For a very small window, this criterion has exactly the variations of contact force.

Simulations over a full section of $1300m$ length were computed with a clean regular section and the same section with $1kg$ masses added at the first and third droppers of the span starting at $805m$. Figure 5.2 shows the contact force (top) and the $Moving(\sigma/F_m)$ (bottom) over the modified and surrounding spans. When computed over the full section, the σ/Fm criterion is exactly the same in both cases, namely 0.202. The $20Hz$ low pass filtering of the contact force also completely hides the perturbation observed when filtering at $70Hz$, whereas the $Moving(\sigma/F_m)$ criterion clearly detects the perturbed zone despite acting as a low-pass filter [88]. This new criterion can thus be a good indicator to localise catenary issues at the scale of the span. The intermediate spatial length thus avoids averaging of σ/F_m and local fluctuations of contact force. Nevertheless, this criterion is again a time-signal and cannot be compared directly between different configurations. The maximum of this signal, $max(\sigma/F_m)_{mov}$, will thus be taken later.

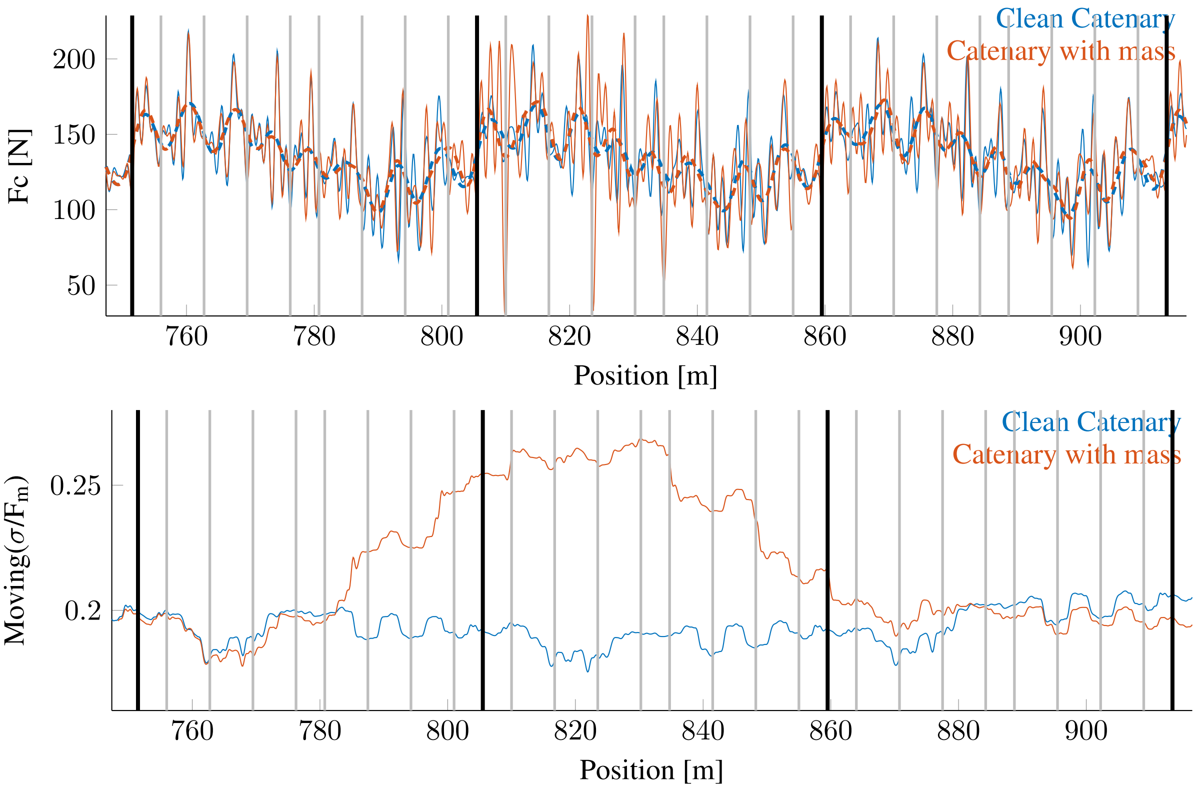

Figure 5.2: $20Hz$ (dashed thick) and $70Hz$ (solid thin) filtered contact forces for a clean catenary (blue) and a catenary with added masses (red) and corresponding $Moving(\sigma/F_m)$ computed on the $70Hz$ filtered contact force over $50m$.

5.1.2 Mechanical equivalent to "NQ"

The "non quality" NQ is a common criterion used in French certification procedures to asses the current collection quality [28] and it has been detailed in section 1.1.3. This electrical criterion is not equivalent to the mechanical $(\sigma/F_m)_{20Hz}$ criterion given by standards since no localisation in the section is given by the mechanical criterion. This section thus aims, using available measurements, to build a mechanical criterion NQ_{meca} equivalent to the electric one.

Contact force is usually measured only for train or catenary certification. The collected signal is thus recorded only after being low pass filtered at $20Hz$. Arcs, which are usually shorter than $10ms$ or at frequencies higher than $100Hz$ can thus hardly be compared with these filtered contact forces. Moreover, as only one of the criteria has to be used for certification, mechanical and electrical data are rarely collected simultaneously.

However, the tests for certification of the VelaroD were used to collect optical and mechanical measurements simultaneously. Three sections of $120s$ at a running speed of $300km/h$ were available in a configuration generating a particularly high quantity of arcing, which might not be representative of the common current collection.

The pantograph used is a CX with a bow composed of two independent bands (see figures 1.6 and 1.7 in section 1.1.2 for pictures). The contact force is thus a composition of four force measurements, at each left and right small plungers of front and rear bands, corrected by inertia forces estimated using accelerations.

The raw contact force is displayed on the left of figure 5.3. The force is sometimes negative, which is physically impossible. The error mainly comes from the bow bending mode which is not taken into account when summing forces. The left figure shows that the position of the contact wire on the bow can be guessed. When the difference is highest between the left and right forces, the contact wire is on the side where the force is the highest.

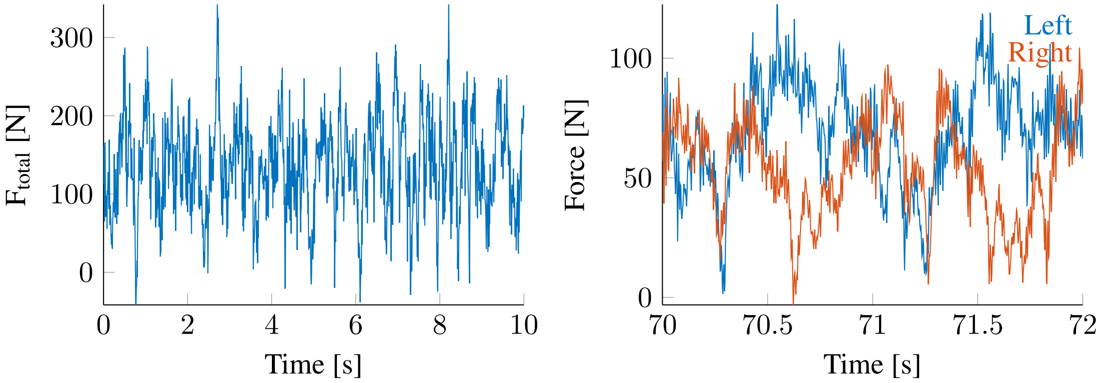

Figure 5.3: Sum of all forces (left), cumulated forces on the left (blue) and right (red) of the bow (right)

Figure 5.4 shows the total front and rear forces at high frequency. The front band seems more solicited than the rear one. This is confirmed by the amplitude of spectrum displayed on the right. For both, a resonance appears around $100Hz$. As detailed in section 3.1 there is a doubt on whether this can be attributed to bow bending or contact stiffness resonance.

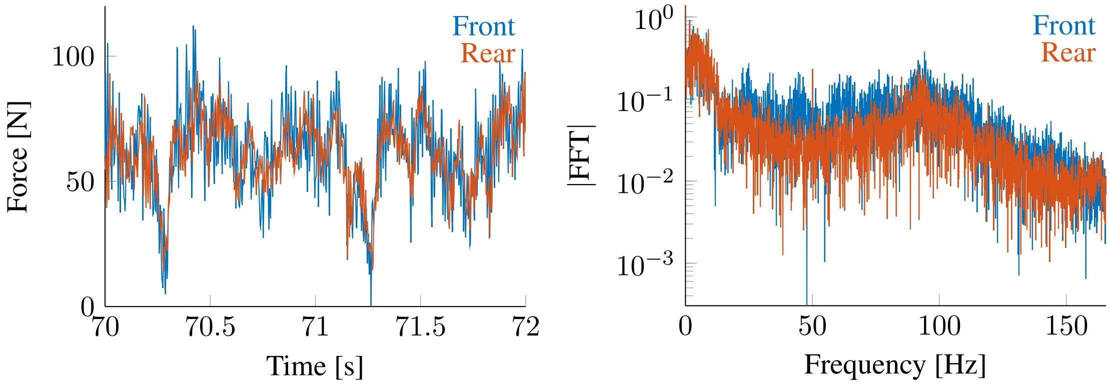

Figure 5.4: Cumulated forces (left) and their amplitude spectrum (right) of the front (blue) and rear (red) contact band

Figure 5.5 shows measured arcs and I the electric current consumed. When I is low, arcs do not appear but pantograph-catenary dynamic interaction is not necessarily better. Standards fix the minimum value $I_{min} = 120A$, representing 30% of the maximum current to avoid taking into account sections where the method cannot assess the interaction quality. The right figure shows the arc rate as a function of the selected threshold I_{mini}. A threshold of $150A$ will be selected to avoid missing detections, in particular for the first measurement (solid).

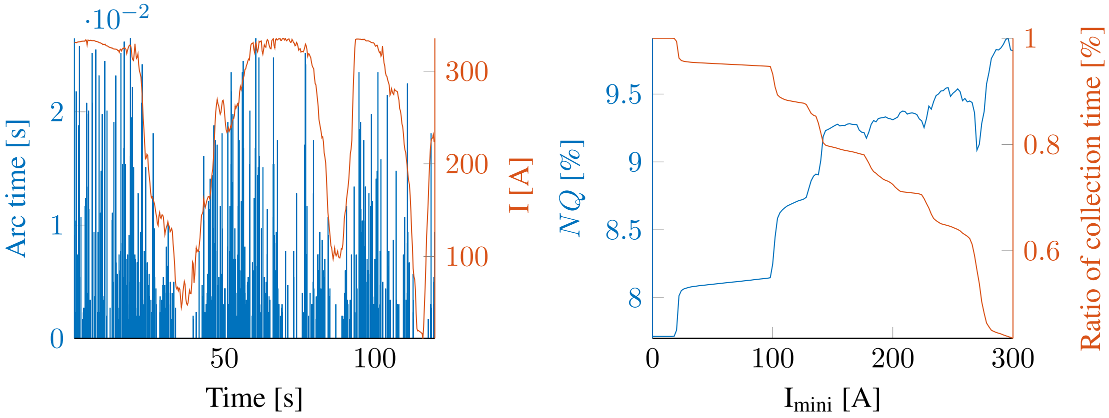

Figure 5.5: Arc time and current collected as a function of time (left), NQ and ratio of collection time as a function of I_{min} (right)

A mechanical equivalent to the NQ can be introduced by making the hypothesis that an optically measurable arc is created when the contact force is below a threshold F_{crit} for a time dt_{min}. The current instrumentation can detect arcs of $1ms$ and standards take into account only arcs of more than $5ms$. Both thresholds are thus kept. Figure 5.6 shows this equivalent, NQ_{meca} computed for different frequencies, thresholds and minimum arcing time. Under $80Hz$, there is no difference between the selected t_{min}, there is a transition zone between $80Hz$ and $120Hz$ after which there is no evolution of NQ_{meca} with frequency. This figure shows that filtering under $120Hz$ introduces a bias in the evaluation of NQ_{meca}. The left figure shows that a threshold F_{min} fixed at $45N$ gives good results for both selected t_{min}.

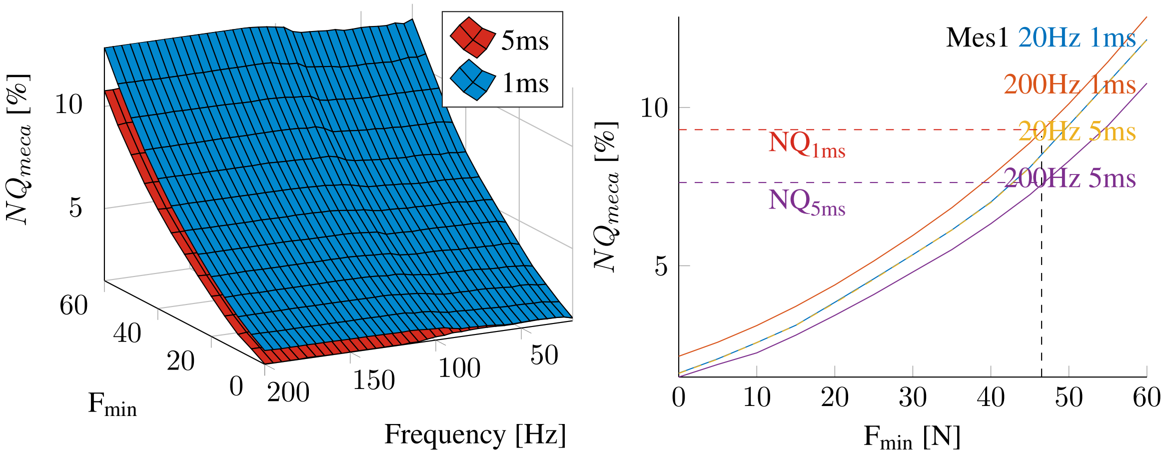

Figure 5.6: NQ_{meca} as a function of F_{min} and filtering frequency for two different t_{min} (left), comparison with the electrical criterion NQ computed for the corresponding thresholds t_{min} (right)

Figure 5.7 shows the resulting F_{min} found using the two other measurements. Despite of the significantly different current collection quality, the equivalent NQ_{meca} is always found for F_{min} between $45N$ and $50N$.

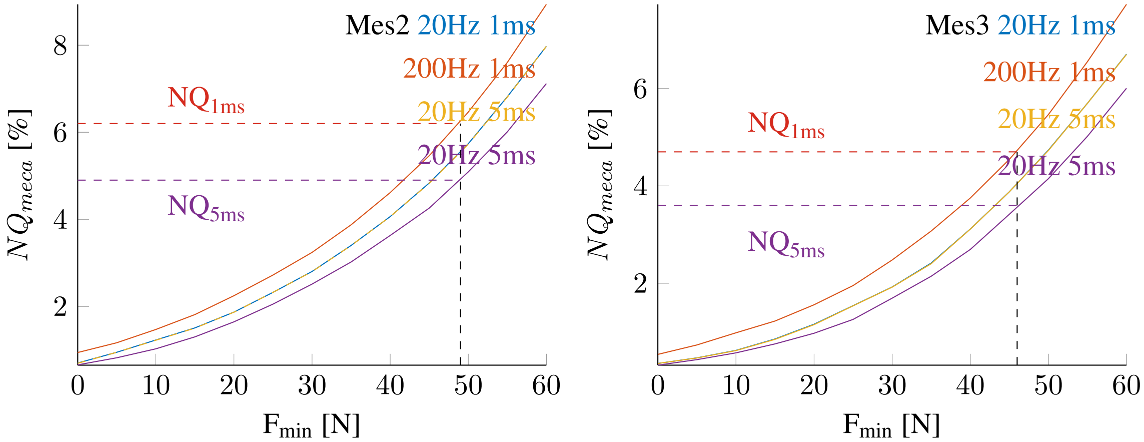

Figure 5.7: Comparison of NQ_{meca} with electrical criterion NQ computed for the corresponding thresholds t_{min} for two other measurements

Figure 5.8 shows the time and length of arcs detected mechanically and electrically. Mechanical criterion (red) detect arcs at good positions. The longer period of mechanically found arcs comes from the fact that an electric arc cannot last more than $25ms$ due to the current frequency of $50Hz$. The cumulative time of multiple local arcs usually is generally equivalent to the long arc found mechanically.

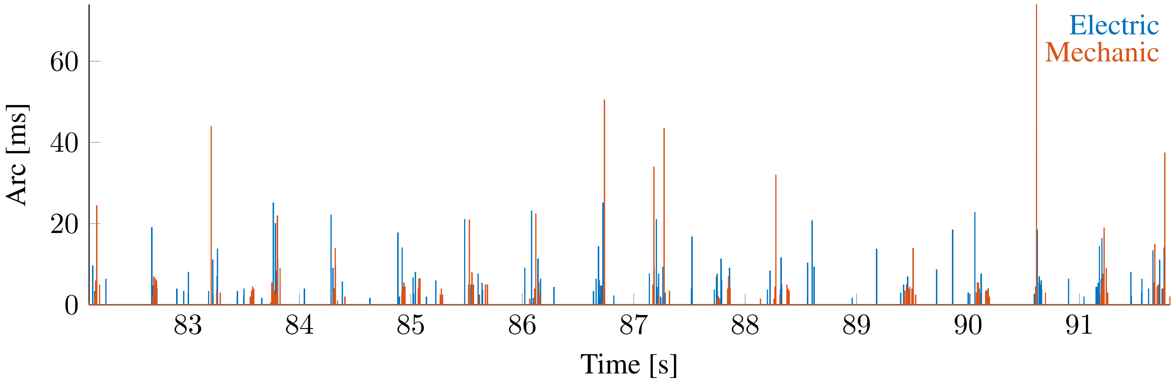

Figure 5.8: Arc time detected by mechanical (red) and electrical (blue) methods

There are nevertheless some cases where an arc is detected only mechanically or electrically. The most common of such cases is displayed in figure 5.9. The CW is on the right side and the right force is over the defined F_{crit} but the left force is evaluated to a negative value and skews the total force.

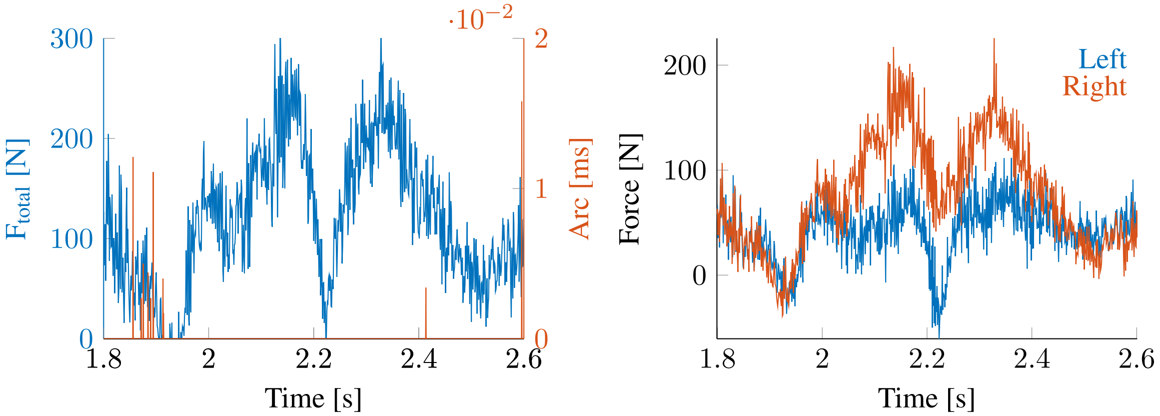

Figure 5.9: Arc detected mechanically and not electrically when CW is on the right side of the contact band

Figure 5.10 shows a second case where an arc should appear when the CW is placed in the middle of the contact band. The total force F_{total} goes under the threshold $F_{min} = 45N$ for a short time at $2.8s$. This corresponds to the first bending mode of the bow which is not taken into account when summing forces.

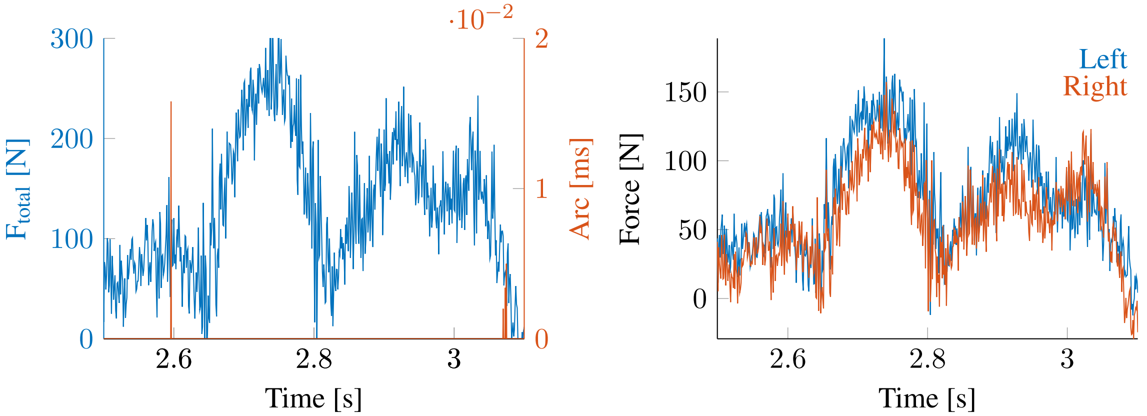

Figure 5.10: Arc detected mechanically and not electrically when CW is in the middle of the contact band

Despite the particularity of the pantograph which might not be representative to those currently used on the French railway network, a good agreement has been found between the mechanical and electrical criteria. The localisation and time duration of arcs fit quite well and a number of exceptions were explained.

This criterion is not equivalent to the usual σ/F_m criterion even if bad current collection quality is usually detected by both criteria. A parametric study of dynamic simulations varying the messenger wire tension T_{MW} underlines this difference. Figure 5.11 shows these two criteria computed for tensions varying between $14kN$ and $22kN$. Both criteria are regularly consistent, they detect a bad current collection quality at $T_{MW} = 14kN$ or $19N$ and good current collection at $T_{MW} = 17.75kN$. But in the case of $T_{MW} = 20.3kN$, results are different, NQ says that current collection is good whereas σ/F_m is more mitigated.

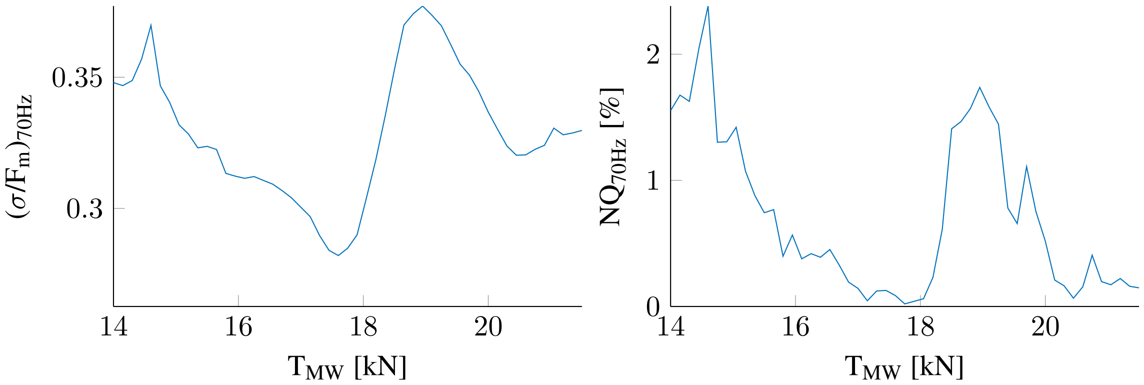

Figure 5.11: $(\sigma/F_m)_{70Hz}$ (left) and NQ_{70Hz} (right) as a function of T_{MW}

Figure 5.12 shows the contact force computed along a span for these three different tensions. The contact force at $20.3kN$ seems as good as that at $17.75kN$ and the NQ_{meca} criterion thus seems more relevant in this case.

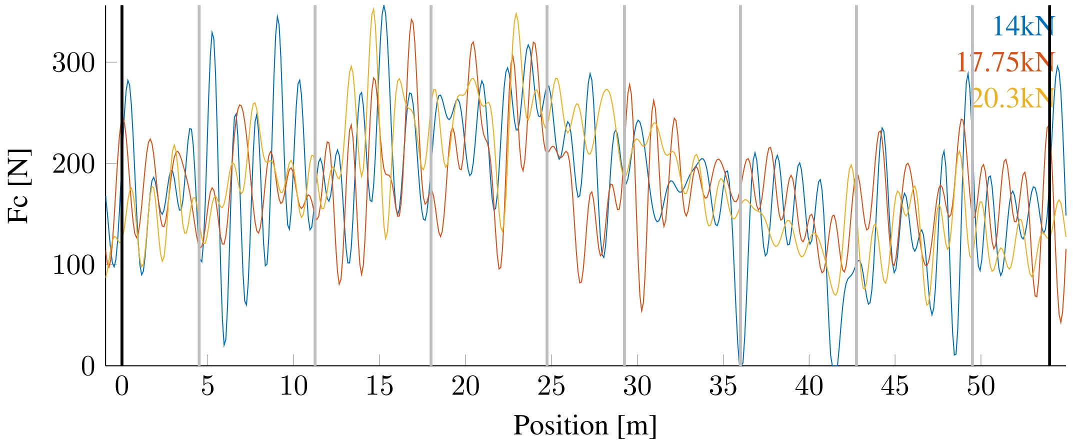

Figure 5.12: Contact force along a span for $T_{MW} = 14, 17.7$ and $20.3kN$

5.1.3 List of output criteria

While $(\sigma/F_m)_{20Hz}$ is a scalar value for a given simulation, H_{CW} and $\Delta H_{CW,Span}$ are vectors. As only scalars are possible for Sobol analysis that will be considered next, these dimensions are converted to scalars, taking for example their maxima or their standard deviation. Thus, H_{CW} is observed as $max(H_{CW})$, $min(H_{CW})$ and $\sigma(H_{CW})$ which could give different information. For a correspondence with maintenance guidelines, threshold overruns are also observed as criteria, which will be denoted, for example with the contact wire height, as $H_{CW} > 5.12m$.

In addition to these classical dimensions, several other that are believed to be relevant [56] are introduced here. The following dimensions are thus observed:

- the difference of span slope at one mast: $\Delta^2 H_{CW,Span}$

- the sag inside a span: Sag
- the slope between the steady arm and the first dropper and between the last dropper of a span and the steady arm: $\Delta H_{CW,Drop}$
- break of slope between $\Delta H_{CW,Drop}$ before and after the mast at mast: $\Delta^2 H_{CW,Drop,Mast}$
- break of slope at droppers before and after masts considering the slope between the closest surrounding dropper or mast
  $\Delta^2 H_{CW,Drop,Drop}$
- NQ_{meca} with a threshold fixed to $80N$ because the pantograph has a good dynamic behaviour for the velocity $v_{panto} = 80m/s$ chosen. Threshold has thus to be increased for NQ_{meca} not to be null.
- $max(\sigma/F_m)_{mov}$, the maximum of coefficient of variation of the contact force computed over $50m$ along the catenary.

Finally, all dynamic criteria are also computed for a $70Hz$-filtered contact force as it is assumed that a significant amount of information is lost if filtering at $20Hz$. OSCAR, the simulation tool used here, is only validated until $20Hz$ by the standards [34], but results are believed to be reliable at much higher frequencies. Table 5.1 summarizes all the selected criteria.

Table 5.1: Geometric and Dynamic criteria

min, max and σ of	
H_{CW}	contact wire height
$\Delta H_{CW,Span}$	slope between two consecutive masts
$\Delta^2 H_{CW,Span}$	difference of slope between two consecutive masts, at a mast
Sag	sag in a span
$\Delta H_{CW,Drop}$	slope between the CW height at steady arm and at the first dropper and between the one at the last dropper of a span and at the steady arm
$\Delta^2 H_{CW,Drop,Mast}$	break of slope between $\Delta H_{CW,Drop}$ before and after the mast at mast
$\Delta^2 H_{CW,Drop,Drop}$	break of slope at droppers before and after masts considering the slope between the closest surrounding dropper or mast
$H_{CW} > 5.12m$	Proportion of H_{CW} over $5.12m$
$H_{CW} < 5m$	Proportion of H_{CW} under $5m$
$\Delta H_{CW,Span} > 4cm$	Proportion of $\Delta H_{CW,Span}$ over $4cm$
$\Delta H_{CW,Span} < -4cm$	Proportion of $\Delta H_{CW,Span}$ under $-4cm$
$\Delta^2 H_{CW,Span} > 4cm$	Proportion of $\Delta^2 H_{CW,Span}$ over $4cm$
$\Delta^2 H_{CW,Span} < -4cm$	Proportion of $\Delta^2 H_{CW,Span}$ under $-4cm$
$Sag > 0.7mm/m$	Proportion of Sag over $0.7mm/m$
$\Delta H_{CW,Drop} > 0.2cm$	Proportion of $\Delta H_{CW,Drop}$ over $0.2cm$
$\Delta H_{CW,Drop} < -0.2cm$	Proportion of $\Delta H_{CW,Drop}$ under $-0.2cm$
$\Delta^2 H_{CW,Drop,Mast} > 0$	Proportion of $\Delta^2 H_{CW,Drop,Mast}$ over $0cm/m$

$\Delta^2 H_{CW,Drop,Mast} < -0.05$	Proportion of $\Delta^2 H_{CW,Drop,Mast}$ under $-0.05cm/m$
$\Delta^2 H_{CW,Drop,Drop} > 0$	Proportion of $\Delta^2 H_{CW,Drop,Drop}$ over $0cm/m$
$\Delta^2 H_{CW,Drop,Drop} < -0.4$	Proportion of $\Delta^2 H_{CW,Drop,Drop}$ over $-0.4cm/m$

$(F_{min})_{20Hz}$	minimum $20Hz$-filtered contact force
$(F_{max})_{20Hz}$	maximum $20Hz$-filtered contact force
$(\sigma/F_m)_{20Hz}$	coefficient of variation of $20Hz$-filtered contact force
$max(\sigma/F_m)_{mov,20Hz}$	maximum of coefficient of variation of $20Hz$-filtered contact force computed over $50m$ along the catenary
$(NQ)_{20Hz}$	proportion of time during which $20Hz$-filtered contact force is under $40N$, if the period is longer than $5ms$
$(F_{min})_{70Hz}$	minimum $70Hz$-filtered contact force
$(F_{max})_{70Hz}$	maximum $70Hz$-filtered contact force
$(\sigma/F_m)_{70Hz}$	coefficient of variation of $70Hz$-filtered contact force
$max(\sigma/F_m)_{mov,70Hz}$	maximum of coefficient of variation of $70Hz$-filtered contact force computed over $50m$ along the catenary
$(NQ)_{70Hz}$	proportion of time during which $70Hz$-filtered contact force is under $80N$, if the period is longer than $5ms$
$max(Uplift)$	maximum uplift at steady arm

5.2 Sobol sensitivity analysis

The simple local sensitivity analysis, consisting in varying parameters one at a time by a small amount around a nominal value, was used in sections 4.1 and 1.3 to quickly eliminate some parameters from the study. The remaining parameters being fully statistically defined, a global sensitivity analysis method is needed. The objective is to let all parameters vary simultaneously over their entire feasible space in order to assess the effects on the output of both individual variables/parameters and interactions between them.

Section 5.2.1 develops the general method of Sobol indices and section 5.2.2 discusses results.

5.2.1 Principles and method selection

Global sensitivity analysis using Sobol indices is based on a decomposition of the variance. The model is viewed as a black-box represented by a function $Y(\boldsymbol{X})$ where $\boldsymbol{X}$ is the random input vector, $\boldsymbol{X} = (T_{MW}, T_{CW}, \boldsymbol{L_{drop}}, \boldsymbol{H_{MW,Mast}})$ and Y an univariate output. Sobol indices are computed separately for each criteria defined in section 5.1.

First order indices $S_{1,i}$ and total-effect indices $S_{T,i}$ are defined by [12, 13]

$$S_{1,i} = \frac{Var_{X_i}(E_{X,\sim i}(Y|X_i))}{Var(Y)}, \tag{5.1}$$

$$S_{T,i} = \frac{E_{X_i}(Var_{X,\sim i}(Y|X_i))}{Var(Y)}, \tag{5.2}$$

where Var is the variance function, E the expectation and $X_{\sim i}$ indicates the set of all input variables except X_i.

The first order Sobol indices $S_{1,i}$ are used to define the sensitivity of an output Y to a parameter X_i alone as a local sensitivity analysis would do. For instance, if the variation of X_i does not impact Y, the expectation $E_{X,\sim i}(Y|X_i))$ is constant when X_i varies and thus, $Var_{X_i}(E_{X,\sim i}(Y|X_i)) = 0$ and $S_{1,i} = 0$. The interactions not being taken into account, the sum of first order indices is bounded,

$$\sum_i S_{1,i} \leq 1. \tag{5.3}$$

Equality to 1 is obtained if the global variation of Y is the sum of those induced by variations of each X_i separately. In this case, the contribution of each parameter is independent of the variation of others and local or global sensitivity analyses give the same results.

Higher order indices can be computed to quantify the sensitivity of Y to an interaction between several parameters. For instance, the second order index of parameters X_i and X_j is given by

$$S_{i,j} = \frac{Var_{X_i,X_j}(E_{X,\sim i}(Y|X_i,X_j))}{Var(Y)}. \tag{5.4}$$

Computing these indices requires a larger number of simulations and they have not been considered in this work.

The total effect index of one parameter X_i corresponds to the variability of Y induced by the variations of X_i and of interactions with every other parameters $X_{j\neq i}$ and can thus be written as

$$S_{T,i} = S_{1,i} + \sum_{j\neq i} S_{i,j} + \sum_{j\neq i\neq k} S_{i,j,k}... + S_{1,...,n}. \tag{5.5}$$

Interactions being taken into account for each total index,

$$\sum_i S_{T,i} \geq 1 \tag{5.6}$$

with equality found again when the model is purely additive. As a result, pie chart representations such as 5.16 will be scaled to 1. The only quantity always representing the total variance [89] is

$$\sum_i S_{1,i} + \sum_i \sum_{j>i} S_{i,j} + ... + S_{1,...,n} = 1. \tag{5.7}$$

The main condition for a proper application of the method is to have independent inputs, which is not the case for the different heights $\boldsymbol{H_{MW,Mast}}$. In that case, the solution of grouping correlated inputs together as proposed by Jacques [90], works well. Moreover, it is more interesting to have the impact of the size $\boldsymbol{H_{MW,Mast}}$ in general than of each span separately. This is also the case of all dropper lengths $\boldsymbol{L_{drop}}$, which are thus also grouped even if they are independently distributed. Besides, reducing the number of group of inputs increases the convergence speed of indices. The random input vector $\boldsymbol{X}$ is thus composed of four groups of parameters,

$$\boldsymbol{X} = [T_{CW}, T_{MW}, \boldsymbol{H_{MW,Mast}}, \boldsymbol{L_{drop}}]. \tag{5.8}$$

The sampling strategy chosen is the simple Monte-Carlo sampling, giving easy control of convergence. The method requires two independent samples A and B of the same random vector $\boldsymbol{X}$, of size N. From these two samples, four mixed samples are defined as follows,

$$\begin{cases} A = [T_{CW}(A), T_{MW}(A), \boldsymbol{H_{MW,Mast}}(A), \boldsymbol{L_{drop}}(A)] \\ B = [T_{CW}(B), T_{MW}(B), \boldsymbol{H_{MW,Mast}}(B), \boldsymbol{L_{drop}}(B)] \\ A_B^1 = [T_{CW}(B), T_{MW}(A), \boldsymbol{H_{MW,Mast}}(A), \boldsymbol{L_{drop}}(A)] \\ A_B^2 = [T_{CW}(A), T_{MW}(B), \boldsymbol{H_{MW,Mast}}(A), \boldsymbol{L_{drop}}(A)] \\ A_B^3 = [T_{CW}(A), T_{MW}(A), \boldsymbol{H_{MW,Mast}}(B), \boldsymbol{L_{drop}}(A)] \\ A_B^4 = [T_{CW}(A), T_{MW}(A), \boldsymbol{H_{MW,Mast}}(A), \boldsymbol{L_{drop}}(B)] \end{cases} \tag{5.9}$$

Sobol indices cannot be computed directly but estimators exist for their approximation. Several estimators of $Var_{X_i}(E_{X,\sim i}(Y|X_i))$ and $E_{X_i}(Var_{X,\sim i}(Y|X_i))$ have been developed mainly by Sobol [12], Homma [13], Satelli [89] and Jansen [91]

$$Var_{X_i}(E_{X,\sim i}(Y|X_i))$$

$$= \frac{1}{N}\sum_{j=1}^{N} Y(A)_j \cdot Y(B_A^i)_j - E(Y)^2 \qquad \text{Sobol} \tag{5.10}$$

$$= \frac{1}{N}\sum_{j=1}^{N} Y(B)_j \cdot \left(Y(A_B^i)_j - Y(A)_j\right) \qquad \text{Satelli} \tag{5.11}$$

$$= Var(Y) - \frac{1}{2N}\sum_{j=1}^{N} \left(Y(B)_j - Y(A_B^i)_j\right)^2 \qquad \text{Jansen} \tag{5.12}$$

and

$$E_{X_i}(Var_{X,\sim i}(Y|X_i))$$

$$= Var(Y) - \frac{1}{N}\sum_{j=1}^{N} Y(A)_j \cdot Y(A_B^i)_j + E(Y)^2 \qquad \text{Homma} \tag{5.13}$$

$$= \frac{1}{N}\sum_{j=1}^{N} Y(A)_j \left(Y(A)_j - Y(A_B^i)_j\right) \qquad \text{Sobol} \tag{5.14}$$

$$= \frac{1}{2N}\sum_{j=1}^{N} \left(Y(A)_j - Y(A_B^i)_j\right)^2 \qquad \text{Jansen} \tag{5.15}$$

The estimation of $E(Y)^2$ in (5.10) and (5.13) and of $Var(Y)$ for the evaluation of $S_{1,i}$ and $S_{t,i}$ is treated by Janon [92] who proposes to replace the usual

$$E(Y)^2 = \left(\overline{Y(A)}\right)^2 = \left(\frac{1}{N}\sum_{j=1}^{N} Y(A)_j\right)^2 \tag{5.16}$$

by taking into account the observation of $Y(A_B^i)$,

$$E(Y)^2 = \left(\frac{\overline{Y(A)} + \overline{Y(A_B^i)}}{2}\right)^2 = \left(\frac{1}{2N}\sum_{j=1}^{N} Y(A)_j + Y(A_B^i)_j\right)^2 \tag{5.17}$$

and similarly, replacing

$$Var(Y) = \frac{1}{N}\sum_{j=1}^{N} Y(A)_j^2 - \overline{Y(A)}^2 \tag{5.18}$$

by

$$Var(Y) = \frac{1}{2N}\sum_{j=1}^{N} \left(Y(A)_j^2 + Y(A_B^i)_j^2\right) - \left(\frac{\overline{Y(A)} + \overline{Y(A_B^i)}}{2}\right)^2 \tag{5.19}$$

Finally, the three estimators of each kind of Sobol sensitivity index kept are those with the numerator defined in equations (5.10) to (5.15) and the denominator defined in equation (5.19). Their convergence speed are compared using the bootstrap method described by Archer [93] or Yang [94]. The principle is to generate a sample of size N with replacement of the set of output, which is also of size N. The Sobol indices can thus be computed from this sub-sample. Repeating the process $B = 1000$ times allows to define 95% confidence intervals from these B values of Sobol indices. Gradually increasing N leads to graphs of convergence. The computation has been stopped at $N = 1000$, which corresponds to 6000 dynamic simulations, after 3 weeks of computation.

Figure 5.13 shows the convergence of two Sobol indices for the NH_{mast} criterion. This criterion is strongly dependent on $H_{MW,Mast}$ and the Jansen estimator is the best for the associated first order Sobol index. For the T_{CW} parameter, the Sobol index is expected to be close to zero and it is observed that the Satelli estimator converges significantly faster. Only the Sobol estimator has problems converging. And it should be reminded that the most interesting indices are those closer to 1.

Based on a selection of similar results it was chosen to retain the Jansen estimator for first order Sobol indices. Its convergence is significantly faster when the link between criterion and parameter is non-linear as observed in figure 5.14 on a dynamic criterion.

Figure 5.15 shows the same analysis on total effect indices. The Homma and Jansen estimators are identical and converge faster than the Sobol estimator. Again, the Jansen estimator of total effect Sobol indices will be kept in the following.

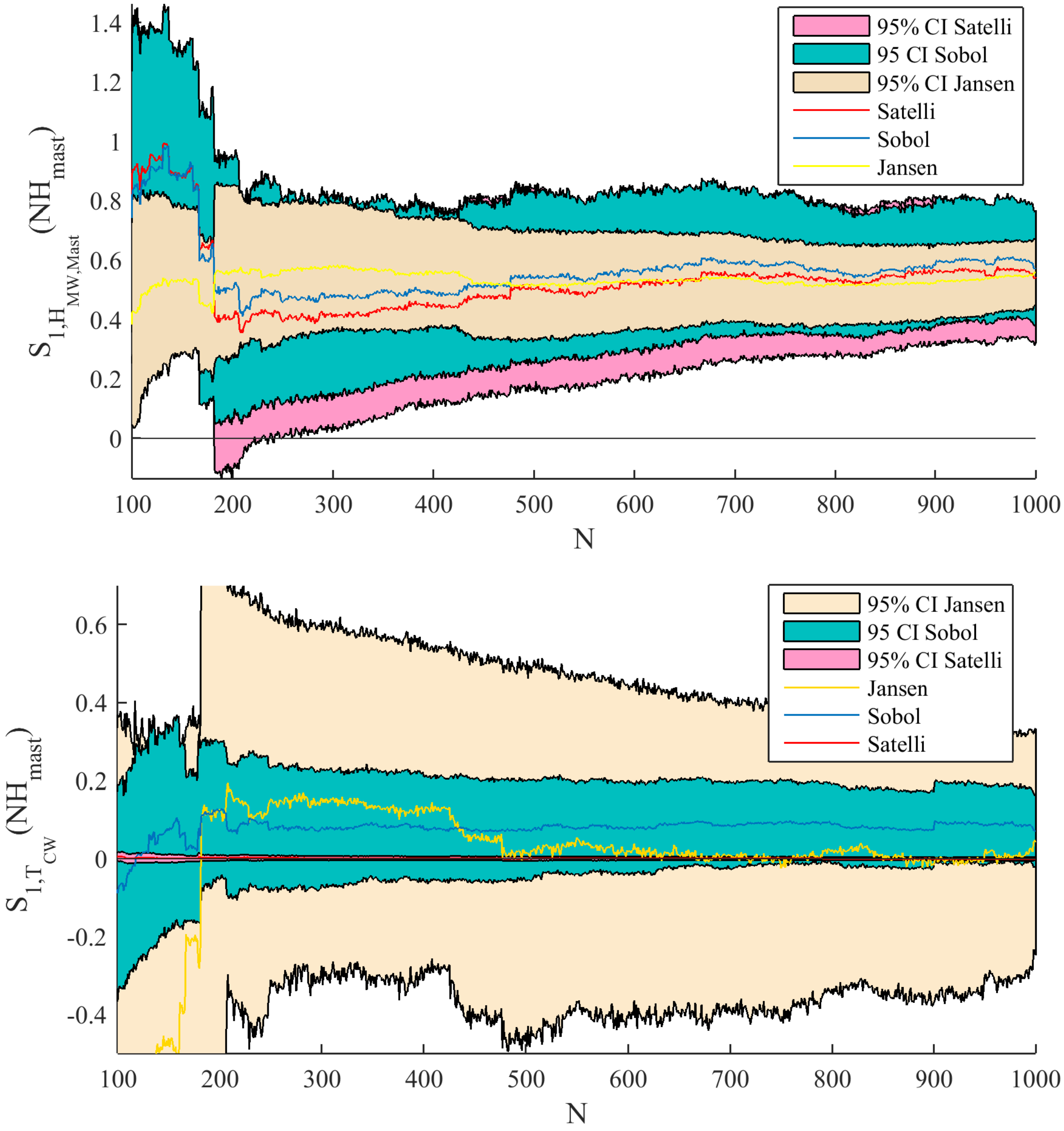

Figure 5.13: Convergence of first order Sobol indices of $H_{MW,Mast}$ (top) and T_{CW} (bottom) on NH_{mast} considering three different estimators and their 95% confidence intervals

More explicitly, the estimations of $S_{1,i}$ and $S_{t,i}$ retained are thus

$$S_{1,i} = 1 - \frac{\frac{1}{2N}\sum_{j=1}^{N}\left(Y(B)_j - Y(A_B^i)_j\right)^2}{\frac{1}{2N}\sum_{j=1}^{N}\left(Y(A)_j^2 + Y(A_B^i)_j^2\right) - \left(\frac{\overline{Y(A)}+\overline{Y(A_B^i)}}{2}\right)^2}, \tag{5.20}$$

$$S_{T,i} = \frac{\frac{1}{2N}\sum_{j=1}^{N}\left(Y(A)_j - Y(A_B^i)_j\right)^2}{\frac{1}{2N}\sum_{j=1}^{N}\left(Y(A)_j^2 + Y(A_B^i)_j^2\right) - \left(\frac{\overline{Y(A)}+\overline{Y(A_B^i)}}{2}\right)^2}. \tag{5.21}$$

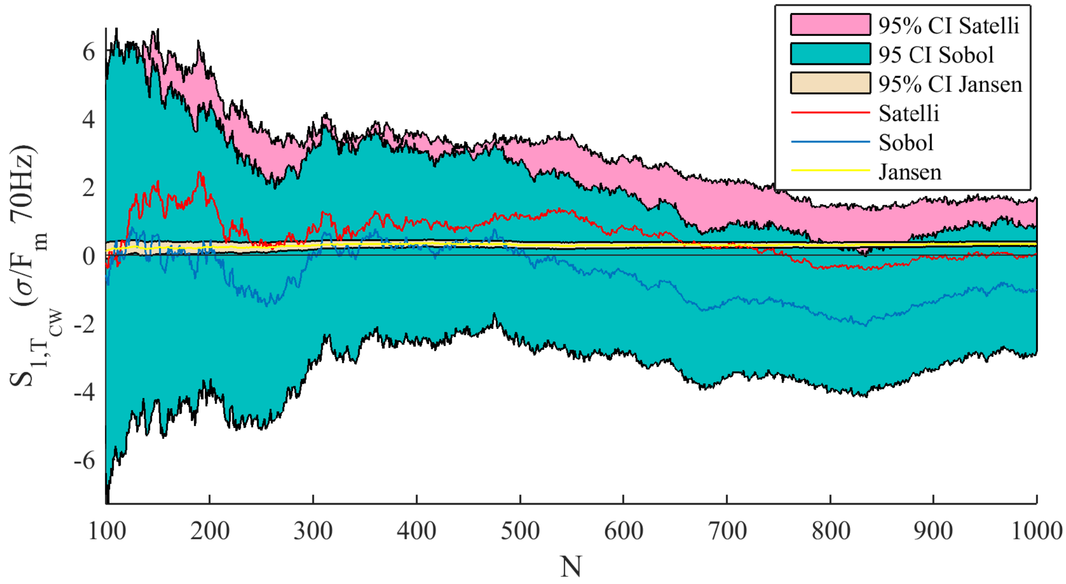

Figure 5.14: Convergence of first order Sobol index of T_{CW} on $\sigma/F_m 70Hz$ considering three different estimators and their 95% confidence intervals

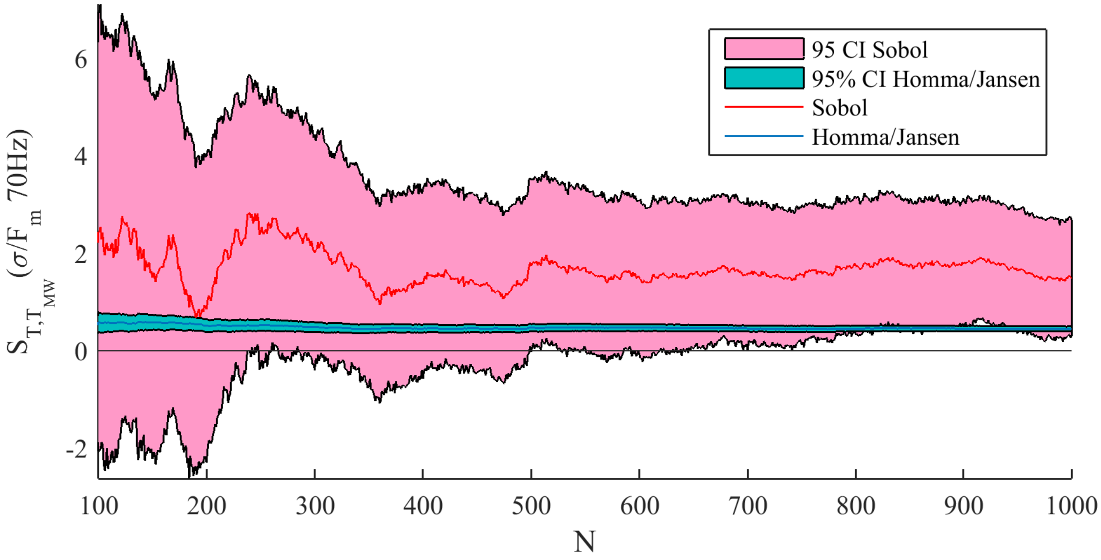

Figure 5.15: Convergence of total effect Sobol index of T_{MW} on $\sigma/F_m 70Hz$ considering three different estimators and their 95% confidence intervals

5.2.2 Results

The objective of this section is to summarize trends found from first order and total effect Sobol indices. The pie charts for all criteria are grouped in E. Simulations were performed using a V350-

type catenary over one existing section of $1.4km$. The velocity of the pantograph was fixed under the nominal velocity of the catenary that is $v_{panto} = 80m/s$. The pantograph used is that of section 2.1.

For several criteria, the sum of first order indices is significantly lower than 1, for instance with $(F_{max})_{20Hz}$ in figure 5.16. This implies that the main part of output criteria variation is due to combined effect of several input parameters. This general trend motivated the use of total order indices instead of local ones.

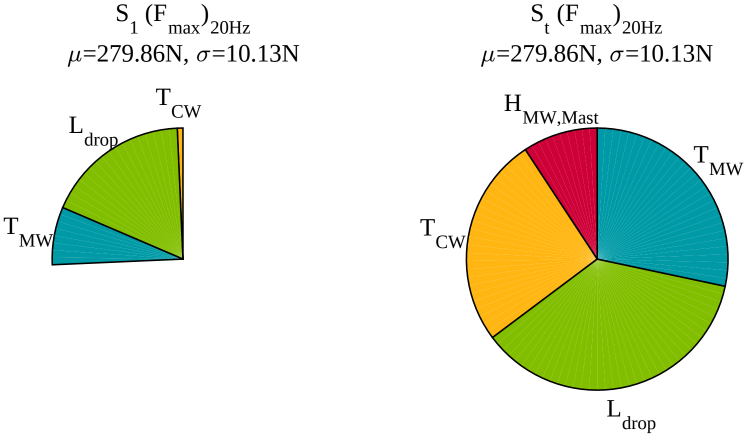

Figure 5.16: First order (left) and total order (right) Sobol indices of the four parameters on $(F_{max})_{20Hz}$

Nevertheless, for many geometric criteria, this sum is close to 1 showing cases where an additive model of uncertainty can be used. In the single case of figure 5.17, the pie corresponding to the total effect indices is significantly different. It is then probable that the concerned criterion has encountered a convergence issue.

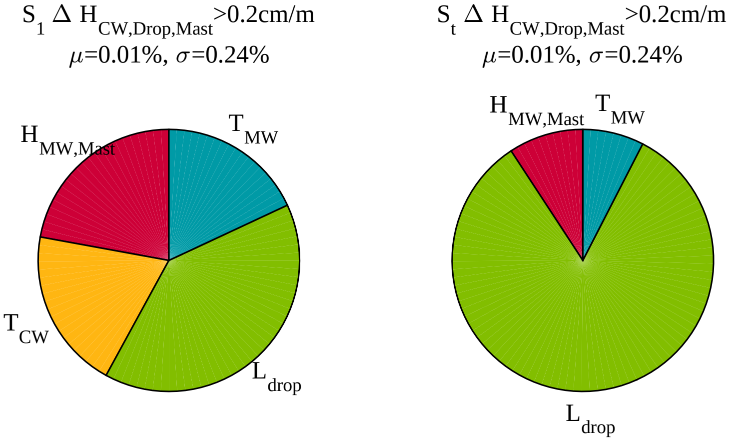

Figure 5.17: First order (left) and total order Sobol indices of the four parameters on $\Delta H_{CW,Drop,Mast} > 0.2cm/m$

Figure 5.18 shows total order indices for a typical geometric criterion. In almost all the currently used geometry criteria, namely $H_{CW,Mast} < 5.04m$, $H_{CW,Mast} > 5.12m$, $\Delta H_{CW,span} > 4cm$, $\Delta H_{CW,Span} < -4cm$, the prominent parameter is $H_{MW,Mast}$. Height of the MW at mast is usually what is changed, when maintenance is performed. The maintenance solution is thus consistent with the geometric criteria.

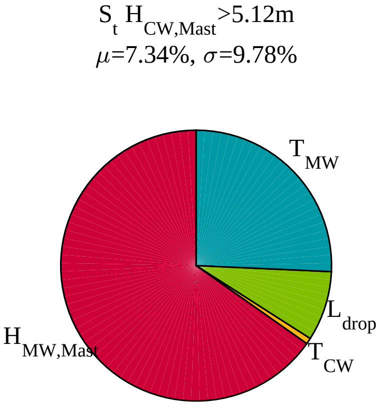

Figure 5.18: Total order Sobol indices of the four parameters on $H_{CW,Mast} > 5.12m$

More local geometric criteria linked to $\Delta H_{CW,Drop,Mast}$ and $\Delta H_{CW,DropDrop}$ are all less sensitive to $H_{MW,Mast}$ but have varying sensitivity to the other parameters. Three criteria, $\sigma(\Delta^2 H_{CW,Drop,Drop})$, $max(\Delta^2 H_{CW,Drop,Mast})$ and Sag_{max}, displayed in figure 5.19, are noticeable since their variability is almost entirely explained by one parameter. They could thus be good criteria to check separately L_{drop}, T_{CW} and T_{MW} respectively. Moreover, the comparison between first order and total effect indices of these three criteria shows that the impact of the main parameter is direct and not mainly due to interactions with others.

First order Sobol indices of dynamic criteria show that their variabilities never follow an additive model of uncertainty.

None of dynamic criteria is sensitive to the $H_{M,Mast}$ parameter. The catenary maintenance policy currently applied thus has no link with current collection quality characterized by dynamic criteria.

Dynamic criteria based on $20Hz$ and $70Hz$ low pass filtered contact force give sensibly the same results. Variations of criteria are always higher when filtering at $70Hz$, showing that a non-negligible part of energy is in the $[20Hz - 70Hz]$ frequency range and that this energy always influences dynamic criteria.

Figure 5.20 shows that the reference global dynamic criterion σ/F_m is mainly sensitive to tensions in cables T_{CW} and T_{MW} even if the impact of messenger wire is due to combined effect with another parameter, probably T_{CW} again.

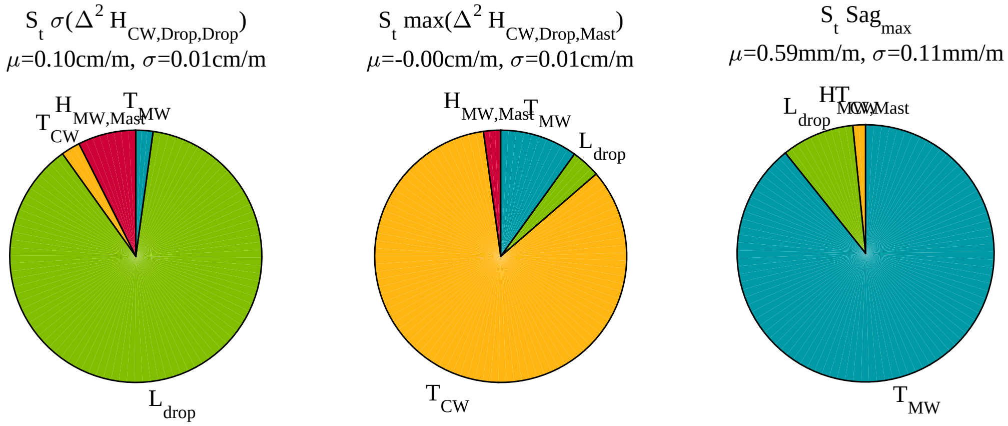

$S_t\ \sigma(\Delta^2 H_{CW,Drop,Drop})$
μ=0.10cm/m, σ=0.01cm/m

$S_t\ max(\Delta^2 H_{CW,Drop,Mast})$
μ=-0.00cm/m, σ=0.01cm/m

$S_t\ Sag_{max}$
μ=0.59mm/m, σ=0.11mm/m

Figure 5.19: Total order Sobol indices of the four parameters on $\sigma(\Delta^2 H_{CW,Drop,Drop})$ (left), $max(\Delta^2 H_{CW,Drop,Mast})$ (center) and Sag_{max} (right)

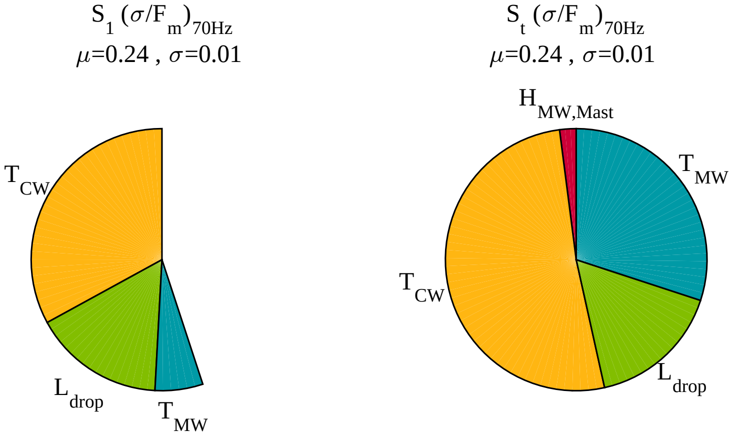

$S_1\ (\sigma/F_m)_{70Hz}$
μ=0.24 , σ=0.01

$S_t\ (\sigma/F_m)_{70Hz}$
μ=0.24 , σ=0.01

Figure 5.20: First order (left) and total order Sobol indices of the four parameters on $(\sigma/F_m)_{70Hz}$

Figure 5.21 shows that more local dynamic criteria such as NQ, $max(\sigma/F_m)_{mov}$ or F_{min} and F_{max} are more sensitive to local accidents induced by L_{drop} than the global σ/F_m shown in figure 5.20, which means that NQ, even if it is computed globally, gives a better representation of the local current collection quality than the global σ/F_m.

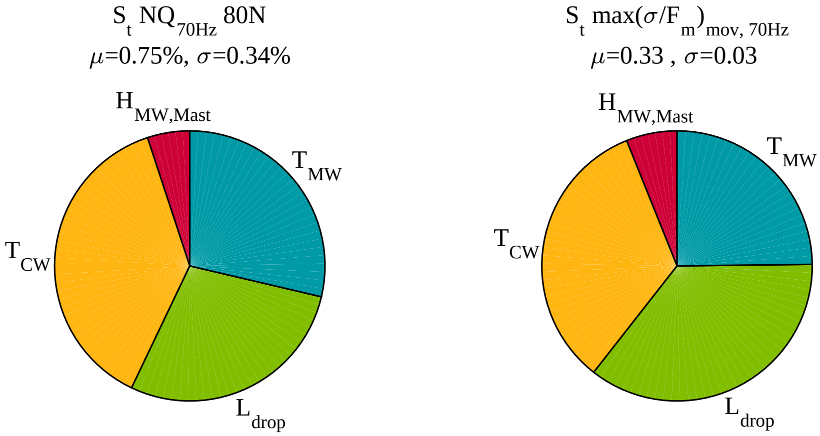

Figure 5.21: Total order Sobol indices of the four parameters on NQ_{70Hz} (left) and $max(\sigma/F_m)_{mov,70Hz}$ (right)

Figure 5.22 shows that the dynamic criterion $max(Uplift)$ has the same repartition of sensitivity to input parameters than other dynamic criteria but its variation is very low. In practice, even if this value can be measured easily directly on the catenary, the value is expected to be more dependent on mean contact force or velocity variation.

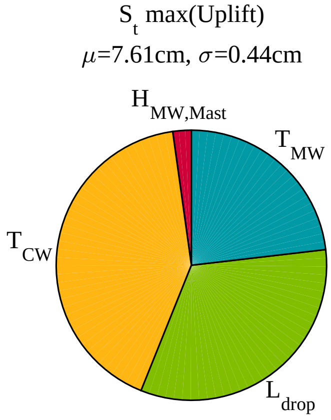

Figure 5.22: Total order Sobol indices of the four parameters on $max(Uplift)$

5.3 Correlation between geometric and dynamic criteria

An interesting objective for maintenance applications is to find a set of geometric criteria that can help assessing the quality of the dynamic interaction. A monotonic relationship between geometric and dynamic criteria is thus needed. The Spearman's rank order correlation, explained in [11] aims to measure the strength of this monotonic relationship.

Table 5.3 shows the most correlated geometric criteria for the four selected dynamic criteria and their correlation coefficients. An absolute coefficient of correlation lower than 0.3 is generally interpreted as very low, which is the case of almost all coefficients. Geometric criteria that have been shown to depend on only one parameter are those better correlated with dynamic criteria. Nevertheless, some correlations are not intuitive as it is the case with Sag_{max}. Collection quality is generally better with a smaller sag and thus dynamic criteria are smaller too, except F_{min}. The opposite trend is thus observed here.

Table 5.2: Spearman correlation coefficients between geometric and dynamic criteria

Dynamic Geometric	$(\sigma/F_m)_{70Hz}$	$max(\sigma/F_m)_{mov,70Hz}$	NQ_{70Hz}	$(F_{min})_{70Hz}$
$max(\Delta^2 H_{CW,Drop,Mast})$	-0.43	-0.42	-0.32	0.03
Sag_{max}	-0.23	-0.31	-0.41	0.35
$\sigma(\Delta^2 H_{CW,Drop,Mast})$	-0.23	-0.27	-0.28	0.20

Figure 5.23 shows the dynamic criteria as a function of their most correlated geometric criteria. The correlation seems poor and it is clear that measuring one of these geometric criteria hardly ensures that current collection quality will be good.

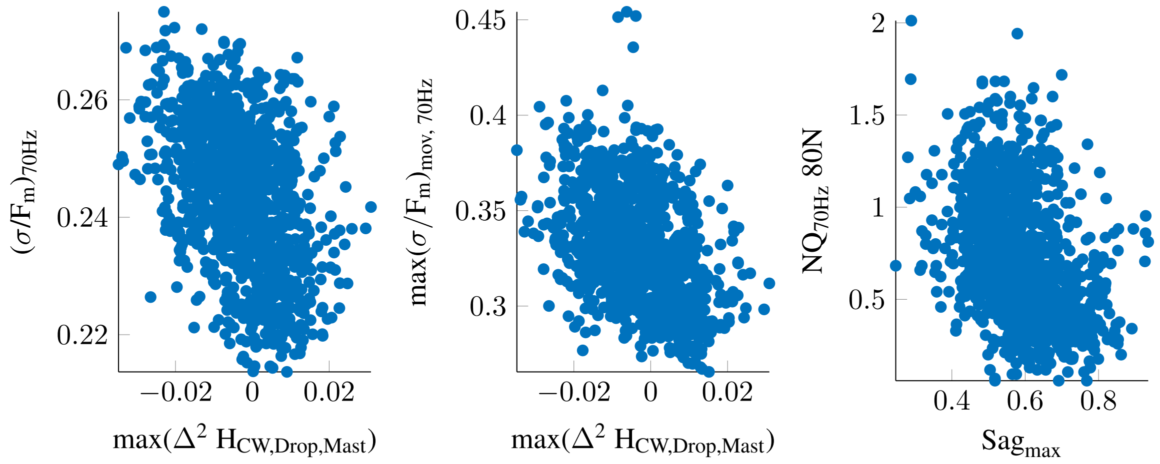

Figure 5.23: Dynamic criteria as a function of their most correlated geometric criteria

A linear combination of geometric criteria can improve the result. A quick optimisation of the linear combination

$$max(\Delta^2 H_{CW,Drop,Mast}) + a \cdot Sag_{max} \tag{5.22}$$

is obtained by maximizing the Spearman correlation coefficient with dynamic criteria for variable a. Figure 5.24 shows that the best correlation is found for the dynamic criterion NQ_{70Hz}. This correlation is still not clear on the left figure.

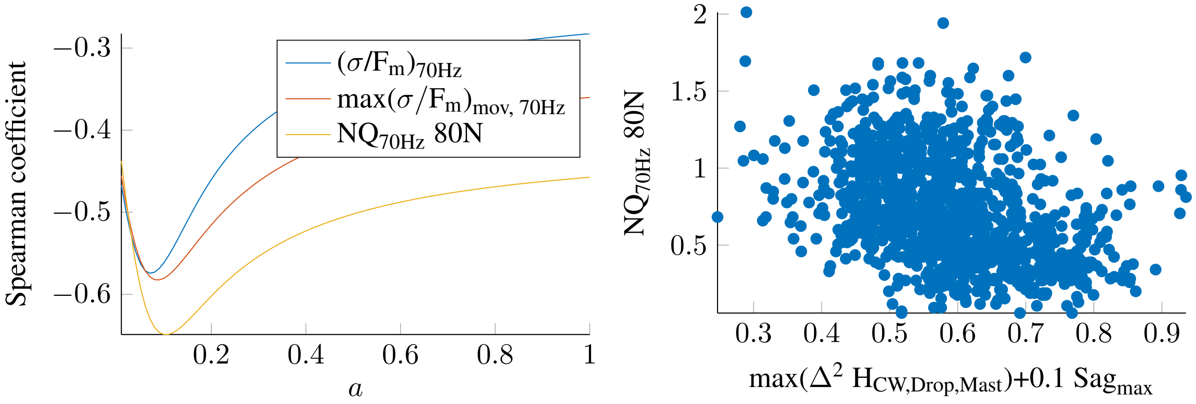

Figure 5.24: Spearman correlation of dynamic criteria as a function of a combination factor a (left), variation of NQ_{70Hz} as a function of the most correlated combination of geometric criteria (right)

None of the exposed geometric criteria can clearly assess the dynamic pantograph-catenary interaction. Maintenance guidelines of the catenary geometry can thus hardly be improved. Thresholds fixed on the catenary geometry only exist for security purpose and cannot be used to guarantee a good current collection quality.

5.4 Dependence of dynamic criteria on input parameters

Dynamic criteria have been shown to be equally sensitive to T_{MW}, T_{CW} and L_{drop}. L_{drop} being a vector linked with local scale of the catenary, a dependency can hardly be found between dynamic criteria and this parameter. Moreover, is not a parameter that changes in time, L_{drop} is thus put aside in this section.

Figure 5.25 shows the variation of $(\sigma/F_m)_{70Hz}$ as a function of tensions. No correlation seems to appear and this is also the case of all other dynamic criteria.

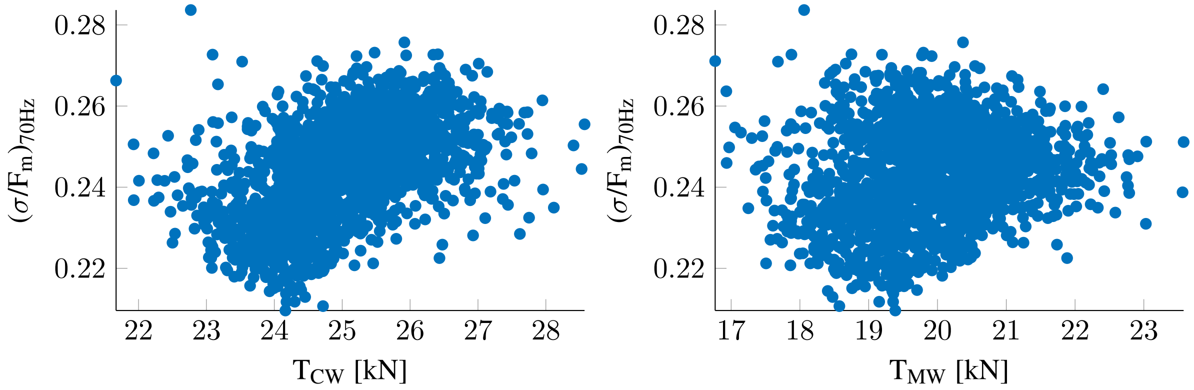

Figure 5.25: Evolution of $(\sigma/F_m)_{70Hz}$ as a function of T_{CW} (left) and T_{MW} (right) when all four parameters vary

Nevertheless, a strong correlation is observed between the global dynamic criterion $(\sigma/F_m)_{70Hz}$ and the sum of tensions, $T_{CW} + T_{MW}$. This correlation shown in figure 5.26 cannot be detected using the correlation coefficient because of its non-monotonic relationship. The observed behaviour is surprising since the dynamic criterion was expected to be monotonically decreasing with tensions increasing. This correlation is less clear on other dynamic criteria which give a more local description of the dynamic interaction.

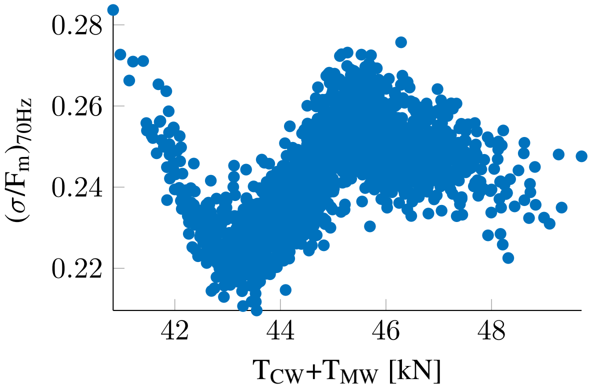

Figure 5.26: Evolution of $(\sigma/F_m)_{70Hz}$ as a function of $T_{CW} + T_{MW}$ when all four parameters vary

Figure 5.27 shows a parametric study where for each value of the sum $T_{CW} + T_{MW}$, four values of T_{CW} and T_{MW} were chosen. The range of values has been extended to $[35 - 55]kN$. It appears that the observed phenomenon is local and happens only around the operating point. This kind of behaviour is certainly the result of coincidences of phenomena studied in chapter 2.

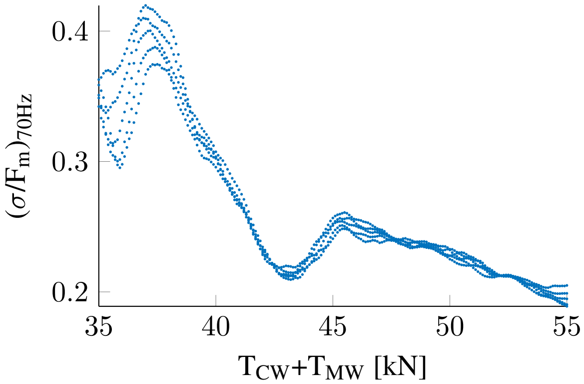

Figure 5.27: Evolution of $(\sigma/F_m)_{70Hz}$ as a function of $T_{CW} + T_{MW}$ with other parameters fixed

Chapter 6

Conclusions and Perspectives

Conclusions

The first set of thesis contributions was related to model validation and physical phenomena understanding.

Starting with the catenary, tests, detailed in chapter 2, were used to confirm the validity of wire models. For messenger wires, the characterisation of wave dispersion showed the influence of voids between yarns. The string model, where bending stiffness is ignored, was shown to be relevant at low frequencies but to induce notable differences in transients. Different cases of wave reflection/transmission were analytically analysed and compared to simulations and measurements. In particular, useful conclusions were drawn:

- a mass placed on the contact wire only induces reflections in medium and high frequencies and thus has only a local impact;
- waves generated at a dropper in the contact and messenger wires offset each other at the next or previous dropper;
- at mast, waves in the messenger wire are fully reflected while reflections on steady arm are negligible. This behaviour confers a high importance to droppers surrounding the mast and to the ratio between dynamic impedances of wires.

Continuing with the dynamic interaction between the pantograph and the catenary, an effort was made to distinguish effects and characteristic frequencies linked with static geometry, wave propagation and modes in the fixed frame associated with the catenary and in the moving frame associated with the pantograph, with a summary given in section 2.3.6.

The coincidence of frequencies or characteristic times were shown to explain most variations in the quantities of interest in particular contact forces and uplift. For instance, if the pantograph velocity v_{panto} is equal to $d_{span} f_{mode}$, then $v_{panto} k_{span} = f_{mode}$ and the current collection quality is significantly improved. Another coincidence is $f_{wave,cat+} = f_{mode}$ which is probably the cause of the local sensitivity of dynamic criteria to the sum of wires mechanical tensions observed in section 5.4. As a result, it can be assessed that the sum of wave velocities in contact and messenger wires is a dimensioning variable of the catenary.

The main epistemic uncertainties linked to model parameters were discussed in chapter 3. The physical contact stiffness value given by the Hertz theory was shown to be relevant. The contact resonance obtained is in the same frequency range than the first bending mode of the bow. Interpreting contact force at frequencies higher than $70Hz$ thus needs to take into account these local flexibilities.

Tests were performed and led to catenary damping values that are significantly lower than the commonly used values for frequencies higher than $5Hz$. These results are compatible with the assumption that energy is only dissipated trough material damping. This implies that the contact force energy in the medium frequency range was significantly under estimated. This poor estimation was in great part due to the fact that standards advise to filter the contact force at $20Hz$. It should be noted that studies led by SDTools have shown that current measurement strategies are actually not compatible with the estimation of contact forces at higher frequencies.

The last epistemic uncertainty considered is linked with the contact wire element size. It was in particular shown that good results in the $[0 - 70Hz]$ frequency range require this element size to be lower than $1m$ for nominal pantograph velocity (typically 300km/h) and even reduced if the velocity decreases.

The second set of thesis contributions was related to uncertainty characterization and derived results. The initial sensitivity analysis presented in section 1.3, addressed catenary geometry, wire wear and aerodynamic loading and was used to motivate the focus of further work on catenary geometry.

In chapter 4, geometry measurements were used to statistically characterize the catenary parameters that influence geometry. The well-posed inverse problem consisting of changing dropper lengths only led to a biased solution. Other input parameters were thus introduced and the ill-posed problem then had to be considered as a statistical inverse problem. Results showed that variations of messenger wire were unexpectedly important for a tension regulated catenary. But later discussions confirmed the plausibility of values obtained through the inverse problem. After having defined parameters that influence the static geometry, the contact wire tension variations were supposed to be similar to the messenger wire ones, because of a lack of information.

These parameter distributions were then used in chapter 5 to perform a sensitivity analysis on geometric and dynamic criteria using Sobol indices. The aim was to find new geometric criteria adapted to dynamic interaction quality that would be more relevant than geometric criteria currently used in maintenance policy. An important conclusion was that no geometric criterion seems well correlated with dynamic ones. Therefore, the only way to ensure a good current collection quality is either to use dynamic measurements or improve the control of mechanical tensions in cables. Nevertheless, maintenance policy on geometry should be kept for security purpose, especially for gauging and sway.

Perspectives

Several observations described in chapter 2 can be taken into account for catenary design. In particular, the reduction of the messenger wire dynamic impedance appeared to greatly improve current collection quality. New shapes or materials for messenger wire that can fulfil the electrical and mechanical requirements that have a smaller linear mass could thus be considered. The wave reflection in the messenger at mast also appeared to have its importance. Current collection could be improved if a way to attenuate the associated wave is found, for instance using a dissipative attachment.

Although, catenaries are usually optimized for a design speed the average exploitation is usual lower. There is thus a trade-off between certification performance at the design speed and average performance at the lower exploitation speed, which may be more relevant in optimizing a maintenance policy. Improvement can also be found in this domain, particularly in the case of multi-pantograph configurations.

The conclusions from the sensitivity analysis have to be extended to other pantographs and multi-pantograph configuration to comfort confidence in their generality. Nevertheless, mechanical tension variations in wires appeared to be high for catenaries that are supposed to be regulated by a tension system. As these variations significantly impact current collection quality, it is interesting to develop a measurement tool that can control these tensions. Moreover, finding the source of this variability and a procedure to reduce it would help future catenary design efforts.

Then, the current methods to measure contact force appeared to be the most blocking point for further development of more adapted dynamic criteria such as NQ_{meca} or for model validations. As a first step, the currently used measurement system could be kept and a more robust estimator, such as a Kalman filter, should be used to obtain valid contact force measurements at higher frequencies. As a second step, revised pantograph instrumentation and force estimation procedures should be investigated.

With improved contact force measurement procedures, measurement trains such as IRIS320, or commercial trains with instrumented pantographs, would provide massive data, as already available for tracks. This would enable tracking of evolutions in time and quantification of other sources of variability. With such data, default detection could become reliable, and dynamic measurements could finally be used for conditional catenary maintenance.

Virtual certification remains an important perspective. The simulations becoming more and more accurate and robust, their use in train certification processes also becomes more legitimate.

Finally, many of the results shown were made possible by the significant performance enhancements of OSCAR and its ability to handle large parametric studies. This work thus illustrates the global shift of computational mechanics from using isolated computations as validations of performance to using large numerical experiments to optimize for performance, maintenance, and robustness to irreducible variabilities.

Appendix A

Test configurations

A.1 Configuration A

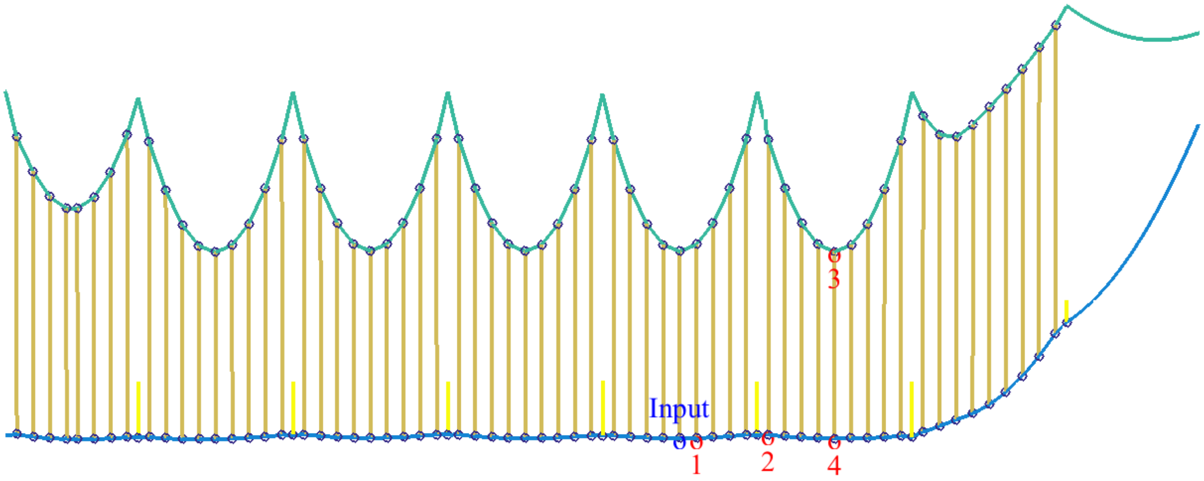

Figure A.1: Sensors (red) and input (blue) for configuration A

Test	Input		Sampling [Hz]	Tension [kN]	
	Position	Mass [kg]		CW	MW
1	1	40.6	1000	20	14

A.2 Configuration B

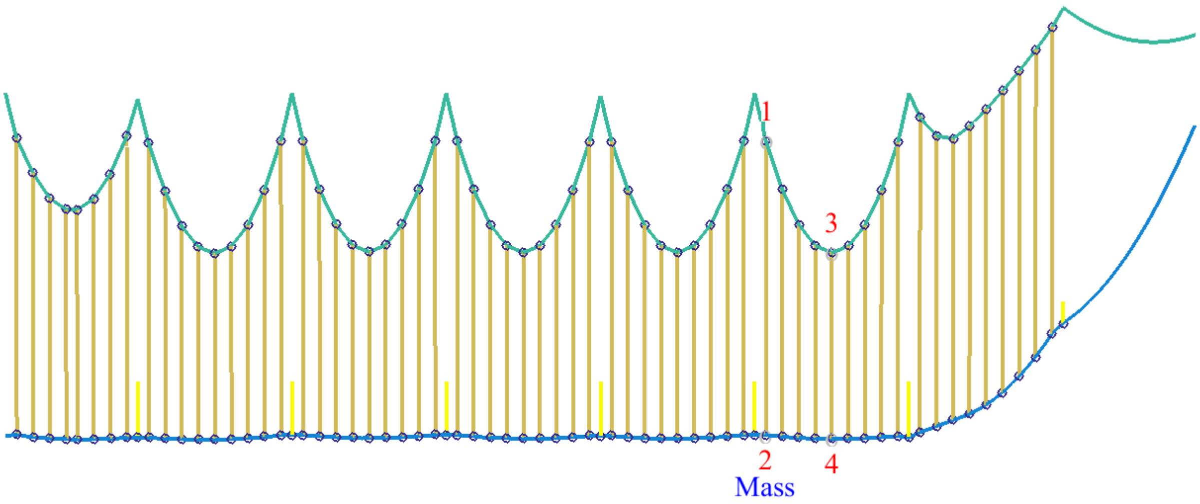

Figure A.2: Sensors (red) and input (blue) for configuration B

Test	Input		Sampling [Hz]	Tension [kN]	
	Position	Mass [kg]		CW	MW
2	1	40.6	500	20	14
3	2	20.2	500	20	14

A.3 Configuration C

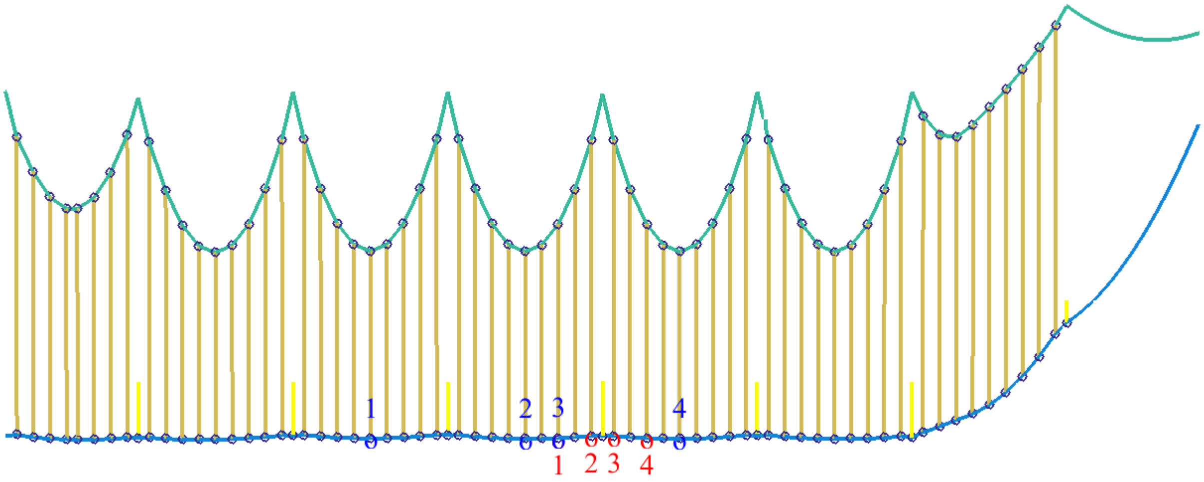

Figure A.3: Sensors (red) and input (blue) for configuration C

Test	Input		Sampling [Hz]	Tension [kN]	
	Position	Mass [kg]		CW	MW
4	1	40.6	1000	20	14
5	2	9.46	1000	20	14
6	2	40.6	1000	20	14
7	3	40.6	1000	20	14
8	4	40.6	1000	20	14

A.4 Configuration D

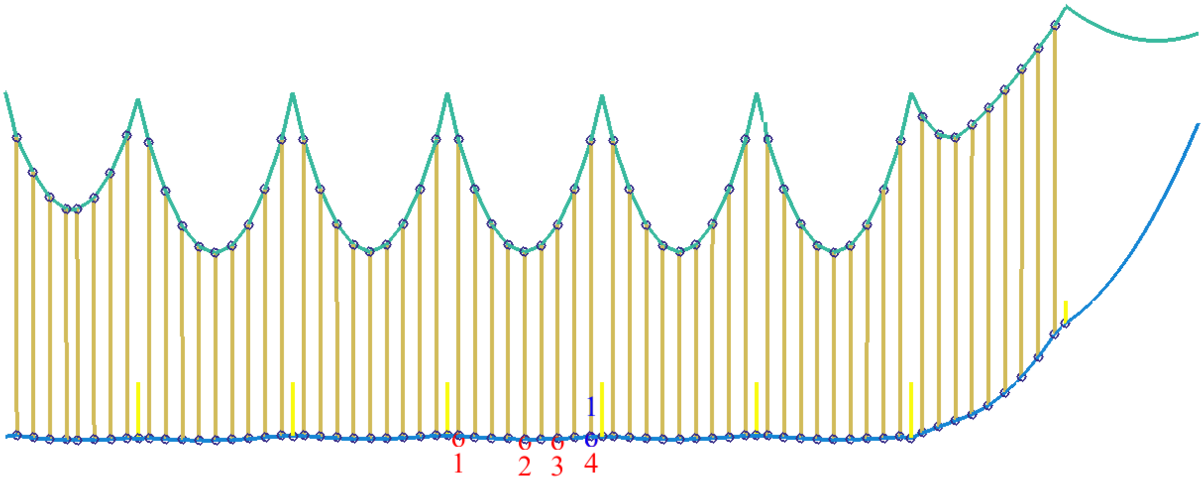

Figure A.4: Sensors (red) and input (blue) for configuration D

Test	Input		Sampling [Hz]	Tension [kN]	
	Position	Mass [kg]		CW	MW
9	1	40.6	1000	20	14

A.5 Configuration E

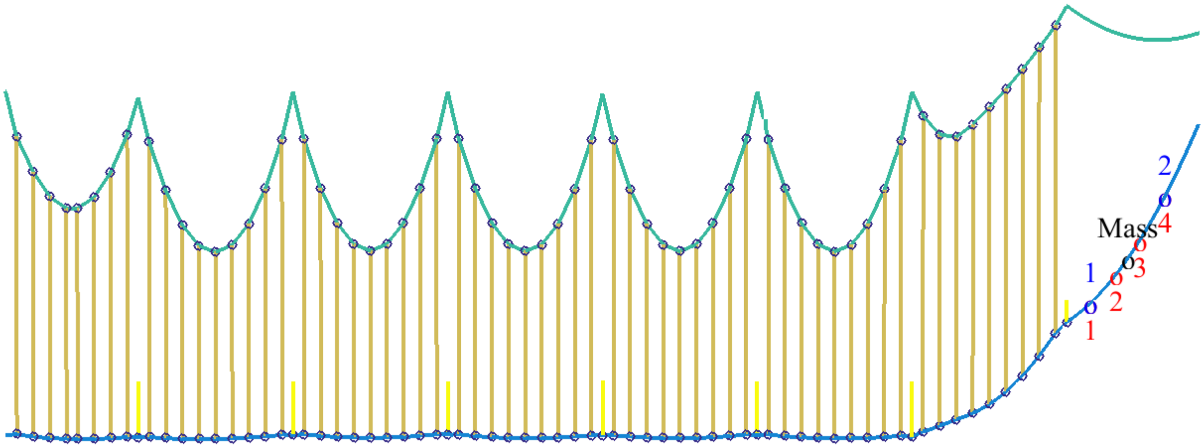

Figure A.5: Sensors (red) and input (blue) for configuration E

Test	Input		Sampling [Hz]	Middle mass [kg]	Tension [kN]	
	Position	Mass [kg]			CW	MW
10	1	20.2	1000	0	18	14
11	1	20.2	1000	0	19	14
12	1	20.2	1000	0	20	14
13	1	20.2	1000	4.87	20	14
14	1	20.2	1000	9.6	20	14
15	1	40.6	1000	0	20	14
16	2	20.2	1000	0	20	14

A.6 Configuration F

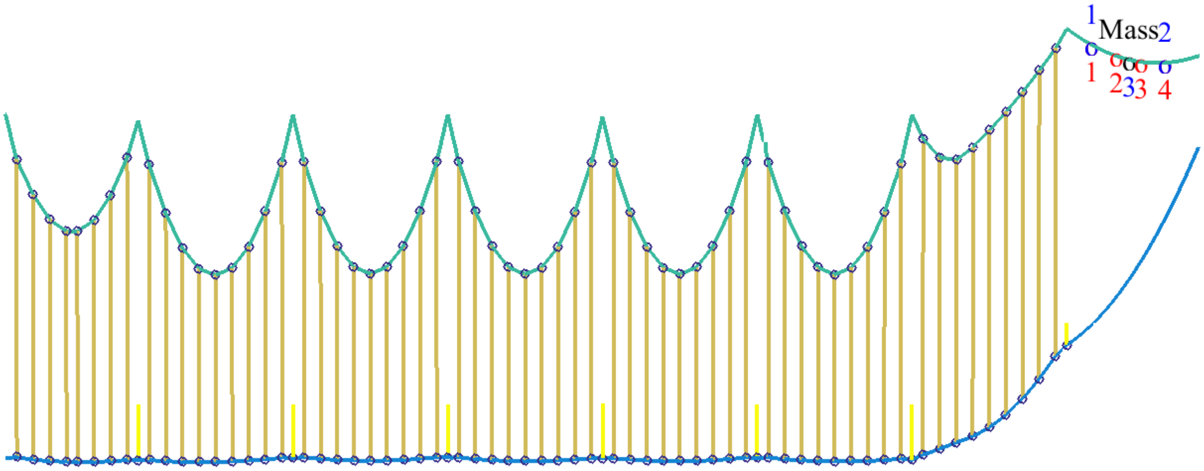

Figure A.6: Sensors (red) and input (blue) for configuration F

Test	Input		Sampling [Hz]	Middle mass [kg]	Tension [kN]	
	Position	Mass [kg]			CW	MW
17	1	20.2	1000	0	20	14
18	2	20.2	1000	0	20	14
19	3	9.6	1000	0	20	14

Appendix B

Damping identifications

B.1 test 1

Frequency [Hz]	Damping [‰]
0.88	3.70
0.90	2.19
0.93	2.31
0.95	8.13
0.99	2.57
1.01	4.03
1.72	1.50
1.76	1.37
1.82	1.08
1.86	1.34
1.90	0.96
1.94	1.16
1.99	1.31
2.03	1.59
2.58	0.85
2.64	1.02
2.74	3.56
2.80	1.24
2.89	1.35
3.02	1.93
6.08	1.15
6.30	0.85
6.48	0.78
6.64	1.00
6.64	0.98

B.2 test 2

Frequency [Hz]	Damping [‰]
0.87	1.60
0.92	1.84
0.93	1.96
0.98	2.57
1.00	2.97
1.70	0.79
1.74	0.87
1.80	1.33
1.84	2.40
1.87	1.33
1.91	1.28
1.96	1.00
2.00	0.77
3.88	2.33
3.97	3.18
4.34	1.59
5.74	1.63
5.87	3.07
6.00	1.87
6.42	1.79
6.47	5.01
6.56	1.40

B.3 test 3

Frequency [Hz]	Damping [‰]
0.86	2.03
0.92	1.41
0.93	1.86
1.00	3.44
1.69	0.92
1.73	1.53
1.80	1.68
1.85	1.67
1.85	1.10
1.86	0.85
1.95	0.55
2.54	0.55
2.60	0.61
2.69	0.73
2.91	1.24
2.98	1.28
6.10	1.44
6.22	1.20
6.30	1.99
6.40	1.19
6.66	1.29
6.75	0.53

B.4 test 4

Frequency [Hz]	Damping [‰]
0.90	3.08
0.94	2.00
0.97	0.55
1.00	5.26
1.71	1.84
1.75	1.87
1.80	1.94
1.84	4.29
1.88	1.44
1.94	0.96
2.01	1.27
2.04	2.03
2.10	2.00
2.57	1.33
2.64	2.90
2.68	1.69
2.73	1.32
2.77	1.42
2.84	2.21
2.88	1.03
2.96	0.93
3.02	0.51
6.07	0.44
6.20	1.10
6.49	0.96
6.64	0.44

B.5 test 5

Frequency [Hz]	Damping [‰]
0.88	5.75
0.90	2.94
0.94	1.86
0.97	2.19
1.00	2.28
1.01	1.43
1.70	0.16
1.74	1.14
1.81	0.88
1.85	1.00
1.97	0.35
2.01	0.69
2.55	0.51
2.62	0.94
2.72	0.60
2.77	0.93
2.87	0.58
2.94	0.42
3.01	0.43
6.15	0.72
6.27	0.65
6.36	0.61
6.49	1.44
6.74	0.28

B.6 test 6

Frequency [Hz]	Damping [‰]
0.90	3.84
0.94	3.82
1.01	2.77
1.70	0.47
1.74	9.14
1.81	1.76
1.93	1.35
1.97	0.98
2.01	0.61
2.56	0.88
2.60	2.92
2.62	0.94
2.65	2.38
2.70	2.45
2.77	0.99
2.81	0.71
2.88	0.35
2.95	1.45
3.01	0.18
3.03	1.12
3.09	1.98
5.91	0.25
6.28	0.65
6.36	0.39
6.49	0.50
6.63	0.63
6.75	0.33

B.7 test 7

Frequency [Hz]	Damping [‰]
0.90	2.88
0.94	2.47
0.97	2.32
0.98	4.07
0.99	4.75
1.01	1.72
1.70	1.32
1.74	1.32
1.80	4.82
1.84	1.22
1.89	2.05
1.93	1.67
1.98	3.72
2.01	1.19
2.62	1.83
2.77	1.33
2.81	1.06
2.87	0.44
3.01	0.42
6.15	1.75
6.26	0.86
6.31	0.88
6.35	0.65
6.47	1.16
6.62	0.29
6.72	1.08
6.83	0.58

B.8 test 8

Frequency [Hz]	Damping [‰]
0.88	4.06
0.90	2.99
0.94	2.53
1.00	1.44
1.01	1.77
1.71	0.89
1.75	1.29
1.81	1.54
1.84	3.68
1.94	1.20
1.97	2.33
1.98	1.43
2.02	0.64
2.58	4.52
2.63	1.14
2.69	1.45
2.76	1.61
2.78	0.79
2.83	1.81
2.88	0.67
5.91	0.65
6.06	0.75
6.16	1.99
6.27	0.55

B.9 test 9

Frequency [Hz]	Damping [‰]
0.91	7.90
0.95	1.50
0.98	3.29
1.00	1.73
1.01	1.98
1.72	2.55
1.75	2.28
1.77	1.90
1.81	3.53
1.84	2.75
1.85	2.40
1.86	1.46
1.87	3.66
1.89	2.61
1.90	2.89
1.94	2.09
1.95	2.29
1.96	1.39
2.02	4.11
2.03	6.81
6.12	0.93
6.33	1.31
6.36	0.86
6.44	0.83
6.54	1.06
6.81	0.58

B.10 test 10

Frequency [Hz]	Damping [‰]
1.07	1.32
2.11	1.14
3.13	1.55
3.16	3.08
4.11	2.90
4.19	4.96
5.01	6.35
6.78	1.81
8.83	2.86
9.91	2.63

Appendix C

Application of the maximum entropy principle

In this section, one discusses about a particular example to choose a parametric distribution using the maximum entropy principle. Other cases can be found in literature and are summarized after.

C.1 Problem

The problem is to identify the probability density function ($p.d.f.$), $p(x)$ which maximizes the uncertainty by applying the maximum entropy principle [9], satisfying the conditions imposed. In this example, these conditions are fixed by the following hypotheses.

- Let $\underline{\mathbf{X}}$ be a random vector of dimension 1 defined by its *p.d.f.* $p(x)$
- $p(x)$ is supposed strictly positive: $\mathcal{C}_{\text{par}} = \mathbb{R}_+^*$
- The expectation of $p(x)$ is supposed to be known : $E\{p(x)\} = \mu$
- The expectation of the logarithm of $\underline{\mathbf{X}}$ is bounded: $E(\log \mathbf{X}) = k, |k| < +\infty$

This last condition is weaker than supposing the variance known but is necessary. Supposing known the variance makes the problem more difficult to solve and not taking any condition leads to a final distribution equal to the exponential *p.d.f.* controlled by a unique parameter λ [85].

All the previous constraints lead to an admissible set $\mathcal{C}_{ad}$ of $p(x)$ defined by

$$\begin{aligned} \mathcal{C}_{ad} = &\{p : \mathcal{C}_{par} \to \mathbb{R}_+, \mathcal{C}_{par} = \mathbb{R}_+^*, \int_{\mathbb{R}_+^*} p(x)\,\mathrm{d}x = 1, \int_{\mathbb{R}_+^*} x \cdot p(x)\,\mathrm{d}x = \mu, \\ &\int_{\mathbb{R}_+^*} \log x \cdot p(x)\,\mathrm{d}x = k, |k| < +\infty\} \end{aligned} \tag{C.1}$$

The maximum entropy principle [95, 9] consists in finding the *p.d.f.* $p(x)$ inside $\mathcal{C}_{\dashv\lceil}$ (i.e. satisfying the constraints defined by the available informations) and verifying

$$p(x) = \arg\max_{p \in \mathcal{C}_{ad}} H(p) \tag{C.2}$$

With H, the entropy function defined by

$$H(p) = -\int_{\mathbb{R}_+^*} p(x) \cdot \log p(x)\, \mathrm{d}x \tag{C.3}$$

To solve this optimization problem under constraint, the Lagrange multiplier method is classically used [85]. It leads to an optimization problem without constraint. Three Lagrange coefficients $(\lambda_1, \lambda_2, \lambda_3)$ are thus introduced such that:

$$\begin{aligned} F(p, \lambda_1, \lambda_2, \lambda_3) = -\int_{\mathbb{R}_+^*} p(x) \cdot \log p(x)\, \mathrm{d}x \quad & +\lambda_1 \left[\int_{\mathbb{R}_+^*} p(x)\, \mathrm{d}x - 1 \right] \\ & +\lambda_2 \left[\int_{\mathbb{R}_+^*} x \cdot p(x)\, \mathrm{d}x - \mu \right] \\ & +\lambda_3 \left[\int_{\mathbb{R}_+^*} \log x \cdot p(x)\, \mathrm{d}x - k \right] \\ = \int_{\mathbb{R}_+^*} \mathcal{L}(x, p(x), \lambda_1, \lambda_2, \lambda_3)\, \mathrm{d}x \quad & -\lambda_1 - \lambda_2 \cdot \mu - \lambda_3 \cdot k \end{aligned}$$

With

$$\mathcal{L}(x, p, \lambda_1, \lambda_2, \lambda_3) = -p \cdot \log p + \lambda_1 p \tag{C.4}$$

The problem is now to find the set $(p, \lambda_1, \lambda_2, \lambda_3)$ which sets the derivative of $\mathcal{L}$ in p to zero,

$$\frac{\partial \mathcal{L}}{\partial p} = 0 \tag{C.5}$$

$$-1 - \log(p) + \lambda_1 + \lambda_2 \cdot x + \lambda_3 \cdot \log(x) = 0 \tag{C.6}$$

Thus,

$$p(x) = e^{\lambda_1 - 1 + \lambda_2 \cdot x} \cdot x^{\lambda_3} \tag{C.7}$$

$$p(x) = a \cdot e^{-b \cdot x} \cdot x^c \tag{C.8}$$

With $b > 0$ for the integral to be defined on $\mathbb{R}_+^*$.
Now the constraint imposed by $\mathcal{C}_{ad}$ are applied,

$$\int_{\mathbb{R}_+^*} p(x)\, \mathrm{d}x = 1 \tag{C.9}$$

$$a \cdot \int_{\mathbb{R}_+^*} e^{-b \cdot x} \cdot x^c\, \mathrm{d}x = 1 \tag{C.10}$$

$$a = \frac{1}{\int_{\mathbb{R}_+^*} x^c \cdot e^{-b \cdot x}\, \mathrm{d}x} \tag{C.11}$$

Thus,

$$p(x) = \frac{1}{\int_{\mathbb{R}_+^*} t^c \cdot e^{-b\cdot t}\,\mathrm{d}t} \cdot e^{-b\cdot x} \cdot x^{-c} \tag{C.12}$$

Then

$$\int_{\mathbb{R}_+^*} x \cdot p(x)\,\mathrm{d}x = \mu \tag{C.13}$$

$$\frac{1}{\int_{\mathbb{R}_+^*} t^c \cdot e^{-b\cdot t}\,\mathrm{d}t} \cdot \int_{\mathbb{R}_+^*} e^{-b\cdot x} \cdot x^{c+1}\,\mathrm{d}x = \mu \tag{C.14}$$

By integration by part,

$$\frac{1}{\int_{\mathbb{R}_+^*} t^c \cdot e^{-b\cdot t}\,\mathrm{d}t} \cdot \left(\left[x^{-c+1} \cdot \frac{e^{-b\cdot x}}{-b} \right]_0^{+\infty} - \int_{\mathbb{R}_+^*} (c+1)x^{-c} \cdot \frac{e^{-b\cdot x}}{-b}\,\mathrm{d}x \right) = \mu \tag{C.15}$$

$$-\frac{\int_{\mathbb{R}_+^*} t^c \cdot e^{-b\cdot t}\,\mathrm{d}t}{\int_{\mathbb{R}_+^*} t^c \cdot e^{-b\cdot t}\,\mathrm{d}t} \cdot \frac{c+1}{-b} = \mu \tag{C.16}$$

$$c = \mu \cdot b - 1 \tag{C.17}$$

Thus,

$$p(x) = \frac{1}{\int_{\mathbb{R}_+^*} t^{\mu\cdot b-1} \cdot e^{-b\cdot t}\,\mathrm{d}t} \cdot e^{-b\cdot x} \cdot x^{\mu\cdot b-1} \tag{C.18}$$

Given that the value of k is not supposed known, it is eliminated by setting arbitrary $b = \frac{1}{\delta^2\cdot\mu}$. Knowing $\mu > 0$, the condition $|k| < +\infty$ is filled.

$$p(x) = \frac{1}{\int_{\mathbb{R}_+^*} t^{\frac{1}{\delta^2}-1} \cdot e^{-\frac{t}{\delta^2\cdot\mu}}\,\mathrm{d}t} \cdot x^{\frac{1}{\delta^2}-1} \cdot e^{-\frac{x}{\delta^2\cdot\mu}} \tag{C.19}$$

By substitution $\frac{t}{\delta^2\cdot\mu} = u$, $t = u \cdot \delta^2 \cdot \mu$ and $\mathrm{d}t = \delta^2 \cdot \mu \cdot \mathrm{d}u$,

$$p(x) = \frac{1}{\int_{\mathbb{R}_+^*} (u \cdot \delta^2 \cdot \mu)^{\frac{1}{\delta^2}-1} \cdot e^{-u} \cdot \delta^2 \cdot \mu\,\mathrm{d}u} \cdot x^{\frac{1}{\delta^2}-1} \cdot e^{-\frac{x}{\delta^2\cdot\mu}} \tag{C.20}$$

$$p(x) = \left(\frac{1}{\delta^2\cdot\mu}\right)^{\frac{1}{\delta^2}} \cdot \frac{1}{\int_{\mathbb{R}_+^*} u^{1-\frac{1}{\delta^2}} \cdot e^{u}\,\mathrm{d}u} \cdot x^{\frac{1}{\delta^2}-1} \cdot e^{-\frac{x}{\delta^2\cdot\mu}} \tag{C.21}$$

$$p(x) = \frac{1}{\mu} \cdot \left(\frac{1}{\delta^2}\right)^{\frac{1}{\delta^2}} \cdot \frac{1}{\Gamma(1/\delta^2)} \cdot \left(\frac{x}{\mu}\right)^{\frac{1}{\delta^2}-1} \cdot e^{-\frac{x}{\delta^2\cdot\mu}} \tag{C.22}$$

With $\Gamma(\alpha)$ the Gamma function.

C.2 Some other dimension 1 cases found in litterature[85]

- If one knows only the expectation and variance of a random variable, the Gaussian distribution must be taken.

- If one knows the expectation, variance and that the variable is positive, it has been shown that the gamma distribution must be taken.
- If one knows the expectation and that the variable is positive, the exponential *p.d.f.* must be taken.
- If one knows nothing about a random variable, the uniform distribution between $-\infty$ and $+\infty$ must be taken.
- If one knows only the boundaries of a random variable, the uniform distribution between these boundaries must be taken.

C.3 Generalization to a random vector of dimension n

Cover has shown[96] (chapter 2) that the maximum entropy of a random vector is found when all the random variables are independent. One thus chooses to take independent distributions except if a correlation is known.

Appendix D

Variation of T_{MW} due to dilatation

The studied catenaries have messenger and contact wire tensions regulated using a system of pulley and masses as shown in figure 1.3. Variations of temperature induce shrinking or dilatation of wires. Brackets, that carry wires can rotate around the vertical axis to keep mechanical tensions in wires constant. Rotation thus induces a translation of the link between the steady arm and the contact wire and between the bracket and the messenger wire.

Coefficients of thermal expansion of contact and messenger wires are approximately the same $25°C$,

$$\begin{cases} \alpha_{th,CW} = 16.5 \cdot 10^{-6} K^{-1} \\ \alpha_{th,MW} = 17.5 \cdot 10^{-6} K^{-1}. \end{cases} \tag{D.1}$$

and will thus be approximated to $\alpha_{th} = 17 \cdot 10^{-6} K^{-1}$.

Wires are axially fixed in the middle of the catenary section by the use of anchors to avoid progressive translation of wires. The axial displacement of a point in wires can thus be computed

$$dx_{th} = \alpha_{th} \delta T D \tag{D.2}$$

where D is the distance of the observed point to the anchor and δT is the temperature variation in $°C$.

Supposing that the catenary has been tuned at a temperature of $20°C$, and knowing that the tension regulation device is designed to work in a temperature range of $[-20°C, 60°C]$, the maximum temperature variation is thus of $\delta T_{max} = 40°C$. The maximum distance to the anchor being around $700m$, the maximum axial displacement of the wires is

$$dx_{th,max} = 47.6cm. \tag{D.3}$$

This wire translation induces a rotation of brackets that can apply an axial force on wires. Taking the worst case for the contact wire, namely, all the steady arms are shifted to the maximum limit fixed by maintenance policy, $dx_{SA,i} = 10cm$, one can define the configuration shown in figure D.1.

In that configuration, considering a periodical catenary composed of spans of length $L_{Span} = 45m$, the displacement of the messenger wire at a bracket positioned at a distance of i spans to the anchor is

$$dx_{B,i} = \alpha_{th} \cdot \delta T_{max} \cdot i \cdot L_{Span}. \tag{D.4}$$

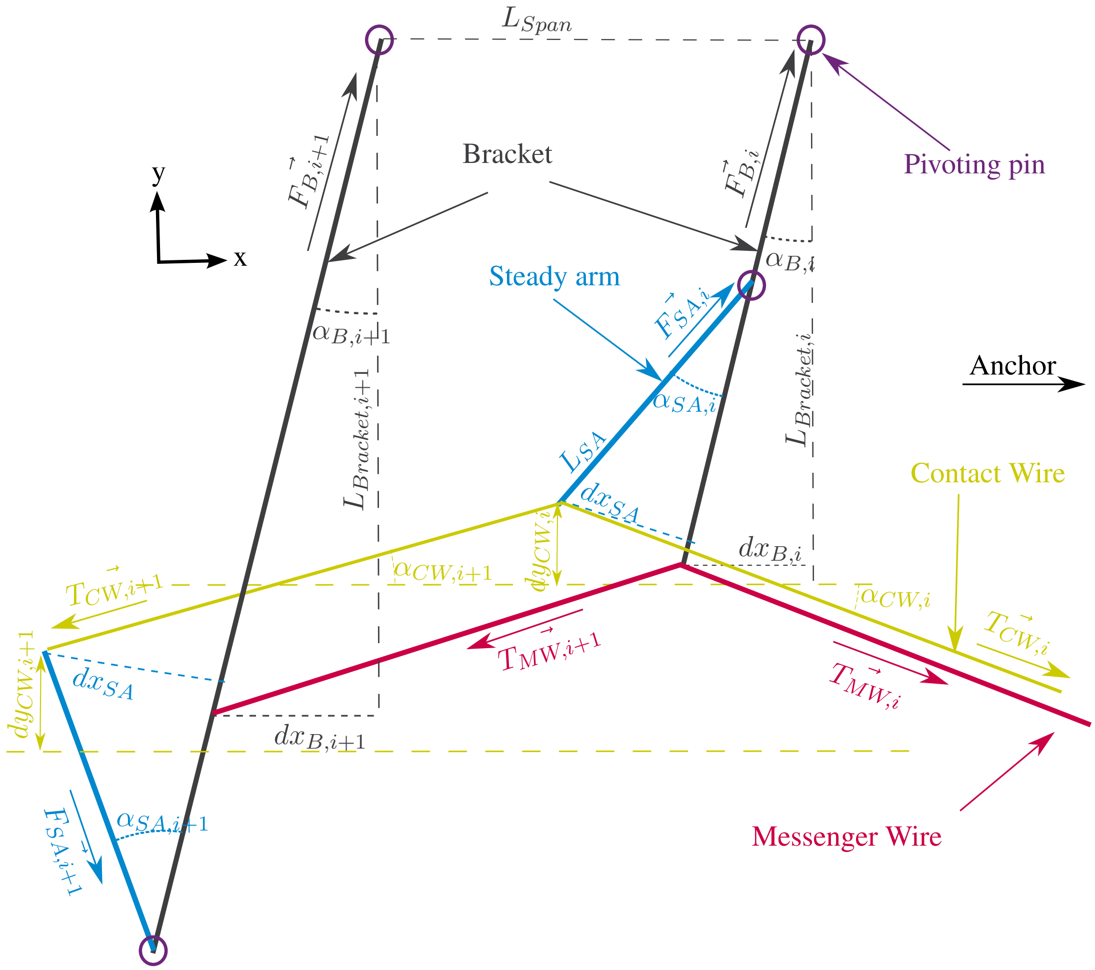

Figure D.1: Position of cantilever

The distance between the mast and the messenger wire at the bracket changes every other span to keep the stagger of $\pm 20cm$. Thus,

$$L_{Bracket,i} = 2.75 - (-1)^i \cdot Stag \tag{D.5}$$

where $Stag$ is of $20cm$ From these data, angles and transversal displacement can be computed,

$$\tan\alpha_{B,i} = \frac{dx_{B,i}}{L_{Bracket,i}} \tag{D.6}$$

$$\sin\alpha_{SA,i} = \frac{dx_{SA}}{L_{Bracket,i}} \tag{D.7}$$

$$dy_{B,i} = L_{Bracket,i} \cdot (1 - \cos\alpha_{B,i}) \tag{D.8}$$

$$dy_{SA,i} = (-1)^i \cdot L_{SA} \cdot (1 - \cos(\alpha_{SA,i} - (-1)^i \cdot \alpha_{B,i})) \tag{D.9}$$

$$dy_{CW,i} = dy_{B,i} + dy_{SA,i} \tag{D.10}$$

$$\tan\alpha_{CW,i} = \frac{Stag - (-1)^i \cdot (dy_{CW,i+1} - dy_{CW,i})}{L_{Span}} \tag{D.11}$$

Equilibrium at link between steady arm and contact wire projected on $\vec{x}$ and $\vec{y}$ gives

$$\begin{cases} F_{SA,i} \cdot \sin(\alpha_{SA,i} + \alpha_{B,i}) + T_{CW,i+1} \cdot \cos\alpha_{CW,i+1} = T_{CW,i} \cdot \cos\alpha_{CW,i} \\ F_{SA,i} \cdot \cos(\alpha_{SA,i} + \alpha_{B,i}) = T_{CW,i} \cdot \sin\alpha_{CW,i} + T_{CW,i+1} \cdot \sin\alpha_{CW,i+1} \end{cases} \tag{D.12}$$

which leads to

$$T_{CW,i+1} = T_{CW,i} \cdot \frac{\cos\alpha_{CW,i} - \tan\alpha_{SA,i} + (-1)^i \cdot \alpha_{B,i}) \cdot \sin\alpha_{CW,i}}{\cos\alpha_{CW,i+1} + \tan(\alpha_{SA,i} + \alpha_{B,i}) \cdot \sin\alpha_{CW,i+1}}. \tag{D.13}$$

Similarly, applied to the messenger wire,

$$T_{MW,i+1} = T_{MW,i} \cdot \frac{\cos\alpha_{MW,i} - \tan\alpha_{B,i} \cdot \sin\alpha_{MW,i}}{\cos\alpha_{MW,i+1} + \tan\alpha_{B,i} \cdot \sin\alpha_{MW,i+1}}. \tag{D.14}$$

Summing these series for which initial values are

$$\begin{cases} T_{CW,1} = 26kN \\ T_{MW,1} = 20kN, \end{cases} \tag{D.15}$$

leads to a cumulated maximum variation of tension between the position of the anchor and $700m$ away of around $655N$ in CW and $512N$ in MW.

Appendix E

Pies of Sobol indices

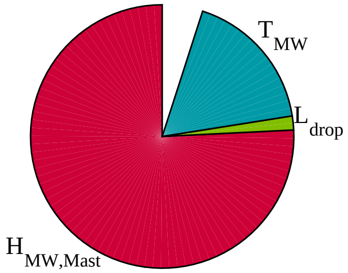
S_1 max(H_{CW})

μ=512.34cm, σ=1.55cm

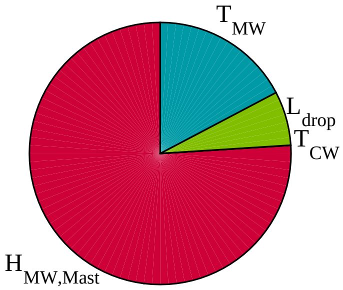
S_t max(H_{CW})

μ=512.34cm, σ=1.55cm

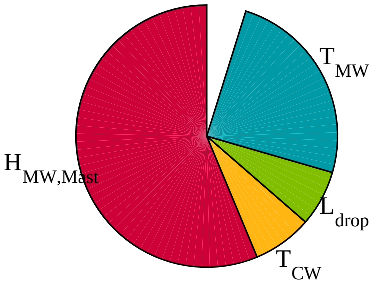
S_1 H_{CW}>5.12m

μ=2.73%, σ=5.14%

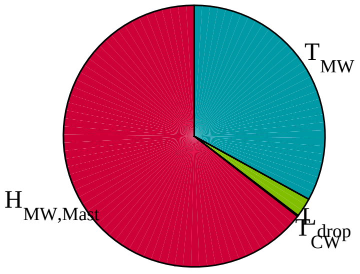
S_t H_{CW}>5.12m

μ=2.73%, σ=5.14%

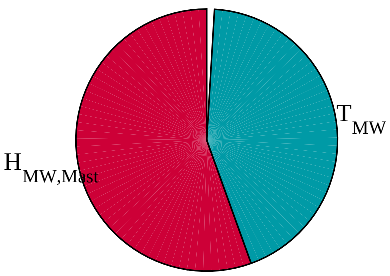

S_1 min(H_{CW})

μ=502.91cm, σ=1.85cm

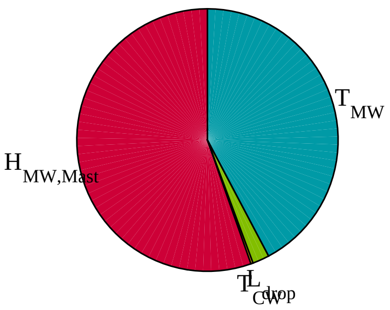

S_t min(H_{CW})

μ=502.91cm, σ=1.85cm

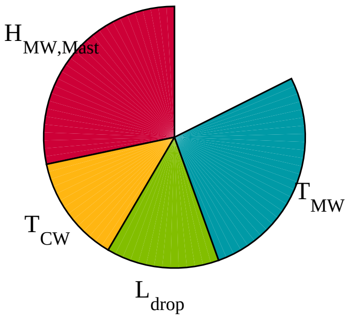

S_1 H_{CW}<5m

μ=0.23%, σ=1.24%

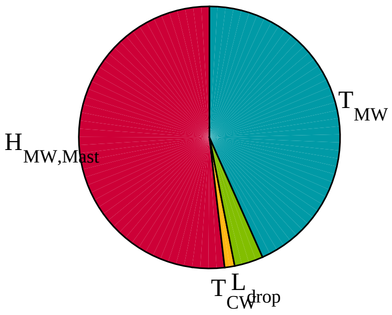

S_t H_{CW}<5m

μ=0.23%, σ=1.24%

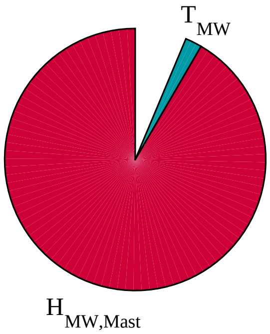

S_1 σ(H_{CW})

μ=2.04cm, σ=0.44cm

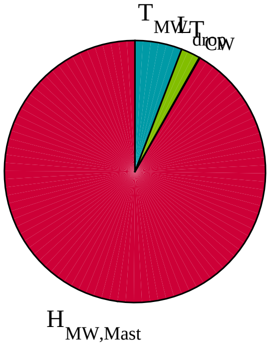

S_t σ(H_{CW})

μ=2.04cm, σ=0.44cm

S_1 $H_{CW,Mast}$>5.12m
μ=7.34%, σ=9.78%

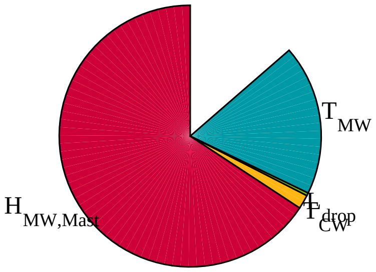

S_t $H_{CW,Mast}$>5.12m
μ=7.34%, σ=9.78%

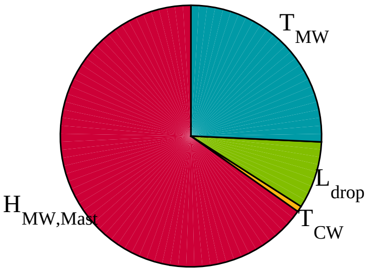

S_1 max($H_{CW,Mast}$)
μ=512.15cm, σ=1.54cm

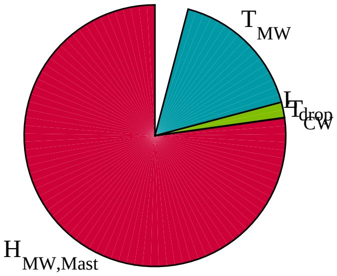

S_t max($H_{CW,Mast}$)
μ=512.15cm, σ=1.54cm

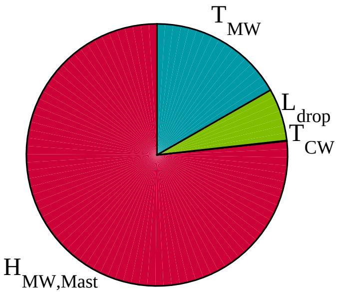

S_1 min($H_{CW,Mast}$)
μ=504.91cm, σ=1.65cm

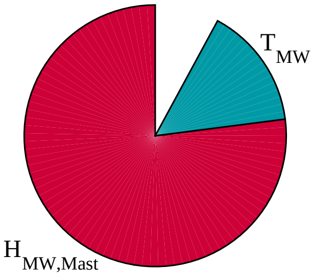

S_t min($H_{CW,Mast}$)
μ=504.91cm, σ=1.65cm

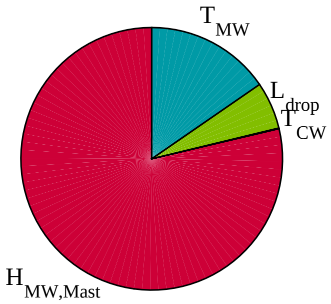

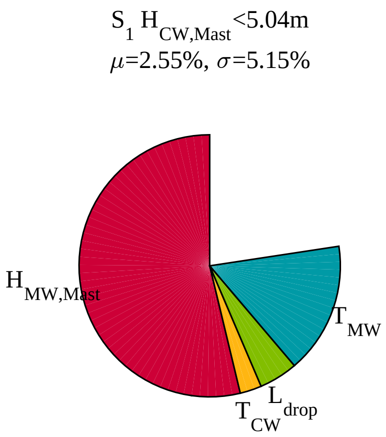

$S_1\ H_{CW,Mast}$<5.04m

μ=2.55%, σ=5.15%

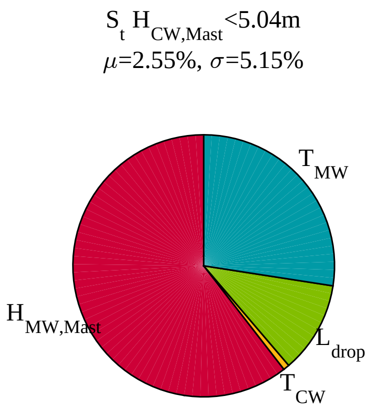

$S_t\ H_{CW,Mast}$<5.04m

μ=2.55%, σ=5.15%

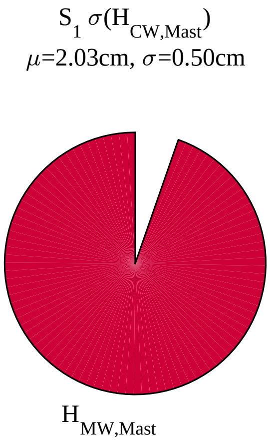

$S_1\ \sigma(H_{CW,Mast})$

μ=2.03cm, σ=0.50cm

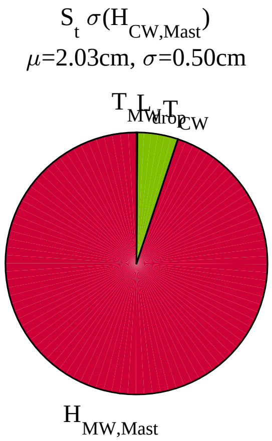

$S_t\ \sigma(H_{CW,Mast})$

μ=2.03cm, σ=0.50cm

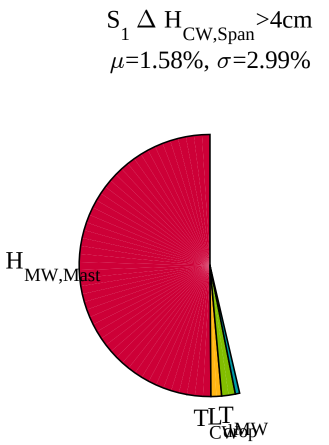

$S_1\ \Delta\ H_{CW,Span}$>4cm

μ=1.58%, σ=2.99%

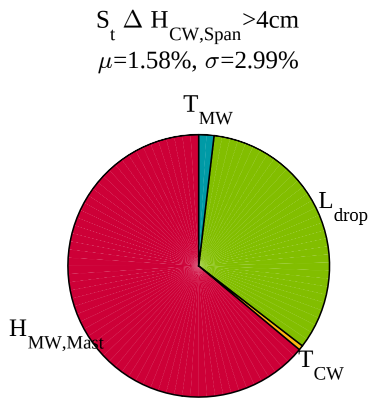

$S_t\ \Delta\ H_{CW,Span}$>4cm

μ=1.58%, σ=2.99%

$S_1 \max(\Delta H_{CW,Span})$

μ=3.34cm, σ=0.96cm

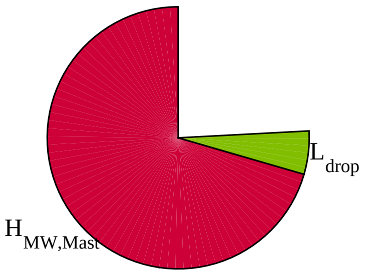

$S_t \max(\Delta H_{CW,Span})$

μ=3.34cm, σ=0.96cm

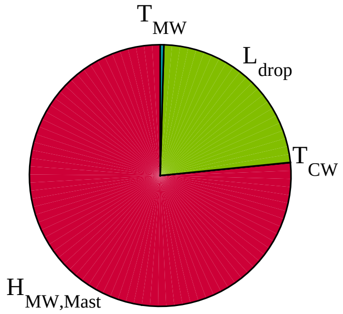

$S_1\ \Delta H_{CW,Span}$<-4cm

μ=2.59%, σ=3.72%

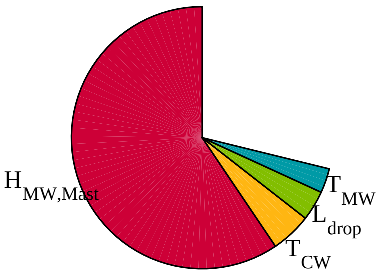

$S_t\ \Delta H_{CW,Span}$<-4cm

μ=2.59%, σ=3.72%

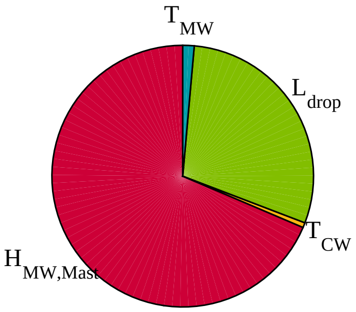

$S_1 \min(\Delta H_{CW,Span})$

μ=-3.73cm, σ=1.07cm

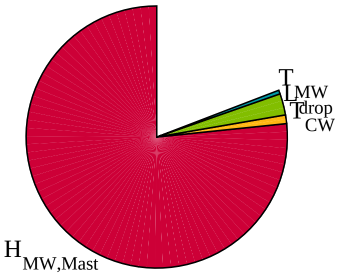

$S_t \min(\Delta H_{CW,Span})$

μ=-3.73cm, σ=1.07cm

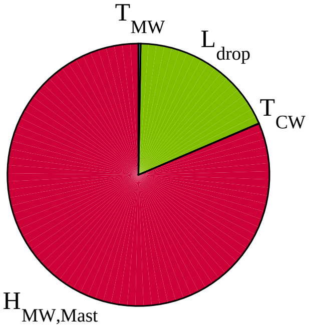

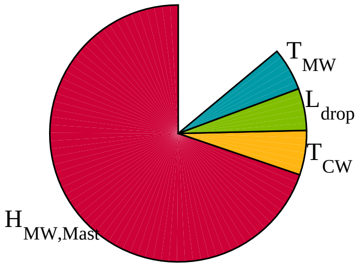

$S_1 \max(\Delta^2 H_{CW,Span})$
μ=5.00cm, σ=1.50cm

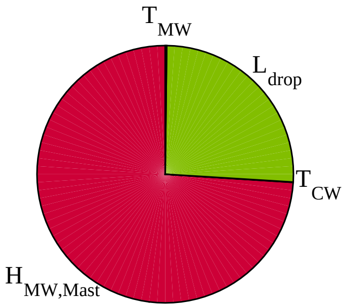

$S_t \max(\Delta^2 H_{CW,Span})$
μ=5.00cm, σ=1.50cm

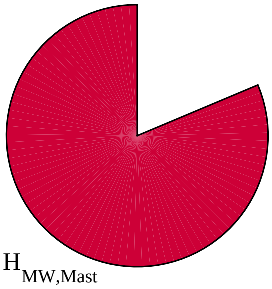

$S_1 \ \sigma(\Delta H_{CW,Span})$
μ=1.96cm, σ=0.37cm

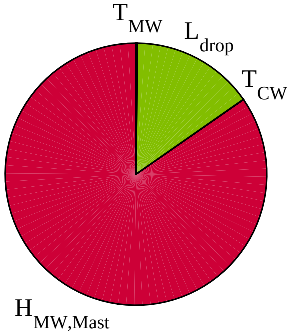

$S_t \ \sigma(\Delta H_{CW,Span})$
μ=1.96cm, σ=0.37cm

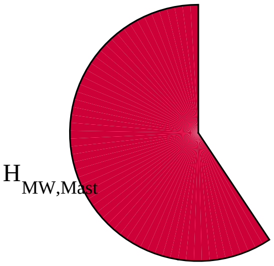

$S_1 \ \Delta^2 H_{CW,Span}$<-4cm
μ=9.69%, σ=7.18%

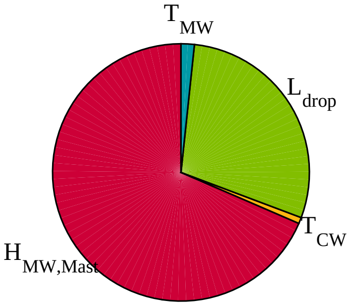

$S_t \ \Delta^2 H_{CW,Span}$<-4cm
μ=9.69%, σ=7.18%

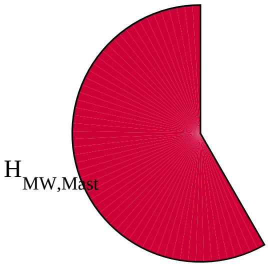

$S_1\ \Delta^2 H_{CW,Span} > 4\text{cm}$

$\mu=7.97\%,\ \sigma=6.63\%$

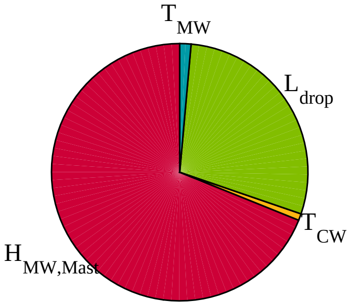

$S_t\ \Delta^2 H_{CW,Span} > 4\text{cm}$

$\mu=7.97\%,\ \sigma=6.63\%$

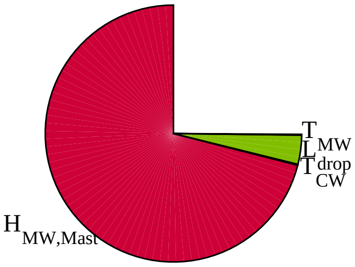

$S_1\ \min(\Delta^2 H_{CW,Span})$

$\mu=-5.33\text{cm},\ \sigma=1.56\text{cm}$

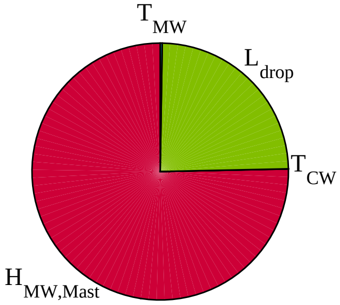

$S_t\ \min(\Delta^2 H_{CW,Span})$

$\mu=-5.33\text{cm},\ \sigma=1.56\text{cm}$

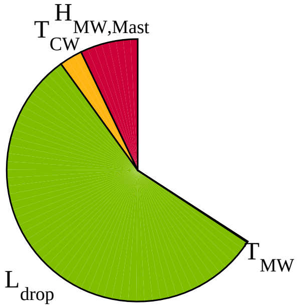

$S_1\ \max(\Delta H_{CW,Drop,Mast})$

$\mu=0.10\text{cm/m},\ \sigma=0.03\text{cm/m}$

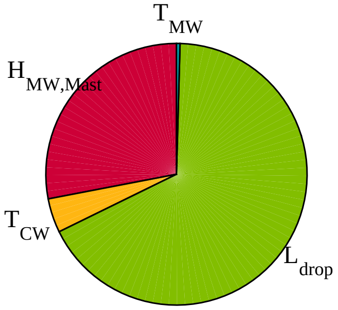

$S_t\ \max(\Delta H_{CW,Drop,Mast})$

$\mu=0.10\text{cm/m},\ \sigma=0.03\text{cm/m}$

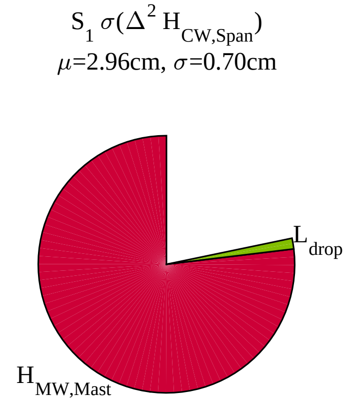
$S_1\ \sigma(\Delta^2 H_{CW,Span})$
μ=2.96cm, σ=0.70cm
L_{drop}
$H_{MW,Mast}$

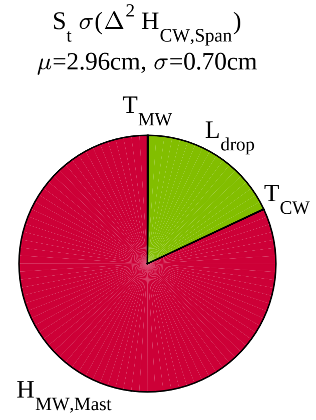
$S_t\ \sigma(\Delta^2 H_{CW,Span})$
μ=2.96cm, σ=0.70cm
T_{MW}
L_{drop}
T_{CW}
$H_{MW,Mast}$

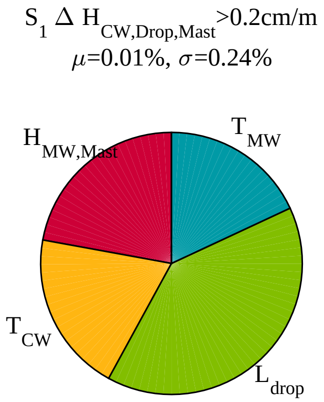
$S_1\ \Delta H_{CW,Drop,Mast}$>0.2cm/m
μ=0.01%, σ=0.24%
$H_{MW,Mast}$
T_{MW}
T_{CW}
L_{drop}

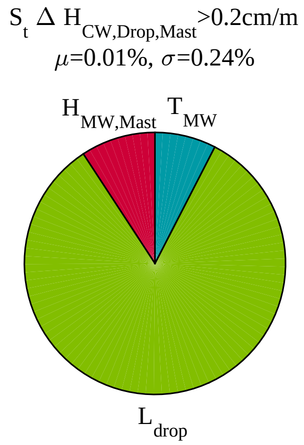
$S_t\ \Delta H_{CW,Drop,Mast}$>0.2cm/m
μ=0.01%, σ=0.24%
$H_{MW,Mast}$
T_{MW}
L_{drop}

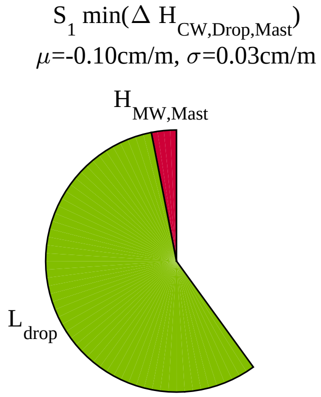
S_1 min($\Delta H_{CW,Drop,Mast}$)
μ=-0.10cm/m, σ=0.03cm/m
$H_{MW,Mast}$
L_{drop}

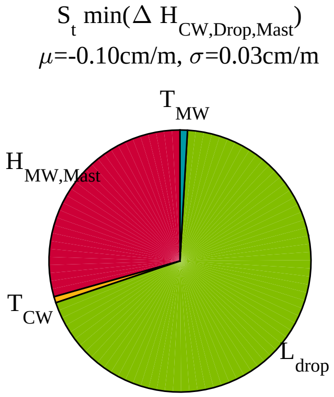
S_t min($\Delta H_{CW,Drop,Mast}$)
μ=-0.10cm/m, σ=0.03cm/m
T_{MW}
$H_{MW,Mast}$
T_{CW}
L_{drop}

$S_1\ \Delta\ H_{CW,Drop,Mast} < -0.2$cm/m
μ=0.01%, σ=0.26%

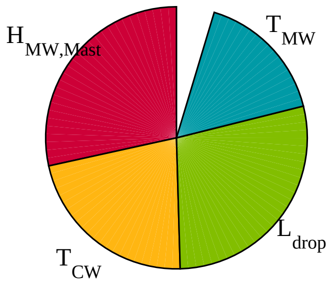

$S_t\ \Delta\ H_{CW,Drop,Mast} < -0.2$cm/m
μ=0.01%, σ=0.26%

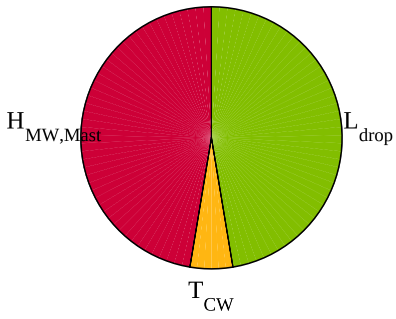

$S_1\ \sigma(\Delta\ H_{CW,Drop,Mast})$
μ=0.05cm/m, σ=0.01cm/m

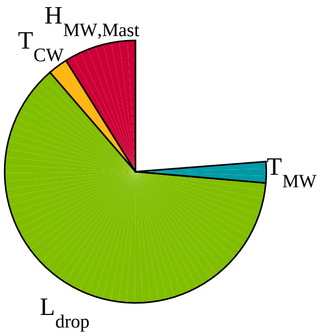

$S_t\ \sigma(\Delta\ H_{CW,Drop,Mast})$
μ=0.05cm/m, σ=0.01cm/m

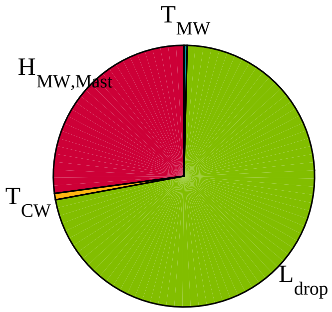

$S_1\ \max(\Delta^2\ H_{CW,Drop,Mast})$
μ=-0.00cm/m, σ=0.01cm/m

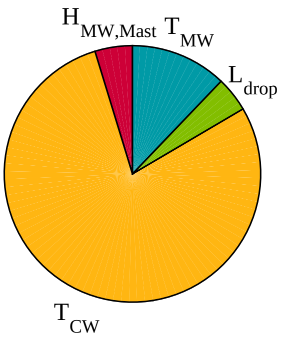

$S_t\ \max(\Delta^2\ H_{CW,Drop,Mast})$
μ=-0.00cm/m, σ=0.01cm/m

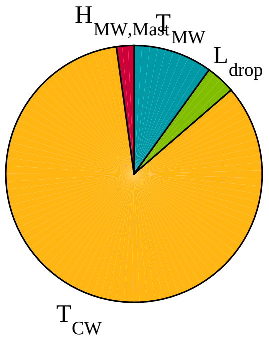

S_1 min($\Delta^2 H_{CW,Drop,Mast}$)
μ=-0.05cm/m, σ=0.01cm/m

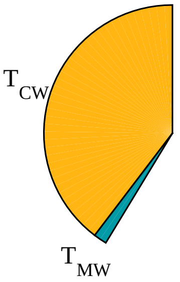

S_t min($\Delta^2 H_{CW,Drop,Mast}$)
μ=-0.05cm/m, σ=0.01cm/m

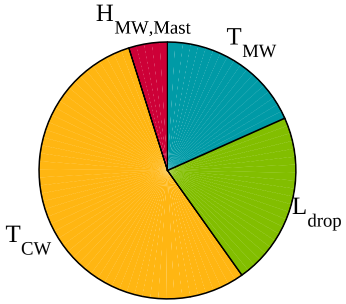

S_1 $\Delta^2 H_{CW,Drop,Mast}$<-0.05cm/m
μ=4.89%, σ=8.82%

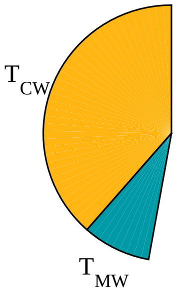

S_t $\Delta^2 H_{CW,Drop,Mast}$<-0.05cm/m
μ=4.89%, σ=8.82%

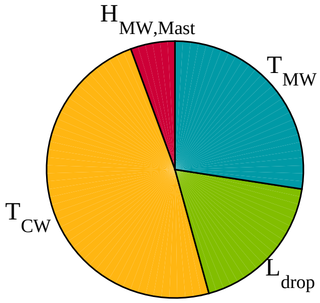

S_1 max($\Delta^2 H_{CW,Drop,Drop}$)
μ=0.02cm/m, σ=0.07cm/m

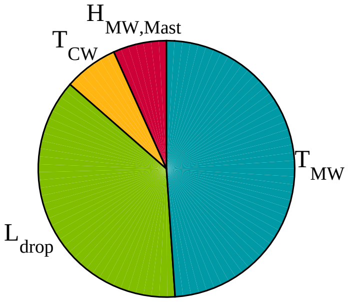

S_t max($\Delta^2 H_{CW,Drop,Drop}$)
μ=0.02cm/m, σ=0.07cm/m

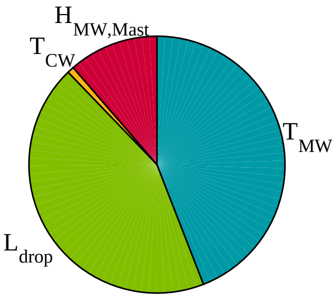

$S_1\ \sigma(\Delta^2\ H_{CW,Drop,Mast})$

μ=0.01cm/m, σ=0.00cm/m

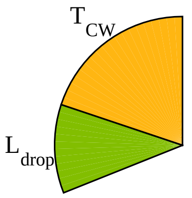

$S_t\ \sigma(\Delta^2\ H_{CW,Drop,Mast})$

μ=0.01cm/m, σ=0.00cm/m

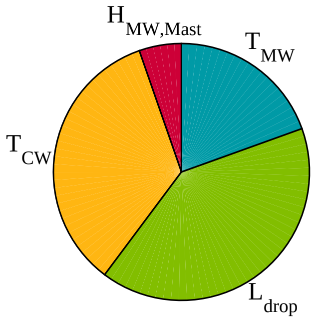

$S_1\ \Delta^2\ H_{CW,Drop,Drop}$>0.001cm/m

μ=4.19%, σ=5.32%

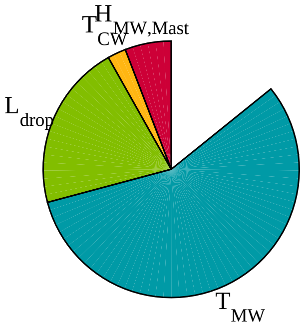

$S_t\ \Delta^2\ H_{CW,Drop,Drop}$>0.001cm/m

μ=4.19%, σ=5.32%

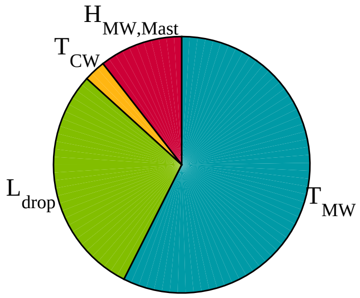

S_1 min($\Delta^2\ H_{CW,Drop,Drop}$)

μ=-0.39cm/m, σ=0.06cm/m

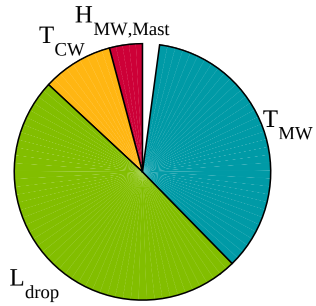

S_t min($\Delta^2\ H_{CW,Drop,Drop}$)

μ=-0.39cm/m, σ=0.06cm/m

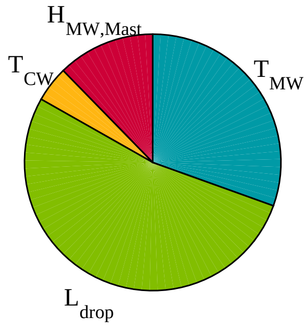

$S_1 \; \Delta^2 H_{CW,Drop,Drop} < -0.4$cm/m
μ=2.03%, σ=3.36%

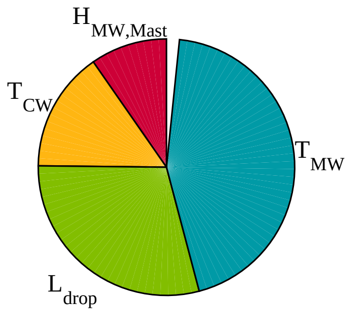

$S_t \; \Delta^2 H_{CW,Drop,Drop} < -0.4$cm/m
μ=2.03%, σ=3.36%

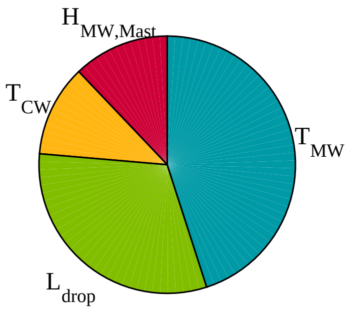

$S_1 \; \sigma(\Delta^2 H_{CW,Drop,Drop})$
μ=0.10cm/m, σ=0.01cm/m

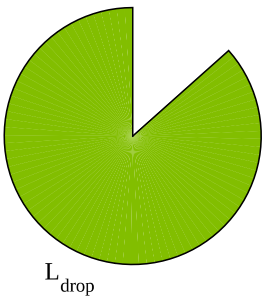

$S_t \; \sigma(\Delta^2 H_{CW,Drop,Drop})$
μ=0.10cm/m, σ=0.01cm/m

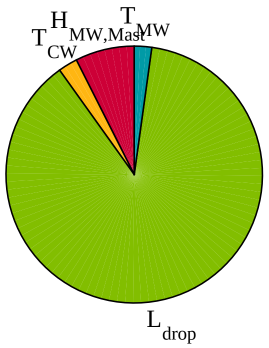

$S_1 \; Sag_{max}$
μ=0.59mm/m, σ=0.11mm/m

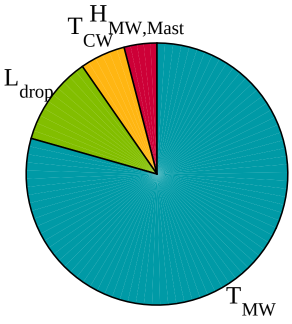

$S_t \; Sag_{max}$
μ=0.59mm/m, σ=0.11mm/m

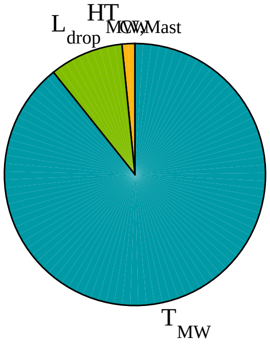

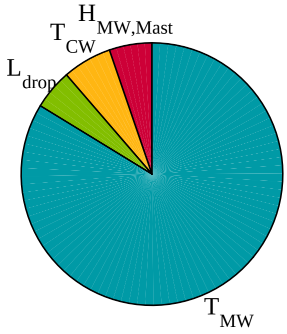

S_1 Sag>0.7mm/m

μ=4.26%, σ=14.41%

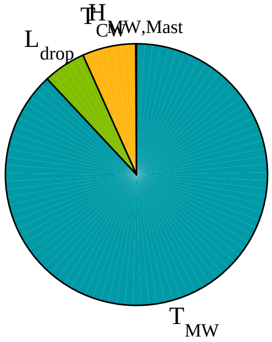

S_t Sag>0.7mm/m

μ=4.26%, σ=14.41%

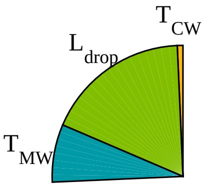

S_1 $(F_{max})_{20Hz}$

μ=279.86N, σ=10.13N

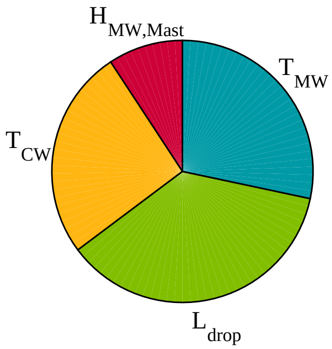

S_t $(F_{max})_{20Hz}$

μ=279.86N, σ=10.13N

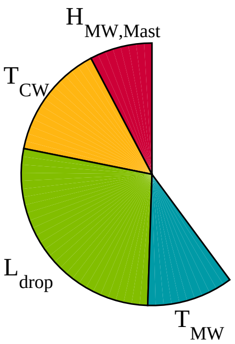

S_1 $(F_{max})_{70Hz}$

μ=345.71N, σ=17.50N

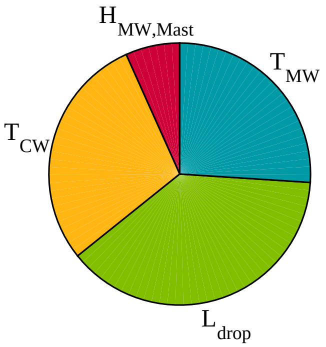

S_t $(F_{max})_{70Hz}$

μ=345.71N, σ=17.50N

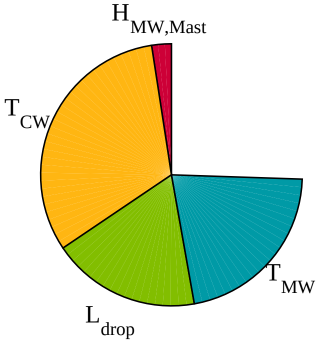

$S_1\ (F_{min})_{20Hz}$

μ=76.84N, σ=14.86N

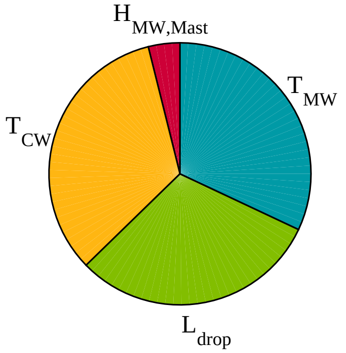

$S_t\ (F_{min})_{20Hz}$

μ=76.84N, σ=14.86N

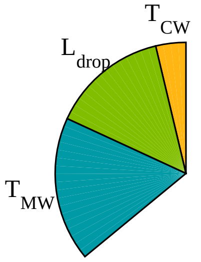

$S_1\ (F_{min})_{70Hz}$

μ=29.16N, σ=19.40N

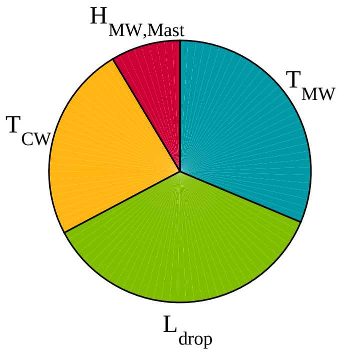

$S_t\ (F_{min})_{70Hz}$

μ=29.16N, σ=19.40N

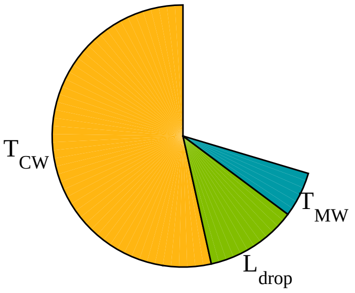

$S_1\ (\sigma/F_m)_{20Hz}$

μ=0.20 , σ=0.02

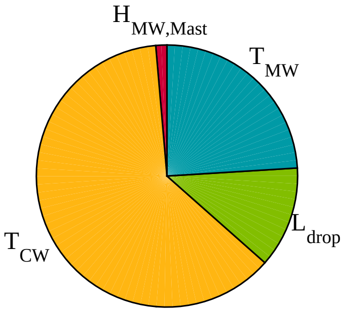

$S_t\ (\sigma/F_m)_{20Hz}$

μ=0.20 , σ=0.02

$S_1\ (\sigma/F_m)_{70Hz}$
$\mu=0.24\ ,\ \sigma=0.01$

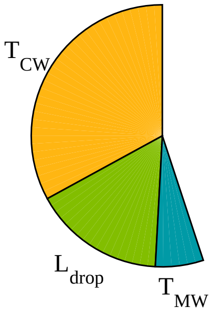

$S_t\ (\sigma/F_m)_{70Hz}$
$\mu=0.24\ ,\ \sigma=0.01$

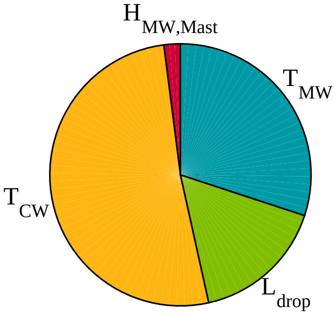

$S_1\ \max(\sigma/F_m)_{mov,\ 20Hz}$
$\mu=0.29\ ,\ \sigma=0.03$

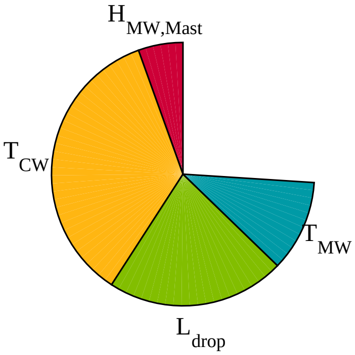

$S_t\ \max(\sigma/F_m)_{mov,\ 20Hz}$
$\mu=0.29\ ,\ \sigma=0.03$

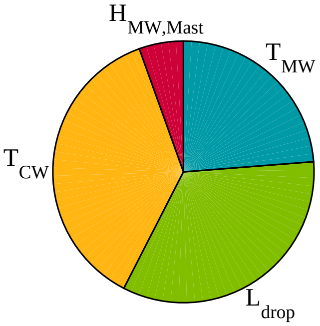

$S_1\ \max(\sigma/F_m)_{mov,\ 70Hz}$
$\mu=0.33\ ,\ \sigma=0.03$

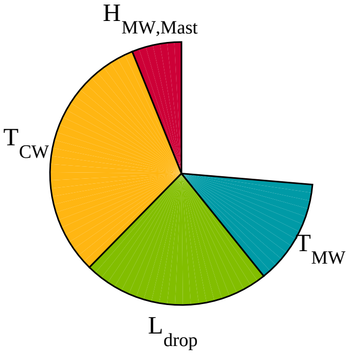

$S_t\ \max(\sigma/F_m)_{mov,\ 70Hz}$
$\mu=0.33\ ,\ \sigma=0.03$

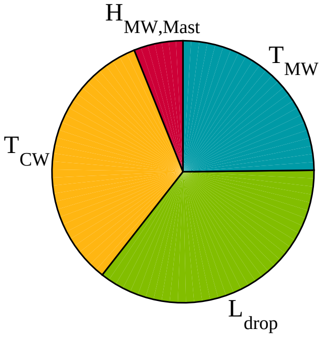

S_1 NQ_{20Hz}

μ=0.15%, σ=0.21%

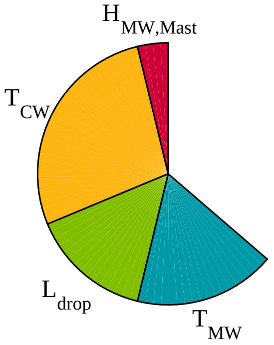

S_t NQ_{20Hz}

μ=0.15%, σ=0.21%

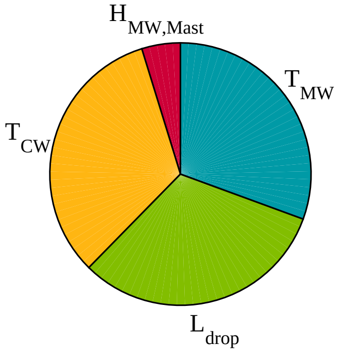

S_1 NQ_{70Hz}

μ=0.75%, σ=0.34%

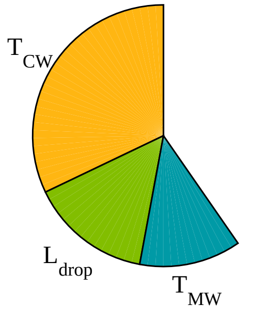

S_t NQ_{70Hz}

μ=0.75%, σ=0.34%

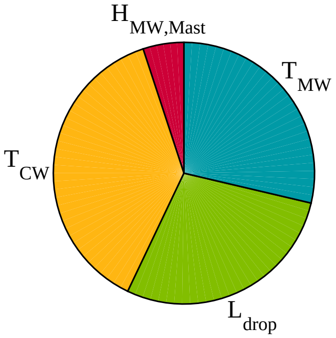

S_1 max(Uplift)

μ=7.61cm, σ=0.44cm

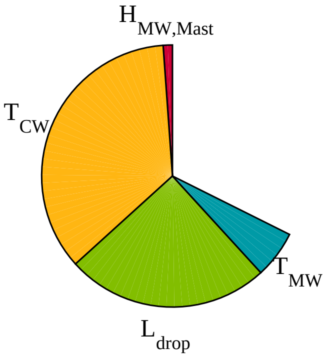

S_t max(Uplift)

μ=7.61cm, σ=0.44cm

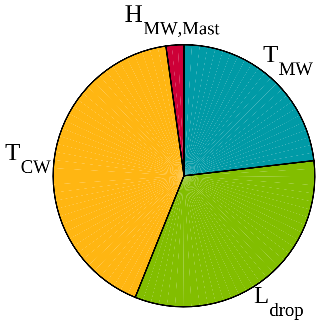

Bibliography

[1] J.-P. Massat. “Modélisation du comportement dynamique du couple pantographe-caténaire. Application à la détection de défauts dans la caténaire”. PhD thesis. Ecole centrale de Lyon, 2007, p. 204.

[2] AFNOR. “Railway application - Current collection systems - Requirements for and validation of measurements of the dynamic interaction between pantograph and overhead contact line”. In: *NF EN50317* (2002).

[3] SNCF. “Collection of standards for overhead contact lines AC/25kV/50Hz”. In: *Internal Report - IN 1797* (2006).

[4] S. Bruni et al. “The results of the pantograph - catenary interaction benchmark”. In: *Vehicle System Dynamics* 53.2 (2014), pp. 1–24. DOI: `10.1080/00423114.2014.953183`.

[5] X. Shi and A. a. Polycarpou. “Measurement and Modeling of Normal Contact Stiffness and Contact Damping at the Meso Scale”. In: *Journal of Vibration and Acoustics* 127.February (2005), p. 52. DOI: `10.1115/1.1857920`.

[6] J.-P. Bianchi et al. “Using modal damping for full model transient analysis . Application to pantograph / catenary vibration .” In: *ISMA* (2010), pp. 1167–1180.

[7] AFNOR. “Railway applications - Fixed installations - Electric traction overhead contact lines”. In: *NF EN50119* (2003).

[8] C. Soize. “Identification of high-dimension polynomial chaos expansions with random coefficients for non-Gaussian tensor-valued random fields using partial and limited experimental data”. In: *Computer Methods in Applied Mechanics and Engineering* 199 (2010), pp. 2150–2164. DOI: `10.1016/j.cma.2010.03.013`.

[9] E. T. Jaynes. “Information theory and statistical mechanics. II”. In: *Physical Review* 108.2 (1957), pp. 171–190. DOI: `10.1103/PhysRev.108.171`.

[10] A. Hald. “On the History of Maximum Likelihood in Relation to Inverse Probability and Least Squares”. In: *Statistical Science* 14 (1999), pp. 214–222. DOI: `10.1214/ss/1009212248`.

[11] OpenTURNS. *Reference Guide*. 2015.

[12] I. M. Sobol. “Global sensitivity indices for nonlinear mathematical models and their Monte Carlo estimates”. In: *Mathematics and Computers in Simulation* 55.1-3 (2001), pp. 271–280.

[13] T. Homma and A. Satelli. “Importance measures in global sensitivity analysis of nonlinear models”. In: *Reliability Engineering & System Safety* 52.1 (1996), pp. 1–17.

[19] ERA. *Guide for the application of the INF TSI*. Tech. rep. 2015, pp. 1–54.

[20] The European Commission. “COMMISSION REGULATION on the technical specifications for interoperability (TSI) relating to the ’energy’ subsystem of the rail system in the Union”. In: *Official Journal of the European Union* 57.1301 (2014), pp. 179–227.

[21] F. Resta, A. Collina, and F. Fossati. “Actively controlled pantograph: an application”. In: *IEEE/ASME International Conference on Advanced Intelligent Mechatronics. Proceedings*. Como, 2001, pp. 243–248.

[22] A. Collina et al. “An application of active control to the collector of an high-speed pantograph: Simulation and laboratory tests”. In: *Proceedings of the 44th IEEE Conference on Decision and Control, and the European Control Conference, CDC-ECC ’05* 2005 (2005), pp. 4602–4609. DOI: `10.1109/CDC.2005.1582888`.

[23] S. Shin, K. Eum, and J. Um. “Contact force control of Pantograph-Catenary System using Block Pulse Function”. In: *WCRR*. Montreal, 2006.

[24] B. Allotta, L. Pugi, and F. Bartolini. “Design and experimental results of an active suspension system for a high-speed pantograph”. In: *IEEE/ASME Transactions on Mechatronics* 13.5 (2008), pp. 548–557. DOI: `10.1109/TMECH.2008.2002145`.

[25] L. Pugi et al. “Design and development of an active suspension system for T-2006 Pantograph”. In: *Mechatronix* 13.5 (2008), pp. 548–557. DOI: `10.1109/TMECH.2008.2002145`.

[26] A. Pisano and E. Usai. “Contact force estimation and regulation in active pantographs: An algebraic observability approach”. In: *Asian Journal of Control* 13 (2011), pp. 761–772. DOI: `10.1002/asjc.237`.

[27] E. Mingozzi et al. “Simulation and Design of a High Speed railway Pantograph for Trenitalia S.p.A”. In: *WCRR*. Montreal, 2006.

[28] AFNOR. “Railway application - Current collection systems - Technical criteria for the interaction between pantograph and overhead line”. In: *EN50367* (2012).

[29] S. Bruni et al. “Pantograph-catenary dynamic interaction in the medium-high frequency range”. In: *Vehicle System Dynamics* 41.Supplement (2004). Ed. by M. Abe, pp. 697–706.

[30] T. Hayasaka, M. Shimizu, and K. Nezu. “Development of Contact-Loss Measuring System Using Ultraviolet Ray Detection”. In: *Quarterly Report of RTRI* 50 (2009), pp. 131–136. DOI: `10.2219/rtriqr.50.131`.

[31] L. Maurin et al. “High speed real-time contact measurements between a smart train pantograph with embedded Fibre Bragg Grating sensors and its overhead contact line”. In: *Structural Health Monitoring 2007: Quantification, Validation, and Implementation, Vols 1 and 2* (2007), pp. 1808–1815.

[32] M. Ikeda, S. Nagasaka, and T. Usuda. “Precise measurement and estimation method for overhead contact line unevenness”. In: *Electrical Engineering in Japan* 160.2 (2007), pp. 77–85. DOI: `10.1002/eej.20209`.

[33] ERA. *Report on railway vehicle authorisation Part1 - The current situation*. Tech. rep. 1.9.5. 2011, p. 57.

[34] AFNOR. “Railway application - Current collection systems - Validation of simulation of the dynamic interaction between pantograph and overhead contact line”. In: *NF EN50318* (2002).

[35] S. Kubo and K. Kato. “Effect of arc discharge on the wear rate and wear mode transition of a copper-impregnated metallized carbon contact strip sliding against a copper disk”. In: *Tribology International* 32 (1999), pp. 367–378.

[36] G. Bucca and A. Collina. “A procedure for the wear prediction of collector strip and contact wire in pantograph-catenary system”. In: *Wear* 266 (2009), pp. 46–59. DOI: 10.1016/j.wear.2008.05.006.

[37] A. Collina, S. Melzi, and A. Facchinetti. “On the prediction of wear of contact wire in OHE lines: a proposed model”. In: *Vehicle System Dynamics* 37.Supplement 1 (2002), pp. 579–592. DOI: 10.1080/00423114.2002.11666264.

[38] T. Usuda. “Estimation of Wear and Strain of Contact Wire Using Contact Force of Pantograph”. In: *Quarterly Report of RTRI* 48 (2007), pp. 170–175. DOI: 10.2219/rtriqr.48.170.

[39] T. Koyama. “Formation Mechanism of Undulating Wear on Overhead Conductor Rails due to Dynamic Characteristics of Pantographs”. In: *Quarterly Report of RTRI* 54.1 (2013), pp. 18–23.

[40] K. Dang Van and M. H. Maitournam. “On some recent trends in modelling of contact fatigue and wear in rail”. In: *Wear* 253 (2002), pp. 219–227. DOI: 10.1016/S0043-1648(02)00104-7.

[41] C. Yamashita and A. Sugahara. “Influence of Mean Stress on Contact Wire Fatigue”. In: *Quarterly Report of RTRI* 47 (2006), pp. 46–51. DOI: 10.2219/rtriqr.47.46.

[42] J.-p. Massat et al. “Fatigue analysis of catenary contact wires for high speed trains”. In: *WCRR*. 2011.

[43] A. Sugahara et al. “Improvement of Anti-fatigue Property of Contact Wire by Modifying Cross-section Shape”. In: *Quarterly Report of RTRI* 54.1 (2013), pp. 30–38.

[44] M.-L. Nguyen-Tajan et al. “Fatigue crack initiation risk analysis and crack propagation modelling in the catenary contact wire of high speed lines”. In: *WCRR*. 2013.

[45] J.-p. Massat, E. Balmes, and J.-P. Bianchi. “Use of FEM models to study fatigue of overhead contact wire”. In: *Railways*. 2016, pp. 1–20.

[46] A. Kumaniecka. “Dynamics of the catenary modelled by a periodical structure”. In: *Journal of theoretical and applied mechanics* (2008), pp. 869–878.

[47] M. Aboshi and K. Manabe. “Analyses of Contact Force Fluctuation between Catenary and Pantograph.” In: *Quarterly Report of RTRI* 41.3 (2000), pp. 182–187. DOI: 10.2219/rtriqr.41.182.

[48] J. W. Kim et al. “State sensitivity analysis of the pantograph system for a high-speed rail vehicle considering span length and static uplift force”. In: *Journal of Sound and Vibration* 303.3-5 (2007), pp. 405–427. DOI: 10.1016/j.jsv.2006.06.073.

[49] A. Bobillot, J. P. Massat, and J. P. Mentel. “Design of Pantograph-Catenary Systems by Simulation”. In: *WCRR*. 2011, pp. 1–13. DOI: 10.4203/ccp.93.2.

[50] T. Wu and M. Brennan. “Dynamic Stiffness of a Railway Overhead Wire System and Its Effect on Pantograph-Catenary System Dynamics”. In: *Journal of Sound and Vibration* 219 (1999), pp. 483–502. DOI: 10.1006/jsvi.1998.1869.

[51] A. V. Metrikine and A. L. Bosch. “Dynamic response of a two-level catenary to a moving load”. In: *Journal of Sound and Vibration* 292 (2006), pp. 676–693. DOI: 10.1016/j.jsv.2005.08.026.

[52] J.-P. Massat et al. “OSCAR statement of methods”. In: *Vehicle System Dynamics* 53.3 (2015), pp. 370–379. DOI: 10.1080/00423114.2015.1005016.

[53] Y. Zhang et al. “An Analysis Method for the Correlation between Catenary Irregularities and Pantograph-catenary Contact Force”. In: *Journal of Central South University* 21.8 (2014), pp. 3353–3360. DOI: 10.1007/s11771-014-2309-5.

[54] Y. H. Cho et al. “Influence of contact wire pre-sag on the dynamics of pantographrailway catenary”. In: *International Journal of Mechanical Sciences* 52.11 (2010), pp. 1471–1490. DOI: 10.1016/j.ijmecsci.2010.04.002.

[55] C. Gomez et al. “A model to obtain optimal designs of railway overhead knuckle junctions using simulation”. In: *Simulation Modelling Practice and Theory* 26 (2012), pp. 16–31. DOI: 10.1016/j.simpat.2012.03.010.

[56] M. Aboshi and M. Tsunemoto. “Installation Guidelines for Shinkansen High Speed Overhead Contact Lines”. In: *Quarterly Report of RTRI* 52.4 (2011), pp. 230–236.

[57] M. Nessi. “Modellazione matmatica e identifaicazione dei parametri per la simulazione dell’interazione dinamica tra pantografo e catenaria”. PhD thesis. Politecnico Di Milano, 2010, p. 103.

[58] Vibratec. *Analyse numérique et expérimentale d’un pantographe*. Tech. rep. 2007, p. 123.

[59] F. G. Rauter et al. “Multi body Modeling of Pantographs for Pantograph- Catenary Interaction”. In: *Third European Conference on Computational Mechanics Solids, Structures and Coupled Problems in Engineering*. June. Lisbon, 2006, pp. 205–226.

[60] A. Matvejevs and A. Matvejevs. “Pantograph-Catenary System Modeling Using MATLAB-Simulink Algorithms”. In: *Scientific Journal of Riga Technical University. Computer Sciences* 42 (2010), pp. 38–44. DOI: 10.2478/v10143-010-0039-1.

[61] J. Ambrósio et al. “A computational procedure for the dynamic analysis of the catenary-pantograph interaction in high-speed train”. In: *Journal of theoretical and applied mechanics* 50.3 (2012), pp. 681–699.

[62] P. Antunes et al. “Development of a computational tool for the dynamic analysis of the pantograph-catenary interaction for high-speed trains”. In: *Civil-Comp Proceedings* 99 (2012), pp. 1–25.

[63] J.-P. Massat et al. “Pantograph catenary dynamic optimisation based on advanced multibody and finite element co-simulation tools”. In: *Vehicle System Dynamics* 52 (2014), pp. 338–354. DOI: 10.1080/00423114.2014.898780.

[64] J. Pombo and J. Ambrósio. “Influence of pantograph suspension characteristics on the contact quality with the catenary for high speed trains”. In: *Computers and Structures* 110-111 (2012), pp. 32–42. DOI: 10.1016/j.compstruc.2012.06.005.

[65] T. J. Park, C. S. Han, and J. H. Jang. “Dynamic sensitivity analysis for the pantograph of a high-speed rail vehicle”. In: *Journal of Sound and Vibration* 266.2 (2003), pp. 235–260. DOI: 10.1016/S0022-460X(02)01280-4.

[66] A. Facchinetti and M. Mauri. "Hardware in the loop test-rig for pantograph active control evaluation". In: *IEEE International Symposium on Industrial Electronics* (2008), pp. 2171–2176. DOI: `10.1109/ISIE.2008.4677159`.

[67] A. Facchinetti and S. Bruni. "Hardware-in-the-loop hybrid simulation of pantographcatenary interaction". In: *Journal of Sound and Vibration* 331.12 (2012), pp. 2783–2797. DOI: `10.1016/j.jsv.2012.01.033`.

[68] F. Labergri. "Modélisation du comportement dynamique du système pantographe-caténaire". PhD thesis. Ecole Centrale L, 2000, p. 183.

[69] The European Commission. *EUROPAC - Publishable Final Activity Report*. Tech. rep. 2.0. 2008, pp. 1–13.

[70] M. Geradin and D. J. Rixen. *Mechanical Vibrations: Theory and Application to Structural Dynamics, 2nd Edition*. Ed. by Masson. Wiley, 1996.

[71] P. M. Morse. *Vibration and Sound*. Ed. by G. HARNWELL. 2nd ed. McGraw-Hill, 1948, p. 468. DOI: `10.1126/science.85.2211.479-a`.

[72] H.-C. Wu et al. "Structural Modeling of Double-Braided Synthetic Fiber Ropes". In: *Textile Research Journal* 65 (1995), pp. 619–631. DOI: `10.1177/004051759506501101`.

[73] T. Vu, D. Durville, and P. Davies. "Finite element simulation of the mechanical behavior of synthetic braided ropes and validation on a tensile test". In: *International Journal of Solids and Structures* 58 (2015), pp. 106–116. DOI: `10.1016/j.ijsolstr.2014.12.022`.

[74] E. Barthel. "Acoustic Scanning Probe Microscopy". In: *Acoustic Scanning Probe Microscopy*. 2013, pp. 21–47. DOI: `10.1007/978-3-642-27494-7`.

[75] V. Popov. "Rigorous Treatment of Contact Problems - Hertzian Contact". In: *Contact Mechanics and Friction - Physical Principles and Applications*. 1st ed. Springer-Verlag Berlin Heidelberg, 2010. Chap. 6, pp. 55–70. DOI: `10.1007/978-3-642-10803-7`.

[76] T. Bausseron. "Etude de l'échauffement du fil de contact de la caténaire lors du captage à l'arrêt - développement d'un outil de simulation". PhD thesis. Université de Franche-Compté, 2014, p. 186.

[77] D. Chamoret et al. "New smoothing procedures in contact mechanics". In: *Journal of Computational and Applied Mathematics* 168 (2004), pp. 107–116. DOI: `10.1016/j.cam.2003.06.007`.

[78] E. Balmes. "Frequency domain identification of structural dynamics using the pole/residue parametrization". In: *IMAC* (1996).

[79] E. Balmes. "New Results on the Identification of Normal Modes From Experimental Complex Modes". In: *Mechanical Systems and Signal Processing* 11 (1997), pp. 229–243. DOI: `10.1006/mssp.1996.0058`.

[80] L. Gaul. "Description of Damping and Applications". In: *Modal Analysis and Testing*. 1999, pp. 409–440. DOI: `10.1007/978-94-011-4503-9\_20`.

[81] T. K. Caughey. "Classical Normal Modes in Damped Linear Dynamic Systems". In: *Journal of Applied Mechanics* 27.6 (1960), pp. 583–588. DOI: `10.1115/1.3643949`.

[82] L. Rogers, C. Johnson, and D. Keinholz. "The modal strain energy finite element method and its application to damped laminated beams". In: *Shock and Vibration Bulletin* 51 (1981).

[83] L. Cremer, M. Heckl, and B. a. T. Petersson. *Structure-borne sound: Structural vibrations and sound radiation at audio frequencies*. 3rd ed. Springer-Verlag Berlin Heidelberg, 2005, pp. 1–607. DOI: `10.1007/b137728`.

[84] IGTE. *Tableaux de pendulage des portées de sectionnement et d'équipement tendeur caténaire V350 STI 20/26kN*. Tech. rep. 1992.

[85] K. Conrad. "Probability distributions and maximum entropy". In: *Entropy* (2004), pp. 1–27.

[86] R. G. Gallager. "Gaussian random vectors and processes". In: *Stochastic Processes, Theory for Applications*. Cambridge: Cambridge University Press, 2014, pp. 101–160.

[87] G. Perrin et al. "A Posteriori error and optimal reduced basis for stochastic processes defined by a finite set of realizations". In: *SIAM/ASA Journal on Uncertainty Quantification* 2 (2014), pp. 745–762. DOI: `10.1137/130905095`.

[88] S. Smith. "Moving Average Filters". In: *Digital Signal Processing: A Practical Guide for Engineers and Scientists*. Ed. by Newnes. 3rd ed. 2003. Chap. 15, pp. 277–284. DOI: `10.1016/B978-0-7506-7444-7/50052-2`.

[89] A. Saltelli et al. "Variance based sensitivity analysis of model output . Design and estimator for the total sensitivity index". In: *Computer Physics Communications* 181.2 (2010), pp. 259–270. DOI: `10.1016/j.cpc.2009.09.018`.

[90] J. Jacques, C. Lavergne, and N. Devictor. "Sensitivity analysis in presence of model uncertainty and correlated inputs". In: *Reliability Engineering & System Safety* 91.10-11 (2006), pp. 1126–1134. DOI: `10.1016/j.ress.2005.11.047`.

[91] M. J. W. Jansen, W. A. H. Rossing, and R. A. Daamen. "Monte Carlo estimation of uncertainty contributions from several independent multivariate sources". In: *Predictability and Nonlinear Modelling in Natural Sciences and Economics*. Ed. by J. Grasman and G. van Straten. SPRINGER-SCIENCE+BUSINESS MEDIA, BV., 1994. Chap. 4, pp. 334–343. DOI: `10.1007/978-94-011-0962-8`.

[92] A. Janon et al. "Asymptotic normality and efficiency of two Sobol index estimators ementine Prieur To cite this version :" in: *ESAIM: Probability and Statistics* 18 (2014), pp. 342–364.

[93] G. E. B. Archer, A. Saltelli, and I. M. Sobol. "Sensitivity measures, ANOVA-like techniques and the use of bootstrap". In: *Journal of Statistical Computation and Simulation* 58.2 (1997), pp. 99–120. DOI: `10.1080/00949659708811825`.

[94] J. Yang. "Environmental Modelling & Software Convergence and uncertainty analyses in Monte-Carlo based sensitivity analysis". In: *Environmental Modelling and Software* 26.4 (2011), pp. 444–457. DOI: `10.1016/j.envsoft.2010.10.007`.

[95] E. T. Jaynes. "Information theory and statistical mechanics. I". In: *Physical Review* 106.4 (1957), pp. 620–630. DOI: `10.1103/PhysRev.106.620`.

[96] T. M. Cover and J. a. Thomas. *Elements of Information Theory*. 2005, pp. 1–748. DOI: `10.1002/047174882X`.

External communications

[14] O. Vo Van, E. Balmes, and X. Lorang. “Damping characterization of a high speed train catenary”. In: *International Symposium on Dynamics of Vehicles on roads and tracks*. 2015. DOI: `10.1201/b21185-159`.

[15] O. Vo Van et al. “Introduction of variability into pantograph- catenary dynamic simulations”. In: *Vehicle System Dynamics* 52.10 (2014), pp. 1254–1269. DOI: `10.1080/00423114.2014.922199`.

[16] O. Vo Van et al. “Introduction of Variability Into Pantograph- Catenary Dynamic Simulations”. In: *International Symposium on Dynamics of Vehicles on roads and tracks*. Qingdao, 2013, pp. 1–8.

[17] O. Vo Van, E. Balmes, and J.-p. Massat. “Statistical identification of geometric parameters for high speed train catenary”. In: *International Conference on Noise and Vibration*. Leuven, 2014, pp. 2–11.

[18] O. Vo Van et al. “Sensitivity analysis of catenary geometry on current collection quality”. In: *Proceedings of the Third International Conference on Railway Technology: Research, Development and Maintenance*. Ed. by J. Pombo. Cagliari: Civil-Comp Press, 2016, pp. 1–17. DOI: `10.4203/ccp.110.108`.

INTRODUCTION DE VARIABILITÉ DANS UN MODÈLE D'INTERACTION DYNAMIQUE PANTOGRAPHE-CATÉNAIRE

RÉSUMÉ : L'alimentation électrique des trains s'effectue en général par une interface pantographe-caténaire représentant un système mécanique couplé complexe. Les phénomènes dynamiques intervenant dans l'interaction entre le pantographe et la caténaire sont encore mal connus. Par ailleurs, le comportement dynamique du système est très variable car sensible à de nombreux paramètres. La première contribution de cette thèse est de proposer une analyse détaillée de l'interaction dynamique pantographe-caténaire en étudiant en particulier la réponse dynamique du pantographe à la géométrie de la caténaire ainsi que les propagations, réflexions et transmissions des ondes dans cette dernière. Il a ainsi été démontré que la coïncidence spatiale, temporelle ou fréquentielle de ces différents phénomènes est à l'origine de la majorité des variations des quantités d'intérêt. Par ailleurs, l'étude des ondes a montré que les pendules entourant le poteau avaient une importance particulière dans l'interaction dynamique et que les paramètres tels que le rapport des impédances dynamiques et la somme des vitesses des ondes dans les câbles étaient des variables dimensionnantes dans la caténaire. La seconde contribution a été de réduire les principales incertitudes épistémiques liées au modèle telles que l'amortissement dans la caténaire, la raideur de contact et la taille des éléments. La dernière contribution était d'implémenter des paramètres variables dans le modèle en utilisant les mesures disponibles. À partir de ce modèle aléatoire, les incertitudes ont été classées en utilisant les indices de Sobol sur des critères géométriques et dynamiques. L'absence de corrélation entre les critères géométriques et dynamique observée a des conséquences notables sur la politique de maintenance. Enfin, le grand nombre d'études de sensibilités réalisés a permis de souligner la maturité de l'outil de simulation et de proposer des orientations pour les travaux futurs pour la conception, maintenance ou homologation de pantographes ou de caténaires.

Mots clé : dynamique pantographe-caténaire, propagation d'ondes, coïncidences de fréquences, amortissement, contact, problème statistique inverse, propagation d'incertitude, qualité de captage

INTRODUCTION OF VARIABILITY INTO PANTOGRAPH-CATENARY DYNAMIC SIMULATIONS

ABSTRACT : In railways, electrical current is generally collected by the train through a complex coupled mechanical system composed of a pantograph and a catenary. Dynamic phenomena that occur during their interaction are still not fully understood. Furthermore, the system behaviour is sensitive to numerous parameters and thus highly variable. The first contribution of this thesis is a detailed analysis of the pantograph-catenary dynamic interaction separating phenomena due to the dynamic response of the pantograph to the catenary geometry from wave propagations, reflections and transmissions that occur in the catenary. The coincidence of frequencies or characteristic times is then shown to explain most variations in the quantities of interest. Moreover, droppers surrounding the mast have been shown to be particularly important in dynamic interaction. Ratio of wire impedances and sum of wave velocities also appeared to be dimensioning quantities for catenary design. The second contribution was to reduce epistemic uncertainty linked with model parameters such as catenary damping, contact stiffness and element size. The final contribution was to use the model in a configuration with random parameters. An initial step was to statistically characterise physical catenary parameters using available measurements. From this random model, ranking of uncertainties using Sobol indices on static and dynamic criteria was shown to be possible. An absence of correlation between geometric and dynamic criteria was also found, which has notable implications for maintenance policies. The high number of sensitivity studies also gave the occasion to highlight the maturity of simulation tool and propose directions for further work on design, maintenance or certification of pantographs and catenaries.

Keywords : Pantograph - catenary dynamics, wave propagation, frequency coincidences, damping, contact, statistical inverse problem, propagation of uncertainty, current collection quality